AD 723989

AD

USAAVLABS TECHNICAL REPORT 71-1

ROTOR BLADE BOUNDARY LAYER CALCULATION PROGRAMS

By

David R. Clark
Douglas R. Arnoldi

March 1971

EUSTIS DIRECTORATE
U. S. ARMY AIR MOBILITY RESEARCH AND DEVELOPMENT LABORATORY
FORT EUSTIS, VIRGINIA

U S ARMY
MATERIEL COMMAND

D D C
RECEIVED
JUN 3 1971
B

262

DISCLAIMERS

The findings in this report are not to be construed as an official Department of the Army position unless so designated by other authorized documents.

When Government drawings, specifications, or other data are used for any purpose other than in connection with a definitely related Government procurement operation, the United States Government thereby incurs no responsibility nor any obligation whatsoever; and the fact that the Government may have formulated, furnished, or in any way supplied the said drawings, specifications, or other data is not to be regarded by implication or otherwise as in any manner licensing the holder or any other person or corporation, or conveying any rights or permission, to manufacture, use, or sell any patented invention that may in any way be related thereto.

DISPOSITION INSTRUCTIONS

Destroy this report when no londer needed. Do not return it to the originator.

DOCUMENT CONTROL DATA - R & D

(Security classification of title, body of abstract and indexing annotation must be entered when the overall report is classified)

1. ORIGINATING ACTIVITY *(Corporate author)*	2a. REPORT SECURITY CLASSIFICATION
Sikorsky Aircraft Division of United Aircraft Corp. Stratford, Connecticut	Unclassified
	2b. GROUP

3. REPORT TITLE

ROTOR BLADE BOUNDARY LAYER CALCULATION PROGRAMS

4. DESCRIPTIVE NOTES *(Type of report and inclusive dates)*
Final Report

5. AUTHOR(S) *(First name, middle initial, last name)*

David R. Clark and Douglas R. Arnoldi

6. REPORT DATE	7a. TOTAL NO. OF PAGES	7b. NO. OF REFS
March 1971	260	28

8a. CONTRACT OR GRANT NO. DAAJ02-69-C-0039	9a. ORIGINATOR'S REPORT NUMBER(S)
b. PROJECT NO. Task 1F162204A14234	USAAVLABS Technical Report 71-1
c.	9b. OTHER REPORT NO(S) *(Any other numbers that may be assigned this report)*
d.	SER-50674

Approved for public release; distribution unlimited.

11. SUPPLEMENTARY NOTES	12. SPONSORING MILITARY ACTIVITY
	Eustis Directorate, U. S. Army Air Mobility Research & Development Laboratory Fort Eustis, Virginia

13. ABSTRACT

The development of the turbulent compressible boundary layer on two typical helicopter rotors, for a range of hover conditions, has been calculated using two different analytical methods: the differential method, which uses the differential form of the boundary layer momentum equations and solves for the local velocity gradients, and the integral method, which uses the integrated form of the momentum equations and solves for the development of the characteristic boundary layer thickness parameters and skew angle. Both methods decouple the chordwise and spanwise boundary layer equations without making any small crossflow assumptions. The effects of rotational speed, vortex-induced crossflows, surface curvature, and applied chordwise pressure gradients were evaluated separately and in combination to simulate rotor airfoil boundary layer growth. The effect of the rotation was found to be small. In all but the pressure gradient cases, boundary layer development along the streamwise direction followed closely two-dimensional behavior. The results from the differential method indicated that the influence of unfavorable chordwise pressure gradients is reduced in rotating flows by the presence of an inward spanwise velocity component aft of the quarter chordline. Correlation between the results predicted by the two methods is good for the characteristic thickness parameters and the surface shear stresses but poor for the calculated skew angles. The use of either, or both, of these methods should improve the prediction of surface skin friction effects in a rotating flow.

DEPARTMENT OF THE ARMY
U. S. ARMY AIR MOBILITY RESEARCH & DEVELOPMENT LABORATORY
EUSTIS DIRECTORATE
FORT EUSTIS, VIRGINIA 23604

This report has been reviewed by the Eustis Directorate,
U. S. Army Air Mobility Research and Development
Laboratory and is considered to be technically sound.
The purpose of this effort was to calculate the turbulent,
compressible boundary layer characteristics of two
representative rotors using both the integral and differ-
ential analytical methods. The program was conducted
under the technical management of Mr. John L. Shipley and
Mr. Paul H. Mirick of the Aeromechanics Division of this
Directorate.

ROTOR BLADE BOUNDARY LAYER
CALCULATION PROGRAMS

SER-50674

by

David R. Clark
and
Douglas R. Arnoldi

Prepared By

United Aircraft Corporation
Sikorsky Aircraft Division
Stratford, Connecticut

for

EUSTIS DIRECTORATE
U. S. ARMY AIR MOBILITY RESEARCH AND DEVELOPMENT LABORATORY
FORT EUSTIS, VIRGINIA

ABSTRACT

The development of the turbulent compressible boundary layer on two
typical helicopter rotors, for a range of hover conditions, has been cal-
culated using two different analytical methods. The techniques used were
the Differential Method, which employs the differential form of the
boundary layer momentum equations and solves for the local velocity
gradients before integrating them over the surface to follow the flow
development, and the Integral Method, which employs the integrated form
of the momentum equations, having assumed a velocity profile form, and
solves for the development of the characteristic boundary layer thickness
parameters and skew angle. Both methods decouple the chordwise and span-
wise boundary layer equations without making any small crossflow assump-
tions. The effects of rotational speed, vortex induced crossflows,
surface curvature and applied chordwise pressure gradients were evaluated
separately and in combination to simulate rotor airfoil boundary layer
growth. The effect of the rotation was found to be small. In all but
the pressure gradient cases, boundary layer development along the stream-
wise direction followed closely two-dimensional behavior. The results
from the Differential Method indicated that the influence of unfavorable
chordwise pressure gradients is reduced in rotating flows by the presence
of an inward spanwise velocity component aft of the quarter chord line.
The influence of typical airfoil upper surface curvature was found to be
negligible. Correlation between the results predicted by the two methods
is good for the characteristic thickness parameters and the surface shear
stresses but poor for the calculated skew angles. The use of either, or
both, of these methods should improve the prediction of surface skin
friction effects and give a more reliable definition of separation point
in a rotating flow.

BLANK PAGE

TABLE OF CONTENTS

LIST OF ILLUSTRATIONS

x

LIST OF TABLES

LIST OF SYMBOLS

a	sound speed, ft/sec
A_O, A_1, A_2	coefficients in the shear stress interpolation
B_O, B_1, B_2	coefficients in the shear stress interpolation
C	chord, ft
c	chordwise velocity ratio $\bar{u}/U_\infty$
Cp	pressure coefficient
H	shape factor
h_1, h_2, h_3	scale factors in curvilinear coordinates
i, j, k	unit vectors in x, y, and z directions
ℓ	turbulent mixing length, ft
M	Mach number
n	velocity component perpendicular to free stream, parallel to surface, ft/sec
p	static pressure, psf
Q	free-stream velocity, ft/sec
q	velocity component parallel to free stream, ft/sec
R	blade radius, ft
Re	Reynolds number
R_O	surface radius of curvature, ft
$\underline{r}$	generalized position vector
s	spanwise velocity ratio $\bar{v}/U_\infty$
T	static temperature, $^\circ K$
U	external flow velocity in chordwise direction, ft/sec
u	velocity component parallel to chordwise direction, ft/sec
u_τ	shear velocity, $(\tau_x/\rho_\infty)^{\frac{1}{2}}$

u_t	shear velocity ratio, u/u_τ
V	external flow velocity in spanwise direction, ft/sec
v	velocity component parallel to spanwise direction, ft/sec
W	external flow velocity in normal direction, ft/sec
w	velocity perpendicular to the surface, ft/sec
x	chordwise coordinate measured from quarter chord parallel to surface
Y	spanwise position of interfering vortex, ft
y	spanwise coordinate measured from axis of rotation
Z	height of vortex above blade surface, ft
z	coordinate measured locally normal to surface
α	angle between local external flow and x coordinate, deg
Γ	circulation strength, ft^2/sec
γ	specific heat ratio
δ	boundary layer thickness, ft
δ^*	displacement thickness, ft
ε	skew angle between surface flow and free-stream direction, deg
η	transformed normal coordinate
θ	momentum thickness, ft
k	constant in turbulent mixing length expression
μ	absolute viscosity, slug/(ft-sec)
ν	kinematic viscosity, ft^2/sec
ρ	density, $slug/ft^3$
τ	local shear stress, psf
ϕ	tangent of the skew angle
ψ	stream function, ft^2/sec

Ω	angular velocity, rad/sec
ω	vorticity, 1/sec

SUBSCRIPTS

a	ambient conditions
∞	conditions just outside the boundary layer
I	inertial
n	perpendicular to free-stream direction
o	surface conditions
q	free-stream direction
R	rotating
x, y, z	components in coordinate directions
ρ	change in boundary layer thickness associated with compressibility

1. INTRODUCTION

With the notable exception of von Karman's exact solution for the flow
over a rotating disk, Reference (1), all the early attempts at solutions
of the boundary layer form of the Navier-Stokes equations were restricted
to flows that could be generally classified as two dimensional; that is,
flows where the mean velocity within the boundary layer is in the same
direction as the external flow. This neglect of flows which make up the
majority of those occurring in practice is not surprising, since the number
of velocity gradient and shear stress terms which must be considered in
the full three-dimensional solution is large and at first sight intimi-
dating. Fortunately, two-dimensional solutions were found to be adequate
for most engineering applications, and activity was concentrated in this
area, with several exact and empirical solutions being found. Solutions
were based for the most part on the results of the experimental programs
which paralleled the analytical studies.

With the arrival of higher aircraft speeds and the adoption of swept lift-
ing surfaces, it became evident that two-dimensional boundary layer solu-
tions would no longer be adequate. This led to a widening of the field of
study to include the whole range of realistic cases from the early work on
the boundary layers on yawed cylinders of Reference (2) to the up-to-date
techniques discussed in References (3), (4), and (5) which make full use of
modern computing machinery and allow the calculation of boundary layer
development not only over simple surfaces but also around involved shapes.
Paralleling the development of techniques to calculate boundary layer
growth over yawed surfaces was the study of the boundary layer on com-
pressor and turbine blades and on aircraft propellers and helicopter
rotors. In both the swept and rotating surface problems, the three-
dimensionality is introduced by the presence of a spanwise, or radial,
pressure distribution and, in the rotating case, by the extra presence of
centrifugal and Coriolis accelerations.

The early rotating disk work by von Karman, Reference (1), and the later
effort in the same area in Reference (6), did little to ease the task of
trying to establish the behavior of viscous flow on a rotating propeller
or rotor blade. The disk flow is dominated by a considerable radial com-
ponent and there is no circumferential growth of the viscous region,
whereas on the blade, with its radially disposed leading edge, the chord-
wise or tangential effects predominate and radial flow effects are com-
paratively small.

The earliest significant study of a rotating blade as opposed to a disk is
given in References (7) and (8), and the analogous problem of flow on the
floor of a curved channel is given in Reference (9). Later work in
Reference (10) investigated the special case of flow over a helical blade,
and most recently work in References (11), (12), and (13) has discussed
the development of boundary layers on helicopter rotors in forward flight.

The basic problem that all of these investigators have had to face, in
addition to the nonlinearity of the governing equations, is that the pair

1

of boundary layer momentum equations used to define the flow are coupled, and the assumptions made to decouple the equations that the methods differ. The approach used in Reference (8) was to consider velocities and gradients of velocity in the radial direction to be of small order compared to chordwise or tangential velocities and gradients. This allows the chordwise equation to be decoupled from the spanwise equation, and, for laminar flows at least, a modified Blasius solution may be developed in the chordwise direction. The limitation of this approach is that it may only be applied on blades of high aspect ratio and at large distances from the center of rotation. Later workers, particularly Reference (9), assumed some characteristic velocity profile form and, on providing some coupling between the streamwise and normal velocity components, solved the equations of motion using integral techniques. In References (11) and (13), the small crossflow work of Reference (8) is used as the departure point in a regular perturbation expansion which allows the calculation of the development of the boundary layer velocity profiles in cases where the translational effects are superimposed on the steady rotation and enables the effects of unfavorable pressure gradients to be included. A Blasius solution for the primary or chordwise flow is still used, however.

The historical background discussed above is not intended to be all-inclusive, but merely to be indicative of the principal approaches to the problem of calculating the development of the boundary layer on a rotating blade. These solution techniques, with the exception of Reference (9), are restricted to laminar flows. It is felt by the authors that this may not be a realistic state of affairs since for most full-scale helicopter applications, the Reynolds number of the flow is well above that required for transition, even on a smooth flat plate, and it is considerably greater than that for transition on the aerodynamically rough airfoils in practical use. Another restriction is that all the presently available techniques deal only with incompressible flows, an inappropriate assumption in light of the high subsonic Mach numbers found on present-day helicopter rotor blades. Consequently, it was felt that if new methods of calculation were to be set up or if existing methods were to be developed further, the effects of the turbulent nature of the flow and compressibility should be taken into account. In addition, it was felt that the unique capabilities of modern computing machines should be exploited as far as possible.

Two-dimensional boundary layer theory has advanced step by step with experimental investigation of actual flows. Unfortunately, no significant body of experimental data is yet available to the worker in three-dimensional flows, and consequently, none of the theories developed or under development can be considered valid until experimental proof is found. With this in mind and the above requirements as a guide, it was decided to develop two separate and independent methods which could be used for comparison and corroboration of the results.

Since the method of Reference (9) was the only one of the early three-dimensional solutions to consider the calculation of turbulent flows, it was decided to use this as the basis for the integral method. Modifications included allowing for the effects of compressibility and adverse

pressure gradients. The resulting method was developed for application with modern computing methods which were unavailable at the time of the original work.

For the second method, it was decided to use an extension of a technique which has received considerable use in two-dimensional applications. This is to carry out a full solution of the differential equations for the chordwise gradients of velocity and to integrate the gradients progressively over the surface. In the three-dimensional case, if the velocity components are known along a radial line, the spanwise velocity gradients can be calculated and the chordwise and spanwise flow equations can be evaluated simultaneously. This differential method has the potential to provide a more exact solution of the viscous flow, but it still relies on certain assumptions concerning the shear stress distribution for which no three-dimensional turbulence data is available.

Using both the integral and differential methods, the development of the boundary layer over two representative rotors was calculated for a range of conditions including various angular velocities, vortex induced crossflows, adverse pressure gradients, and blade surface curvatures. The development and use of these methods and the results are discussed in the following sections.

2. DEVELOPMENT OF THEORY

2.1 THE GOVERNING EQUATIONS

2.1.1 The Momentum Equation

Reference (14) gives the generalized vector form of the equation of motion for an incompressible viscous fluid moving relative to a fixed reference frame as

$$\frac{\partial}{\partial t}(\rho\underline{q}) + \tfrac{1}{2}\rho\nabla q^2 - \rho\underline{q}\times\underline{\omega} = -\nabla p - \mu\nabla\times\underline{\omega}, \tag{1}$$

where $\underline{q}$ is the general velocity vector and $\underline{\omega}$, the vorticity, is given by

$$\underline{\omega} = \nabla\times\underline{q}$$

If the axis system is now rotated with angular velocity $\underline{\Omega}$, all terms, with the exception of the unsteady contribution, apply unchanged relative to the rotating frame. The relation between rates of change of a vector transformed from a fixed to a rotating frame is given in Reference (15) as

$$\frac{\partial}{\partial t}(\rho\underline{q})_I = \frac{\partial}{\partial t}(\rho\underline{q})_R + 2\underline{\Omega}\times\rho\underline{q} + \rho\underline{\Omega}\times(\underline{\Omega}\times\underline{r}) + \frac{\partial}{\partial t}(\rho\underline{\Omega})\times\underline{r}$$

The vector $\underline{r}$ is the position vector of a point in the rotating frame. If only steady flow in the rotating system is considered, then the above equation reduces to

$$\frac{\partial}{\partial t}(\rho\underline{q})_I = 2\underline{\Omega}\times\rho\underline{q} + \rho\underline{\Omega}\times(\underline{\Omega}\times\underline{r})$$

The first term on the right-hand side represents the Coriolis and the second the centrifugal force. When this is substituted into Equation (1), the general equation of motion for a fluid in a rotating axis system becomes

$$\underbrace{2\underline{\Omega}\times\rho\underline{q}}_{\text{I}} + \underbrace{\rho\underline{\Omega}\times(\underline{\Omega}\times\underline{r})}_{\text{II}} + \underbrace{\tfrac{1}{2}\rho\nabla q^2}_{\text{III}} - \underbrace{\rho\underline{q}\times\underline{\omega}}_{\text{IV}} = -\underbrace{\nabla p}_{\text{V}} - \underbrace{\mu\nabla\times\underline{\omega}}_{\text{VI}} \tag{2}$$

Again following Reference (14), the component equations of motion will be written relative to an orthogonal curvilinear axis system with axes x, y and z. The scaling factors will be h_1, h_2 and h_3, which will generally be functions of x, y and z, and the unit vectors $\underline{i}$, $\underline{j}$ and $\underline{k}$ respectively.

The vector quantities may be written in terms of their components,

$$\underline{r} = x\underline{i} + y\underline{j} + z\underline{k},$$

4

$$\underline{q} = u\underline{i} + v\underline{j} + w\underline{k}$$

and

$$\underline{\Omega} = \Omega_x\underline{i} + \Omega_y\underline{j} + \Omega_z\underline{k}$$

The vorticity may also be expanded in like form with

$$\underline{\omega} = \omega_x\underline{i} + \omega_y\underline{j} + \omega_z\underline{k}$$

Now the vorticity is defined as equal to $\nabla \times \underline{q}$ and may also be written

$$\underline{\omega} = \frac{1}{h_1 h_2 h_3}
\begin{vmatrix}
h_1\underline{i} & h_2\underline{j} & h_3\underline{k} \\[6pt]
\dfrac{\partial}{\partial x} & \dfrac{\partial}{\partial y} & \dfrac{\partial}{\partial z} \\[6pt]
h_1 u & h_2 v & h_3 w
\end{vmatrix}$$

with components

$$\omega_x = \frac{1}{h_2 h_3} \left[\frac{\partial}{\partial y}(h_3 w) - \frac{\partial}{\partial z}(h_2 v) \right]$$

$$\omega_y = \frac{1}{h_3 h_1} \left[\frac{\partial}{\partial z}(h_1 u) - \frac{\partial}{\partial x}(h_3 w) \right]$$

and

$$\omega_z = \frac{1}{h_1 h_2} \left[\frac{\partial}{\partial x}(h_2 v) - \frac{\partial}{\partial y}(h_1 u) \right]$$

Equation (2) may now be expanded term by term into its component parts. Term I, $2\underline{\Omega} \times \rho\underline{q}$, becomes on expanding,

$$\left.
\begin{aligned}
& 2\rho(w\Omega_y - v\Omega_z)\underline{i} \\
& + 2\rho(u\Omega_z - w\Omega_x)\underline{j} \\
& + 2\rho(v\Omega_x - u\Omega_y)\underline{k}
\end{aligned}
\right\} \tag{3}$$

Term II, $\rho\underline{\Omega} \times (\underline{\Omega} \times \underline{r})$, gives

$$\left.
\begin{aligned}
& \rho\left[(y\Omega_y + z\Omega_z)\Omega_x - (\Omega_y{}^2 + \Omega_z{}^2)x \right]\underline{i} \\
& + \rho\left[(x\Omega_x + z\Omega_z)\Omega_y - (\Omega_z{}^2 + \Omega_x{}^2)y \right]\underline{j} \\
& + \rho\left[(x\Omega_x + y\Omega_y)\Omega_z - (\Omega_x{}^2 + \Omega_y{}^2)z \right]\underline{k}
\end{aligned}
\right\} \tag{4}$$

Since the operator ∇ in curvilinear coordinates is given by

$$\nabla = \frac{1}{h_1}\frac{\partial}{\partial x}\underline{i} + \frac{1}{h_2}\frac{\partial}{\partial y}\underline{j} + \frac{1}{h_3}\frac{\partial}{\partial z}\underline{k}$$

5

and $q^2 = u^2 + v^2 + w^2$, term III may be expanded to give

$$\tfrac{1}{2}\rho\nabla q^2 = \frac{\rho}{h_1}\left[u\frac{\partial u}{\partial x} + v\frac{\partial v}{\partial x} + w\frac{\partial w}{\partial x}\right]\underline{i}$$

$$+ \frac{\rho}{h_2}\left[u\frac{\partial u}{\partial y} + v\frac{\partial v}{\partial y} + w\frac{\partial w}{\partial y}\right]\underline{j} \qquad (5)$$

$$+ \frac{\rho}{h_3}\left[u\frac{\partial u}{\partial z} + v\frac{\partial v}{\partial z} + w\frac{\partial w}{\partial z}\right]\underline{k}$$

Taking the component form of the vorticity $\underline{\omega}$ and expanding it, together with the components of the velocity $\underline{q}$, gives term 1V,

$$\rho\underline{q}\times\underline{\omega} = \rho(v\omega_z - w\omega_y)\underline{i}$$

$$+ \rho(w\omega_x - u\omega_z)\underline{j} \qquad (6)$$

$$+ \rho(u\omega_y - v\omega_x)\underline{k}$$

The pressure term, term V, is simply

$$\nabla p = \frac{1}{h_1}\frac{\partial p}{\partial x}\underline{i} + \frac{1}{h_2}\frac{\partial p}{\partial y}\underline{j} + \frac{1}{h_3}\frac{\partial p}{\partial z}\underline{k} \qquad (7)$$

with the viscous effects, as represented by term VI, being given by

$$\mu\nabla\times\underline{\omega} = \frac{\mu}{h_2h_3}\left[\frac{\partial}{\partial y}(h_3\omega_z) - \frac{\partial}{\partial z}(h_2\omega_y)\right]\underline{i}$$

$$+ \frac{\mu}{h_1h_3}\left[\frac{\partial}{\partial z}(h_1\omega_x) - \frac{\partial}{\partial x}(h_3\omega_z)\right]\underline{j} \qquad (8)$$

$$+ \frac{\mu}{h_1h_2}\left[\frac{\partial}{\partial x}(h_2\omega_y) - \frac{\partial}{\partial y}(h_1\omega_x)\right]\underline{k}$$

Collecting the $\underline{i}$, $\underline{j}$ and $\underline{k}$ groups from the expanded terms gives the component equations of motion in the x, y and z directions respectively:

x Equation:

$$2\rho\left[w\Omega_y - v\Omega_z\right] + \rho\left[(y\Omega_y + z\Omega_z)\Omega_x - (\Omega_y^2 + \Omega_z^2)x\right] + \frac{\rho}{h_1}\left[u\frac{\partial u}{\partial x} + v\frac{\partial v}{\partial x} + w\frac{\partial w}{\partial x}\right]$$

$$- \rho\left[v\omega_z - w\omega_y\right] = -\frac{1}{h_1}\frac{\partial p}{\partial x} - \frac{\mu}{h_2h_3}\left[\frac{\partial}{\partial y}(h_3\omega_z) - \frac{\partial}{\partial z}(h_2\omega_y)\right] \qquad (9x)$$

6

y Equation:

$$2\rho \left[u\Omega_z - w\Omega_x \right] + \rho \left[(x\Omega_x + z\Omega_z)\Omega_y - (\Omega_z{}^2 + \Omega_x{}^2)y \right] + \frac{\rho}{h_2} \left[u\frac{\partial u}{\partial y} + v\frac{\partial v}{\partial y} + w\frac{\partial w}{\partial y} \right]$$

$$- \rho \left[w\omega_x - u\omega_z \right] = - \frac{1}{h_2} \frac{\partial p}{\partial y} - \frac{\mu}{h_3 h_1} \left[\frac{\partial}{\partial z}(h_1\omega_x) - \frac{\partial}{\partial x}(h_3\omega_z) \right] \tag{9y}$$

z Equation:

$$2\rho \left[v\Omega_x - u\Omega_y \right] + \rho \left[(x\Omega_x + y\Omega_y)\Omega_z - (\Omega_x{}^2 + \Omega_y{}^2)z \right] + \frac{\rho}{h_3} \left[u\frac{\partial u}{\partial z} + v\frac{\partial v}{\partial z} + w\frac{\partial w}{\partial z} \right]$$

$$- \rho \left[u\omega_y - v\omega_x \right] = - \frac{1}{h_3} \frac{\partial p}{\partial z} + \frac{\mu}{h_1 h_2} \left[\frac{\partial}{\partial x}(h_2\omega_y) - \frac{\partial}{\partial y}(h_1\omega_x) \right] \tag{9z}$$

At this point in the development of two-dimensional boundary layer
equations, it would   .ormal to carry out an order of magnitude compar-
ison of terms and reu .ce the equations to the standard short form.
Before this is done in the present case, it is useful to consider the
surface over which the flow is taking place, the orientation of the axes
relative to the surface, and the dependence of the scaling factors on x,
y and z. Figure (1) gives the system of axes used in the present work.
Following References (8) and (11), and others, the axes will be fixed in
the rotating surface. The x and y coordinates will define the surface
z = 0, and z will follow the local normal to the surface. Curvature
will be restricted to the x axis, making scaling factors h_2 and h_3 equal
unity. Since the blade may be represented by a cylindrical surface,
the scale factor h_1 becomes a function of z alone.

It is conventional, in treating the boundary layer equations in two
dimensions with the flow in the x direction, to assume that x, u and p
are all of order unity, 0 (1), and that z and w are of the order of the
boundary layer thickness, $O(\delta)$. In addition to these, the existence of
the crossflow field introduces terms involving y, v, h_1, h_2, h_3 and Ω_z,
which are all of order $O(1)$, and Ω_y, and Ω_x or order $O(\delta)$. The angular
velocity Ω_z is generally large and will be treated as equal to Ω, the
angular velocity of the rotor about its axis. By expanding equations 9x,
9y and 9z and discarding terms on the basis of their relative orders of
magnitude, and at the same time substituting Ω for Ω_z and replacing the
scaling factors h_2 and h_3 with their value of 1.0, the full equations of
motion are reduced to the equations of motion for the steady flow of a
viscous fluid over a singly curved rotating surface:

7

x Equation:

$$-2\rho v\Omega - \rho\Omega^2 x + \frac{\rho u}{h_1}\frac{\partial u}{\partial x} + \rho v\frac{\partial u}{\partial y} + \rho w\frac{\partial u}{\partial z} + \frac{\rho wu}{h_1}\frac{\partial}{\partial z}(h_1) = -\frac{1}{h_1}\frac{\partial p}{\partial x} + \mu\frac{\partial}{\partial z}\left[\frac{1}{h_1}\frac{\partial}{\partial z}(h_1 u)\right]$$

(10x)

y Equation:

$$2\rho\iota \qquad \frac{\rho u}{h_1}\frac{\partial v}{\partial x} + \rho v\frac{\partial v}{\partial y} + \rho w\frac{\partial v}{\partial z} = \frac{\partial p}{\partial y} + \frac{\mu}{h_1}\frac{\partial}{\partial z}\left[h_1\frac{\partial}{\partial z}(v)\right]$$

(10y)

z Equation:

$$\frac{u}{h_1}\frac{\partial}{\partial z}(h_1) = -\frac{1}{\rho}\frac{\partial p}{\partial z}$$

(10z)

This completes the development of the boundary layer momentum equations.

2.1.2 The Continuity Equation

The generalized vector form of the equation of continuity in a fixed axis frame is given by

$$\frac{\partial\rho}{\partial t} + \nabla\cdot(\rho\underline{q}) = 0$$

(11)

Since the density ρ is not a vector quantity, Equation (11) will apply unchanged if the coordinate system is rotated. If the further requirement is made that the flow relative to the rotating axis system not be time-dependent, then the continuity equation for steady flow relative to a rotating axis system is simply

$$\nabla\cdot(\rho\underline{q}) = 0$$

(12)

Bearing in mind that in the curvilinear coordinate system the operator ∇ is given by

$$\nabla = \frac{1}{h_1}\frac{\partial}{\partial x}\underline{i} + \frac{1}{h_2}\frac{\partial}{\partial y}\underline{j} + \frac{1}{h_3}\frac{\partial}{\partial z}\underline{k} \ ,$$

Equation (12) may be expanded into

$$\nabla\cdot(\rho\underline{q}) = \frac{\partial}{\partial x}(h_2 h_3\rho u) + \frac{\partial}{\partial y}(h_3 h_1\rho v) + \frac{\partial}{\partial z}(h_1 h_2\rho w) = 0$$

(13)

In defining the surface and coordinate system for the rotor blade problem, h_2 and h_3 were specified above as unity and h_1 as a function of z alone. With this in mind the continuity equation (Equation (13)) now becomes

$$\frac{1}{h_1}\frac{\partial}{\partial x}(\rho u) + \frac{\partial}{\partial y}(\rho v) + \frac{\partial}{\partial z}(\rho w) + \frac{1}{h_1}(\rho w)\frac{\partial h_1}{\partial z} = 0$$

(14)

8

2.1.3 The Energy Equation

No original treatment of the energy equation will be attempted here; the solution of the equation derived in Reference (14) will be used. For the case of the adiabatic wall to be assumed here, a relation for the local temperature is given of the form

$$T = T_\infty + \frac{1}{2C_p} \left[U_\infty^2 + V_\infty^2 - u^2 - v^2 \right] \tag{15}$$

If this is rearranged to give the local density in terms of the local velocity and the Mach number of the external flow, it becomes

$$\frac{\rho_\infty}{\rho} = 1 + \frac{(\gamma-1)}{2} M_\infty^2 - \frac{(\gamma-1)}{2} M_\infty^2 \left[\frac{u^2 + v^2}{U_\infty^2 + V_\infty^2} \right] \tag{16}$$

2.1.4 Reynolds Stress Effects

The flow equations developed above have been in terms of the instantaneous values of the flow variables. To determine the effect of the turbulent velocity fluctuations in the boundary layer, it is conventional to replace the instantaneous values of the flow variables with the sum of the time mean and fluctuating parts. For example,

$$u = \bar{u} + u'$$

The bar denotes a time-mean, and the dash a fluctuating quantity. The mechanics of performing this operation are covered in References (16) and (17), and will not be dwelt on in this analysis. In the absence of any significant body of experimental turbulence data in three-dimensional flows, only those terms known to be significant in two-dimensional flows will be considered, together with their obvious cross-flow partners. Bearing this in mind and neglecting triple and higher order products of the fluctuating terms, the motion and continuity equations become

$$-2\,\overline{\rho v}\,\Omega - \overline{\rho}\Omega^2 x + \frac{\overline{\rho u}}{h_1}\frac{\partial \bar{u}}{\partial x} + \overline{\rho v}\,\frac{\partial \bar{u}}{\partial y} + (\overline{\rho w} + \overline{\rho' w'}) \left[\frac{\partial \bar{u}}{\partial z} + \frac{\bar{u}}{h_1}\frac{\partial h_1}{\partial z} \right]$$

$$= -\frac{1}{h_1}\frac{\partial \bar{p}}{\partial x} + \frac{\partial}{\partial z}\left[\frac{\bar{\mu}}{h_1}\frac{\partial}{\partial z}(h_1\bar{u}) \right] - \frac{\partial}{\partial z}\left[\bar{\rho}\,\overline{u'w'} \right] \quad , \quad (17x)$$

$$2\,\overline{\rho u}\,\Omega - \overline{\rho}\Omega^2 y + \frac{\overline{\rho u}}{h_1}\frac{\partial \bar{v}}{\partial x} + \overline{\rho v}\,\frac{\partial \bar{v}}{\partial y} + (\overline{\rho w} + \overline{\rho' w'})\frac{\partial \bar{v}}{\partial z}$$

$$= -\frac{\partial \bar{p}}{\partial y} + \frac{1}{h_1}\frac{\partial}{\partial z}\left[\bar{\mu}\, h_1\frac{\partial \bar{v}}{\partial z} \right] - \frac{\partial}{\partial z}\left[\bar{\rho}\,\overline{v'w'} \right] \quad , \quad (17y)$$

9

and

$$\frac{1}{h_1} \frac{\partial}{\partial x} (\overline{\rho u}) + \frac{\partial}{\partial y} (\overline{\rho v}) + \frac{\partial}{\partial z} (\overline{\rho w} + \overline{\rho' w'})$$

$$+ \frac{1}{h_1} (\overline{\rho w} + \overline{\rho' w'}) \frac{\partial h_1}{\partial z} = 0 \qquad (18)$$

The most significant effect of turbulence is the addition of an apparent shear stress term to each of the momentum equations. These are the Reynolds stress terms, the time mean of the product of the fluctuating velocities in the x and y directions, and the normal velocity fluctuation. The precise form of these terms and their dependence on the mean flow parameters will be discussed in a later section.

2.2 THE SOLUTIONS

2.2.1 Limiting Conditions

The equations governing the flow over a cylindrical surface rotating about some axis perpendicular to its length were developed in Equations (17x) and (17y), the momentum equations, in Equation (18), the continuity equation, and in Equation (16), a solution of the energy equation for the special case of adiabatic flow. In succeeding sections, they will be manipulated and subsequently solved to determine the development of the boundary layer over the surface. The two methods of solution used differ considerably, but they must both satisfy the same boundary conditions: that there be zero slip at the wall, $z = 0$, with $u = v = 0$ and consequently

$$\frac{\partial u}{\partial x} = \frac{\partial u}{\partial y} = \frac{\partial v}{\partial x} = \frac{\partial v}{\partial y} = 0$$

In the case of the flow over a solid wall with no transpiration, w_0 is also equal to zero. A further condition is that at large distances from the surface, u and v must approach U_∞ and V_∞, the velocities of the external flow.

2.2.2 The Differential Method

It is convenient at the outset to nondimensionalize the velocity components in the x (chordwise) and y (spanwise) directions by dividing by U_∞, the velocity of the external flow in the chordwise direction. They become

$$\text{chordwise} \qquad c = \frac{\bar{u}}{U_\infty}$$

and $\quad$ spanwise $\qquad \mathfrak{z} = \frac{\bar{v}}{U_\infty}$

10

The equations of motion written in terms of c and s become

$$-2\Omega\rho s U_\infty - \rho\Omega^2 x + \frac{\rho U_\infty^2}{h_1} c \frac{\partial c}{\partial x} + \rho U_\infty^2 s \frac{\partial c}{\partial y} + U_\infty(\overline{\rho w} + \overline{\rho'w'})\left[\frac{\partial c}{\partial z} + \frac{c}{h_1}\frac{\partial}{\partial z}(h_1)\right]$$

$$= -\frac{1}{h_1}\frac{\partial p}{\partial x} + \frac{\partial \tau_x}{\partial z} \qquad (19x)$$

and

$$2\Omega\rho c U_\infty - \rho\Omega^2 y + \frac{\rho U_\infty^2}{h_1} c \frac{\partial s}{\partial x} + \rho U_\infty^2 s \frac{\partial s}{\partial y} + U_\infty(\overline{\rho w} + \overline{\rho'w'}) \frac{\partial s}{\partial z}$$

$$= -\frac{\partial p}{\partial y} + \frac{1}{h_1}\frac{\partial \tau_y}{\partial z} \qquad (19y)$$

(In the interest of clarity, the bars have been dropped from the time mean quantities except for the $(\overline{\rho w} + \overline{\rho'w'})$ term.) The viscous and Reynolds stress terms have been combined in the terms $\partial\tau_x/\partial z$ and $\partial\tau_y/\partial z$ above.

The main object of the solution is to isolate the gradients of velocity in the chordwise direction, $\partial c/\partial x$ and $\partial s/\partial x$, and these are the principal unknowns in the above equations. Before they can be determined, however, substitutions must be made for the pressure gradient terms, the normal velocity term $(\overline{\rho w} + \overline{\rho'w'})$, and the shear stress variation normal to the surface.

The pressure gradient terms may be found by evaluating Equations (17x) and (17y) at the surface in the absence of viscous effects or by considering the differentiated form of Bernoulli's equation in a rotating system. Bernoulli's equation for the flow being considered here may be written as

$$\frac{p}{\rho_\infty} = -\frac{1}{2}(U_\infty^2 + V_\infty^2) + \frac{\Omega^2}{2}(x^2 + y^2) + p_{stag}/\rho_\infty$$

If this is differentiated with respect to x and y, it is found that

$$\frac{\partial p}{\partial x} = -\rho_\infty(U_\infty \frac{\partial U_\infty}{\partial x} + V_\infty \frac{\partial V_\infty}{\partial x}) + \rho_\infty\Omega^2 x + \left.\begin{array}{c} \\ \\ \end{array}\right\}\begin{array}{l}\text{density}\\ \text{gradient}\\ \text{terms of}\\ \text{small order}\end{array} \quad (20)$$

and

$$\frac{\partial p}{\partial y} = -\rho_\infty(U_\infty \frac{\partial U_\infty}{\partial y} + V_\infty \frac{\partial V_\infty}{\partial y}) + \rho_\infty\Omega^2 y +$$

The term containing the normal velocity may be removed by substitution from Equation (18), the continuity equation. Equation (18) must first be rearranged and integrated along a normal to the surface to give

11

$$\left(\overline{\rho w} + \overline{\rho' w'}\right) = - \frac{1}{h_1} \int_0^z \left[\frac{\partial}{\partial x}(\rho u) + h_1 \frac{\partial}{\partial y}(\rho v) \right] dz \qquad (21)$$

Equation (16) gives an expression for the density in terms of the velocity components, and if this is differentiated with respect to x and y, the integrand of Equation (21) becomes

$$\frac{\partial}{\partial x}(\rho u) + h_1 \frac{\partial}{\partial y}(\rho v) = \rho \frac{\partial u}{\partial x} + h_1 \rho \frac{\partial v}{\partial y}$$

$$- u \left(\frac{\rho}{\rho_\infty}\right)^2 \rho_\infty \left[(\gamma-1)M_\infty \frac{\partial M_\infty}{\partial x} - (\gamma-1) M_\infty \frac{\partial M_\infty}{\partial x} \frac{(u^2+v^2)}{(U_\infty^2+V_\infty^2)} - \frac{(\gamma-1)M_\infty^2}{(U_\infty^2+V_\infty^2)} \left(u \frac{\partial u}{\partial x} + v \frac{\partial v}{\partial x} \right) \right]$$

$$- h_1 v \left(\frac{\rho}{\rho_\infty}\right)^2 \rho_\infty \left[(\gamma-1)M_\infty \frac{\partial M_\infty}{\partial y} - (\gamma-1)M_\infty \frac{\partial M_\infty}{\partial y} \frac{(u^2+v^2)}{(U_\infty^2+V_\infty^2)} - \frac{(\gamma-1)M_\infty^2}{(U_\infty^2+V_\infty^2)} \left(u \frac{\partial u}{\partial y} + v \frac{\partial v}{\partial y} \right) \right]$$

Collecting terms involving the spanwise and chordwise velocity gradients and expressing the velocities in terms of the velocity ratios c and s leads to the final form of Equation (21):

$$\left(\overline{\rho v} + \overline{\rho' w'}\right) = - \frac{\rho_\infty U_\infty}{h_1} \int_0^z \left\{ \frac{\partial c}{\partial x} \left[\left(\frac{\rho}{\rho_\infty}\right) + c^2 F^2 \right] + \frac{\partial s}{\partial x} cs F^2 + \frac{\partial c}{\partial y} cs h_1 F^2 \right.$$

$$\left. + \frac{\partial s}{\partial y} \left[\left(\frac{\rho}{\rho_\infty}\right) h_1 + s^2 F^2 \right] - \left[1 + \left(\frac{V_\infty}{U_\infty}\right)^2 - c^2 - s^2 \right] \left[\frac{c}{M_\infty} \frac{\partial M_\infty}{\partial x} + \frac{s}{M_\infty} \frac{\partial M_\infty}{\partial y} \right] F^2 \right\} dz \quad (22)$$

where

$$F^2 = U_\infty^2 M_\infty^2 \left(\frac{\rho}{\rho_\infty}\right)^2 \frac{(\gamma-1)}{U_\infty^2 + V_\infty^2}$$

The shear stress terms in Equations (19x) and (19y) must now be expressed in terms of the mean flow quantities. From Equations (17x) and (17y), the shear stress terms $\partial \tau_x / \partial z$ and $\partial \tau_y / \partial z$ are given by

$$\frac{\partial \tau_x}{\partial z} = \frac{\partial}{\partial z} \left[\frac{\mu}{h_1} \frac{\partial}{\partial z}(h_1 u) - \rho \overline{u'w'} \right]$$

and

$$\frac{\partial \tau_y}{\partial z} = \frac{\partial}{\partial z} \left[\mu h_1 \frac{\partial v}{\partial z} - h_1 \rho \overline{v'w'} \right] \qquad (23)$$

Knowing the velocity profiles, the viscous shear stresses may be determined directly. Unfortunately, some assumptions must be made to obtain an

12

expression for the Reynolds stress terms. In two-dimensional boundary layer solutions, the relation between turbulent shear stress and mean flow is most commonly supplied by the eddy viscosity or related mixing length hypotheses. Other approaches involve solutions of the turbulent kinetic energy equation or an eddy viscosity transport equation. However, as a result of the present poor state of knowledge of the behavior of turbulence, all methods employ empirical relationships to some degree. Reference (18) gives an up-to-date summary of all the methods in common use and an assessment of their applicability. In three-dimensional flows, the data available is very limited and the relationship between the turbulent shear stress and the mean flow is still a matter of argument. Considering this, it will be assumed for the present solution that a mixing length relationship may be applied and the turbulent shear stress may be related to the normal gradient of the local resultant velocity by

$$\rho\overline{r'w'} = \rho\ell^2 \left| \frac{\partial r}{\partial z} \right| \frac{\partial r}{\partial z} \tag{24}$$

where $r = (u^2 + v^2)^{\frac{1}{2}}$ is the local resultant velocity and $\rho\overline{r'w'}$ is the resultant turbulent shear stress. The two do not necessarily act in the same direction. Reference (5) suggests that it is most probable that the turbulent shear stress acts in the direction of the maximum rate of strain of the mean flow given by

$$\frac{\overline{u'w'}}{\overline{v'w'}} = \frac{\frac{\partial u}{\partial z}}{\frac{\partial v}{\partial z}} \tag{25}$$

With the magnitude of the resultant shear stress given by Equation (24) and the direction by Equation (25), it may be further assumed that

$$(\overline{r'w'})^2 = (\overline{u'w'})^2 + (\overline{v'w'})^2$$

It is now possible to arrive at expressions for the Reynolds stress components in the x and y directions:

$$\rho\overline{u'w'} = \rho\ell^2 \left| \frac{\partial r}{\partial z} \right| \frac{\partial r}{\partial z} \frac{\frac{\partial c}{\partial z}}{\left[\left(\frac{\partial c}{\partial z} \right)^2 + \left(\frac{\partial s}{\partial z} \right)^2 \right]^{\frac{1}{2}}}$$

and $\tag{26}$

$$\rho\overline{v'w'} = \rho\ell^2 \left| \frac{\partial r}{\partial z} \right| \frac{\partial r}{\partial z} \frac{\frac{\partial s}{\partial z}}{\left[\left(\frac{\partial c}{\partial z} \right)^2 + \left(\frac{\partial s}{\partial z} \right)^2 \right]^{\frac{1}{2}}}$$

The form of the mixing length ℓ suggested for two-dimensional flow in

13

Reference (19) has been used in the present work. It is given by

$$\frac{l}{\delta} = \frac{l_\infty}{\delta} \tanh \left(\frac{z}{\delta} \frac{\delta}{l_\infty} \kappa \right)$$

where l_∞ is the value of l in the outer boundary layer, typically $l_\infty/\delta = 0.09$ to 0.095, and κ is the von Karman constant relating the mixing length to distance normal to the wall. The two-dimensional value of κ is typically 0.4, and this will be used here. The relations given in Equations (26) only apply in that part of the boundary layer where turbulent stresses predominate. In the regions close to the wall, viscous effects control the flow, and the expression for the mixing length has to be modified. This has been done for two-dimensional flows in Reference (20), but it was felt that, because of the approximations made in the turbulent region and the three-dimensionality of the flow, the refinement suggested would be inappropriate. Instead, the shear stress gradients in the laminar region were determined by interpolating between conditions at the wall and at the edge of the sublayer.

Since flow in this region is controlled by the effects of viscosity, and References (20 and (27) highlight the significance of the shear velocity, u^*, close to the wall, this was used as the basis for the interpolation. The shear stress gradients are given by

$$\frac{\partial \tau_x}{\partial z} = A_0 + A_1 f_x(z) + A_2 u_*^2$$

and

$$\frac{\partial \tau_y}{\partial z} = B_0 + B_1 f_y(z) + B_2 u_*^2$$

with

$$u_* = u/(\tau_x/\rho_\infty)^{\frac{1}{2}}$$

The interpolation is given in full in the appendix.
The expressions for the pressure gradient, Equation (20), the term $(\overline{\rho v} + \rho' v')$, Equation (22), and the shear stress gradient, Equation (26), may now be substituted into the boundary layer momentum equations, (19x) and (19y), to give the unknown chordwise gradients in terms of known parameters:

$$-2\Omega \rho s U_\infty - \Omega^2 x (\rho - \frac{\rho_\infty}{h_1}) + \frac{\rho U_\infty^2}{h_1} c \frac{\partial c}{\partial x} + \rho U_\infty^2 s \frac{\partial c}{\partial y}$$

$$- \frac{\rho_\infty U_\infty^2}{h_1} \left[\frac{\partial c}{\partial z} + \frac{c}{h_1} \frac{\partial}{\partial z}(h_1) \right] \int_0^z (b_1 \frac{\partial c}{\partial x} + b_2 \frac{\partial r}{\partial x} + b_3 \frac{\partial c}{\partial y} + b_4 \frac{\partial s}{\partial y} + b_5) dz$$

$$= \frac{\partial \tau_x}{\partial z} + \frac{\rho_\infty U_\infty}{h_1} (\frac{\partial U_\infty}{\partial x} + \frac{V_\infty}{U_\infty} \frac{\partial V_\infty}{\partial x}) \qquad (27x)$$

14

and

$$2\Omega\rho c U_\infty - \Omega^2 y(\rho-\rho_\infty) + \frac{\rho U_\infty{}^2}{h_1} c \frac{\partial s}{\partial x} + \rho U_\infty{}^2 s \frac{\partial s}{\partial y}$$

$$- \frac{\rho_\infty U_\infty{}^2}{h_1} \frac{\partial s}{\partial z} \int_0^z (b_1\frac{\partial c}{\partial x} + b_2\frac{\partial s}{\partial x} + b_3\frac{\partial c}{\partial y} + b_4\frac{\partial s}{\partial y} + b_5)dz = \frac{1}{h_1} \frac{\partial \tau_y}{\partial z} + \rho_\infty U_\infty(\frac{\partial U_\infty}{\partial y} + \frac{V_\infty}{U_\infty} \frac{\partial V_\infty}{\partial y})$$

$$(27y)$$

where $\quad b_1 = \left[\frac{\rho}{\rho_\infty} + c^2F^2\right]$

$$b_2 = csF^2$$

$$b_3 = csF^2h_1$$

$$b_4 = \left[h_1\frac{\rho}{\rho_\infty} + s^2F^2\right]$$

and $\quad b_5 = - \left[1 + (\frac{V_\infty}{U_\infty})^2 - c^2 - s^2\right] \left[\frac{c}{M_\infty} \frac{\partial M_\infty}{\partial x} + \frac{s}{M_\infty} \frac{\partial M_\infty}{\partial y}\right] F^2$

The shear stress gradients $\partial\tau_x/\partial z$ and $\partial\tau_y/\partial z$ have been left in the general form since Equations (26) are strictly only applicable outside of the laminar sublayer. Equations (27x) and (27y) represent a pair of equations with two unknowns, and as such they are soluble. They are, however, coupled through the integral term which contains both unknowns and appears in both equations. The group $\rho_\infty U_\infty{}^2$ may be removed as a factor and the equations rearranged to give

$$\frac{\partial c}{\partial x} - \frac{1}{c} \frac{\rho_\infty}{\rho} \left[\frac{\partial c}{\partial z} + \frac{c}{h_1} \frac{\partial}{\partial z} (h_1)\right] \int_0^z (b_1\frac{\partial c}{\partial x} + b_2\frac{\partial s}{\partial x})dz$$

$$= \frac{h_1}{c} \frac{\rho_\infty}{\rho} \left\{ 2s \frac{\rho}{\rho_\infty} \frac{\Omega}{U_\infty} + x \frac{\Omega^2}{U_\infty^2} (\frac{\rho}{\rho_\infty} - \frac{1}{h_1}) + \frac{1}{\rho_\infty U_\infty{}^2} \frac{\partial\tau_x}{\partial z} + \frac{1}{U_\infty}(\frac{\partial U_\infty}{\partial x} + \frac{V_\infty}{U_\infty} \frac{\partial V_\infty}{\partial x}) \frac{1}{h_1} \right.$$

$$\left. - s \frac{\rho}{\rho_\infty} \frac{\partial c}{\partial y} + \frac{1}{h_1} \left[\frac{\partial c}{\partial z} + \frac{c}{h_1} \frac{\partial}{\partial z} (h_1)\right] \int_0^z (b_3\frac{\partial c}{\partial y} + b_4\frac{\partial s}{\partial y} + b_5)dz \right\} \qquad (28x)$$

15

and

$$\frac{\partial s}{\partial x} - \frac{1}{c} \frac{\rho_\infty}{\rho} \frac{\partial s}{\partial z} \int_0^z (b_1 \frac{\partial c}{\partial x} + b_2 \frac{\partial s}{\partial x}) dz$$

$$= \frac{h_1}{c} \frac{\rho_\infty}{\rho} \left\{ - 2c \frac{\rho}{\rho_\infty} \frac{\Omega}{U_\infty} + y \frac{\Omega^2}{U_\infty^2} (\frac{\rho}{\rho_\infty} - 1) + \frac{1}{\rho_\alpha U_\infty^2} \frac{\partial \tau_y}{\partial z} + \frac{1}{U_\infty} (\frac{\partial U_\infty}{\partial y} + \frac{V_\infty}{U_\infty} \frac{\partial V_\infty}{\partial y}) \right.$$

$$\left. - s \frac{\rho}{\rho_\infty} \frac{\partial s}{\partial y} + \frac{\partial s}{\partial z} \int_0^z (b_3 \frac{\partial c}{\partial y} + b_4 \frac{\partial s}{\partial y} + b_5) dz \right\} \quad (28y)$$

or

$$\frac{\partial c}{\partial x} - f_{x1} \int_0^z (b_1 \frac{\partial c}{\partial x} + b_2 \frac{\partial s}{\partial x}) dz = f_{x2} \quad (29x)$$

and

$$\frac{\partial s}{\partial x} - f_{y1} \int_0^z (b_1 \frac{\partial c}{\partial x} + b_2 \frac{\partial s}{\partial x}) dz = f_{y2} \quad (29y)$$

with

$$f_{x1} = \frac{1}{c} \frac{\rho_\infty}{\rho} \left[\frac{\partial c}{\partial z} + \frac{c}{h_1} \frac{\partial}{\partial z} (h_1) \right]$$

$$f_{y1} = \frac{1}{c} \frac{\rho_\infty}{\rho} \frac{\partial s}{\partial z}$$

The right sides of Equations (28x) and (28y) are represented by f_{x2} and f_{y2}, respectively. Multiplying Equation (29x) by f_{y1} and Equation (29y) by f_{x1} and subtracting one from the other gives

$$f_{y1} \frac{\partial c}{\partial x} - f_{x1} \frac{\partial s}{\partial x} = f_{x2} f_{y1} - f_{y2} f_{x1} \quad (30)$$

If Equations (29x) and (29y) are then multiplied by b_1 and b_2 respectively and added, they become

$$(b_1 \frac{\partial c}{\partial x} + b_2 \frac{\partial s}{\partial x}) - (b_1 f_{x1} + b_2 f_{y2}) \int_0^z (b_1 \frac{\partial c}{\partial x} + b_2 \frac{\partial s}{\partial x}) dz = (b_1 f_{x2} + b_2 f_{y2}) \quad (31)$$

Equation (31) may be expressed in terms of a new unknown,

$$G(z) = b_1 \frac{\partial c}{\partial x} + b_2 \frac{\partial s}{\partial x}$$

$$G(z) = (b_1 f_{x1} + b_2 f_{y1}) \int_0^z G(z) dz + (b_1 f_{x2} + b_2 f_{y2}) \quad (32)$$

16

This may be easily solved for G using iterative techniques which are ideally suited for machine computation. The problem has now been reduced to the solution of two simultaneous equations in $\partial c/\partial x$ and $\partial s/\partial x$:

$$f_{y1} \frac{\partial c}{\partial x} - f_{x1} \frac{\partial s}{\partial x} = f_{x2}f_{y1} - f_{y2}f_{x1} \tag{33}$$

$$b_1\frac{\partial c}{\partial x} + b_2 \frac{\partial s}{\partial x} = G(z) \tag{34}$$

The solution is now a routine matter of separating the unknowns using Equations (33) and (34).

The calculation of the gradients $\partial c/\partial x$ and $\partial s/\partial x$ described above is carried out at a number of points along the normal to the surface within the boundary layer. The actual number of solution points is determined by the need to accurately specify the velocity profiles, and their spacing is determined by the need to adequately describe the rates of change of quantities normal to the wall. In the present calculation, the points have been distributed logarithmically from the wall with a minimum of twenty points within the boundary layer. It is then possible to integrate the chordwise gradients to the next point using a forward stepping finite difference technique. If this id done for a number of stations along a constant x line, for which the flow conditions are known, then the development of the boundary layer over the surface may be calculated.

2.2.3 The Integral Method

The principal difficulty in turbulence work lies in specifying the shear stress. Most work thus relies on some type of semiempirical model to define the turbulent shear stress throughout the boundary layer. By using an integral technique, this necessary approximation may be partially avoided. The momentum equations may be integrated with respect to the distance normal to the surface out to the free stream. The integral of the shear stress term is the value of the skin friction at the surface for which an empirical model must then be provided. This can be done without affecting the accuracy of the results in many cases, and at the same time, numerical complexity can be significantly reduced. However, variations normal to the surface are eliminated because the boundary layer is defined in terms of overall parameters. This technique has proven its usefulness in two-dimensional work, and its extension to three dimensions is shown to be practical in Reference (9).

Several steps must be taken before integration of the momentum equations becomes feasible. The pressure gradient terms can be evaluated directly from Equations (17x) and (17y) by inserting the free stream density and velocities. The effect of variation of pressure normal to the surface is considered to be negligible. Thus, the resulting pressure gradient expressions are applicable from the free stream to the surface. The value of the shear stress term outside the boundary layer is zero. The pressure

17

gradient expressions then become

$$-\frac{1}{h_1}\frac{\partial p}{\partial x} = \frac{\rho_\infty U_\infty}{h_1}\frac{\partial U_\infty}{\partial x} + \rho_\infty V_\infty \frac{\partial U_\infty}{\partial y} + \rho_\infty W_\infty \frac{\partial U_\infty}{\partial z} + \rho_\infty W_\infty U_\infty \frac{1}{h_1}\frac{\partial h_1}{\partial z} - 2\Omega\rho V_\infty - \rho_\infty\Omega^2 x$$

$$\tag{35x}$$

$$-\frac{\partial p}{\partial y} = \frac{\rho_\infty U_\infty}{h_1}\frac{\partial V_\infty}{\partial x} + \rho_\infty V_\infty \frac{\partial V_\infty}{\partial y} + \rho_\infty W_\infty \frac{\partial V_\infty}{\partial z} + 2\Omega\rho_\infty U_\infty - \rho_\infty\Omega^2 y \tag{35y}$$

When these expressions are substituted into the momentum equations and written with the intended integration, the following equations result:

$$\int_0^\delta \frac{1}{h_1}\left(\rho_\infty U_\infty \frac{\partial U_\infty}{\partial x} - \rho u \frac{\partial u}{\partial x}\right)dz + \int_0^\delta \left(\rho_\infty V_\infty \frac{\partial U_\infty}{\partial y} - \rho v \frac{\partial u}{\partial y}\right)dz$$

$$-\int_0^\delta \frac{(\overline{\rho w} + \overline{\rho'w'})}{h_1}\frac{\partial(uh_1)}{\partial z}dz - 2\Omega\int_0^\delta (\rho_\infty V_\infty - \rho v)dz - \Omega^2 x \int_0^\delta(\rho_\infty - \rho)dz$$

$$= -\int_0^\delta \frac{\partial \tau_x}{\partial z}dz \tag{36x}$$

$$\int_0^\delta \frac{1}{h_1}\left(\rho_\infty U_\infty \frac{\partial V_\infty}{\partial x} - \rho u \frac{\partial v}{\partial x}\right)dz + \int_0^\delta \left(\rho_\infty V_\infty \frac{\partial V_\infty}{\partial y} - \rho v \frac{\partial v}{\partial y}\right)dz$$

$$-\int_0^\delta (\overline{\rho w} + \overline{\rho'w'})\frac{\partial v}{\partial z}dz + 2\Omega\int_0^\delta (\rho_\infty U_\infty - \rho u)dz - \Omega^2 y \int_0^\delta(\rho_\infty - \rho)dz$$

$$= -\int_0^\delta \frac{\partial \tau_y}{\partial z}dz \tag{36y}$$

Since the external flow is considered to be parallel to the surface, terms involving W_∞ have been set equal to zero. The bars have been dropped from the time mean quantities except for the $(\overline{\rho w} + \overline{\rho'w'})$ term. In the x component, the two terms with coefficients of $(\overline{\rho w} + \overline{\rho'w'})$ have been combined.

Equation (18), the continuity equation, may be employed to supply an expression for $(\overline{\rho w} + \overline{\rho'w'})$ in terms of the remaining variables, as was done in section 2.2.1. The result, Equation (21), is repeated here.

$$(\overline{\rho w} + \overline{\rho'w'}) = -\frac{1}{h_1}\int_0^z \left[\frac{\partial}{\partial x}(\rho u) + h_1\frac{\partial}{\partial y}(\rho v)\right]dz \tag{21}$$

Now $(\overline{\rho w} + \overline{\rho'w'})$ may be eliminated from the momentum equations, and the

18

resulting double integral terms

$$-\int_0^\delta \frac{(\overline{\rho w} + \overline{\rho' w'})}{h_1} \frac{\partial(u h_1)}{\partial z} \, dz = \int_0^\delta \frac{1}{h_1} \frac{\partial(u h_1)}{\partial z} \int_0^z \left[\left(\frac{\partial(\rho u)}{\partial x} \right) + h_1 \frac{\partial(\rho u)}{\partial y} \right] dz \, dz \quad (37x)$$

and

$$-\int_0^\delta (\overline{\rho w} + \overline{\rho' w'}) \frac{\partial v}{\partial z} \, dz = \int_0^\delta \frac{\partial v}{\partial z} \int_0^z \left[\frac{\partial(\rho u)}{\partial x} + h_1 \frac{\partial(\rho u)}{\partial y} \right] dz \, dz \quad (37y)$$

may be integrated by parts in the same manner as their two-dimensional counterparts. The actual change in the scale factor h_1 over a distance equivalent to a typical boundary layer is small; therefore, this term has been considered invariant. The complete momentum equations can then be written

$$\int_0^\delta \frac{1}{h_1} \left[\rho_\infty U_\infty \frac{\partial U_\infty}{\partial x} - \rho u \frac{\partial u}{\partial x} + U_\infty \frac{\partial(\rho u)}{\partial x} - u \frac{\partial(\rho u)}{\partial x} \right] dz$$

$$+ \int_0^\delta \left[\rho_\infty V_\infty \frac{\partial U_\infty}{\partial y} - \rho v \frac{\partial u}{\partial y} + U_\infty \frac{\partial(\rho v)}{\partial y} - u \frac{\partial(\rho v)}{\partial y} \right] dz$$

$$- 2\Omega \int_0^\delta (\rho_\infty V_\infty - \rho v) dz - \Omega^2 x \int_0^\delta (\rho_\infty - \rho) dz = \tau_{ox} \quad (38x)$$

and

$$\int_0^\delta \frac{1}{h_1} \left[\rho_\infty U_\infty \frac{\partial V_\infty}{\partial x} - \rho u \frac{\partial v}{\partial x} + V_\infty \frac{\partial(\rho u)}{\partial x} - v \frac{\partial(\rho u)}{\partial x} \right] dz$$

$$+ \int_0^\delta \left[\rho_\infty V_\infty \frac{\partial V_\infty}{\partial y} - \rho v \frac{\partial v}{\partial y} + V_\infty \frac{\partial(\rho v)}{\partial y} - v \frac{\partial(\rho v)}{\partial y} \right] dz$$

$$+ 2\Omega \int_0^\delta (\rho_\infty U_\infty - \rho u) dz - \Omega^2 y \int_0^\delta (\rho_\infty - \rho) dz = \tau_{oy} \quad (38y)$$

where the second half of each of the first two integral terms comes from the continuity equation. Since the shear stress gradients vanish in the free stream, their integrals have values only at the lower limits. These are the chordwise and spanwise skin frictions, τ_{ox} and τ_{oy}. These equations can be rewritten as

19

$$\frac{1}{h_1} \frac{\partial U}{\partial x} \rho_\infty U_\infty \int_0^\delta (1 - \frac{\rho u}{\rho_\infty U_\infty}) dz + \frac{1}{h_1} \frac{\partial}{\partial x} \left[\rho_\infty U_\infty^2 \int_0^\delta \frac{\rho u}{\rho_\infty U_\infty} (1 - \frac{u}{U_\infty}) dz \right]$$

$$+ \frac{\partial U}{\partial y} \rho_\infty U_\infty \int_0^\delta (\frac{V_\infty}{U_\infty} - \frac{\rho v}{\rho_\infty U_\infty}) dz + \frac{\partial}{\partial y} \left[\rho_\infty U_\infty^2 \int_0^\delta \frac{\rho v}{\rho_\infty U_\infty} (1 - \frac{u}{U_\infty}) dz \right]$$

$$- 2\Omega \rho_\infty U_\infty \int_0^\delta (\frac{V_\infty}{U_\infty} - \frac{\rho v}{\rho_\infty U_\infty}) dz - \Omega^2 x \int_0^\delta (\rho_\infty - \rho) dz = \tau_{ox} \quad (39x)$$

and

$$\frac{1}{h_1} \frac{\partial V_\infty}{\partial x} \rho_\infty U_\infty \int_0^\delta (1 - \frac{\rho u}{\rho_\infty U_\infty}) dz + \frac{1}{h_1} \frac{\partial}{\partial x} \left[\rho_\infty U_\infty^2 \int_0^\delta \frac{\rho u}{\rho_\infty U_\infty} (\frac{V_\infty}{U_\infty} - \frac{v}{U_\infty}) dz \right]$$

$$+ \frac{\partial V_\infty}{\partial y} \rho_\infty U_\infty \int_0^\delta (\frac{V_\infty}{U_\infty} - \frac{\rho v}{\rho_\infty U_\infty}) dz + \frac{\partial}{\partial y} \left[\rho_\infty U_\infty^2 \int_0^\delta \frac{\rho v}{\rho_\infty U_\infty} (\frac{V_\infty}{U_\infty} - \frac{v}{U_\infty}) dz \right]$$

$$+ 2\Omega \rho_\infty U_\infty \int_0^\delta (1 - \frac{\rho u}{\rho_\infty U_\infty}) dz - \Omega^2 y \int_0^\delta (\rho_\infty - \rho) dz = \tau_{oy} \quad (39y)$$

At this stage it is convenient to transform the distance normal to the wall by using a Stewartson transformation of the form

$$d\eta = \frac{\rho}{\rho_\infty} dz \quad (40)$$

The integral terms can then be written in an incompressible form as

$$\delta_x^* + \delta_\rho = \int_0^\delta (1 - \frac{\rho u}{\rho_\infty U_\infty}) dz = \int_0^\Delta (1 - \frac{u}{U_\infty}) d\eta + \int_0^\Delta (1 - \frac{\rho}{\rho_\infty}) d\eta \quad (41a)$$

$$\delta_y^* + \frac{V_\infty}{U_\infty} \delta_\rho = \int_0^\delta (\frac{V_\infty}{U_\infty} - \frac{\rho v}{\rho_\infty V_\infty}) dz = \int_0^\Delta (\frac{V_\infty}{U_\infty} - \frac{v}{U_\infty}) d\eta + \frac{V_\infty}{U_\infty} \int_0^\Delta (1 - \frac{\rho}{\rho_\infty}) d\eta \quad (41b)$$

$$\theta_{xx} = \int_0^\delta \frac{\rho u}{\rho_\infty U_\infty} (1 - \frac{u}{U_\infty}) dz = \int_0^\Delta \frac{u}{U_\infty} (1 - \frac{u}{U_\infty}) d\eta \quad (41c)$$

$$\theta_{xy} = \int_0^\delta \frac{\rho v}{\rho_\infty U_\infty} (1 - \frac{u}{U_\infty}) dz = \int_0^\Delta \frac{v}{U_\infty} (1 - \frac{u}{U_\infty}) d\eta \quad (41d)$$

$$\theta_{yx} = \int_0^\Delta (\frac{\rho u}{\rho_\infty U_\infty} (\frac{V_\infty}{U_\infty} - \frac{v}{U_\infty})dz = \int_0^\Delta \frac{u}{U_\infty} (\frac{V_\infty}{U_\infty} - \frac{v}{U_\infty})d\eta \tag{41e}$$

$$\theta_{yy} = \int_0^\Delta (\frac{\rho v}{\rho_\infty U_\infty} (\frac{V_\infty}{U_\infty} - \frac{v}{U_\infty})dz = \int_0^\Delta \frac{v}{U_\infty} (\frac{V_\infty}{U_\infty} - \frac{v}{U_\infty})d\eta \ , \tag{41f}$$

where Δ is the thickness of some related incompressible boundary layer. These are the three-dimensional forms of the displacement and momentum thicknesses. The terms δ_x^* and θ_{xx} are the same as in two-dimensional boundary layer theory. The term δ_ρ represents a change in thickness due to compressibility. The other thickness parameters, δ_y^*, θ_{xy}, θ_{yy} and θ_{yx}, arise from the existence of the velocities in the y direction and are not present in two-dimensional flows. If the density ratio can be related to the local velocities, the only unknowns remaining on the left side of the momentum equations are the integral terms involving u and v. The solution of the energy equation (Equation (16)) can be used to supply this ratio.

In two-dimensional work, only the momentum and displacement thicknesses in the x direction appear. A shape factor, $H = \delta_x^*/\theta_{xx}$, can be used to relate these variables, thereby permitting a solution of the momentum equations without a knowledge of the velocity profiles. In the three-dimensional case, velocity profiles are required to relate the numerous thickness parameters and reduce the number of variables in the integrated equations. Power law profiles of a form suggested in Reference (9),

$$\frac{q}{Q_\infty} = (\frac{\eta}{\Delta})^{1/N} \tag{42}$$

and

$$\frac{n}{Q_\infty} = (1 - \frac{\eta}{\Delta})^2 (\frac{\eta}{\Delta})^{1/N} \phi \ , \tag{43}$$

where

$$\phi = \frac{\tau_{oy}}{\tau_{ox}} = \tan(\epsilon) \quad , \tag{44}$$

are used in the streamwise and crossflow directions. Their shapes are shown for various exponents in Figure (2). The angle ϵ is the angle between the surface streamline and the external flow. Since the overall thickness parameters rather than the details of the velocity profiles are required in the equations, these profiles are considered to be sufficiently representative without involving the complexity of integrating a three-dimensional form of a perhaps more rigorous law of the wall/law of the wake profile. Thus, power law profiles are resolved into streamwise and chordwise directions,

21

$$\frac{u}{U_\infty} = \left(\frac{\eta}{\Delta}\right)^{1/N} - \frac{V_\infty}{U_\infty}\left(1 - \frac{\eta}{\Delta}\right)\left(\frac{\eta}{\Delta}\right)^{1/N}\phi$$

and

$$\frac{v}{U_\infty} = \frac{V_\infty}{U_\infty}\left(\frac{\eta}{\Delta}\right)^{1/N} + \left(1 - \frac{\eta}{\Delta}\right)^2\left(\frac{\eta}{\Delta}\right)^{1/N}\phi ,$$

and are then used to evaluate the integrals in terms of the thickness Δ, the skew angle ε, and the quantity N:

$$\delta_x^* + \delta_\rho = \Delta\left[1 - A + \frac{V_\infty}{U_\infty}\phi B\right] + \frac{\gamma-1}{2} M_\infty^2 \Delta\left[1 - C - \phi^2 E\right] \tag{45a}$$

$$\theta_{xx} = \Delta\left[A - \frac{V_\infty}{U_\infty}\phi B - C + 2\frac{V_\infty}{U_\infty}\phi D - \frac{V_\infty^2}{U_\infty^2}\phi^2 E\right] \tag{45b}$$

$$\theta_{xy} = \Delta\left[\frac{V_\infty}{U_\infty}A + \phi B - \frac{V_\infty}{U_\infty}C - \left(1 - \frac{V_\infty^2}{U_\infty^2}\right)D\phi + \frac{V_\infty}{U_\infty}\phi^2 E\right] \tag{45c}$$

$$\delta_y^* + \frac{V_\infty}{U_\infty}\delta_\rho = \Delta\left[\frac{V_\infty}{U_\infty}(1 - A) - \phi B\right] + \frac{V_\infty}{U_\infty}\frac{\gamma-1}{2} M_\infty^2\Delta\left[1 - C - \phi^2 E\right] \tag{45d}$$

$$\theta_{yy} = \Delta\left[\frac{V_\infty^2}{U_\infty^2}(A - C) + \phi\frac{V_\infty}{U_\infty}(B - 2D) - \phi^2 E\right] \tag{45e}$$

$$\theta_{yx} = \Delta\left[\frac{V_\infty}{U_\infty}(A - C) - \frac{V_\infty^2}{U_\infty^2}\phi B - \left(1 - \frac{V_\infty^2}{U_\infty^2}\right)\phi D + \frac{V_\infty}{U_\infty}\phi^2 E\right] \tag{45f}$$

where $\quad A = \dfrac{N}{N + 1}$

$$B = \frac{N}{N + 1} - \frac{2N}{2N + 1} + \frac{N}{3N + 1}$$

$$C = \frac{N}{N + 2}$$

$$D = \frac{N}{N + 2} - \frac{N}{N + 1} + \frac{N}{3N + 2}$$

$$E = \frac{N}{N + 2} - \frac{2N}{N + 1} + \frac{6N}{3N + 2} - \frac{2N}{2N + 1} + \frac{N}{5N + 2}$$

The momentum equations, normalized by $\rho_\infty U_\infty^2$, now appear as

$$\frac{1}{h_1} \frac{1}{U_\infty} \frac{\partial U_\infty}{\partial x} (\delta_x^* + \delta_\rho) + \frac{1}{h_1} \frac{1}{\rho_\infty U_\infty^2} \frac{\partial}{\partial x} (\rho_\infty U_\infty^2 \theta_{xx})$$

$$+ \frac{1}{U_\infty} \frac{\partial U_\infty}{\partial y} (\delta_y^* + \frac{V_\infty}{U_\infty} \delta_\rho) + \frac{1}{\rho_\infty U_\infty^2} \frac{\partial}{\partial y} (\rho_\infty U_\infty^2 \theta_{xy})$$

$$- 2 \frac{\Omega}{U_\infty} (\delta_y^* + \frac{V_\infty}{U_\infty} \delta_\rho) - \frac{\Omega^2 x}{U_\infty^2} \delta_\rho = \frac{\tau_{ox}}{\rho_\infty U_\infty^2} \quad (46x)$$

$$\frac{1}{h_1} \frac{1}{U_\infty} \frac{\partial V_\infty}{\partial x} (\delta_x^* + \delta_\rho) + \frac{1}{h_1} \frac{1}{\rho_\infty U_\infty^2} \frac{\partial}{\partial x} (\rho_\infty U_\infty^2 \theta_{yx})$$

$$+ \frac{1}{U_\infty} \frac{\partial V_\infty}{\partial y} (\delta_y^* + \frac{V_\infty}{U_\infty} \delta_\rho) + \frac{1}{\rho_\infty U_\infty^2} \frac{\partial}{\partial y} (\rho_\infty U_\infty^2 \theta_{yy})$$

$$+ 2 \frac{\Omega}{U_\infty} (\delta_x^* + \delta_\rho) - \frac{\Omega^2 y}{U_\infty^2} \delta_\rho = \frac{\tau_{oy}}{\rho_\infty U_\infty^2} \quad (46y)$$

Two things remain to be specified: the skin friction and the quantity N from the power law. In zero pressure gradient cases, a value of seven is commonly used for N; however, for more general use, 1/N may be related to the shape factor H by evaluating δ_x^*/θ_{xx} in two-dimensional form, giving

$$\frac{1}{N} = \frac{H-1}{2} \quad (47)$$

The change in H as the boundary layer develops in pressure gradient cases can be obtained from an empirical relation such as that given by von Doenhoff and Tetervin, Reference (21),

$$\theta_q \frac{dH}{dx} = e^{4.680(H - 2.975)} \left[-\frac{\theta_q}{\rho_\infty Q_\infty^2} \frac{d(\rho_\infty Q_\infty^2)}{dx} \frac{\rho_\infty Q_\infty^2}{\tau_o} - 2.035(H - 1.286) \right] \quad (48)$$

The momentum thickness, θ_q, is evaluated using the streamwise velocity profile. There are several other methods of accounting for shape factor changes, but the above relationship is the most readily compatible with the present integral technique. Since the conditions under which it was determined are similar to the cases with which it will be used, good results might be expected. These conditions include turbulent boundary

23

layers under moderate adverse pressure gradients on the upper surface of an airfoil.

The skin friction must also be obtained from an empirical relation. Integral techniques have most commonly relied on the Ludweig-Tillman law from Reference (22),

$$\frac{\tau_{oq}}{\rho_\infty Q_\infty^2} = .123 \times 10^{-0.678H} \left(Re_{\theta_q} \right)^{-0.268}$$

This relationship illustrates the dependence of the skin friction on the shape factor, H. However, since the work of von Doenhoff and Tetervin was based on the skin friction law of Squire and Young, Reference (23), their relation

$$\frac{\tau_{oq}}{\rho_\infty Q_\infty^2} = 1/ \left[5.890 \log_{10}(4.074 \, Re_{\theta_q}) \right]^2 \tag{49}$$

must be used. Since H does not enter into this relation, it may be inaccurate for large values of the shape factor. However, the growth of the calculated boundary layer should be unaffected by this since it is controlled by the empirical shape factor relationship.

Both the shape factor relation and the skin friction law are two-dimensional in origin and are to be applied along the streamwise direction. The skin friction can be resolved into spanwise and chordwise components,

$$\frac{\tau_{ox}}{\rho_\infty U_\infty^2} = \frac{\tau_{oq}}{\rho_\infty Q_\infty^2} \left(\frac{Q_\infty}{U_\infty} - \phi \, \frac{V_\infty Q_\infty}{U_\infty^2} \right)$$

$$\frac{\tau_{oy}}{\rho_\infty U_\infty^2} = \frac{\tau_{oq}}{\rho_\infty Q_\infty^2} \left(\frac{Q_\infty V_\infty}{U_\infty^2} + \phi \, \frac{Q_\infty}{U_\infty} \right)$$

This follows from the definition of ϕ. The shape factor is not a directional property. Its value is considered to be unique at every point and therefore determinable from the two-dimensional relation.

A solution of the momentum equations is now possible. This becomes clear if they are rewritten as two simultaneous partial differential equations in the form

$$F \frac{\partial \Delta}{\partial x} + G \frac{\partial \phi}{\partial x} = H \tag{50x}$$

24

$$R \frac{\partial \Delta}{\partial x} + S \frac{\partial \phi}{\partial x} = T \qquad\qquad (50y)$$

where $\quad F = \frac{1}{h_1} \frac{\theta_{xx}}{\Delta}$

$$G = \frac{\Delta}{h_1} \left[\frac{V_\infty}{U_\infty} (2D - B) - 2 \frac{V_\infty^2}{U_\infty^2} \phi E \right]$$

$$H = - \frac{1}{h_1} \frac{1}{U_\infty} \frac{\partial U_\infty}{\partial x} (\delta_x^* + \delta_\rho) - \frac{1}{\rho_\infty U_\infty^2} \frac{\partial}{\partial x} (\rho_\infty U_\infty^2) \frac{\theta_{xx}}{h_1}$$

$$- \frac{\Delta}{h_1} \frac{\partial}{\partial x} (\frac{V_\infty}{U_\infty}) \left[\phi(2D - B) - 2 \frac{V_\infty}{U_\infty} \phi^2 E \right]$$

$$- \frac{1}{U_\infty} \frac{\partial U_\infty}{\partial y} (\delta_y^* + \frac{V_\infty}{U_\infty} \delta_\rho) - \frac{1}{\rho_\infty U_\infty^2} \frac{\partial}{\partial y} (\rho_\infty U_\infty^2 \theta_{xy})$$

$$+ \frac{2\Omega}{U_\infty} (\delta_y^* + \frac{V_\infty}{U_\infty} \delta_\rho) + \frac{\Omega^2 x}{U_\infty^2} \delta_\rho + \frac{\tau_{ox}}{\rho_\infty U_\infty^2}$$

$$R = \frac{1}{h_1} \frac{\theta_{yx}}{\Delta}$$

$$S = \frac{\Delta}{h_1} \left[- \frac{V_\infty^2}{U_\infty^2} B - (1 - \frac{V_\infty^2}{U_\infty^2})D + 2 \frac{V_\infty}{U_\infty} \phi E \right]$$

$$T = - \frac{1}{U_\infty} \frac{\partial V_\infty}{\partial x} \frac{1}{h_1} (\delta_x^* + \delta_\rho) - \frac{1}{\rho_\infty U_\infty^2} \frac{\partial}{\partial x} (\rho_\infty U_\infty^2) \frac{\theta_{yx}}{h_1}$$

$$- \frac{\Delta}{h_1} \frac{\partial}{\partial x} (\frac{V_\infty}{U_\infty}) \left[A - C + 2 \frac{V_\infty}{U_\infty} \phi(D - B) + \phi^2 E \right]$$

$$- \frac{1}{U_\infty} \frac{\partial V_\infty}{\partial y} (\delta_y^* + \frac{V_\infty}{U_\infty} \delta_\rho) - \frac{1}{\rho_\infty U_\infty^2} \frac{\partial}{\partial} (\rho_\infty U_\infty^2 \theta_{yy})$$

$$- \frac{2\Omega}{U_\infty} (\delta_x^* + \delta_\rho) + \frac{\Omega^2 y}{U_\infty^2} \delta_\rho + \frac{\tau_{oy}}{\rho_\infty U_\infty^2}$$

25

If initial values of Δ, ϕ, and H are specified along a line parallel to
the leading edge, the spanwise gradients can be evaluated and the skin
friction and shape factor gradient can be calculated at regular points
along this line. The momentum equations can then be solved for the chord-
wise gradients at each of these points; these gradients may then be inte-
grated in the x direction from each point to determine the parameters Δ,
ϕ and H along a new line parallel to the leading edge. The process can
then be repeated as far downstream as required. The value of δ_0 can be
used to transform the results back into a compressible coordinate system.

2.3 THE BOUNDARY CONDITIONS

2.3.1 The External Flow

The two independent methods of predicting turbulent boundary layer develop-
ment on a rotor blade require that the external flow magnitude and direc-
tion be specified beforehand. This flow is comprised of the rotational
velocity, the velocity induced by the pressure distribution on the blade,
and a superimposed crossflow velocity component due to the close passage
of the trailing tip vortex from the preceding blade.

In a rotating rectangular coordinate system, the spanwise and chordwise
rotational velocity components can be expressed as

$$U_a = \Omega y \tag{51a}$$

and

$$V_a = -\Omega(x - \frac{c}{4}) \tag{51b}$$

respectively; y is measured from the axis of rotation, as described in
Figure (1). In performing the calculation on a rotor blade, the $x = c/4$
line is made to coincide with the quarter chord line. Spanwise rotational
flow is outward ahead of this line (negative x) and inward behind this
line (positive x).

The flow over a rotating flat plate is described completely by the above
rotational velocities. When the surface assumes a thickness distribution
such as that of an airfoil, the local flow velocities are altered by the
resulting pressure distribution. The pressure distribution is expressed
in terms of the pressure coefficient,

$$Cp = \frac{p_\infty - p_a}{\frac{1}{2} \rho_a U_a^2} \, ,$$

which, for later use, can be rewritten as

$$\frac{p_\infty}{p_a} = 1 + \frac{\frac{1}{2} \rho_a U_a^2 Cp}{p_a} \tag{52}$$

26

The subscript (a) refers to the ambient conditions, which are also the static conditions in the rotating system, and the subscript (∞) refers to the local conditions just outside the boundary layer. In the absence of exact pressure distribution data which includes the effect of the external crossflows, an approximate two-dimensional pressure distribution based on the chordwise flow is used.

To solve for the local velocity, U_∞, in terms of the pressure coefficient and the ambient conditions, the pressures are first related to the Mach numbers,

$$\frac{p_a}{p_\infty} = \frac{\left[1 + (\frac{\gamma-1}{2}) \, M_\infty^{\,2} \right]^{\frac{\gamma}{\gamma-1}}}{\left[1 + (\frac{\gamma-1}{2}) \, M_a^{\,2} \right]^{\frac{\gamma}{\gamma-1}}}$$

This may be combined with Equation (52) to eliminate the pressure p_∞.

$$\frac{\left[1 + (\frac{\gamma-1}{2}) \, M_\infty^{\,2} \right]}{\left[1 + (\frac{\gamma-1}{2}) \, M_a^{\,2} \right]} = \left(1 + \frac{\frac{1}{2} \rho_a U_a^{\,2} Cp}{p_a} \right)^{-\frac{\gamma-1}{\gamma}} \tag{53}$$

The local Mach number may then be expressed as

$$M_\infty^{\,2} = \frac{2}{\gamma-1} \left\{ \left[1 + (\frac{\gamma-1}{2}) \, M_a^{\,2} \right] \left(1 + \frac{\frac{1}{2} \rho_a U_a^{\,2} Cp}{p_a} \right)^{-\frac{\gamma-1}{\gamma}} - 1 \right\}$$

The local velocity can be obtained from $U_\infty = M_\infty a_\infty$, but first the local sound speed, a_∞, must be defined. The adiabatic temperature ratio and Equation (53) are used to find an expression for the ratio of local to ambient sound speeds,

$$\frac{T_\infty}{T_a} = \frac{\left[1 + (\frac{\gamma-1}{2}) \, M_a^{\,2} \right]}{\left[1 + (\frac{\gamma-1}{2}) \, M_\infty^{\,2} \right]} = \frac{a_\infty^{\,2}}{a_a^{\,2}} = \left(1 + \frac{\frac{1}{2} \rho_a U_a^{\,2} Cp}{p_a} \right)^{\frac{\gamma-1}{\gamma}} \tag{54}$$

The local velocity is then written in terms of the pressure coefficient and the static conditions,

$$U_\infty^{\,2} = \frac{2}{\gamma-1} \, a_a^{\,2} \left[1 + \frac{\gamma-1}{2} \left(\frac{U_a}{a_a} \right)^2 - \left(1 + \frac{\frac{1}{2} \rho_a U_a^{\,2} Cp}{p_a} \right)^{\frac{\gamma-1}{\gamma}} \right] \tag{55}$$

27

By using the adiabatic density ratio, the local density, ρ_∞, can be obtained in a similar manner and expressed as

$$\rho_\infty = \rho_a \left(1 + \frac{\frac{1}{2} \rho_a U_a^2 Cp}{P_a} \right)^{\frac{1+\gamma}{2\gamma}} \tag{56}$$

The local velocity and density are thus known in terms of the ambient conditions and the pressure distribution of the airfoil. Typical upper surface pressure distributions at angles of attack of 0° and 4° for a Mach number of 0.65 from Reference (24) are plotted in Figure (3). They were obtained from two-dimensional tests conducted on a 12%-thick symmetrical airfoil section. In both cases, an approximation of the measured pressure distribution has been made by assuming a constant pressure over the first quarter of the chord and an increasing pressure over the remainder. Since the actual pressure distributions are also functions of the Mach number, the approximations are meant to be representative of the adverse pressure gradients that may be encountered on an airfoil. These pressure gradients cause a deceleration of the flow and a thickening of the boundary layer toward the trailing edge. It is this region of an airfoil on which a turbulent boundary layer is most likely to separate. Lower surface pressure distributions at positive angles of attack may be adequately presented by a constant or mildly adverse pressure distribution.

The magnitude of the pressure gradient may be obtained from the slope of the pressure coefficient, and if this is nondimensionalized by the chord, the approximated distributions have values of $dCp/d(x/C)$ of 1 and 2. The local velocity gradient to which the boundary layer is subjected is obtained by differentiating the velocity expression, Equation (55), to give

$$\frac{\partial U_\infty}{\partial x} = - \frac{\frac{1}{2} \rho_a U_a^2 a_a^2}{\gamma U_\infty P_a} \left[\frac{1}{C} \frac{dCp}{d(x/C)} \right] \left(1 + \frac{\frac{1}{2} \rho_a U_a^2 Cp}{P_a} \right)^{-\frac{1}{\gamma}} \tag{57}$$

Similarly, the density gradient is given by

$$\frac{\partial \rho_\infty}{\partial x} = \rho_a \frac{1+\gamma}{2\gamma} \left(1 + \frac{\frac{1}{2} \rho_a U_a^2 Cp}{P_a} \right)^{\frac{1-\gamma}{2\gamma}} \frac{\frac{1}{2} \rho_a U_a^2}{P_a} \left[\frac{1}{C} \frac{dCp}{d(x/C)} \right] \tag{58}$$

In multibladed rotors, a significant external spanwise flow may be imposed by the presence of a trailing tip vortex from the preceding blade. It has been shown in References (25) and (26) that such vortices remain near the plane of the rotor until they pass the following blade and are then swept down away from the blades. The region of blade-vortex interference is somewhat inboard of the tip due to wake contraction; for this analysis, it can be assumed to be centered at the 90-percent radial station. A more

28

precise positioning of the vortex would be necessary for rotor performance calculations.

The magnitude of this spanwise flow can be estimated from potential theory by writing the stream function of a line vortex and its image, each of which is parallel to the x direction at a distance Z from the surface $z = 0$ and at a distance Y from $y = 0$,

$$\psi = \frac{\Gamma}{4\pi} \log_e \frac{(Y-y)^2 + (Z-z)^2}{(Y-y)^2 + (Z+z)^2} \tag{59}$$

The resultant spanwise velocity at the surface is determined by differentiating the stream function with respect to z and setting z equal to zero,

$$V_\infty = \frac{\partial \psi}{\partial z} = \frac{1}{\pi} \frac{\Gamma}{Z} \frac{Z^2}{(Y-y)^2 + Z^2} \tag{60}$$

The portion of the vortex which is in the region of the blade is represented as a straight segment parallel to the x direction. This spanwise velocity distribution may be superimposed on the chordwise flow to create a representative rotor blade flow to which a boundary layer may be subjected. The thickness of the boundary layer on the surface has been neglected in e or acing V_∞ since it is much less than the height Z, which itself has on. an approximate value.

2.3.2 The Rotor Blade

In the development of the equations of motion and of the two solution methods, the scale factor depicting coordinate curvature in the chordwise direction, h_1, was retained. This scale factor is related to the radius of curvature of the x coordinate in the z direction by

$$\frac{1}{h_1} \frac{\partial h_1}{\partial z} = \frac{1}{R_{zx}}$$

Since h_1 has been taken to be solely a function of z, the derivative can be written as a total rather than a partial, and the scale factor can be determined as a function of z by integration. This gives

$$h_1 = \frac{R_O + z}{R_O} \tag{61}$$

where R_{zx} has been written as the radius of curvature of the surface plus the distance from the surface, $R_O + z$, and the constant of integration has been determined by letting $h_1 = 1$ at $z = 0$. In the integral method, one-half of the boundary layer thickness, δ, is used as the appropriate

29

value of z. The gradient of the scale factor can be obtained by differentiation,

$$\frac{dh_1}{dz} = \frac{1}{R_o} \qquad (62)$$

and can be seen to be constant above every point on the surface. If the surface is assumed to be a circular arc, R_o will be fixed for all points on the blade. Such an arc is shown in Figure (4), along with an NACA 0012 airfoil for comparison. The two curves are tangent at the 30-percent station, and they intersect at the trailing edge. It can be shown by trigonometry that the radius of such an arc is $R_o = 4.1C$, where C is the chord in feet. This approximation will be used in conjunction with the assumed pressure distribution and the vortex crossflow representation to simulate actual conditions for the prediction of turbulent boundary layer growth on a rotating blade.

3. APPLICATION OF THEORY

3.1 DEVELOPMENT OF THE NUMERICAL METHODS

3.1.1 The Differential Method

With the exception of some difficulty with the shear stress gradients the development of the numerical methods for the differential technique was comparatively routine. A computer program was written first to solve the reduced form of the equations of motion, Equations (33) and (34), for the local chordwise velocity gradients along normals to the surface in the initial X plane, and then to integrate them over the surface to follow the flow development.

A simple fixed mesh structure was used as a basis for the solution. The spacing of the solution points in the direction of solution, the X or chordwise direction, was determined by a compromise between several factors: the sensitivity of the integration procedure to step size; the requirement, noted in Reference (5), that for a stable solution the ratio of the chordwise and spanwise steps, $\Delta x/\Delta y$, should not exceed U_∞/V_∞; and the more practical economic factor that excessively small chordwise steps would result in unacceptably long computation times. In the early stages of development, a fixed chordwise step size of 0.5 times the smallest boundary layer thickness present on the surface was used. It was found that this could be increased considerably, and an initial step size of 0.01 ft was eventually used for all the conditions examined. This initial step size was used for the first four steps of the calculation to allow conditions to stabilize and was then increased by a factor of 2× for the remainder of the calculation. The regular step size was felt to be acceptable in view of the simple forward stepping integration technique being used. If an iterative technique were employed, or if an implicit solution were being considered, then variable chordwise steps would perhaps be more appropriate. The step size in the spanwise direction was also chosen to give economic computation times without sacrificing definition of the flow field in regions of high spanwise rates of change or compromising the stability requirement noted above. The steps used were 1.0 ft on the large blade, $\Delta y/R = 0.025$, and 0.5 ft on the small blade, $\Delta y/R = 0.05$. In a differential solution, and particularly in one in which numerical differentiation of the variation of parameters normal to the surface has to be carried out, the distribution of points normal to the surface must be considered with particular care. Points must be distributed with not only the rates of change of conditions normal to the wall in mind but also the peculiarities of the differentiating techniques to be used. In order to keep the computation as simple as possible, a fixed normal coordinate system was used with the points distributed exponentially away from the wall following

$$z_k = 0.5 \times 10^{-4} \left[10^{0.1(k-1)} - 1 \right]$$

The dimensions of z are in ft, and k is an integer with value 1 at the wall

and 40 at the point furthest from the wall. This distribution gave at least 20 points within the boundary layer for the thinnest case considered, with a minimum of 8 points in the laminar sublayer.

Evaluation of the coefficients of Equations (33) and (34) requires that the gradients of several quantities, in a normal and spanwise direction, be known. Since the mesh size is regular in the spanwise direction and rates of change are comparatively low, a simple three-point Lagrangian interpolation formula was used to determine the gradients in this direction. The nonuniform step size normal to the wall presented some problems, however. Initially, a five-point Lagrangian interpolation scheme with nonuniform intervals was used. It was found that this method introduced significant errors in the first and unacceptable errors in the second derivative because of the concentration of points in the lower end of the groups. The problem was overcome and the errors were minimized by transforming the normal coordinate into a form where the intervals between solution points were uniform and carring out the differentiation using a second order, orthogonal Lagrangian polynomial fit on five adjacent points. The transformation used was simply the inverse of the expression used above to define z_k, the differentiation being carried out in terms of k.

In order to give a basis for comparison, the two calcualtion methods used identical initial conditions. The boundary layer was fully developed and turbulent from the leading edge, and initially, both the skin friction and the total boundary layer thickness were given by the simple zero pressure gradient forms

$$\delta = 0.37x \left[\frac{Q_{\infty}x}{\nu} \right]^{-\frac{1}{5}} \quad \text{and}$$

$$C_f = 0.0296 \left[\frac{Q_{\infty}x}{\nu} \right]^{-\frac{1}{5}}$$

Since the external flow is specified, the above expressions may be used to give the skin friction and boundary layer thickness along the starting line, $x/c = 0.1$. The law of the wall/law of the wake form for the turbulent profile suggested in Reference (27) and the tanh form of the sublayer profile suggested in Reference (28) were used, together with the surface skin friction and boundary layer thickness given above, to define the initial velocity profile. The initial crossflow velocity profile was assumed to be given by Equation (43). The calculation was found to be insensitive to the initial value of the surface skew, ϕ in Equation (43), the spanwise velocity profile being dominated by the spanwise component of the streamwise profile, and an initial value of zero was subsequently used.

The most significant effort during the development of the method was in finding satisfactory form for the shear stress gradient normal to the wall. It was originally intended that the shear stress gradients in the turbulent part of the layer be determined by differentiating the stresses

32

calculated using the mixing length approach, Equation (26). These would then be faired into the wall values using an interpolation based on the tanh series suggested in Reference (19) and extended to the three-dimensional case. This method was found to be impractical since it was very sensitive to the quality of the match at the edge of the sublayer. Any nonuniformity in the shear stress gradient normal to the feeds into the calculation of the chordwise velocity gradient, and this tends to magnify the irregularity as the solution proceeds. This is associated with the difficulty of obtaining precise gradients using a numerical differentiation scheme discussed above. The problem is accentuated because obtaining the gradient of the shear stress involves differentiating the product of several previous differentiation operations, Equations (26). The errors are compounded and the difficulty of obtaining a uniform match at the edge of the sublayer arises. Considerable effort was put into finding a solution to this problem, but with little success. Eventually, the first five points outside the sublayer were fitted by a least mean square process to follow $u+^2$, and the interpolation outlined in the appendix was used.

3.1.2 The Integral Method

The development of the integral method entailed no major problems. A computer program was initially written to evaluate the integral form of the momentum equations (Equations (50x) and (50y)) simultaneously over a simulated rotor blade surface. The Ludweig-Tillman skin friction relation was originally used in this program to calculate boundary layer growth with zero pressure gradient. The shape factor was assumed to have a constant value of $H = 1.286$. This corresponds to a power law profile with an exponent of $1/7$, as indicated by Equation (47). The required initial values of δ were obtained from a two-dimensional relationship suggested in Reference (16).

$$\delta = 0.37x \left[\frac{Q_{\infty}x}{\nu} \right]^{-\frac{1}{5}}$$

This presupposes a turbulent boundary layer from the leading edge $(x = 0)$ onward, as was previously indicated.

The initial value of the tangent of the skew angle, ϕ, is not as readily estimated. At first, this was done by assuming $\phi = 0.0$ along the first row of chordwise stations. This appeared reasonable, since the solutions that followed over the remainder of the blade indicated that the crossflow stayed small. Nevertheless, several initial values for ϕ, including negative numbers, were tried; the solutions were found to be unaffected after four or five steps. Thus, $\phi = 0.0$ has been used in starting all subsequent calculations.

With these initial conditions and a knowledge of the external flow, the integral momentum equations can be evaluated according to the procedure outlined at the end of Section 2.2.3. No spanwise boundary conditions are required; all variables are determined either from the preceding chordwise

33

station or from the external flow conditions. The spanwise gradients are calculated with a three-point Lagrangian interpolation. The end gradients are determined from the last three spanwise points with an appropriate form of the interpolation, which is justifiable except when the spanwise flow is entering the calculation region, as pointed out in Reference (5). This condition occurs at the tip aft of the quarter chord due to the circular form of the streamlines. The possible ill effects of this are considered to be small because the external flow and its gradients are well defined in these regions and because they behave smoothly in all cases.

The next major step in the development of the integral method was the use of a variable shape factor to allow consideration of adverse pressure gradients. Equations (55) through (58) are used to specify the free stream velocity and density and their chordwise gradients when pressure distributions of the form discussed in Section 2.3.1 are applied. The computation procedure was modified to calculate the shape factor gradient from the von Doenhoff-Tetervin relation before solving the motion equations. The shape factor at each step is determined from its value and gradient at the previous step. In constant pressure regions, the gradient is zero. The skin friction law was replaced with the Squire-Young relation, Equation (49), as is required for compatibility with the von Doenhoff-Tetervin equation. The change of skin friction relationships decreased δ in zero pressure gradient cases. This is examined more fully in the discussion of results.

The chordwise step size was chosen to be 0.1 foot. Steps which were an order of magnitude smaller were tried, but no significant difference was observed without pressure gradients. For adverse pressure gradient cases, the 0.1-foot step is larger than von Doenhoff and Tetervin recommend, but the location of the separation point on a blade with a chord of 2 feet is changed less than 5 percent. Larger chordwise steps would significantly impair the results. Spanwise gradients were found to be very small in relation to chordwise gradients. Thus, the use of a larger spanwise step size is considered appropriate. A step of 1 foot was used in this direction.

3.2.1 Data Input

Data input to the boundary layer programs is accomplished via punched cards. This allows the greatest ease and flexibility in setting various conditions for the computation. Details of the usage of the programs are covered in the Documentation of Software Report. The data required by both programs is basically the same. Ambient air conditions, including density, temperature, pressure, and sound speed, are read in. The blade geometry is specified by inputting the blade radius, chord and the blade surface radius of curvature, along with the inboard radial station for starting the calculation. Spanwise and chordwise step sizes are also read in. The angular velocity combined with the minimum pressure coefficient and the nondimensionalized pressure gradient enable the programs to calculate the chordwise external flow field. A nonrotating case can be run by setting $\Omega = 0.0$ and giving a positive value for the two-dimensional free-stream velocity. (Use of both this velocity and a nonzero Ω will not simulate forward

34

flight.) The amount of the blade which is subjected to constant pressure in the adverse pressure gradient cases is an input variable, but values other than one quarter of the chord have not been used. The vortex cross-flow is defined by supplying values of the circulation strength and the spanwise and normal positions of the vortex core. In addition, the integral method requires the initial value of the shape factor. The data output format is selected in each method by a series of inputs which are discussed in the Documentation of Software Report.

A wide range of input data is acceptable, although a few reservations should be observed. Singularities that should be avoided occur when the external chordwise velocity is zero and when the surface radius of curvature is zero. The first will happen when both the two-dimensional velocity and Ω are zero. Free stream flows should generally remain subsonic. Even though the solution of the energy equation which has been used is appropriate above these velocities, no consideration has been given to the possibility of shock formation or shock wave/boundary layer interaction. The general choice of step sizes has been discussed in Section 3.1.

In performing the calculations, standard sea level conditions were used for the ambient air. Since the effects of rotation are to be considered relative to helicopter applications, two blade radii, 40 feet and 10 feet, were selected as representative of large present-day helicopter main and tail rotors. The large and small blades have chords of 2 feet and 1 foot, respectively. Angular velocities of 10, 15, and 20 rad/sec for the large blade and 40, 60, and 80 rad/sec for the small blade were chosen. These speeds encompass a wide range of angular velocities without introducing locally supersonic flow even in the strong pressure gradient cases. The form of the pressure distribution, along with the magnitudes of the surface radii of curvature, was discussed in Section 2.3.

Circulation strengths of ± 200 and ± 400 ft^2/sec and a passage distance from the surface of $Z = 2$ feet are considered appropriate for the vortex interfering with the 40-foot blade. The positive values represent a vortex passing over the top surface by imposing an outward flow and the negative values represent a vortex passing under the lower surface by imposing an inward flow. The circulation strengths for the 10-foot blade are ± 25 and ± 50 ft^2/sec at a distance from the surface of $Z = 1$ foot.

3.2.2 Data Output

Calculated data is printed out in tabular form for each of the programs, as is described in detail in the Documentation of Software Report. Data is listed according to chordwise and spanwise position. The variables available for output include the various thickness related parameters, the shear stresses, the skew angles, and the calculated external flow. The differential method inherently has more output information available in the form of a listing of the actual velocity profiles, as well as a breakdown normal to the surface of the forces that influence the flow. The available information is used as a practical aid in the data analysis. To obtain a record of the output that can be put to future use by the computer, the most vital data was punched on cards. This is detailed in the Documentation of

Software Report. This form of output was the source for the data summary presented in Tables I through XII and the plotted data in Figures (5) through (40). In both cases, the original output cards were used to supply the required information which was repunched in the necessary format. The tables were generated by listing these punched output cards. The output for the figures was used to generate curves for a numerically controlled drafting machine. The displacement thickness curves in Figures (5) through (16) and the skew angle curves in Figures (17) through (28) were obtained by fitting a curve with second derivative continuity through the data points. Irregularities in the velocity profiles near the surface where the calculation points are extremely close together prevented this curve fit routine from being used, so Figures (29) through (4), the velocity profiles, were drawn with straight line segments connecting each point. The figures are grouped to illustrate separately the effects of variation of angular velocity, vortex crossflow, pressure gradient, and surface curvature. The order of these groups is repeated for both the large and small blades, and this pattern is repeated for the presentation of the displacement thickness, the skew angles, and the velocity profiles of the flow. The summary data is similarly arranged in Tables I through XII.

4. DISCUSSION OF RESULTS

4.1 EFFECTS OF ROTATION

The equations of motion for the development of a turbulent boundary layer
on a rotating blade were obtained in Section 2. The equation for the
chordwise flow is analogous to the two-dimensional form of the boundary
layer equation with extra forcing and inertial terms added by the presence
of a crossflow velocity component and the fact that the whole system is
rotating about axis with some angular velocity Ω. The basic form of the
boundary layer equations used in both solution methods is given in
Equations (17x) and (17y), and they are repeated below for convenience.

$$-2\,\overline{\rho v}\,\Omega - \overline{\rho}\Omega^2 x + \frac{\overline{\rho u}}{h_1}\frac{\partial \overline{u}}{\partial x} + \overline{\rho v}\,\frac{\partial \overline{u}}{\partial y} + (\overline{\rho w} + \overline{\rho'w'})\left[\frac{\partial \overline{u}}{\partial z} + \frac{\overline{u}}{h_1}\frac{\partial h_1}{\partial z}\right]$$

$$= -\frac{1}{h_1}\frac{\partial \overline{p}}{\partial x} + \frac{\partial}{\partial z}\left[\frac{\overline{\mu}}{h_1}\frac{\partial}{\partial z}(h_1\overline{u})\right] - \frac{\partial}{\partial z}\left[\overline{\rho}\,\overline{u'w'}\right]$$

$$2\,\overline{\rho u}\,\Omega - \overline{\rho}\Omega^2 y + \frac{\overline{\rho u}}{h_1}\frac{\partial \overline{v}}{\partial x} + \rho v\,\frac{\partial \overline{v}}{\partial y} + (\overline{\rho w} + \overline{\rho'w'})\,\frac{\partial \overline{v}}{\partial z}$$

$$= -\frac{\partial \overline{p}}{\partial y} + \frac{1}{h_1}\frac{\partial}{\partial z}\left[\overline{\mu}\,h_1\frac{\partial \overline{v}}{\partial z}\right] - \frac{\partial}{\partial z}\left[\overline{\rho}\,\overline{v'w'}\right]$$

The terms $-\rho\Omega^2 x$ and $-\rho\Omega^2 y$ in Equations (17x) and (17y), respectively, are
components of the acceleration of the rotating coordinate system toward
the center of rotation. Except for the origin, all points which are
stationary in the rotating system have an acceleration in the inertial
frame of reference. In addition, a point moving in the rotating system
has a Coriolis acceleration perpendicular to its direction of motion and
the axis of rotation. The terms $-2\rho v\Omega$ and $+2\rho u\Omega$ represent the chordwise
and spanwise rates of change of momentum of a point as it traverses a re-
gion of varying rotational velocity. These two sets of acceleration terms
represent the direct effects of the rotation. Further indirect effects
are associated with the choice of the coordinate system. The flow is
being defined relative to a rectangular coordinate system fixed on the
blade surface and rotating about an axis on the blade quarter chord line.
Because of this, the spanwise external flow velocity is positive ahead of
the quarter chord line and negative aft, and an effective pressure gradient
term is introduced into the chordwise equation even when no chordwise
pressure gradient is present, Equation (20). The spanwise equation, (17y),
is of course dominated by the radial gradient of the chordwise velocity
associated with the rotation.

The effect of centrifugal force on the boundary layer is small and only
becomes significant close to the wall when compressibility effects become

37

large. This is apparent from Equations (27x) and (27y) where the centrifugal contribution is given as $-\Omega^2 x(\rho-\rho_\infty/h_1)$ and $-\Omega^2 y(\rho-\rho_\infty)$ respectively. The ρ_∞ terms are introduced from the pressure gradient substitution. For low Mach number flows, $\rho \approx \rho_\infty$ and the centrifugal effect are essentially zero. The influence of the Coriolis force, on the other hand, is significant, particularly on the spanwise flow. Since the chordwise velocity u is, for attached flows at least, positive, the effect of the Coriolis force will be to decelerate the spanwise flow. In the chordwise flow, the small effect of Coriolis force may be either accelerative or decelerative depending on whether the spanwise flow is outward or inward. Again, in the chordwise flow, the effect of the "pseudo" pressure gradient term, $V_\infty \partial V_\infty/\partial x$ in Equations (20), introduced by the external spanwise flow, is generally small. In rotating flat plate flow, $V_\infty = -\Omega(x-c/4)$ with $\partial V_\infty/\partial x = -\Omega$, making the effect of the term decelerative ahead of the quarter chord line and accelerative behind. Since the effect is proportional to Ω^2, it may be expected to be more significant on the smaller blades with the higher rotational speeds. The equivalent term in the spanwise equation, $U_\infty \partial U_\infty/\partial y$, is dominant and controls the flow in this direction.

The first noticeable feature of the boundary layer on the rotating surface is the spanwise variation of its characteristics due to the distribution of free stream velocity caused by rotation. This is most readily observed from the figures that compare results for various angular velocities, Figures (5), (11), (17), (23), (29), and (35), and from Tables I and VII. The increase in velocity with radius has a thinning effect on the thickness parameters and results in lower values of the skin friction, just as an increase in free stream velocity affects two-dimensional boundary layer growth. The boundary layer also becomes thinner for a given spanwise station as the angular velocity is increased, as can be seen by comparing parts (a), (b), and (c) of Figures (5) and (11).

When the chordwise momentum and displacement thicknesses are compared with two-dimensional results obtained at the same chordwise velocity, the differences are almost negligible. There is a very slight thinning in the three-dimensional case because the resultant velocity $Q_\infty^2 = U_\infty^2 + V_\infty^2$ along the chordwise line used for comparison is larger than that of the two-dimensional case. Further adjustments to U_∞ in the two-dimensional case for the sake of comparison would not be meaningful because the differences in results are already beyond the limits of practical significance. The behavior of the rotating boundary layer in terms of its growth rate is virtually two dimensional. The effects of rotation of the chordwise growth are negligible on both blades. The terms which describe these effects in the x momentum equation are typically two or three orders of magnitude less than the shear stress term which controls the development.

In Figures (5c) and (11c), the displacement thickness can be seen to increase with span rather than decrease. This occurs on the outer portion of both the large and small blades for the highest angular velocity cases and for the pressure gradient cases, but only when the free stream velocity exceeds approximately 600 ft/sec. Its origin may be traced to the effect of compressibility and the definition of the displacement thickness. From the solution of the energy equation (Equation (16)), the density within the

38

boundary layer can be seen to decrease near the surface as the Mach number increases. The displacement thickness,

$$\delta_x^* = \int_0^\infty (1 - \frac{\rho u}{\rho_\infty U_\infty}) dz$$

is thus increased as the ratio ρ/ρ_∞ becomes less than one. This thickness can be defined as the distance by which the surface would need to be moved if the flow were inviscid to produce the same external flow character-istics. If the density in the boundary layer is reduced, then the dis-placement thickness will correspondingly increase if the velocity profile is unchanged.

The boundary layer thickness, δ, remains unaffected because the velocity distribution is not significantly affected. A similar increase does not occur for the momentum thickness. The density ratio would appear from the definition

$$\theta_{xx} = \int_0^\infty \frac{\rho u}{\rho_\infty U_\infty} (1 - \frac{u}{U_\infty}) dz$$

to reduce this quantity, but the effect is not noticeable. The momentum thickness is the thickness of a unit depth of the external flow which contains a momentum flux deficiency of the boundary layer. It is thus directly relatable to the profile drag of the surface.

Values of the thickness parameters calculated using the two different methods are in relatively good agreement for the flat plate case being discussed here. The results of the differential method show somewhat more sensitivity to the effects of Ω than do those from the integral method.

The growth of the skew angle, ϵ, is a function of chordwise and spanwise position. In the integral method, the skew angle is practically independent of Ω in the zero pressure gradient cases. In Figure (41), ϵ is plotted versus y for a chordwise position of 1 foot for both the large and small blades. The intermediate angular velocity for each blade was used. This curve shows the inverse relationship between ϵ and y. Of particular interest is the close match between the skew angle predicted by the integral method at the tip of the 10-foot blade, which is traveling at 600 ft/sec, and at the y = 10-ft position of the 40-foot blade, which is traveling at 150 ft/sec. This occurs because in the final integral form of the momentum equations, (50x) and (50y), the terms in the solution of $\partial \epsilon/\partial x$ are either constant in the spanwise direction or proportional to 1/y.

Skew angles predicted by the differential method are generally larger, in an absolute sense, than those predicted by the integral method. This is not surprising, since ϵ is calculated by taking the difference between the external and wall flow directions and the latter is calculated by obtaining a ratio of the wall shear stresses. In the integral method the shear

39

stress is analytically defined, whereas in the differential method it is calculated from the velocity profiles. The differences between the values of ϵ presented are within those indicated by the shear stresses.

The chordwise skin friction coefficient is higher in the rotating cases with the same chordwise velocity. Since the equations are normalized with respect to $\rho_\infty U_\infty{}^2$, the streamwise skin friction coefficient in the integral method is resolved into chordwise and spanwise components as

$$\frac{\tau_{ox}}{\rho_\infty U_\infty{}^2} = \frac{\tau_{oq}}{\rho_\infty U_\infty{}^2} \; \frac{Q_\infty}{U_\infty} \; (1 - \phi \, \frac{V_\infty}{U_\infty})$$

and

$$\frac{\tau_{oy}}{\rho_\infty U_\infty{}^2} = \frac{\tau_{oq}}{\rho_\infty U_\infty{}^2} \; \frac{1}{U_\infty} \; (\frac{Q_\infty}{U_\infty} - \phi)$$

The tangent of the skew angle, ϕ, is usually positive while the crossflow, V_∞, is negative, and thus the chordwise skin friction coefficient is greater than $\tau_{oq}/\rho_\infty U_\infty{}^2$ by at least a factor of Q_∞/U_∞; τ_{ox} is not necessarily less than τ_{oq}.

The spanwise skin friction coefficient indicates the relative amount of spanwise flow. From the tabulated results it can be seen that there is a difference of two orders of magnitude between the spanwise and the chordwise coefficients. The relative sizes of these two variables is controlled by the relative size of their respective external flow velocity components and the value of the skew angle, as indicated in Equations (50). Both V_∞ and ϕ remain small in most cases. Values for the flat plate skin friction coefficients calculated by the two methods are in good agreement with the differential method, again indicating a greater sensitivity to the effects of external crossflow than does the integral method. This is reflected in smaller absolute values of the spanwise skin friction coefficient at the inboard stations, where the ratio of spanwise to chordwise external flow velocities is greatest.

Figure (42) shows the chordwise skin friction coefficient plotted against Reynolds number for a wide range of conditions as calculated by the differential method on both large and small blades and the two-dimensional values. Agreement is generally very good except at the high Reynolds number values where compressibility plays a significant role.

4.2 Effect of Vortex Crossflow

The details of the interference of a tip vortex shed from a preceding blade can be best observed by studying the spanwise distribution of δ_x^* and ϵ at a constant chordwise position over the outer portion of the blade. This has been plotted in Figure (43) for the 40-foot blade for both methods. The effects are not shown as well in the machine-plotted figures due to the

40

different scale. The displacement thickness increases on one side and decreases on the other side of the centerline of the vortex, depending on the sign of the circulation strength, Γ. The same effect is manifest in δ and θ_x. Near the centerline of the vortex these variables remain almost unchanged even though the crossflow velocity, V_∞, is the highest in this position. However, the velocity gradient $\partial V_\infty/\partial y$ has an inflection with a zero value at the vortex centerline, and this quantity influences the chordwise growth of the boundary layer and causes the spanwise inflection in the thickness parameters.

When Γ is positive, the velocity V_∞ at the centerline is outward, or positive, whereas the original undisturbed flow would have been negative. Inboard of the centerline there is a divergence of the external stream-lines where $\partial V_\infty/\partial y$ is positive, and the boundary layer is reduced in thickness. Outboard, $\partial V_\infty/\partial y$ is negative and the streamlines tend to be convergent. In this region, the boundary layer is thicker. The opposite situation occurs when Γ is negative. The influence of $\partial V_\infty/\partial y$ is confirmed when the results from the $\Gamma/h = \pm 200$ ft/sec cases are examined. Here, $\partial V_\infty/\partial y$ is smaller, and as would be expected the deviations from the $\Gamma = 0$ case are reduced proportionately.

The skew angle predicted by the integral method increases inboard of the vortex centerline and decreases outboard of it, regardless of the sign of Γ. Figure (43) shows that the variation is larger for negative values of Γ than for positive. In the integral solution for ϵ, terms with coefficients of $V_\infty \partial V_\infty/\partial y$ have a dominant effect. The sign of this expression will always be positive inboard of the vortex and negative outboard, causing the skew angle to develop as it does.

The skew angle variation predicted by the differential method is radically different from that discussed for the integral method. The reason for this difference is not hard to find. The variation of ϵ in the differential method, while being influenced by $V_\infty \partial V_\infty/\partial y$ like the integral method, is more strongly controlled by the radial variation of the chordwise skin friction. Figure (44) shows the sensitivity of c_{fx} predicted by the differential method at the trailing edge to the presence of the vortex. The integral method shows no comparable effect. The differential method calculates skew angle by taking the difference between external and wall flow directions and determines the latter from the ratio of c_{fx}/c_{fy} at the wall. This explains the form of the ϵ variation when the radial variation of c_{fx} and c_{fy} under the vortex is considered.

4.3 Effect of Surface Curvature

The characteristics of the boundary layer are virtually unaffected by the surface curvature tested on both the large and small blades. Careful examination of the complete data listings reveals that there is occasion-ally an insignificant increase of the order of 0.1 percent in the thickness related parameters. There is no detectable change in the surface shear stress as predicted by either method. The slight increase in the growth rate is a result of the factor of $1/h_1$ in the chordwise velocity gradient term of Equation (17x), $\rho u/h_1(\partial u/\partial x)$. Since $1/h_1$ is less than 1, the

41

magnitude of $\partial u/\partial x$ will be increased. This term is generally negative; the increased magnitude produces a thickening of the boundary layer. From Equation (61), the value of h_1 is seen to be equal to, or less than, $(1 + \delta/R_o)$. The changes noted in δ are consistent with this.

Similar effects were noted on blades with vortex crossflows and in the cases which combined surface curvature and adverse pressure gradients. In general, for the surface radii tested in this report, the effects of surface curvature are negligible. The radius of curvature of a real blade decreases sharply toward the leading edge, and in a rigorous analysis, this should be considered. In the present approach, however, the blade surface has been assumed to have a simply curved surface from a leading edge at $x = 0$.

In these analyses, the application of pressure gradients is independent of surface curvature, whereas aerodynamically this is not the case. Properly sophisticated usage of these methods would entail supplying detailed pressure distributions in conjunction with the corresponding surface radii of curvature. The present simple approach is employed to separate the effects of these various conditions.

4.4 Effect of Pressure Gradients

Pressure gradients of the form described in Section 2.3.1 were applied to the large and small blades to determine the behavior of a boundary layer on a rotor blade under typical operating conditions. The effects on the displacement thickness are depicted in Figures (7) and (13), the corresponding skew angle plots are in Figures (19) and (25), and the velocity profiles are in Figures (31) and (37). Relevant data are summarized in Tables III and IX.

Over the first quarter of the chord, the free stream velocity is uniformly higher than it is for the zero pressure gradient cases. This causes a reduction in the boundary layer thickness and in the shear stress, as is expected. At the quarter chord, the velocity gradient region begins and the boundary layer is subjected to a decelerating external flow. The increasing pressure acts in the same direction as the shear stress, further retarding the flow and causing an increased growth rate of the boundary layer. There is an associated lowering of the normal velocity gradients and thus an increase in the shear stress near the surface. The boundary layer continues to grow rapidly, but the momentum of the viscous flow increases more gradually. A relative measure of these two quantities is the shape factor, $H = \delta_x^*/\theta_{xx}$. In the integral method, the shape factor controls the growth of the boundary layer via the empirical von Doenhoff-Tetervin relation. In this type of method where the exact velocity profile is unknown, H is used to evaluate the location of the separation point making a comparison with analogous experimental results. When a predetermined value is exceeded, the flow is said to have separated. If the velocity profiles are known, as in the differential method, the location of separation is determined by the occurrence of reverse flow near the surface, or more precisely, when the gradient of the chordwise velocity normal to the surface at the wall passes through zero.

From Figures (7) and (13), the boundary layer growth as represented by δ_x^* is seen to be very rapid after the quarter chord. For the integral method, separation occurs in all cases before the trailing edge. The thickness δ grows in a similar manner while the momentum thickness θ_{xx} increases less rapidly. A nonrotating, two-dimensional boundary layer with a free stream velocity which is identical to the corresponding chordwise velocity at any spanwise location has been found to exhibit the same characteristics; rotation does not appear to affect the growth and separation of the viscous flow in the integral method.

In Figure (45), the growth of the shape factor is presented as a function of the chordwise position for both pressure gradient cases on the large blade. As the shape factor nears a value of 2.0 for the integral method, its gradient increases very rapidly. The value of 2.0 was assumed to be the separation point for this method. This is within the range of $H = 1.8$ to $H = 2.6$ suggested by von Doenhoff and Tetervin for the occurrence of separation. The slope of H in this range is such that the location of the separation point is not significantly affected by the value chosen as the criterion for separation. In the spanwise direction, H was found to increase toward the tip in the integral method when the adverse pressure gradients were applied. This is in part related to the increase in δ_x^* caused by compressibility, but more importantly, it is a function of the rate of deceleration of the flow. Although the pressure coefficients are constant in the spanwise direction, the increasing rotational velocity yields stronger adverse pressure gradients, and therefore velocity gradients, toward the tip. This causes the increased growth rate and earlier separation compared to inboard regions.

The skew angles are noticeably smaller in the pressure gradient cases, even over the constant pressure region ahead of the quarter-chord. It should be remembered that, for the integral method, ϵ was found to be an inverse function of the spanwise position y and relatively independent of free stream velocity or angular velocity. The reduction in ϵ is due to the increase in U_∞ relative to Ωy. In Equation (17y), this has the effects of increasing the Coriolis term while the centrifugal term remains unchanged. This reduces $\partial v/\partial x$, which in turn results in a lower skew angle.

The shape factor variation, however, does not follow that of the integral method; a comparison of the two methods is given in Figure (45). The zero pressure gradient value calculated by the differential method is slightly higher than the constant 1.286 assumed in the integral method. The calculated value, however, remains constant over the chord. When pressure gradient is present, the differential method does not show the rapid divergence predicted by the integral method. If shape factor is to be used as an indicator of the proximity to separation, then the variation of H predicted by the differential method is consistent with the variation in skin friction calculated, since separation is not indicated in any of the cases Figure (46) shows the comparable surface shear stress variations for both the integral and differential methods. In view of the comparatively good agreement between the results from the two methods, it may be concluded

43

that the shape factor form used in the integral method is inappropriate in the three-dimensional flows examined.

No experimental data is available to correlate the separation position for the rotating case, but unpublished two-dimensional results indicate that some separation should occur for the $\partial C_p / \partial (x/c) = 2.0$ cases close to the trailing edge. The fact that it does not occur in the calculated cases, but is obviously close, (Figure (46)), is an indication of the pseudo favorable pressure gradient effect introduced by the radial gradients of chordwise velocity and the chordwise gradients of spanwise velocity.

4.5 Combined Effects of Pressure Gradient, Crossflow, and Curvature

The final effort in the present study is a complete rotor blade simulation for which the effects of surface curvature, pressure gradient, and circulation strengths were used on both blades with the intermediate angular velocities. These conditions are felt to be a reasonable duplication of a typical rotor. The resultant displacement thicknesses are shown in Figures (10) and (16), the skew angles are plotted in Figures (22) and (28), and the velocity profiles are shown in Figures (34) and (40). The summary data is tabulated in Tables VI and XII.

The influence of surface curvature is negligibly small for both the vortex crossflow and the pressure gradient cases. Its effect is independent of either of these two conditions, and thus the combination of them is not expected to induce any unusual surface curvature effects. Therefore, only the relationship of the results to the applied pressure gradients and vortex crossflows will be considered.

On the inboard portion of the blade where the influence of the vortex is small, the results are substantially the same as the previous pressure gradient cases. The outer portion experiences the full strength of both flow conditions. The effect on the spanwise distribution of the displacement thickness and the skew angle is shown in Figure (47). These plots are similar to Figure (43) in which only the crossflow was present, but the change to an optimum scale size should be noted, as well as the difference in chordwise position. Separation forced the use of an earlier position in the present case. Nevertheless, a comparison of the trends reveals distinctive features for each situation.

The displacement thickness increases in the spanwise direction with the pressure gradient condition; this compressibility effect is discussed in Sections 4.1 and 4.3. The presence of the interfering vortex causes an alternate thinning and thickening of the boundary layer as it did without the pressure gradient. The magnitude of the effect is about the same in either case, but the proportion of the thickness deviation is less in the combined vortex, pressure gradient case. This is caused by the higher chordwise velocity which reduces the significance of the imposed spanwise velocity. The boundary layer thickness and the momentum thickness both decrease with span because they are relatively unaffected by compressibility; in this respect they are more similar to the zero pressure gradient

44

cases, although the general thickness level is greater.

The skew angle for the integral method exhibits a remarkable change between the previous vortex cases and the present combined cases. The relatively small inflection noted then becomes masked by a large skew angle with a peak value near the centerline of the vortex and a sign which is the same as that of the imposed external spanwise flow. This behavior arises from a term containing the product $U_\infty(\partial V_\infty/\partial y)$ in the complete expansion of the spanwise integral equation. Its occurrence is related to the form of the power law velocity profiles; its practical significance is dubious.

Skew angle variation predicted for these flows by the differential method is largely the same as that for the zero pressure gradient, vortex crossflow cases discussed earlier; the form of the curves is identical, and the scale only varied in chordwise external velocity and surface shear stress.

The chordwise shear stress retains its sensitivity to the crossflow noted above, and vortex induced reduction brings the flow even closer to separation than the chordwise pressure gradient indicates. This is highlighted in Figure (44), where the possibility exists that an interfering vortex could cause local separation if the chordwise pressure were any larger than the value of $\partial C_p/\partial(x/c) = 2.0$ used here.

4.6 The Velocity Profiles

In addition to providing overall boundary layer development, the differential method printed out at selected points the velocity profiles as a function of both z and z/δ. In addition to the chordwise and spanwise velocity ratios, c and s, presented in Figures (29) through (40), streamwise and normal velocity profiles were available. There is nothing remarkable about the chordwise and spanwise velocity profiles presented. The chordwise profile follows a typical two-dimensional form closely matching the typical 1/7 power law form commonly assumed. The spanwise profile, as far as can be determined from the data available, follows the external spanwise velocity, with a form closely resembling the chordwise profile. The parallels between the rotating and two-dimensional velocity profiles are reinforced by Figure (48) where a typical chordwise profile is compared with the standard law of the wall form. Agreement is remarkably close, the effect of the rotation being essentially negligible. When a pressure gradient case is compared, the characteristic wake contribution appears in the outer levels of the boundary layer. The addition of a large external crossflow, vortex induced, causes only minor changes in the wake portion of the flow. For Figure (48), the chordwise shear velocity was defined as $u_\tau = (\tau_x/\rho_\infty)^{\frac{1}{2}}$. The effect of the pressure gradient on the velocity profile in the typical z/δ vs u/U_∞ plot is clear in Figure (49) with the increased fullness of a profile approaching separation.

Velocity profiles were printed out at x/chord = 0.3 and 0.8; consequently, no profiles of flows at or immediately prior to separation are presented. Figure (50) gives the typical variation of the chordwise, spanwise, and normal velocity ratios for a case with zero pressure gradient and no vortex crossflow. The normal velocity component does not follow directly the

external crossflow. At x/chord = 0.3, the spanwise ratio, ε, has already crossed over, following the changes in V_∞, and is negative. The normal velocity, n, is still positive. By the time x/chord = 0.8, n has also become negative. This tendency for the normal component sign to lag the external flow is more marked for the inboard sections and is particularly noticeable on the small blade.

The general form of the profiles, if not the sign of the crossflow profile, agrees with those assumed for the integral method and presented in Figure (2).

4.7 The Shear Stress Profiles

As with the velocity profiles, there was very little to distinguish the chordwise shear stress profiles from similar profiles in an equivalent nonrotating flow. Figure (51) shows typical chordwise shear stress profiles for two cases with and without pressure gradient. The zero pressure profile has the characteristic triangular shape, with the shear stress falling away from the edge of the laminar sublayer. When the flow is subjected to an unfavorable pressure gradient, the shear stress profile takes on the characteristic form of Figure (50). The shear stress increases away from the wall to a maximum of about twice the wall value at z/δ = 0.25. Outside this, the shear stress falls off to zero in the external stream. Since the shear stresses in the turbulent part of the layer are determined by resolving the total shear stress based on the resultant flow, the spanwise and chordwise shear stresses are related through the ratios $\partial s/\partial z$ and $\partial c/\partial z$. The spanwise stress normal variation is consequently similar to that of the chordwise stress; the two values away from the wall are of relative magnitude c_{fy}/c_{fx}.

It is the gradient of shear stress normal to the wall, rather than the shear stresses themselves, that determines the boundary layer growth. The variation of the shear stress gradient normal to the wall for the two cases discussed above is presented in Figure (52). The portions of these curves outside the sublayer have been obtained by differentiating the shear stress profiles. The balance of the curve is found from the interpolation based on $u_+{}^2$ discussed in Section 3.1.1. The portion of the curve close to the wall shown in an expanded scale illustrates the importance of the form of the interpolation, particularly in the pressure gradient case where large positive values of $\partial\tau/\partial z$ are present close to the wall.

4.8 General Discussion

The results predicted for the characteristic thickness parameters and the chordwise surface shear stress coefficient were in remarkably good agreement for all the cases where there was zero chordwise pressure gradient. There was, however, a divergence in the predicted values of skew angle. Both methods predicted an initially positive value ahead of the quarter chord line. The differential method showed a tendency toward negative values behind this point, whereas the integral method continued to show growing positive values. A typical example is in Case 2 with Ω = 15 rad/sec, $\partial C_p/\partial(x/C)$ = 0 and Γ = 0. At x/chord = 1.0 and y/R = 0.3, the

46

integral and differential methods show ε = 0.590 and - 0.255 degrees respectively. The apparent difference is smaller when it is realized that these represent surface flow angularity of -6.536 and -7.381 degrees relative to the free stream velocity in a direction of -7.126 degrees. The correlation between the surface shear stresses in the spanwise direction is fair with values of -0.000229 and -0.000183 from the differential and integral methods.

The small difference between the skew angles predicted by the two methods is basic and results from the assumption in the integral method that the crossflow velocity profile is coupled to the streamwise flow through a function containing ε. The questions arising from this assumption are fully discussed in Reference (9). They must be kept in mind when evaluating the skew angles predicted by the integral method.

The difference in predicted skew angle is obvious in Figures (43) and (47) where the effect of vortex crossflow is examined with and without the influence of chordwise pressure gradient. The inability of the integral method to accurately predict skew angle is highlighted here with an apparently significant influence from imposed pressure gradient. It is felt, on the basis of the above discussion and the similar form of the skew angles predicted by the differential method with and without pressure gradient, that the differential method gives the more appropriate description of what is happening.

The two methods also differ on the position at which the chordwise surface shear stress becomes zero. The integral method invokes the assumption that when the shape factor H equals two, then the flow has separated. This is inappropriate in three-dimensional, rotating flow, as seen in Figures (45) and (46) where the chordwise variations of H and c_{fx} are plotted for a range of pressure gradients for the two methods. Even after a value of H greater than 2.0 has been reached in the integral method and the flow has theoretically separated, the correlation between the skin friction values predicted by the two methods is still fair. On the basis of this, the shape factor skin friction relationships used are suspect in the flows presented here and should be reexamined before extending the study to more involved pressure distributions. They appear to be adequate in the zero chordwise pressure gradient cases.

No reliable experimental data is available to correlate the separation points calculated, although unpublished two-dimensional data indicates that separation might be expected close to the trailing edge for the $\partial C_{p}/\partial(x/C)$ = 2.0 cases on the large blade. That it is not predicted using the differential method could be an alleviation of the unfavorable pressure gradient by the effects of the rotation, or a failure of the method. A final decision on this point cannot be made until more realistic pressure distributions are calculated and relevant experimental data becomes available.

47

CONCLUSIONS AND RECOMMENDATIONS

CONCLUSIONS

The present analyses indicate that on rotating flat or slightly curved surfaces of typical helicopter rotor size, in the absence of chordwise pressure gradients, the boundary layer behaves in an essentially two-dimensional manner when followed along the streamlines of the external flow.

The influence of large amounts of vortex induced crossflow on the zero pressure gradient rotating boundary layer is small.

Centrifugal force has very little influence on the flow at the angular velocities examined and only becomes moderately significant when compressibility is a controlling factor at high subsonic Mach numbers.

Coriolis force is the most significant force present. Together with the radial variation of chordwise velocity, it dominates the development of the spanwise flow.

The influence of chordwise pressure gradients is reduced by the presence of a negative spanwise external flow. This effect is most noticeable at small radii and close to the trailing edge where the spanwise flow is large relative to the chordwise velocity.

Both the differential and integral methods agree remarkably well on the prediction of the boundary layer characteristic thicknesses for the range of conditions examined. Correlation between the methods for the skin friction values, in all but the pressure gradient cases, is also good. It may be concluded that the empirical skin friction laws used in the integral technique are applicable in three-dimensional flows, at least for zero pressure gradient.

It would be inappropriate to conclude that since the two widely differing methods give results which are generally in good agreement that they are capable of giving a complete picture of turbulent boundary layers on helicopter rotors. It is however encouraging that such good agreement has been reached, over a wide range of conditions, using two comparatively basic analyses with the minimum of restrictive assumptions.

Despite the question marks which must remain over the analyses until confirmatory experimental data becomes available, it should now be possible to more realistically allow for the effects of rotation on airfoil skin friction and maximum lift capability.

RECOMMENDATIONS

Before extending the current analyses to unsteady flows, or even more exotic steady flows, some experimental data on boundary layer development on rotating blades must be found. Data needed include velocity profiles, surface shear stresses and thickness parameters, as well as some measurement

48

of the fluctuating velocities and the determination of turbulent shear stress variation normal to the wall in rotating flows. These data are essential for meaningful analysis of the present analytical work and any future developments of the theory.

In addition, the use of the present methods can be expanded by the following steps. Extend the analysis from its present form now handling simply curved surfaces to one capable of handling the sharp leading edge curves of airfoils. Develop the capability of calculating complete viscous flows from stagnation point, through laminar and transition phases, to the fully developed turbulent flow in a rotating field. Modify the present analyses to allow the calculation of the behavior of the boundary layer in unsteady conditions and particularly in the forward flight regime.

TABLE I. COMPARISON OF RESULTS OF THE INTEGRAL AND DIFFERENTIAL METHODS FOR VARIOUS ANGULAR VELOCITIES, BLADE RADIUS = 40 ft, Γ/h = 0 ft/sec, dCp/d(x/C) = 0, FLAT SURFACE

(a) Ω = 10 rad/sec

		X/CHORD = .30 Y/RADIUS = .30		X/CHORD = .30 Y/RADIUS = .60		X/CHORD = .30 Y/RADIUS = .90		X/CHORD = .30 Y/RADIUS = .95	
		D	I	D	I	D	I	D	I
δ	(ft)	.01680	.01680	.01530	.01460	.01430	.01360	.01410	.01340
δ*	(ft)	.00211	.00211	.00186	.00186	.00174	.00175	.00172	.00174
θxx	(ft)	.00151	.00163	.00136	.00142	.00127	.00132	.00125	.00130
CFX		.00215	.00210	.00197	.00185	.00186	.00172	.00184	.00171
CFY		-.00001	-.00001	-.00001	-.00000	-.00000	-.00000	-.00000	-.00000
U∞	(ft/sec)	120.0		240.0		360.0		380.0	
V∞	(ft/sec)	-1.00		-1.00		-1.00		-1.00	
α	(deg)	-.48		-.24		-.16		-.15	

		X/CHORD = .80 Y/RADIUS = .30		X/CHORD = .80 Y/RADIUS = .60		X/CHORD = .80 Y/RADIUS = .90		X/CHORD = .80 Y/RADIUS = .95	
		D	I	D	I	D	I	D	I
δ	(ft)	.04170	.03640	.03860	.03210	.03640	.02990	.03610	.02960
δ*	(ft)	.00465	.00457	.00397	.00407	.00387	.00386	.00377	.00384
θxx	(ft)	.00351	.00354	.00305	.00311	.00291	.00290	.00285	.00287
CFX		.00185	.00177	.00179	.00157	.00159	.00147	.00161	.00145
CFY		-.00018	-.00015	-.00008	-.00006	-.00005	-.00004	-.00005	-.00004
U∞	(ft/sec)	120.0		240.0		360.0		380.0	
V∞	(ft/sec)	-11.00		-11.00		-11.00		-11.00	
α	(deg)	-5.25		-2.63		-1.75		-1.66	

50

TABLE I - Continued

(b) Ω = 15 rad/sec

		X/CHORD = .30 Y/RADIUS = .30		X/CHORD = .30 Y/RADIUS = .60		X/CHORD = .30 Y/RADIUS = .90		X/CHORD = .30 Y/RADIUS = .95	
		D	I	D	I	D	I	D	I
δ^*	(ft)	.01540	.01550	.01420	.01360	.01300	.01270	.01340	.01260
δ_x	(ft)	.00197	.00195	.00174	.00175	.00163	.00170	.00163	.00170
θ_{xx}	(ft)	.00142	.00150	.00127	.00132	.00115	.00122	.00114	.00121
CFX		.00202	.00195	.00186	.00172	.00171	.00161	.00168	.00159
CFY		-.00001	-.00001	-.00001	-.00000	-.00000	-.00000	-.00000	-.00000
U_∞	(ft/sec)	180.0		360.0		540.0		570.0	
V_∞	(ft/sec)	-1.50		-1.50		-1.50		-1.50	
α	(deg)	-.48		-.24		-.16		-.15	

		X/CHORD = .80 Y/RADIUS = .30		X/CHORD = .80 Y/RADIUS = .60		X/CHORD = .80 Y/RADIUS = .90		X/CHORD = .80 Y/RADIUS = .95	
		D	I	D	I	D	I	D	I
δ	(ft)	.04100	.03380	.03650	.02990	.03390	.02800	.03400	.02780
δ_x	(ft)	.00432	.00425	.00386	.00386	.00354	.00376	.00352	.00376
θ_{xx}	(ft)	.00329	.00328	.00291	.00290	.00260	.00270	.00258	.00267
CFX		.00182	.00165	.00162	.00147	.00149	.00138	.00143	.00136
CFY		-.00017	-.00014	-.00008	-.00006	-.00005	-.00004	-.00004	-.00004
U_∞	(ft/sec)	180.0		360.0		540.0		570.0	
V_∞	(ft/sec)	-16.50		-16.50		-16.50		-16.50	
α	(deg)	-5.25		-2.63		-1.75		-1.66	

51

TABLE I – Concluded

(c) Ω = 20 rad/sec

	X/CHORD = .30 Y/RADIUS = .30		X/CHORD = .30 Y/RADIUS = .60		X/CHORD = .30 Y/RADIUS = .90		X/CHORD = .30 Y/RADIUS = .95	
	D	I	D	I	D	I	D	I
δ (ft)	.01530	.01460	.01360	.01290	.01280	.01210	.01270	.01200
δ^*_x (ft)	.00187	.00186	.00165	.00171	.00164	.00171	.00163	.00172
θ_{xx} (ft)	.00136	.00142	.00118	.00125	.00110	.00116	.00109	.00115
CFX	.00197	.00185	.00176	.00164	.00156	.00153	.00153	.00152
CFY	-.00001	-.00001	-.00001	-.00000	-.00000	-.00000	-.00000	-.00000
U_∞ (ft/sec)	240.0		480.0		720.0		760.0	
V_∞ (ft/sec)	-22.00		-22.00					
α (deg)	-.48		-.24		-.16		-.15	

	X/CHORD = .80 Y/RADIUS = .30		X/CHORD = .80 Y/RADIUS = .60		X/CHORD = .80 Y/RADIUS = .90		X/CHORD = .80 Y/RADIUS = .95	
	D	I	D	I	D	I	D	I
δ (ft)	.03860	.03210	.03480	.02860	.03320	.02690	.03310	.02670
δ^*_x (ft)	.00398	.00406	.00372	.00377	.00363	.00379	.00379	.00381
θ_{xx} (ft)	.00305	.00311	.00275	.00275	.00252	.00257	.00256	.00255
CFX	.00178	.00157	.00147	.00140	.00126	.00131	.00115	.00130
CFY	-.00017	-.00013	-.00007	-.00006	-.00004	-.00004	-.00004	-.00003
U_∞ (ft/sec)	240.0		480.0		720.0		760.0	
V_∞ (ft/sec)	-22.00		-22.00		-22.00		-22.00	
α (deg)	-5.25		-2.63		-1.75		-1.66	

TABLE II. COMPARISON OF RESULTS OF THE INTEGRAL AND DIFFERENTIAL METHODS FOR VARIOUS VORTEX STRENGTHS, BLADE RADIUS = 40 ft, Ω = 15 rad/sec, dCp/d(x/C) = 0, FLAT SURFACE

(a) Γ/h = +100 ft/sec

	X/CHORD = .30 Y/RADIUS = .30		X/CHORD = .30 Y/RADIUS = .60		X/CHORD = .30 Y/RADIUS = .90		X/CHORD = .30 Y/RADIUS = .95	
	D	I	D	I	D	I	D	I
δ (ft)	.01540	.01550	.01420	.01360	.01300	.01270	.01290	.01260
δ* (ft)	.00197	.00195	.00194	.00175	.00163	.00170	.00163	.00170
θxx (ft)	.00142	.00150	.00127	.00131	.00116	.00122	.00114	.00121
CFX	.00202	.00195	.00186	.00172	.00171	.00161	.00167	.00159
CFY	-.00001	-.00001	-.00000	-.00000	-.00009	-.00009	.00005	-.00004
U∞ (ft/sec)	180.0		360.0		540.0		570.0	
V∞ (ft/sec)	-1.30		-.60		30.30		14.40	
α (deg)	-.41		-.10		3.22		1.95	

	X/CHORD = .80 Y/RADIUS = .30		X/CHORD = .80 Y/RADIUS = .60		X/CHORD = .80 Y/RADIUS = .90		X/CHORD = .80 Y/RADIUS = .95	
	D	I	D	I	D	I	D	I
δ (ft)	.04100	.03380	.03650	.02990	.03380	.02810	.03410	.02810
δ* (ft)	.00432	.00425	.00386	.00386	.00354	.00376	.00362	.00380
θxx (ft)	.00329	.00328	.00291	.00290	.00260	.00270	.00263	.00270
CFX	.00182	.00165	.00162	.00147	.00149	.00137	.00137	.00136
CFY	-.00017	-.00014	-.00007	-.00006	-.00004	-.00004	.00001	-.00000
U∞ (ft/sec)	180.0		360.0		540.0		570.0	
V∞ (ft/sec)	-16.30		-15.60		15.30		-.60	
α (deg)	-5.18		-2.42		1.63		-.06	

TABLE II - Continued

(b) $\Gamma/h = -100$ ft/sec

	X/CHORD = .30 Y/RADIUS = .30		X/CHORD = .30 Y/RADIUS = .60		X/CHORD = .30 Y/RADIUS = .90		X/CHORD = .30 Y/RADIUS = .95	
	D	I	D	I	D	I	D	I
δ (ft)	.01540	.01550	.01420	.01360	.01300	.01270	.01330	.01250
δ^* (ft)	.00197	.00195	.00174	.00175	.00163	.00170	.00162	.00169
θ_{xx} (ft)	.00142	.00150	.00127	.00132	.00116	.00122	.00114	.00120
CFX	.00202	.00195	.00186	.00172	.00171	.00161	.00169	.00159
CFY	-.00002	-.00001	-.00001	-.00001	-.00010	-.00010	-.00006	-.00005
U_∞ (ft/sec)	180.0		360.0		540.0		570.0	
V_∞ (ft/sec)	-1.70		-2.40		-33.30		-17.40	
α (deg)	-.54		-.38		-3.54		-1.75	

	X/CHORD = .80 Y/RADIUS = .30		X/CHORD = .80 Y/RADIUS = .60		X/CHORD = .80 Y/RADIUS = .90		X/CHORD = .80 Y/RADIUS = .95	
	D	I	D	I	D	I	D	I
δ (ft)	.04110	.03380	.03650	.02990	.03390	.02810	.03340	.02750
δ^* (ft)	.00432	.00425	.00387	.00386	.00354	.00376	.00346	.00372
θ_{xx} (ft)	.00330	.00328	.00291	.00290	.00261	.00270	.00254	.00265
CFX	.00182	.00165	.00162	.00147	.00149	.00138	.00146	.00137
CFY	-.00017	-.00014	-.00008	-.00006	-.00014	-.00012	-.00009	-.00007
U_∞ (ft/sec)	180.0		360.0		540.0		570.0	
V_∞ (ft/sec)	-16.70		-17.40		-48.30		-32.40	
α (deg)	-5.31		-2.77		-5.12		-3.26	

54

TABLE II – Continued

(c) $\Gamma/h = +200$ ft/sec

	X/CHORD = .30 Y/RADIUS = .30		X/CHORD = .30 Y/RADIUS = .60		X/CHORD = .30 Y/RADIUS = .90		X/CHORD = .30 Y/RADIUS = .95	
	D	I	D	I	D	I	D	I
δ (ft)	.01540	.01550	.01420	.01360	.01300	.01270	.01310	.01270
δ^*_x (ft)	.00197	.00195	.00174	.00175	.00164	.00171	.00164	.00171
θ_{xx} (ft)	.00142	.00150	.00127	.00131	.00116	.00122	.00115	.00122
CFX	.00202	.00195	.00186	.00172	.00171	.00161	.00167	.00159
CFY	-.00001	-.00001	.00000	-.00000	.00019	-.00019	.00011	-.00009
U_∞ (ft/sec)	180.0		360.0		540.0		570.0	
V_∞ (ft/sec)	-1.10		.20		62.20		30.30	
α (deg)	-.35		.03		6.58		3.05	

	X/CHORD = .80 Y/RADIUS = .30		X/CHORD = .80 Y/RADIUS = .60		X/CHORD = .80 Y/RADIUS = .90		X/CHORD = .80 Y/RADIUS = .95	
	D	I	D	I	D	I	D	I
δ (ft)	.04100	.03380	.03640	.02990	.03390	.02810	.03440	.02840
δ^*_x (ft)	.00432	.00425	.00386	.00386	.00355	.00378	.00373	.00384
θ_{xx} (ft)	.00329	.00328	.00291	.00289	.00261	.00271	.00269	.00274
CFX	.00182	.00165	.00162	.00147	.00146	.00138	.00130	.00136
CFY	-.00017	-.00013	-.00007	-.00005	-.00013	-.00012	-.00005	-.00004
U_∞ (ft/sec)	180.0		360.0		540.0		570.0	
V_∞ (ft/sec)	-16.10		-14.80		47.20		15.30	
α (deg)	-5.12		-2.36		5.00		1.54	

55

TABLE II – Concluded

(d) $\Gamma/h = -200$ ft/sec

		X/CHORD = .30 Y/RADIUS = .30		X/CHORD = .30 Y/RADIUS = .60		X/CHORD = .30 Y/RADIUS = .90		X/CHORD = .30 Y/RADIUS = .95	
		R	I	R	I	R	I	R	I
δ	(ft)	.01540	.01550	.01420	.01360	.01300	.01270	.01320	.01250
δ^*_x	(ft)	.00197	.00195	.00174	.00175	.00164	.00171	.00164	.00169
θ_{xx}	(ft)	.00142	.00150	.00127	.00132	.00116	.00122	.00113	.00120
CFX		.00202	.00195	.00186	.00172	.00171	.00162	.00163	.00160
CFY		-.00002	-.00001	-.00002	-.00001	-.00020	-.00019	-.00012	-.00009
U_∞	(ft/sec)	180.0		360.0		540.0		570.0	
V_∞	(ft/sec)	-1.90		-3.20		-65.20		-33.30	
α	(deg)	-.61		-.51		-6.90		-3.35	

		X/CHORD = .80 Y/RADIUS = .30		X/CHORD = .80 Y/RADIUS = .60		X/CHORD = .80 Y/RADIUS = .90		X/CHORD = .80 Y/RADIUS = .95	
		R	I	R	I	R	I	R	I
δ	(ft)	.04110	.03380	.03630	.02990	.03380	.02810	.03280	.02730
δ^*_x	(ft)	.00432	.00425	.00386	.00386	.00354	.00378	.00340	.00368
θ_{xx}	(ft)	.00330	.00328	.00291	.00290	.00261	.00271	.00249	.00262
CFX		.00182	.00165	.00162	.00147	.00149	.00139	.00149	.00137
CFY		-.00018	-.00014	-.00008	-.00007	-.00022	-.00020	-.00015	-.00012
U_∞	(ft/sec)	180.0		360.0		540.0		570.0	
V_∞	(ft/sec)	-16.90		-18.20		-80.20		-48.30	
α	(deg)	-5.37		-2.90		-8.46		-4.85	

56

TABLE III. COMPARISON OF RESULTS OF THE INTEGRAL AND DIFFERENTIAL METHODS FOR VARIOUS PRESSURE GRADIENTS, BLADE RADIUS = 40 ft, Ω = 15 rad/sec, Γ/h = 0 ft/sec, FLAT SURFACE

(a) $dCp/d(x/C) = 1$

		X/CHORD = .30 Y/RADIUS = .30		X/CHORD = .30 Y/RADIUS = .60		X/CHORD = .30 Y/RADIUS = .90		X/CHORD = .30 Y/RADIUS = .95	
		D	I	D	I	D	I	D	I
δ	(ft)	.01590	.01500	.01390	.01320	.01310	.01250	.01330	.01240
δ^*	(ft)	.00200	.00190	.00173	.00173	.00173	.00172	.00174	.00173
θ_{xx}	(ft)	.00145	.00146	.00125	.00128	.00118	.00119	.00117	.00118
CFX	(ft)	.00199	.00188	.00181	.00167	.00162	.00157	.00159	.00154
CFY		-.00001	-.00001	-.00001	-.00000	-.00000	-.00000	-.00000	-.00000
U_∞	(ft/sec)	216.9		434.5		653.3		649.9	
V_∞	(ft/sec)	-1.50		-1.50		-1.50		-1.50	
α	(deg)	-.40		-.20		-.13		-.12	

		X/CHORD = .80 Y/RADIUS = .30		X/CHORD = .80 Y/RADIUS = .60		X/CHORD = .80 Y/RADIUS = .90		X/CHORD = .80 Y/RADIUS = .95	
		D	I	D	I	D	I	D	I
δ	(ft)	.05080	.03820	.04830	.03300	.04680	.03080	.04760	.03060
δ^*	(ft)	.00628	.00843	.00568	.00803	.00564	.00819	.00569	.00825
θ_{xx}	(ft)	.00470	.00535	.00423	.00479	.00405	.00456	.00407	.00454
CFX	(ft)	.00195	.00150	.00172	.00134	.00148	.00125	.00146	.00124
CFY		-.00020	-.00014	-.00009	-.00006	-.00005	-.00004	-.00005	-.00003
U_∞	(ft/sec)	175.4		350.9		526.3		555.6	
V_∞	(ft/sec)	-16.50		-16.50		-16.50		-16.50	
α	(deg)	-5.38		-2.70		-1.80		-1.70	

57

TABLE III - Concluded

(b) $dC_p/d(x/C) = 2$

	X/CHORD = .30 Y/RADIUS = .30		X/CHORD = .30 Y/RADIUS = .60		X/CHORD = .30 Y/RADIUS = .90		X/CHORD = .30 Y/RADIUS = .95	
	D	I	D	I	D	I	D	I
δ (ft)	.01540	.01450	.01350	.01300	.01310	.01240	.01290	.01230
δ^* (ft)	.00191	.00185	.00174	.00174	.00180	.00180	.00180	.00182
θ_{xx} (ft)	.00139	.00141	.00122	.00125	.00115	.00118	.00114	.00117
CFX	.00196	.00182	.00173	.00163	.00156	.00155	.00154	.00154
CFY	-.00001	-.00001	-.00000	-.00000	-.00000	-.00000	-.00000	-.00000
U_∞ (ft/sec)	269.6		532.6		808.2		855.3	
V_∞ (ft/sec)	-1.50		-1.50		-1.50		-1.50	
α (deg)	-.33		-.16		-.11		-.10	

	X/CHORD = .80 Y/RADIUS = .30		X/CHORD = .80 Y/RADIUS = .60		X/CHORD = .80 Y/RADIUS = .90		X/CHORD = .80 Y/RADIUS = .95	
	D	I	D	I	D	I	D	I
δ (ft)	.05900	–	.05470	–	.05450	–	.05580	–
δ^* (ft)	.00801	–	.00756	–	.00783	–	.00798	–
θ_{xx} (ft)	.00582	–	.00539	–	.00533	–	.00539	–
CFX	.00186	–	.00156	–	.00132	–	.00128	–
CFY	-.00018	–	-.00008	–	-.00004	–	-.00004	–
U_∞ (ft/sec)	193.1		386.2		579.5		611.8	
V_∞ (ft/sec)	-16.50		-16.50		-16.50		-16.50	
α (deg)	-4.89		-2.45		-1.63		-1.55	

58

TABLE IV.   COMPARISON OF RESULTS OF THE INTEGRAL AND DIFFERENTIAL METHODS FOR VARIOUS
VORTEX STRENGTHS, BLADE RADIUS = 40 ft, Ω = 15 rad/sec,
dCp/d(x/C) = 0, SURFACE RADIUS OF CURVATURE = 8.25 ft

(a) Γ/h = +100 ft/sec

| | X/CHORD = .30 Y/RADIUS = .30 | | X/CHORD = .30 Y/RADIUS = .60 | | X/CHORD = .30 Y/RADIUS = .90 | | X/CHORD = .30 Y/RADIUS = .95 | |
	D	I	D	I	D	I	D	I
δ (ft)	.01550	.01550	.01430	.01360	.01310	.01270	.01300	.01260
δ^* (ft)	.00197	.00195	.00174	.00175	.00164	.00170	.00163	.00170
θ_{xx} (ft)	.00142	.00150	.00127	.00132	.00116	.00122	.00115	.00121
CFX	.00202	.00195	.00186	.00172	.00171	.00161	.00168	.00159
CFY	-.00001	-.00001	-.00000	-.00000	-.00009	-.00009	.00005	-.00004
U_∞ (ft/sec)	180.0		360.0		540.0		570.0	
V_∞ (ft/sec)	-1.30		-.60		30.30		14.40	
α (deg)	-.41		-.10		3.22		1.45	

| | X/CHORD = .80 Y/RADIUS = .30 | | X/CHORD = .80 Y/RADIUS = .60 | | X/CHORD = .80 Y/RADIUS = .90 | | X/CHORD = .80 Y/RADIUS = .95 | |
	D	I	D	I	D	I	D	I
δ (ft)	.04010	.03380	.03660	.02990	.03400	.02810	.03430	.02810
δ^* (ft)	.00430	.00426	.00387	.00386	.00355	.00377	.00362	.00380
θ_{xx} (ft)	.00327	.00328	.00292	.00290	.00261	.00270	.00263	.00271
CFX	.00182	.00165	.00162	.00147	.00149	.00137	.00138	.00136
CFY	-.00017	-.00014	-.00007	-.00006	-.00004	-.00004	-.00001	-.00000
U_∞ (ft/sec)	180.0		360.0		540.0		570.0	
V_∞ (ft/sec)	-16.30		-15.60		15.30		-.60	
α (deg)	-5.18		-2.40		1.63		-.06	

TABLE IV – Continued

(b) Γ/h = -100 ft/sec

		X/CHORD = .30 Y/RADIUS = .30		X/CHORD = .30 Y/RADIUS = .60		X/CHORD = .30 Y/RADIUS = .90		X/CHORD = .30 Y/RADIUS = .95	
		D	I	D	I	D	I	D	I
δ	(ft)	.01550	.01550	.01430	.01360	.01310	.01270	.01340	.01250
δ*x	(ft)	.00197	.00195	.00174	.00175	.00164	.00170	.00162	.00169
θxx	(ft)	.00142	.00150	.00127	.00132	.00116	.00122	.00114	.00120
CFX		.00202	.00195	.00186	.00172	.00171	.00161	.00169	.00159
CFY		-.00002	-.00001	-.00001	-.00001	-.00010	-.00010	-.00006	-.00005
U∞	(ft/sec)	180.0		360.0		540.0		570.0	
V∞	(ft/sec)	-1.70		-2.40		-33.30		-17.40	
α	(deg)	-.54		-.38		-3.54		-1.75	

		X/CHORD = .80 Y/RADIUS = .30		X/CHORD = .80 Y/RADIUS = .60		X/CHORD = .80 Y/RADIUS = .90		X/CHORD = .80 Y/RADIUS = .95	
		D	I	D	I	D	I	D	I
δ	(ft)	.04010	.03380	.03670	.02990	.03390	.02810	.03350	.02750
δ*x	(ft)	.00430	.00426	.00388	.00387	.00355	.00377	.00347	.00372
θxx	(ft)	.00327	.00328	.00292	.00290	.00261	.00270	.00254	.00265
CFX		.00182	.00165	.00162	.00147	.00149	.00138	.00146	.00137
CFY		-.00017	-.00014	-.00008	-.00006	-.00014	-.00012	-.00009	-.00007
U∞	(ft/sec)	180.0		360.0		540.0		570.0	
V∞	(ft/sec)	-16.70		-17.40		-48.30		-32.40	
α	(deg)	-5.31		-2.77		-5.12		-3.26	

60

TABLE IV - Continued

(c) Γ/h = +200 ft/sec

		X/CHORD = .30 Y/RADIUS = .30		X/CHORD = .30 Y/RADIUS = .60		X/CHORD = .30 Y/RADIUS = .90		X/CHORD = .30 Y/RADIUS = .95	
		D	I	D	I	D	I	D	I
δ	(ft)	.01550	.01550	.01430	.01360	.01300	.01270	.01320	.01270
δ*	(ft)	.00197	.00195	.00174	.00175	.00164	.00171	.00164	.00171
θxx	(ft)	.00142	.00150	.00127	.00132	.00116	.00123	.00115	.00122
CFX		.00202	.00195	.00187	.00172	.00171	.00161	.00167	.00159
CFY		-.00001	-.00001	.00000	-.00000	.00019	-.00019	.00011	-.00009
U∞	(ft/sec)	180.0		360.0		540.0		570.0	
V∞	(ft/sec)	-1.10		.20		62.20		30.30	
α	(deg)	-.35		.03		6.58		3.05	

		X/CHORD = .80 Y/RADIUS = .30		X/CHORD = .80 Y/RADIUS = .60		X/CHORD = .80 Y/RADIUS = .90		X/CHORD = .80 Y/RADIUS = .95	
		D	I	D	I	D	I	D	I
δ	(ft)	.04010	.03380	.03650	.02990	.03410	.02820	.03520	.02850
δ*	(ft)	.00430	.00426	.00387	.00386	.00356	.00378	.00377	.00385
θxx	(ft)	.00327	.00328	.00292	.00290	.00262	.00271	.00272	.00274
CFX		.00182	.00165	.00162	.00147	.00146	.00138	.00130	.00136
CFY		-.00017	-.00013	-.00007	-.00005	.00013	-.00012	.00005	-.00004
U∞	(ft/sec)	180.0		360.0		540.0		570.0	
V∞	(ft/sec)	-16.10		-14.80		47.20		15.30	
α	(deg)	-5.12		-2.36		5.00		1.54	

61

TABLE IV – Concluded

(a) $\Gamma/h = -200$ ft/sec

		X/CHORD = .30, Y/RADIUS = .30		X/CHORD = .30, Y/RADIUS = .60		X/CHORD = .30, Y/RADIUS = .90		X/CHORD = .30, Y/RADIUS = .95	
		R	I	R	I	R	I	R	I
δ	(ft)	.01550	.01550	.01430	.01360	.01300	.01270	.01330	.01250
δ^*x	(ft)	.00197	.00195	.00174	.00175	.00164	.00171	.00161	.00169
θ_{xx}	(ft)	.00142	.00150	.00127	.00132	.00116	.00122	.00113	.00120
CFX		.00202	.00195	.00186	.00172	.00171	.00162	.00169	.00160
CFY		-.00002	-.00001	-.00002	-.00001	-.00020	-.00019	-.00012	-.00009
U_∞	(ft/sec)	180.0		360.0		540.0		570.0	
V_∞	(ft/sec)	-1.90		-3.20		-65.20		-33.30	
α	(deg)	-.61		-.51		-6.90		-3.35	

		X/CHORD = .80, Y/RADIUS = .30		X/CHORD = .80, Y/RADIUS = .60		X/CHORD = .80, Y/RADIUS = .90		X/CHORD = .80, Y/RADIUS = .95	
		R	I	R	I	R	I	R	I
δ	(ft)	.04010	.03380	.03680	.03000	.03380	.02820	.03300	.02730
δ^*x	(ft)	.00430	.00426	.00388	.00387	.00355	.00378	.00341	.00369
θ_{xx}	(ft)	.00328	.00328	.00293	.00290	.00261	.00271	.00250	.00262
CFX		.00182	.00165	.00162	.00147	.00149	.00139	.00149	.00137
CFY		-.00018	-.00014	-.00008	-.00007	-.00022	-.00020	-.00015	-.00011
U_∞	(ft/sec)	180.0		360.0		540.0		570.0	
V_∞	(ft/sec)	-16.90		-18.20		-80.20		-48.30	
α	(deg)	-5.37		-2.90		-8.46		-4.85	

62

TABLE V. COMPARISON OF RESULTS OF THE INTEGRAL AND DIFFERENTIAL METHODS FOR VARIOUS PRESSURE GRADIENTS, BLADE RADIUS = 40 ft, Ω = 15 rad/sec, Γ/h = 0 ft/sec, SURFACE RADIUS OF CURVATURE = 8.25 ft

(a) dCp/d(x/C) = 1

		X/CHORD = .30 Y/RADIUS = .30		X/CHORD = .30 Y/RADIUS = .60		X/CHORD = .30 Y/RADIUS = .90		X/CHORD = .30 Y/RADIUS = .95	
		D	I	D	I	D	I	D	I
δ	(ft)	.01510	.01500	.01390	.01320	.01320	.01250	.01390	.01290
δ*x	(ft)	.00196	.00190	.00174	.00173	.00173	.00172	.00178	.00173
θxx	(ft)	.00142	.00146	.00125	.00128	.00118	.00119	.00117	.00118
CFX		.00199	.00188	.00181	.00167	.00161	.00157	.00160	.00156
CFY		-.00001	-.00001	-.00001	-.00000	-.00000	-.00000	-.00000	-.00000
U∞	(ft/sec)	216.9		434.5		653.3		689.9	
V∞	(ft/sec)	-1.50		-1.50		-1.50		-1.50	
α	(deg)	-.40		-.20		-.13		-.12	

		X/CHORD = .80 Y/RADIUS = .30		X/CHORD = .80 Y/RADIUS = .60		X/CHORD = .80 Y/RADIUS = .90		X/CHORD = .80 Y/RADIUS = .95	
		D	I	D	I	D	I	D	I
δ	(ft)	.05250	.03820	.04940	.03300	.04770	.03080	.04800	.03060
δ*x	(ft)	.00634	.00844	.00573	.00804	.00571	.00819	.00573	.00826
θxx	(ft)	.00475	.00536	.00428	.00479	.00411	.00456	.00410	.00454
CFX		.00196	.00150	.00172	.00134	.00178	.00125	.00146	.00129
CFY		-.00020	-.00013	-.00009	-.00006	-.00005	-.00004	-.00005	-.00003
U∞	(ft/sec)	175.4		350.9		526.3		555.6	
V∞	(ft/sec)	-16.50		-16.50		-16.50		-16.50	
α	(deg)	-5.38		-2.70		-1.80		-1.70	

63

TABLE V – Concluded

(b) $\partial Cp/\partial(x/C) = 2$

		X/CHORD = .30 Y/RADIUS = .30		X/CHORD = .30 Y/RADIUS = .60		X/CHORD = .30 Y/RADIUS = .90		X/CHORD = .30 Y/RADIUS = .95	
		D	I	D	I	D	I	D	I
δ	(ft)	.01550	.01460	.01350	.01300	.01320	.01240	.01300	.01240
δ^*x	(ft)	.00192	.00185	.00174	.00174	.00180	.00181	.00181	.00188
θxx	(ft)	.00140	.00141	.00122	.00125	.00116	.00118	.00114	.00117
CFX		.00196	.00182	.00173	.00163	.00156	.00155	.00154	.00154
CFY		-.00001	-.00000	-.00000	-.00000	-.00000	-.00000	-.00000	-.00000
U_∞	(ft/sec)	64.6		32.6		8.2		55.3	
V_∞	(ft/sec)	-1.50		-1.50		-1.50		-1.50	
α	(deg)	-1.33		-2.64		-10.39		-1.56	

		X/CHORD = .80 Y/RADIUS = .30		X/CHORD = .80 Y/RADIUS = .60		X/CHORD = .80 Y/RADIUS = .90		X/CHORD = .80 Y/RADIUS = .95	
		D	I	D	I	D	I	D	I
δ	(ft)	.06200	-	.05560	-	.05650	-	.05630	-
δ^*x	(ft)	.00816	-	.00763	-	.00790	-	.00807	-
θxx	(ft)	.00596	-	.00544	-	.00545	-	.00545	-
CFX		.00187	-	.00156	-	.00131	-	.00128	-
CFY		-.00018	-	-.00008	-	-.00004	-	-.00004	-
U_∞	(ft/sec)	.0		.0		.0		.0	
V_∞	(ft/sec)	.00		.00		.00		.00	
α	(deg)	.00		.00		.00		.00	

64

TABLE VI. COMPARISON OF RESULTS OF THE INTEGRAL AND DIFFERENTIAL METHODS FOR VARIOUS VORTEX STRENGTHS, BLADE RADIUS = 40 ft, Ω = 15 rad/sec, dCp/d(x/C) = 2, SURFACE RADIUS OF CURVATURE = 8.25 ft

(a) Γ/h = +200 ft/sec

	X/CHORD = .30 Y/RADIUS = .30		X/CHORD = .30 Y/RADIUS = .60		X/CHORD = .30 Y/RADIUS = .90		X/CHORD = .30 Y/RADIUS = .95	
	D	I	D	I	D	I	D	I
δ (ft)	.01550	.01450	.01350	.01300	.01320	.01240	.01310	.01240
δ*x (ft)	.00192	.00185	.00174	.00174	.00180	.00182	.00182	.00185
θxx (ft)	.00140	.00141	.00122	.00125	.00116	.00118	.00115	.00110
CFX	.00196	.00182	.00173	.00163	.00155	.00155	.00153	.00154
CFY	-.00001	-.00000	.00000	-.00000	.00012	-.00000	.00007	-.00000
U∞ (ft/sec)	64.6		32.6		8.2		55.3	
V∞ (ft/sec)	-1.10		.20		62.20		30.30	
α (deg)	-.98		.35		82.64		28.77	

	X/CHORD = .80 Y/RADIUS = .30		X/CHORD = .80 Y/RADIUS = .60		X/CHORD = .80 Y/RADIUS = .90		X/CHORD = .80 Y/RADIUS = .95	
	D	I	D	I	D	I	D	I
δ (ft)	.06200	—	.05640	—	.05620	—	.05630	—
δ*x (ft)	.00816	—	.00763	—	.00790	—	.00835	—
θxx (ft)	.00596	—	.00545	—	.00545	—	.00562	—
CFX	.00187	—	.00156	—	.00131	—	.00124	—
CFY	-.00618	—	-.00007	—	.00013	—	.00006	—
U∞ (ft/sec)	.0		.0		.0		.0	
V∞ (ft/sec)	.00		.00		.00		.00	
α (deg)	.00		.00		.00		.00	

65

TABLE VI - Concluded

(b) Γ/h = -200 ft/sec

	X/CHORD = .30 Y/RADIUS = .30		X/CHORD = .30 Y/RADIUS = .60		X/CHORD = .30 Y/RADIUS = .90		X/CHORD = .30 Y/RADIUS = .95	
	D	I	D	I	D	I	D	I
δ (ft)	.01550	.01450	.01350	.01300	.01320	.01240	.01280	.01230
$\delta*x$ (ft)	.00192	.00185	.00174	.00174	.00180	.00181	.00180	.00183
θxx (ft)	.00140	.00141	.00122	.00125	.00116	.00118	.00113	.00116
CFX	.00196	.00182	.00173	.00163	.00155	.00155	.00154	.00154
CFY	-.00001	-.00620	-.00001	-.00000	-.00012	-.00000	-.00007	-.00000
U_∞ (ft/sec)	64.6		32.6		8.2		55.3	
V_∞ (ft/sec)	-1.90		-3.20		65.20		33.30	
α (deg)	-1.69		-5.62		82.98		31.11	

	X/CHORD = .80 Y/RADIUS = .30		X/CHORD = .80 Y/RADIUS = .60		X/CHORD = .80 Y/RADIUS = .90		X/CHORD = .80 Y/RADIUS = .95	
	D	I	D	I	D	I	D	I
δ (ft)	.06120	---	.05570	---	.05650	---	.05550	---
$\delta*x$ (ft)	.00814	---	.00763	---	.00804	---	.00787	---
θxx (ft)	.00594	---	.00545	---	.00548	---	.00533	---
CFX	.00187	---	.00156	---	.00130	---	.00131	---
CFY	.00019	---	-.00009	---	-.00022	---	-.00014	---
U_∞ (ft/sec)	.0		.0		.0		.0	
V_∞ (ft/sec)	.00		.00		.00		.00	
α (deg)	.00		.00		.00		.00	

66

TABLE VII. COMPARISON OF RESULTS OF THE INTEGRAL AND DIFFERENTIAL METHODS FOR VARIOUS ANGULAR VELOCITIES, BLADE RADIUS = 10 ft, Γ/h = 0 ft/sec, $dCp/d(x/C)$ = 0, FLAT SURFACE

(a) Ω = 40 rad/sec

	X/CHORD = .30 Y/RADIUS = .30		X/CHORD = .30 Y/RADIUS = .60		X/CHORD = .30 Y/RADIUS = .90		X/CHORD = .30 Y/RADIUS = .95	
	D	I	D	I	D	I	D	I
δ (ft)	.00892	.00969	.00792	.00840	.00711	.00776	.00722	.00768
δ^*x (ft)	.00126	.00122	.00107	.00107	.00100	.00100	.00100	.00100
θ_{xx} (ft)	.00085	.00094	.00075	.00081	.00069	.00075	.00070	.00074
CFX	.00246	.00240	.00220	.00210	.00207	.00195	.00205	.00193
CFY	-.00904	-.00002	-.00002	-.00001	-.00001	-.00001	-.00001	-.00001
U_∞ (ft/sec)	120.0		240.0		360.0		380.0	
V_∞ (ft/sec)	-2.00		-2.00		-2.00		-2.00	
α (deg)	-.96		-.48		-.32		-.30	

	X/CHORD = .80 Y/RADIUS = .30		X/CHORD = .80 Y/RADIUS = .60		X/CHORD = .80 Y/RADIUS = .90		X/CHORD = .80 Y/RADIUS = .95	
	D	I	D	I	D	I	D	I
δ (ft)	.02090	.02080	.01900	.01820	.01830	.01700	.01800	.01680
δ^*x (ft)	.00270	.00260	.00240	.00231	.00229	.00219	.00229	.00218
θ_{xx} (ft)	.00193	.00201	.00174	.00177	.00165	.00164	.00164	.00162
CFX	.00202	.00203	.00186	.00177	.00169	.00165	.00166	.00163
CFY	-.00040	-.00034	-.00018	-.00015	-.00011	-.00009	-.00010	-.00009
U_∞ (ft/sec)	120.0		240.0		360.0		380.0	
V_∞ (ft/sec)	-22.00		-22.00		-22.00		-22.00	
α (deg)	-10.41		-5.25		-3.50		-3.32	

TABLE VII – Continued

(b) Ω = 60 rad/sec

		X/CHORD = .30 Y/RADIUS = .30		X/CHORD = .30 Y/RADIUS = .60		X/CHORD = .30 Y/RADIUS = .90		X/CHORD = .30 Y/RADIUS = .95	
		D	I	D	I	D	I	D	I
δ	(ft)	.00803	.00890	.00706	.00776	.00675	.00721	.00666	.00715
δ^*_x	(ft)	.00113	.00112	.00099	.00100	.00096	.00097	.00096	.00097
θ_{xx}	(ft)	.00078	.00086	.00069	.00075	.00065	.00069	.00064	.00069
CFX		.00234	.00221	.00207	.00195	.00188	.00181	.00185	.00179
CFY		-.00003	-.00002	-.00002	-.00001	-.00001	-.00001	-.00001	-.00001
U_∞	(ft/sec)	180.0		360.0		540.0		570.0	
V_∞	(ft/sec)	-3.00		-3.00		-3.00		-3.00	
α	(deg)	-.96		-.48		-.32		-.30	

		X/CHORD = .80 Y/RADIUS = .30		X/CHORD = .80 Y/RADIUS = .60		X/CHORD = .80 Y/RADIUS = .90		X/CHORD = .80 Y/RADIUS = .95	
		D	I	D	I	D	I	D	I
δ	(ft)	.01940	.01920	.01830	.01690	.01760	.01580	.01670	.01570
δ^*_x	(ft)	.00251	.00241	.00230	.00219	.00225	.00212	.00223	.00212
θ_{xx}	(ft)	.00181	.00186	.00166	.00164	.00157	.00152	.00154	.00151
CFX		.00194	.00188	.00169	.00165	.00150	.00154	.00147	.00153
CFY		-.00038	-.00031	-.00016	-.00014	-.00009	-.00009	-.00009	-.00008
U_∞	(ft/sec)	180.0		360.0		540.0		570.0	
V_∞	(ft/sec)	-33.00		-33.00		-33.00		-33.60	
α	(deg)	-10.41		-5.25		-3.50		-3.32	

68

TABLE VII – Concluded

(c) Ω = 80 rad/sec

	X/CHORD = .30 Y/RADIUS = .30		X/CHORD = .30 Y/RADIUS = .60		X/CHORD = .30 Y/RADIUS = .90		X/CHORD = .30 Y/RADIUS = .95	
	D	I	D	I	D	I	D	I
δ (ft)	.00791	.00840	.00679	.00736	.00638	.00688	.00640	.00683
δ^*_x (ft)	.00107	.00107	.00097	.00097	.00094	.00097	.00095	.00097
θ_{xx} (ft)	.00075	.00081	.00067	.00071	.00060	.00066	.00060	.00065
CFX	.00221	.00210	.00195	.00185	.00171	.00172	.00167	.00171
CFY	-.00003	-.00002	-.00001	-.00001	-.00001	-.00001	-.00001	-.00001
U_∞ (ft/sec)	240.0		480.0		720.0		760.0	
V_∞ (ft/sec)	-4.00		-4.00		-4.00		-4.00	
α (deg)	-.98		-.48		-.32		-.30	

	X/CHORD = .80 Y/RADIUS = .30		X/CHORD = .80 Y/RADIUS = .60		X/CHORD = .80 Y/RADIUS = .90		X/CHORD = .80 Y/RADIUS = .95	
	D	I	D	I	D	I	D	I
δ (ft)	.01890	.01820	.01750	.01610	.01670	.01520	.01670	.01510
δ^*_x (ft)	.00240	.00230	.00223	.00213	.00223	.00214	.00224	.00215
θ_{xx} (ft)	.00173	.00176	.00157	.00156	.00147	.00145	.00147	.00143
CFX	.00185	.00179	.00155	.00157	.00137	.00147	.00135	.00146
CFY	-.00037	-.00030	-.00015	-.00013	-.00009	-.00008	-.00008	-.00008
U_∞ (ft/sec)	240.0		480.0		720.0		760.0	
V_∞ (ft/sec)	-44.00		-44.00		-44.00		-44.00	
α (deg)	-10.41		-5.25		-3.50		-3.32	

69

TABLE VIII. COMPARISON OF RESULTS OF THE INTEGRAL AND DIFFERENTIAL METHODS FOR VARIOUS VORTEX STRENGTHS, BLADE RADIUS = 10 ft, Ω = 60 rad/sec, $dC_p/d(x/C) = 0$, FLAT SURFACE

(a) Γ/h = +25 ft/sec

	X/CHORD = .30 Y/RADIUS = .30		X/CHORD = .30 Y/RADIUS = .60		X/CHORD = .30 Y/RADIUS = .90		X/CHORD = .30 Y/RADIUS = .95	
	D	I	D	I	D	I	D	I
δ (ft)	.00903	.00890	.00706	.00776	.00675	.00721	.00668	.00716
δ*x (ft)	.00113	.00112	.00096	.00100	.00096	.00097	.00096	.00097
θxx (ft)	.00078	.00086	.00069	.00075	.00065	.00069	.00065	.00069
CFX	.00230	.00221	.00207	.00195	.00188	.00181	.00185	.00179
CFY	-.00003	-.00002	-.00001	-.00001	-.00002	-.00002	-.00001	-.00001
U∞ (ft/sec)	180.0		360.0		540.0		570.0	
V∞ (ft/sec)	-2.80		-2.20		5.00		3.40	
α (deg)	-.89		-.35		.53		.34	

	X/CHORD = .80 Y/RADIUS = .30		X/CHORD = .80 Y/RADIUS = .60		X/CHORD = .80 Y/RADIUS = .90		X/CHORD = .80 Y/RADIUS = .95	
	D	I	D	I	D	I	D	I
δ (ft)	.01940	.01920	.01820	.01690	.01760	.01580	.01730	.01580
δ*x (ft)	.00251	.00241	.00230	.00218	.00225	.00212	.00225	.00213
θxx (ft)	.00181	.00186	.00165	.00164	.00157	.00152	.00155	.00151
CFX	.00194	.00188	.00169	.00165	.00150	.00154	.00147	.00152
CFY	-.00038	-.00031	-.00016	-.00013	-.00007	-.00006	-.00007	-.00006
U∞ (ft/sec)	180.0		360.0		540.0		570.0	
V∞ (ft/sec)	-32.80		-32.20		-25.00		-26.60	
α (deg)	-10.35		-5.12		-2.66		-2.68	

TABLE VIII - Continued

(b) $\Gamma/h = -25$ ft/sec

	X/CHORD = .30 Y/RADIUS = .30		X/CHORD = .30 Y/RADIUS = .60		X/CHORD = .30 Y/RADIUS = .90		X/CHORD = .30 Y/RADIUS = .95	
	D	I	D	I	D	I	D	I
δ (ft)	.00803	.00890	.00706	.00776	.00674	.00721	.00665	.00714
δ^*_x (ft)	.00113	.00112	.00096	.00100	.00096	.00097	.00096	.00096
θ_{xx} (ft)	.00078	.00086	.00069	.00075	.00065	.00069	.00064	.00069
CFX	.00230	.00221	.00207	.00195	.00188	.00181	.00186	.00179
CFY	-.00004	-.00002	-.00002	-.00001	-.00004	-.00003	-.00003	-.00003
U_∞ (ft/sec)	180.0		360.0		540.0		570.0	
V_∞ (ft/sec)	-3.20		-3.80		-11.00		-9.40	
α (deg)	-1.02		-.61		-1.17		-.95	

	X/CHORD = .80 Y/RADIUS = .30		X/CHORD = .80 Y/RADIUS = .60		X/CHORD = .80 Y/RADIUS = .90		X/CHORD = .80 Y/RADIUS = .95	
	D	I	D	I	D	I	D	I
δ (ft)	.01990	.01920	.01830	.01700	.01760	.01580	.01710	.01570
δ^*_x (ft)	.00251	.00241	.00230	.00219	.00225	.00212	.00222	.00211
θ_{xx} (ft)	.00181	.00186	.00166	.00164	.00157	.00152	.00153	.00150
CFX	.00194	.00188	.00169	.00165	.00150	.00154	.00148	.00153
CFY	-.00039	-.00032	-.00017	-.00014	-.00012	-.00011	-.00011	-.00010
U_∞ (ft/sec)	180.0		360.0		540.0		570.0	
V_∞ (ft/sec)	-33.20		-33.80		-41.00		-39.40	
α (deg)	-10.47		-5.57		-4.35		-3.96	

TABLE VIII - Continued

(c) Γ/h = +50 ft/sec

		X/CHORD = .30 Y/RADIUS = .30		X/CHORD = .30 Y/RADIUS = .60		X/CHORD = .30 Y/RADIUS = .90		X/CHORD = .30 Y/RADIUS = .95	
		D	I	D	I	D	I	D	I
δ	(ft)	.00803	.00890	.00705	.00776	.00675	.00722	.00669	.00717
δ^*	(ft)	.00113	.00112	.00099	.00100	.00096	.00097	.00096	.00097
θ_{xx}	(ft)	.00976	.00086	.00069	.00075	.00065	.00069	.00065	.00069
CFX		.00234	.00221	.00407	.00195	.00188	.00181	.00185	.00179
CFY		-.00003	-.00002	-.00001	-.00000	-.00004	-.00005	-.00004	-.00003
U_∞	(ft/sec)	180.0		360.0		540.0		570.0	
V_∞	(ft/sec)	-2.60		-1.40		12.90		9.70	
α	(deg)	-.83		-.22		1.37		.98	

		X/CHORD = .80 Y/RADIUS = .30		X/CHORD = .80 Y/RADIUS = .60		X/CHORD = .80 Y/RADIUS = .90		X/CHORD = .80 Y/RADIUS = .95	
		D	I	D	I	D	I	D	I
δ	(ft)	.01940	.01920	.01820	.01690	.01760	.01580	.01750	.01580
δ^*	(ft)	.00250	.00241	.00230	.00218	.00225	.00212	.00226	.00214
θ_{xx}	(ft)	.00181	.00186	.00165	.00164	.00157	.00152	.00156	.00152
CFX		.00194	.00188	.00169	.00165	.00150	.00154	.00146	.00152
CFY		-.00038	-.00031	-.00015	-.00013	-.00005	-.00004	-.00005	-.00005
U_∞	(ft/sec)	180.0		360.0		540.0		570.0	
V_∞	(ft/sec)	-32.60		-31.40		-17.10		-20.30	
α	(deg)	-10.28		-4.99		-1.82		-2.04	

72

TABLE VIII - Concluded

(d) Γ/h = -50 ft/sec

		X/CHORD = .30 Y/RADIUS = .30		X/CHORD = .30 Y/RADIUS = .60		X/CHORD = .30 Y/RADIUS = .90		X/CHORD = .30 Y/RADIUS = .95	
		D	I	D	I	D	I	D	I
δ	(ft)	.00803	.00890	.00706	.00776	.00674	.00721	.00663	.00713
δ*	(ft)	.00113	.00112	.00099	.00100	.00096	.00097	.00096	.00096
θxx	(ft)	.00078	.00086	.00069	.00075	.00065	.00069	.00064	.00069
CFX		.00230	.00221	.00207	.00195	.00188	.00181	.00186	.00180
CFY		-.00004	-.00003	-.00003	-.00002	-.00006	-.00006	-.00005	-.00005
U∞	(ft/sec)	180.0		360.0		540.0		570.0	
V∞	(ft/sec)	-3.40		-4.60		-18.90		-15.70	
α	(deg)	-1.08		-.73		-2.01		-1.58	

		X/CHORD = .80 Y/RADIUS = .30		X/CHORD = .80 Y/RADIUS = .60		X/CHORD = .80 Y/RADIUS = .90		X/CHORD = .80 Y/RADIUS = .95	
		D	I	D	I	D	I	D	I
δ	(ft)	.01950	.01920	.01780	.01700	.01760	.01580	.01690	.01560
δ*	(ft)	.00251	.00241	.00230	.00219	.00225	.00212	.00222	.00211
θxx	(ft)	.00181	.00186	.00165	.00164	.00157	.00152	.00154	.00150
CFX		.00194	.00188	.00169	.00165	.00150	.00154	.00149	.00153
CFY		-.00039	-.00032	-.00017	-.00014	-.00014	-.00013	-.00013	-.00012
U∞	(ft/sec)	180.0		360.0		540.0		570.0	
V∞	(ft/sec)	-33.40		-34.60		-48.90		-45.70	
α	(deg)	-10.53		-5.50		-5.18		-4.59	

73

TABLE IX. COMPARISON OF RESULTS OF THE INTEGRAL AND DIFFERENTIAL METHODS FOR VARIOUS PRESSURE GRADIENTS, BLADE RADIUS = 10 ft, Ω = 60 rad/sec, Γ/h = 0 ft/sec, FLAT SURFACE

(a) $dCp/d(x/C) = 1$

|		X/CHORD = .30 Y/RADIUS = .30		X/CHORD = .30 Y/RADIUS = .60		X/CHORD = .30 Y/RADIUS = .90		X/CHORD = .30 Y/RADIUS = .95	
		D	I	D	I	D	I	D	I
δ	(ft)	.00806	.00860	.00778	.00756	.00678	.00709	.00686	.00704
δ^*x	(ft)	.00116	.00109	.00110	.00099	.00105	.00098	.00106	.00098
θxx	(ft)	.00080	.00083	.00075	.00073	.00068	.00068	.00068	.00067
CFX		.00213	.00214	.00177	.00189	.00164	.00177	.00161	.00176
CFY		-.00002	-.00002	-.00001	-.00001	-.00001	-.00000	-.00001	-.00000
U_∞	(ft/sec)	216.9		434.5		653.3		689.9	
V_∞	(ft/sec)	-3.00		-3.00		-3.00		-3.00	
α	(deg)	-.79		-.40		-.26		-.25	

		X/CHORD = .80 Y/RADIUS = .30		X/CHORD = .80 Y/RADIUS = .60		X/CHORD = .80 Y/RADIUS = .90		X/CHORD = .80 Y/RADIUS = .95	
		D	I	D	I	D	I	D	I
δ	(ft)	.02480	.02250	.02450	.01940	.02340	.01810	.02350	.01800
δ^*x	(ft)	.00373	.00464	.00355	.00439	.00362	.00444	.00362	.00447
θxx	(ft)	.00263	.00303	.00249	.00271	.00241	.00258	.00242	.00257
CFX		.00187	.00170	.00154	.00150	.00134	.00139	.00129	.00138
CFY		-.00039	-.00031	-.00016	-.00013	-.00009	-.00008	-.00008	-.00008
U_∞	(ft/sec)	175.4		350.9		526.3		555.6	
V_∞	(ft/sec)	-33.00		-33.00		-33.00		-33.00	
α	(deg)	-10.67		-5.38		-3.59		-3.41	

74

TABLE IX – Concluded

(b) $dCp/d(x/C) = 2$

		X/CHORD = .30 Y/RADIUS = .30		X/CHORD = .30 Y/RADIUS = .60		X/CHORD = .30 Y/RADIUS = .90		X/CHORD = .30 Y/RADIUS = .95	
		D	I	D	I	D	I	D	I
δ	(ft)	.00813	.00832	.00702	.00739	.00673	.00704	.00657	.00701
$\delta*x$	(ft)	.00117	.00106	.00110	.00099	.00110	.00102	.00110	.00103
θxx	(ft)	.00080	.00081	.00073	.00071	.00067	.00067	.00066	.00066
CFX		.00200	.00206	.00171	.00184	.00155	.00174	.00153	.00173
CFY		-.00002	-.00001	-.00001	.00001	-.00000	-.00000	-.00000	-.00000
U_∞	(ft/sec)	264.6		532.6		808.2		855.3	
V_∞	(ft/sec)	-3.00		-3.00		-3.00		-3.00	
α	(deg)	-.65		-.32		-.21		-.20	

		X/CHORD = .80 Y/RADIUS = .30		X/CHORD = .80 Y/RADIUS = .60		X/CHORD = .80 Y/RADIUS = .90		X/CHORD = .80 Y/RADIUS = .95	
		D	I	D	I	D	I	D	I
δ	(ft)	.02830	.02330	.02670	---	.02650	---	.02770	---
$\delta*x$	(ft)	.00493	.00713	.00476	---	.00503	---	.00507	---
θxx	(ft)	.00331	.00377	.00310	---	.00310	---	.00312	---
CFX		.00165	.00159	.00128	---	.00106	---	.00103	---
CFY		-.00034	-.00028	-.00014	---	-.00007	---	-.00007	---
U_∞	(ft/sec)	193.1		386.2		579.5		611.8	
V_∞	(ft/sec)	-33.00		-33.00		-33.00		-33.00	
α	(deg)	-9.72		-4.89		-3.27		-3.09	

75

TABLE X. COMPARISON OF RESULTS OF THE INTEGRAL AND DIFFERENTIAL METHODS FOR VARIOUS VORTEX STRENGTHS, BLADE RADIUS = 10 ft, Ω = 60 rad/sec, $dcp/d(x/C)$ = 0, SURFACE RADIUS OF CURVATURE = 4.125 ft

(a) Γ/h = +25 ft/sec

|	X/CHORD = .30 Y/RADIUS = .30		X/CHORD = .30 Y/RADIUS = .60		X/CHORD = .30 Y/RADIUS = .90		X/CHORD = .30 Y/RADIUS = .95	
	D	I	D	I	D	I	D	I
δ (ft)	.00780	.00891	.00711	.00776	.00677	.00722	.00669	.00716
δ*x (ft)	.00112	.00112	.00090	.00100	.00096	.00097	.00096	.00097
θxx (ft)	.00077	.00086	.00069	.00075	.00065	.00069	.00065	.00069
CFX	.00230	.00221	.00207	.00195	.00188	.00181	.00185	.00179
CFY	-.00003	-.00002	-.00001	-.00001	-.00002	-.00002	-.00001	-.00001
U∞ (ft/sec)	180.0		360.0		540.0		570.0	
V∞ (ft/sec)	-2.80		-2.20		5.00		3.40	
α (deg)	-.89		-.35		.53		.34	

	X/CHORD = .80 Y/RADIUS = .30		X/CHORD = .80 Y/RADIUS = .60		X/CHORD = .80 Y/RADIUS = .90		X/CHORD = .80 Y/RADIUS = .95	
	D	I	D	I	D	I	D	I
δ (ft)	.01990	.01920	.01790	.01700	.01730	.01580	.01750	.01580
δ*x (ft)	.00250	.00241	.00229	.00219	.00224	.00212	.00226	.00213
θxx (ft)	.00181	.00186	.00165	.00164	.00156	.00153	.00156	.00152
CFX	.00194	.00188	.00169	.00165	.00150	.00154	.00147	.00152
CFY	-.00038	-.00031	-.00016	-.00013	-.00007	-.00006	-.00007	-.00006
U∞ (ft/sec)	180.0		360.0		540.0		570.0	
V∞ (ft/sec)	-32.80		-32.20		-25.00		-26.60	
α (deg)	-10.35		-5.12		-2.66		-2.68	

TABLE X - Continued

(b) Γ/h = -25 ft/sec

		X/CHORD = .30 Y/RADIUS = .30		X/CHORD = .30 Y/RADIUS = .60		X/CHORD = .30 Y/RADIUS = .90		X/CHORD = .30 Y/RADIUS = .95	
		D	I	D	I	D	I	D	I
δ	(ft)	.00780	.00891	.00711	.00777	.00676	.00722	.00667	.00714
δ*	(ft)	.00112	.00112	.00100	.00100	.00096	.00097	.00096	.00096
θxx	(ft)	.00077	.00086	.00069	.00075	.00065	.00069	.00064	.00069
CFX		.00230	.00221	.00207	.00195	.00188	.00181	.00186	.00179
CFY		-.00004	-.00002	-.00002	-.00001	-.00004	-.00003	-.00003	-.00003
U∞	(ft/sec)	180.0		360.0		540.0		570.0	
V∞	(ft/sec)	-3.20		-3.80		-11.00		-9.40	
α	(deg)	-1.02		-.61		-1.17		-.95	

		X/CHORD = .80 Y/RADIUS = .30		X/CHORD = .80 Y/RADIUS = .60		X/CHORD = .80 Y/RADIUS = .90		X/CHORD = .80 Y/RADIUS = .95	
		D	I	D	I	D	I	D	I
δ	(ft)	.01990	.01920	.01790	.01700	.01730	.01590	.01680	.01570
δ*	(ft)	.00251	.00241	.00230	.00219	.00224	.00212	.00222	.00212
θxx	(ft)	.00182	.00186	.00165	.00164	.00156	.00153	.00153	.00151
CFX		.00194	.00188	.00169	.00165	.00150	.00154	.00148	.00153
CFY		-.00038	-.00032	-.00017	-.00014	-.00012	-.00011	-.00011	-.00010
U∞	(ft/sec)	180.0		360.0		540.0		570.0	
V∞	(ft/sec)	-33.20		-33.80		-41.00		-39.40	
α	(deg)	-10.47		-5.37		-9.35		-3.96	

77

TABLE X - Continued

(c) Γ/h = +50 ft/sec

	X/CHORD = .30 Y/RADIUS = .30		X/CHORD = .30 Y/RADIUS = .60		X/CHORD = .30 Y/RADIUS = .90		X/CHORD = .30 Y/RADIUS = .95	
	D	I	D	I	D	I	D	I
δ (ft)	.00780	.00890	.00710	.00776	.00677	.00722	.00671	.00717
δ* (ft)	.00112	.00112	.00099	.00100	.00096	.00097	.00096	.00097
θxx (ft)	.00077	.00086	.00069	.00075	.00065	.00069	.00065	.00069
CFX	.00230	.00221	.00207	.00195	.00188	.00181	.00185	.00179
CFY	-.00003	-.00002	-.00001	-.00000	-.00004	-.00005	-.00004	-.00003
U∞ (ft/sec)	180.0		360.0		540.0		570.0	
V∞ (ft/sec)	-2.60		-1.40		12.90		9.70	
α (deg)	-.83		-.22		1.37		.98	

	X/CHORD = .80 Y/RADIUS = .30		X/CHORD = .80 Y/RADIUS = .60		X/CHORD = .80 Y/RADIUS = .90		X/CHORD = .80 Y/RADIUS = .95	
	D	I	D	I	D	I	D	I
δ (ft)	.01990	.01920	.01830	.01690	.01730	.01590	.01770	.01580
δ* (ft)	.00250	.00241	.00230	.00219	.00224	.00213	.00227	.00214
θxx (ft)	.00181	.00186	.00166	.00164	.00156	.00153	.00157	.00152
CFX	.00194	.00188	.00169	.00165	.00150	.00154	.00146	.00152
CFY	-.00038	-.00031	-.00015	-.00013	-.00005	-.00004	-.00005	-.00005
U∞ (ft/sec)	180.0		360.0		540.0		570.0	
V∞ (ft/sec)	-32.60		-31.40		-17.10		-20.30	
α (deg)	-10.28		-4.99		-1.82		-2.04	

78

TABLE X – Concluded

(d) $\Gamma/h = -50$ ft/sec

		X/CHORD = .30, Y/RADIUS = .30		X/CHORD = .30, Y/RADIUS = .60		X/CHORD = .30, Y/RADIUS = .90		X/CHORD = .30, Y/RADIUS = .95	
		D	I	D	I	D	I	D	I
δ^*	(ft)	.00781	.00891	.00711	.00777	.00676	.00722	.00666	.00713
δx	(ft)	.00112	.00112	.00100	.00100	.00096	.00097	.00096	.00096
θ_{xx}	(ft)	.00077	.00086	.00069	.00075	.00065	.00069	.00064	.00069
CFX		.00230	.00221	.00207	.00195	.00188	.00181	.00186	.00179
CFY		-.00004	-.00003	-.00003	-.00002	-.00006	-.00006	-.00005	-.00005
U_∞	(ft/sec)	180.0		360.0		540.0		570.0	
V_∞	(ft/sec)	-3.40		-4.60		-18.90		-15.70	
α	(deg)	-1.08		-.73		-2.01		-1.58	

		X/CHORD = .80, Y/RADIUS = .30		X/CHORD = .80, Y/RADIUS = .60		X/CHORD = .80, Y/RADIUS = .90		X/CHORD = .80, Y/RADIUS = .95	
		D	I	D	I	D	I	D	I
δ^*	(ft)	.01990	.01930	.01790	.01700	.01720	.01590	.01720	.01560
δx	(ft)	.00251	.00241	.00229	.00219	.00224	.00213	.00222	.00211
θ_{xx}	(ft)	.00182	.00186	.00164	.00164	.00156	.00153	.00153	.00150
CFX		.00194	.00188	.00169	.00165	.00150	.00154	.00149	.00153
CFY		-.00039	-.00032	-.00017	-.00014	-.00014	-.00013	-.00013	-.00012
U_∞	(ft/sec)	180.0		360.0		540.0		570.0	
V_∞	(ft/sec)	-33.40		-34.60		-48.90		-45.70	
α	(deg)	-10.53		-5.50		-5.18		-4.59	

79

TABLE XI. COMPARISON OF RESULTS OF THE INTEGRAL AND DIFFERENTIAL METHODS FOR VARIOUS PRESSURE GRADIENTS, BLADE RADIUS = 10 ft, Ω = 60 rad/sec, Γ/h = 0 ft/sec, SURFACE RADIUS OF CURVATURE = 4.125 ft

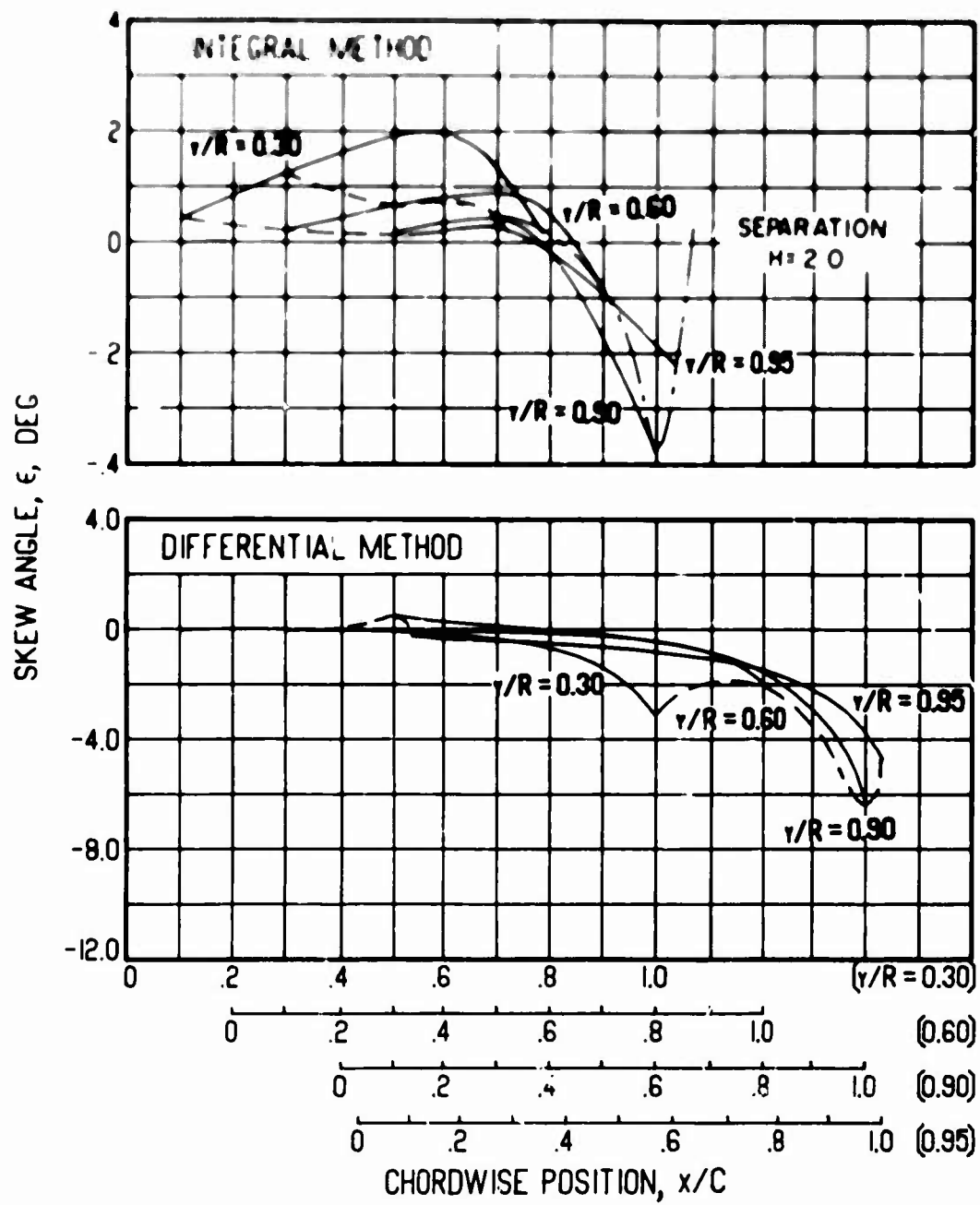(a) $dCp/d(x/C) = 1$

|	X/CHORD = .30 Y/RADIUS = .30		X/CHORD = .30 Y/RADIUS = .60		X/CHORD = .30 Y/RADIUS = .90		X/CHORD = .30 Y/RADIUS = .95	
	D	I	D	I	D	I	D	I
δ (ft)	.00809	.00860	.00756	.00756	.00680	.00709	.00689	.00704
δ_x^* (ft)	.00116	.00109	.00110	.00099	.00106	.00098	.00106	.00098
θ_{xx} (ft)	.00081	.00083	.00075	.00073	.00068	.00068	.00068	.00067
CFX	.00214	.00214	.00178	.00189	.00164	.00177	.00161	.00176
CFY	-.00002	-.00002	-.00001	-.00001	-.00001	-.00000	-.00001	-.00000
U_∞ (ft/sec)	216.9		434.5		653.3		689.9	
V_∞ (ft/sec)	-3.00		-3.00		-3.00		-3.00	
α (deg)	-.79		-.40		-.26		-.25	

	X/CHORD = .80 Y/RADIUS = .30		X/CHORD = .80 Y/RADIUS = .60		X/CHORD = .80 Y/RADIUS = .90		X/CHORD = .80 Y/RADIUS = .95	
	D	I	D	I	D	I	D	I
δ (ft)	.02670	.02250	.02480	.01940	.02350	.01810	.02390	.01800
δ_x^* (ft)	.00382	.00464	.00357	.00439	.00365	.00445	.00362	.00448
θ_{xx} (ft)	.00271	.00304	.00251	.00271	.00244	.00258	.00241	.00257
CFX	.00187	.00170	.00155	.00150	.00133	.00139	.00129	.00138
CFY	-.00039	-.00031	-.00016	-.00013	-.00009	-.00008	-.00008	-.00008
U_∞ (ft/sec)	175.4		350.9		526.3		555.6	
V_∞ (ft/sec)	-33.00		-33.00		-33.00		-33.00	
α (deg)	-10.67		-5.38		-3.59		-3.41	

TABLE XI – Concluded

(b) $dCp/d(x/C) = 2$

		X/CHORD = .30 Y/RADIUS = .30		X/CHORD = .30 Y/RADIUS = .60		X/CHORD = .30 Y/RADIUS = .90		X/CHORD = .30 Y/RADIUS = .95	
		D	I	D	I	D	I	D	I
δ	(ft)	.00816	.00833	.00705	.00739	.00676	.00704	.00660	.00701
δ*x	(ft)	.00117	.00106	.00110	.00099	.00110	.00102	.00111	.00103
θxx	(ft)	.00081	.00081	.00073	.00071	.00067	.00067	.00066	.00066
CFX		.00201	.00206	.00171	.00184	.00155	.00174	.00153	.00173
CFY		-.00002	-.00001	-.00001	-.00001	-.00000	-.00000	-.00000	-.00000
U∞	(ft/sec)	264.6		532.6		808.2		855.3	
V∞	(ft/sec)	-3.00		-3.00		-3.00		-3.00	
α	(deg)	-.65		-.32		-.21		-.20	

		X/CHORD = .80 Y/RADIUS = .30		X/CHORD = .80 Y/RADIUS = .60		X/CHORD = .80 Y/RADIUS = .90		X/CHORD = .80 Y/RADIUS = .95	
		D	I	D	I	D	I	D	I
δ	(ft)	.02860	.02330	.02400	---	.02710	---	.02780	---
δ*x	(ft)	.00502	.00713	.00484	---	.00512	---	.00510	---
θxx	(ft)	.00336	.00377	.00315	---	.00318	---	.00313	---
CFX		.00166	.00159	.00120	---	.00106	---	.00103	---
CFY		-.00034	-.00028	-.00014	---	-.00007	---	-.00007	---
U∞	(ft/sec)	193.1		386.2		579.5		611.8	
V∞	(ft/sec)	-33.00		-33.00		-33.00		-33.00	
α	(deg)	-9.72		-4.89		-3.27		-3.09	

81

TABLE XII. COMPARISON OF RESULTS OF THE INTEGRAL AND DIFFERENTIAL METHODS FOR VARIOUS VORTEX STRENGTHS, BLADE RADIUS = 10 ft, Ω = 60 rad/sec, dCp/d(x/c) = 2, SURFACE RADIUS OF CURVATURE = 4.125 ft

(a) Γ/h = +50 ft/sec

|	X/CHORD = .30 Y/RADIUS = .30		X/CHORD = .30 Y/RADIUS = .60		X/CHORD = .30 Y/RADIUS = .90		X/CHORD = .30 Y/RADIUS = .95	
	D	I	D	I	D	I	D	I
δ (ft)	.00816	.00833	.00704	.00739	.00676	.00704	.00663	.00702
δ^*_x (ft)	.00117	.00106	.00110	.00099	.00110	.00102	.00111	.00103
θ_{xx} (ft)	.00081	.00081	.00073	.00071	.00067	.00067	.00066	.00067
CFX	.00201	.00206	.00172	.00184	.00155	.00174	.00153	.00173
CFY	-.00001	-.00001	.00001	-.00000	-.00006	-.00003	.00005	-.00002
U_∞ (ft/sec)	264.6		532.6		808.2		855.3	
V_∞ (ft/sec)	-2.60		-1.40		12.90		9.70	
α (deg)	-.56		-.15		.92		.65	

	X/CHORD = .80 Y/RADIUS = .30		X/CHORD = .80 Y/RADIUS = .60		X/CHORD = .80 Y/RADIUS = .90		X/CHORD = .80 Y/RADIUS = .95	
	D	I	D	I	D	I	D	I
δ (ft)	.02960	.02330	.02770	—	.02720	—	.02740	—
δ^*_x (ft)	.00504	.00713	.00481	—	.00509	—	.00519	—
θ_{xx} (ft)	.00339	.00377	.00313	—	.00317	—	.00319	—
CFX	.00167	.00159	.00129	—	.00106	—	.00102	—
CFY	-.00033	-.00028	-.00012	—	.00001	—	.00000	—
U_∞ (ft/sec)	193.1		366.2		579.5		611.8	
V_∞ (ft/sec)	-32.60		-31.40		-17.10		-20.30	
α (deg)	-4.60		-4.66		-1.69		-1.90	

TABLE XII - Concluded

(b) Γ/h = -50 ft/sec

	X/CHORD = .30 Y/RADIUS = .30		X/CHORD = .30 Y/RADIUS = .60		X/CHORD = .30 Y/RADIUS = .90		X/CHORD = .30 Y/RADIUS = .95	
	C	I	C	I	D	I	D	I
δ (ft)	.00817	.00833	.00705	.00739	.00676	.00704	.00657	.00700
δ* (ft)	.00117	.00106	.00110	.00099	.00110	.00102	.00110	.00103
θxx (ft)	.00081	.00081	.00073	.00071	.00067	.00067	.00066	.00066
CFX	.00201	.00206	.00171	.00184	.00155	.00174	.00153	.00173
CFY	-.00003	-.00002	-.00002	-.00001	-.00007	-.00004	-.00006	-.00003
U∞ (ft/sec)	264.6		532.0		808.2		855.3	
V∞ (ft/sec)	-3.40		-4.60		-18.90		-15.70	
α (deg)	-.00		-.49		-1.34		-1.06	

	X/CHORD = .80 Y/RADIUS = .30		X/CHORD = .80 Y/RADIUS = .60		X/CHORD = .80 Y/RADIUS = .90		X/CHORD = .80 Y/RADIUS = .95	
	C	I	D	I	D	I	D	I
δ (ft)	.02670	.02330	.02670	--	.02720	--	.02760	--
δ* (ft)	.00502	.00714	.00484	--	.00513	--	.00503	--
θxx (ft)	.00336	.00378	.00314	--	.00318	--	.00310	--
CFX	.00166	.00159	.00128	--	.00106	--	.00105	--
CFY	-.00036	-.00029	-.00015	--	-.00016	--	-.00015	--
U∞ (ft/sec)	193.1		386.2		579.5		611.8	
V∞ (ft/sec)	-33.40		-34.60		-48.9		-45.70	
α (deg)	-.00		-5.13		-4.83		-4.28	

X – POSITIVE MEASURED
FROM QUARTER CHORD
PARALLEL TO SURFACE

Y – POSITIVE MEASURED
PARALLEL TO SPANWISE
DIRECTION FROM AXIS
OF ROTATION

Z – POSITIVE MEASURED
NORMAL TO BLADE SURFACE
AT EACH POINT

Figure 1. Rotating Orthogonal Curvilinear
Coordinate System.
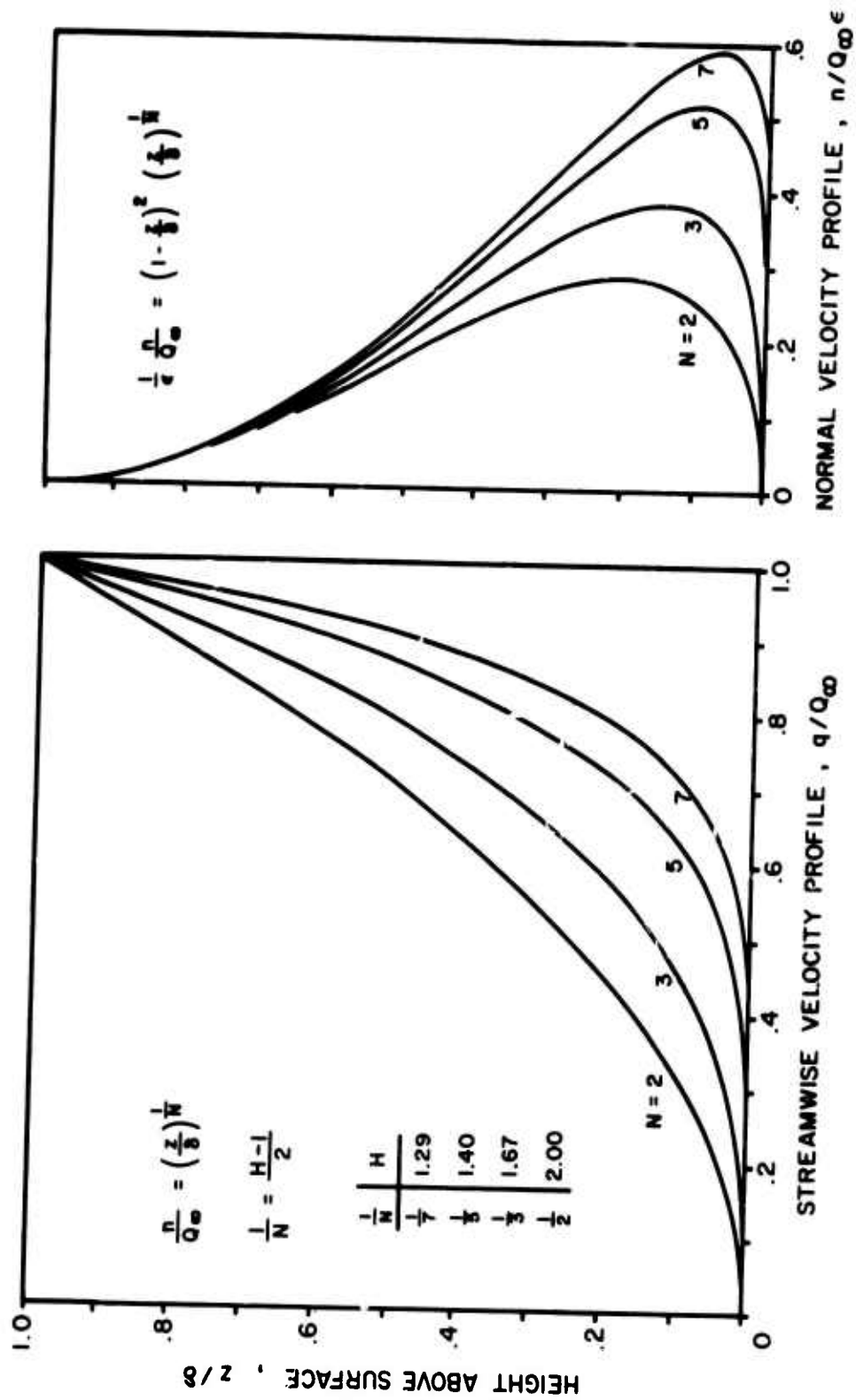
Figure 2. Power Law Velocity Profiles.

APPROXIMATED PRESSURE

DISTRIBUTION , $\frac{dC_p}{dx/C} = 1$

---- MEASURED PRESSURE DISTRIBUTION ,
ANGLE OF ATTACK = 0° ,
MACH NUMBER = 0.65

-1.0

PRESSURE COEFFICIENT, C_P

0

1.0

-2.0

APPROXIMATED PRESSURE

DISTRIBUTION , $\frac{dC_p}{dx/C} = 2$

---- MEASURED PRESSURE DISTRIBUTION,
ANGLE OF ATTACK = 4° ,
MACH NUMBER = 0.65

-1.0

0

1.0

0   0.2   0.4   0.6   0.8   1.0

CHORDWISE POSITION , x/C
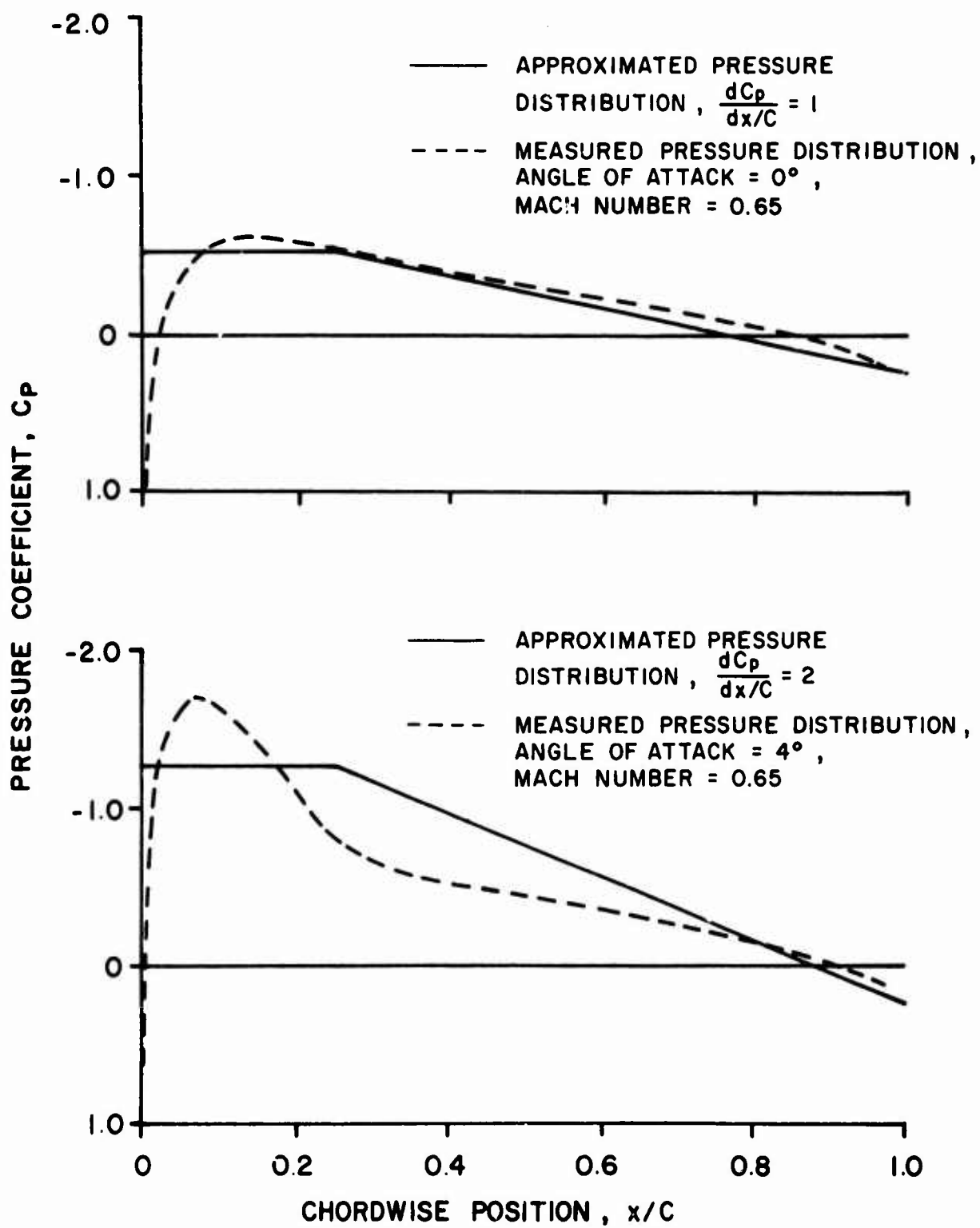
Figure 3.   Comparison of Approximated Pressure Distribution
and Measured H-34 Airfoil Data.
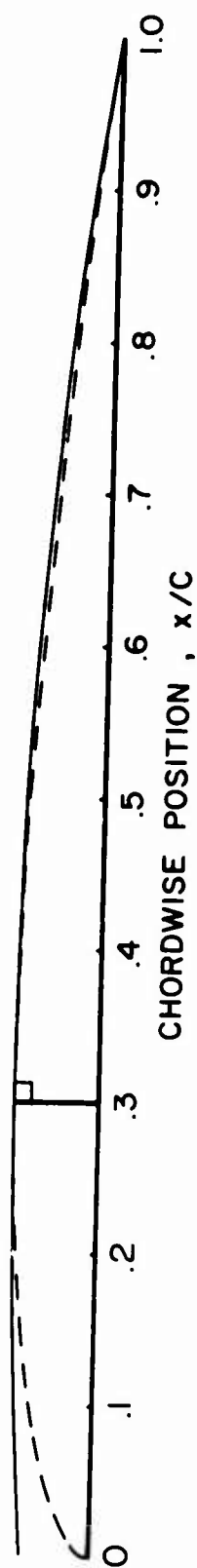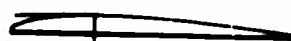
Figure 4. Comparison of NACA 0012 Airfoil Section and Curved Airfoil Approximation.
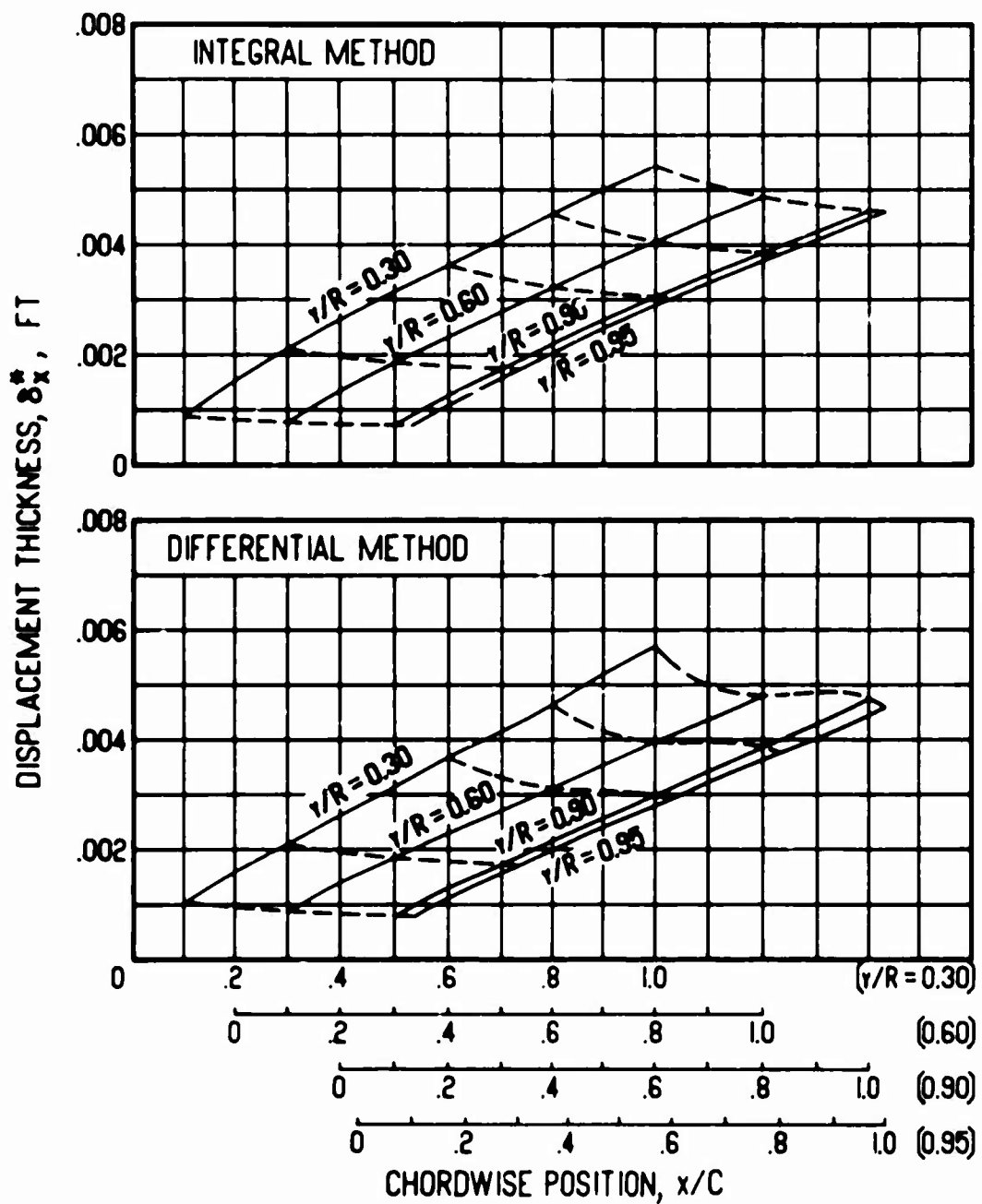
(a) $\Omega = 10$ rad/sec

Figure 5.   Displacement Thickness Versus Chordwise Position for
Various Angular Velocities, Blade Radius = 40 ft,
$\Gamma/h = 0$ ft/sec, $dCp/d(x/C) = 0$, Flat Surface.
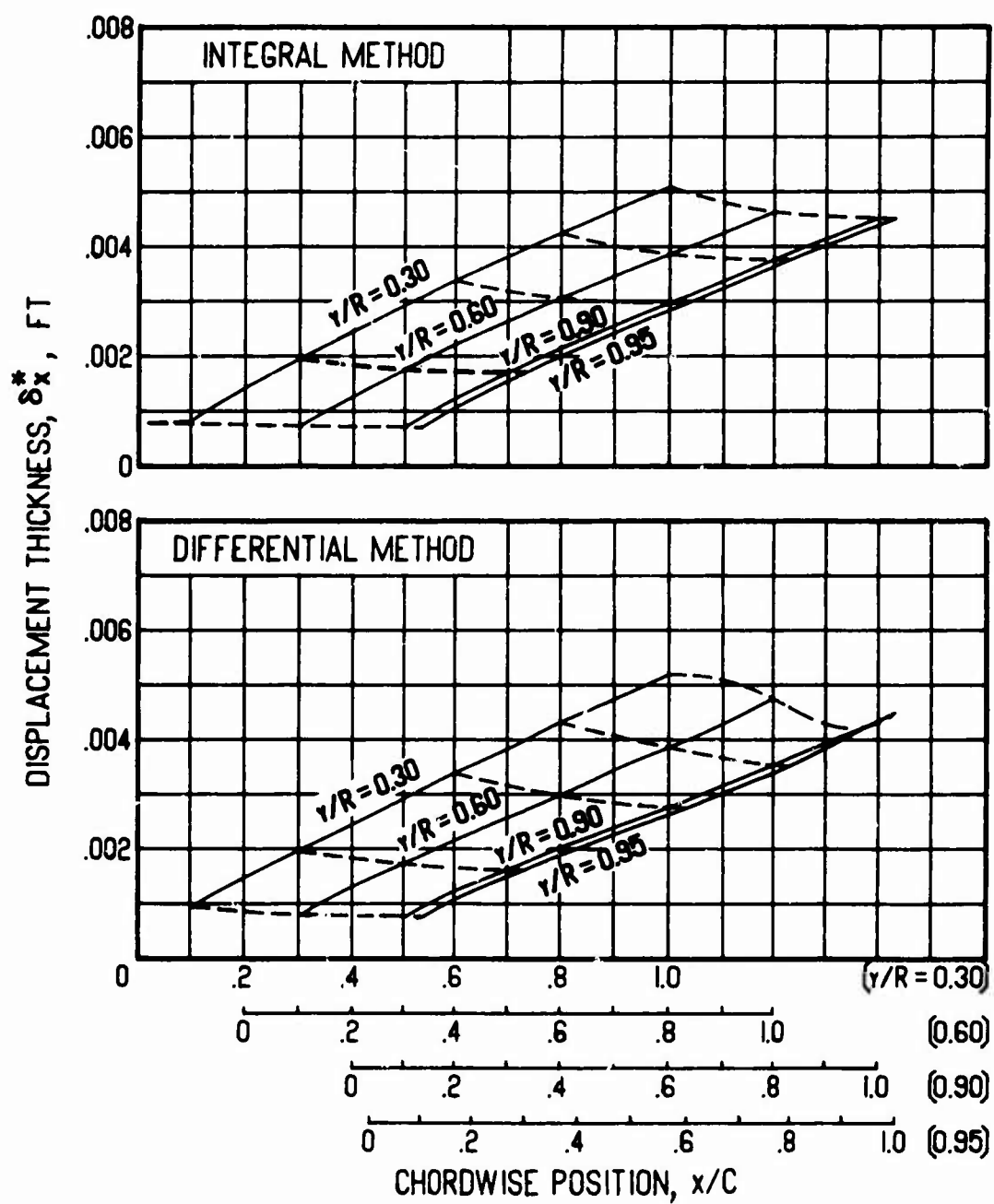
(b) $\Omega = 15$ rad/sec

Figure 5. Continued.

89
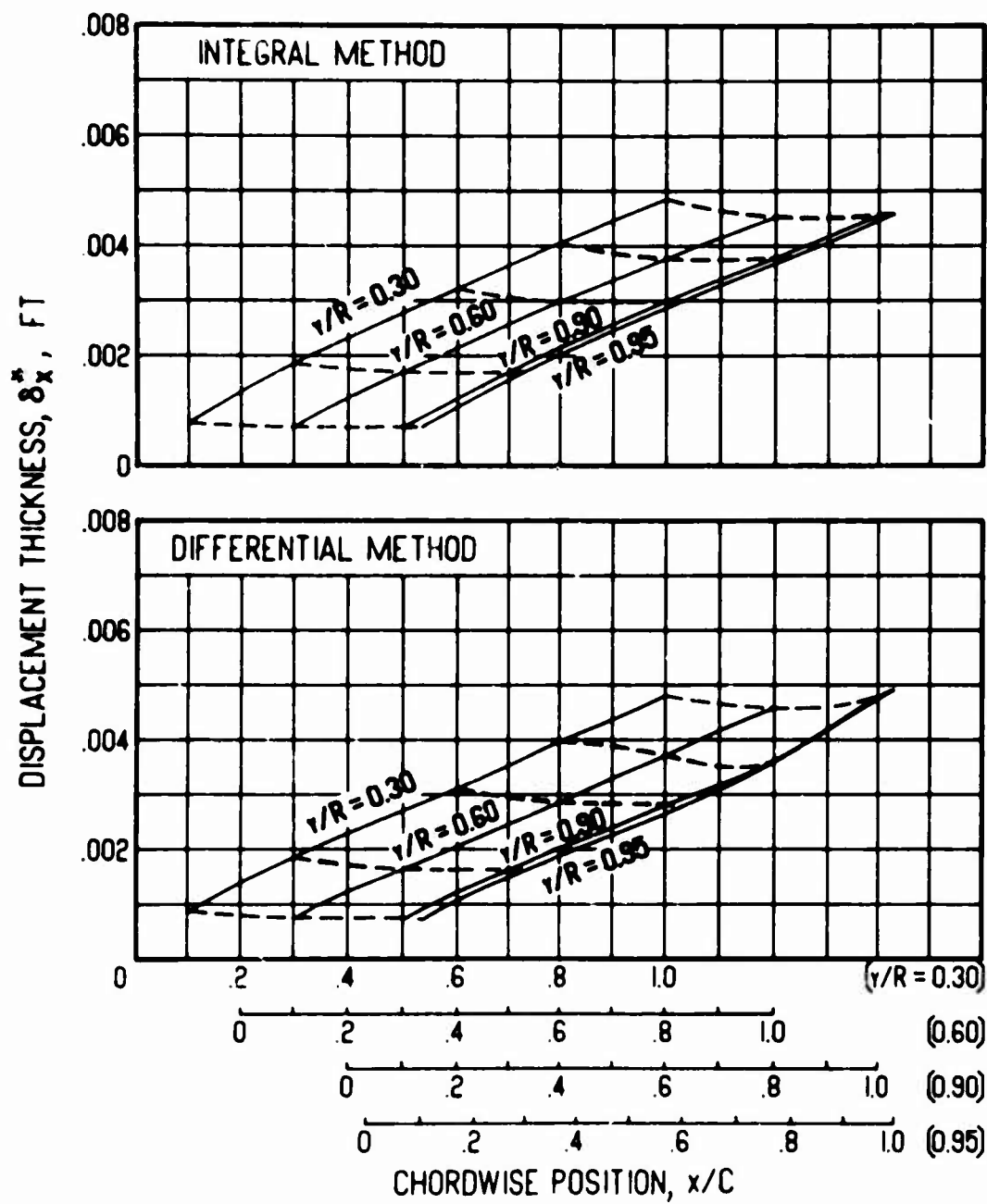
(c) $\Omega = 20$ rad/sec

Figure 5. Concluded.
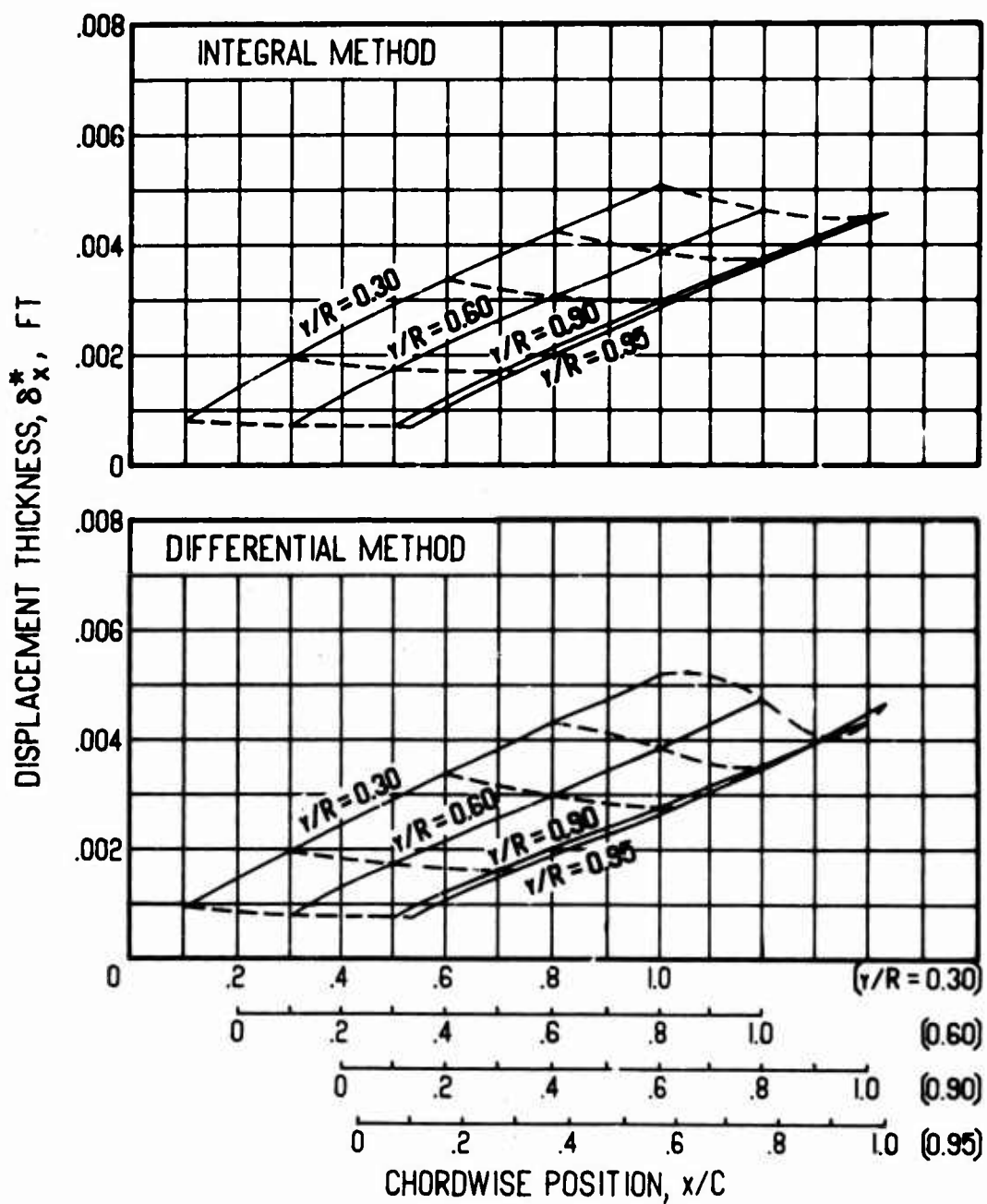
(a) Γ/h = +100 ft/sec

Figure 6. Displacement Thickness Versus Chordwise Position for Various Vortex Strengths, Blade Radius = 40 ft, Ω = 15 rad/sec, $dCp/d(x/C)$ = 0, Flat Surface.

91
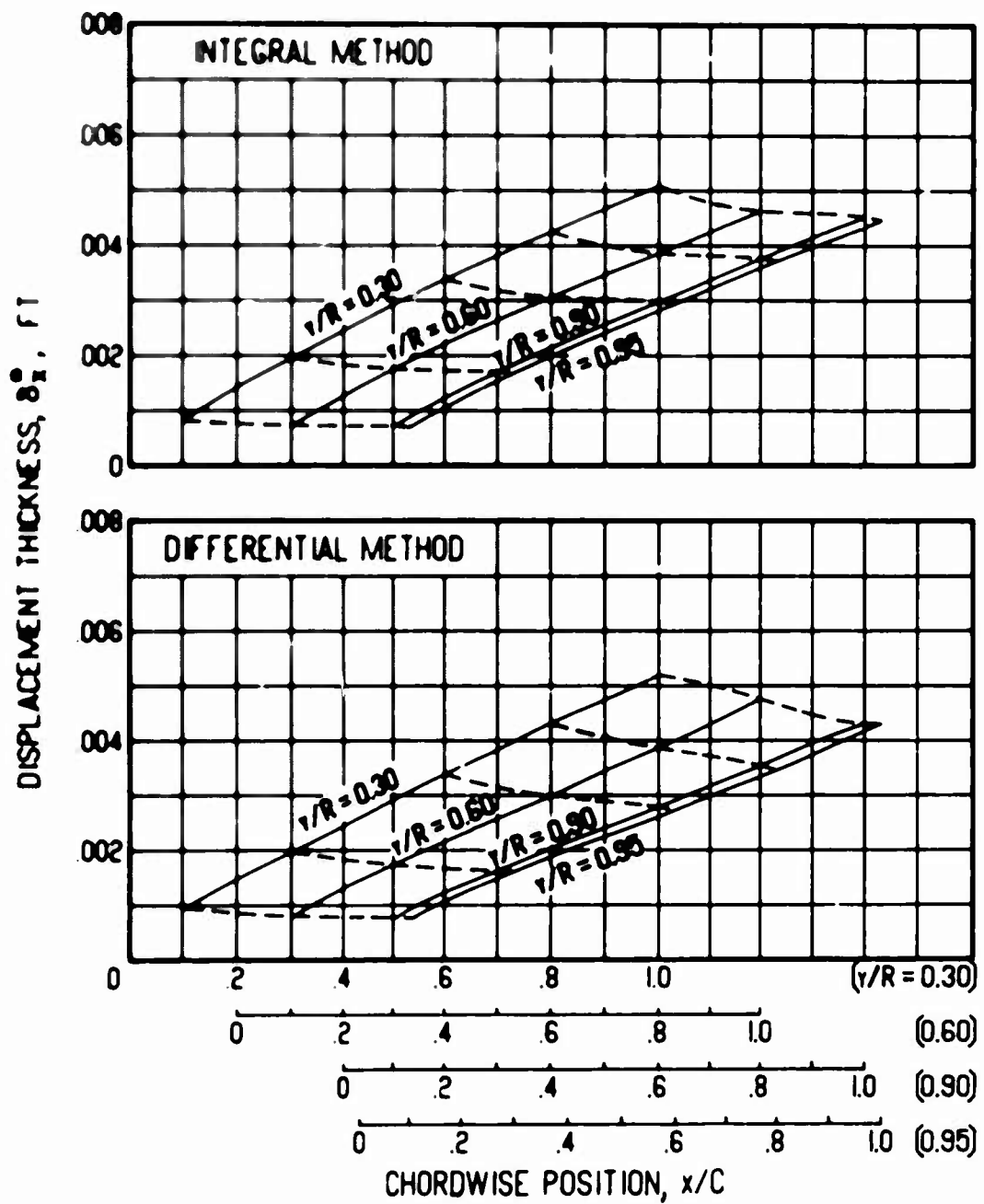
(b) $\Gamma/h = -100$ ft/sec

Figure 6. Continued.

92

(c) $\Gamma/h = +200$ ft/sec

Figure 6. Continued.

93
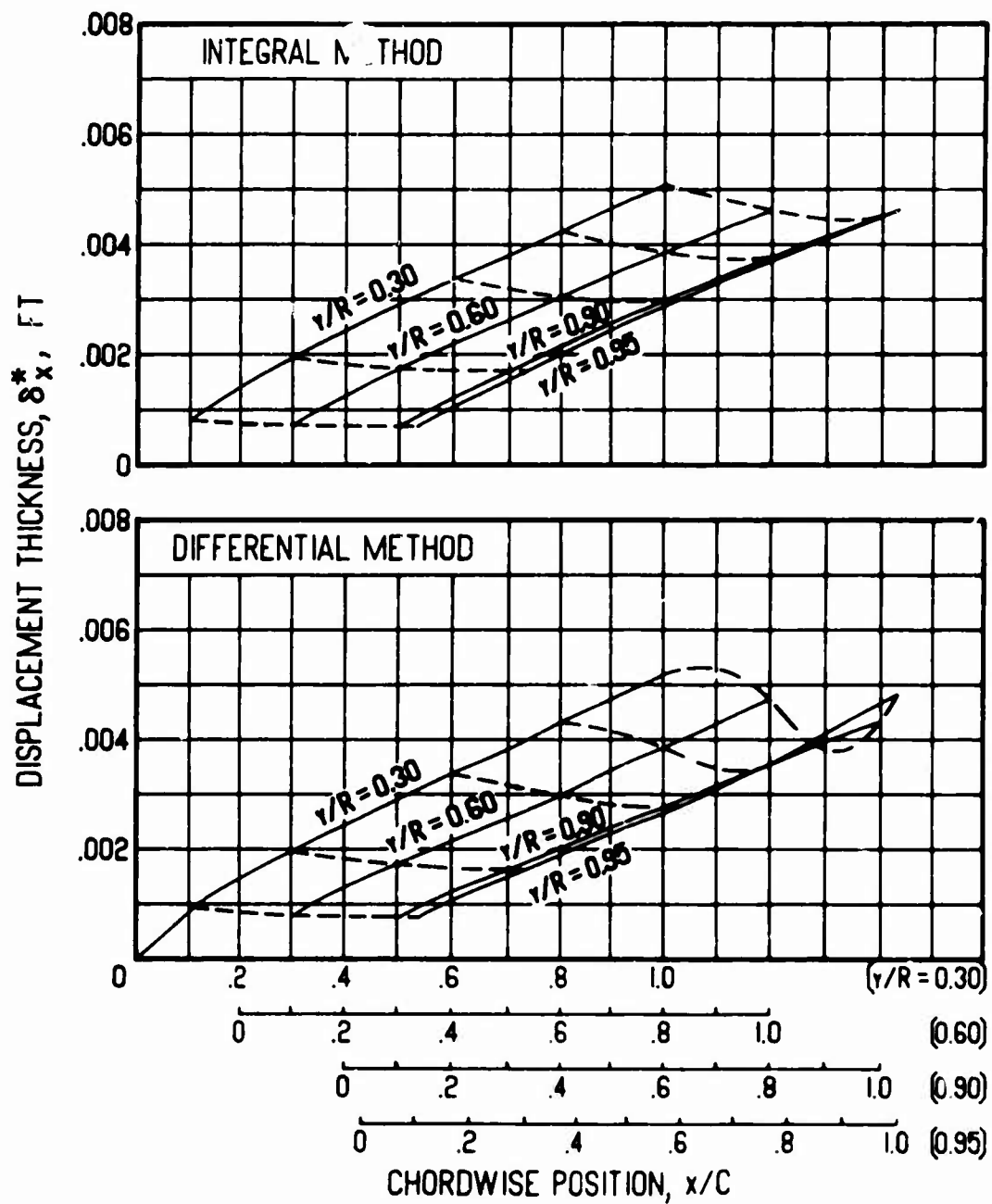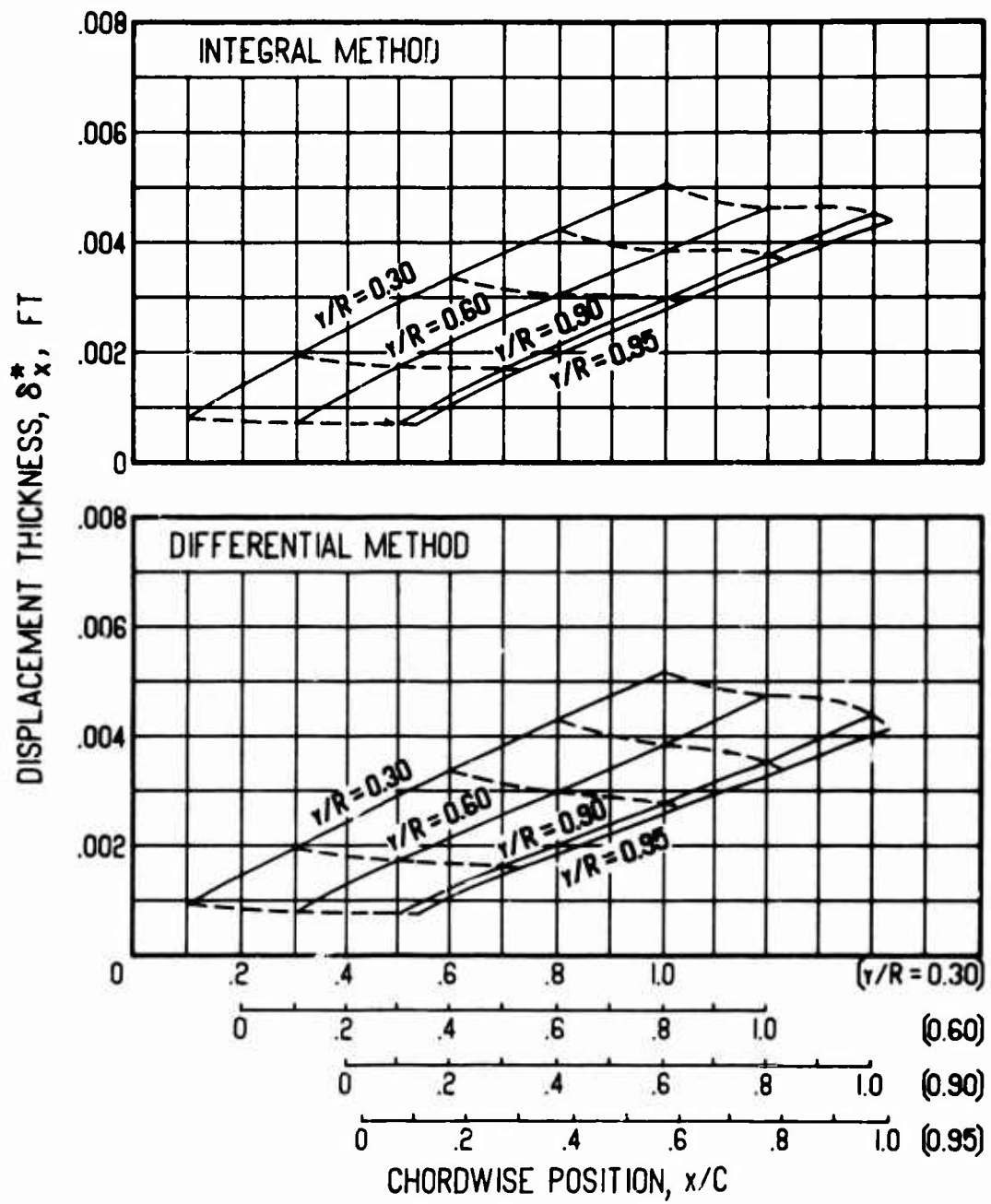
(d) $\Gamma/h = -200$ ft/sec

Figure 6. Concluded.
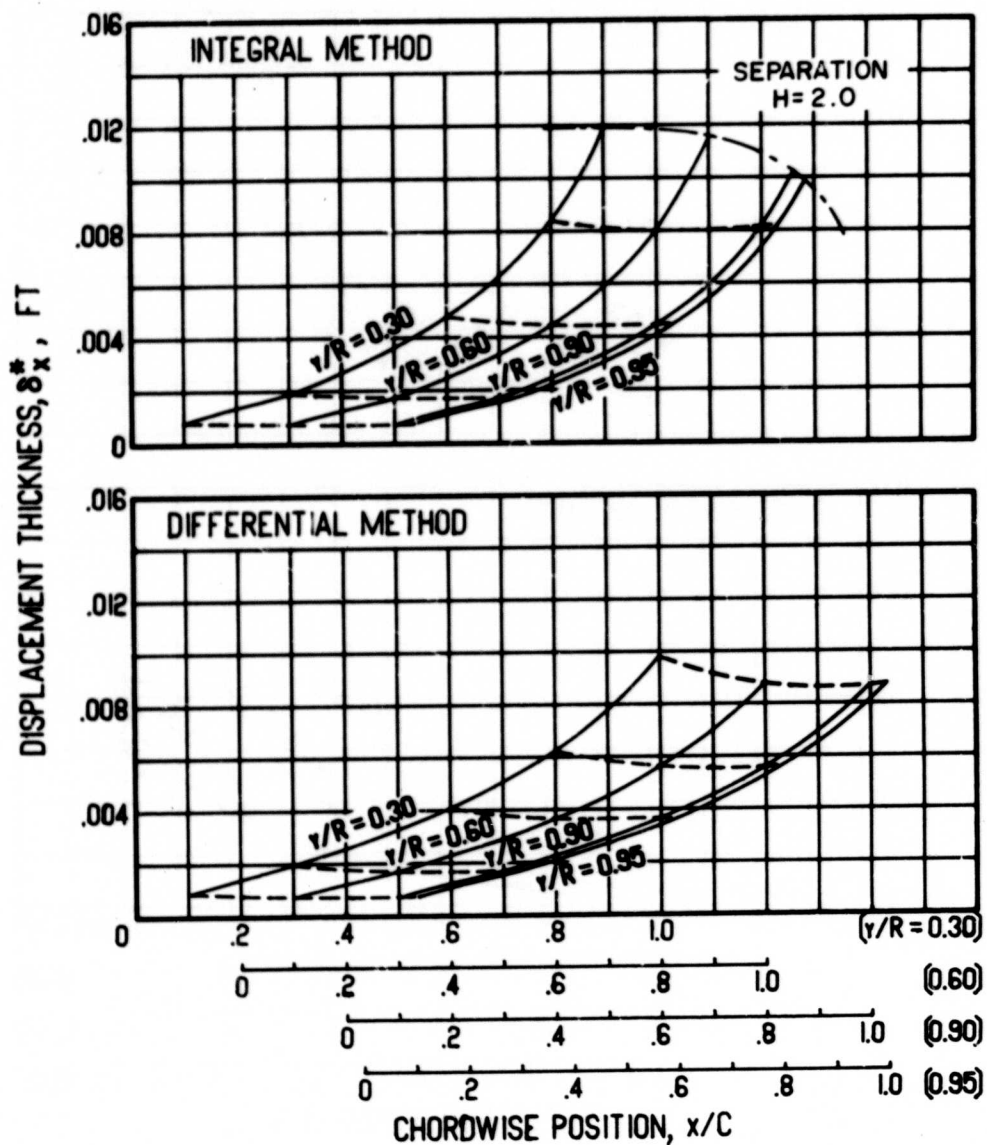
(a) $dCp/d(x/C) = 1$

Figure 7. Displacement Thickness Versus Chordwise Position for
Various Pressure Gradients, Blade Radius = 40 ft,
Ω = 15 rad/sec, Γ/h = 0 ft/sec, Flat Surface.

(b) dCp/d(x/C) = 2

Figure 7. Concluded.
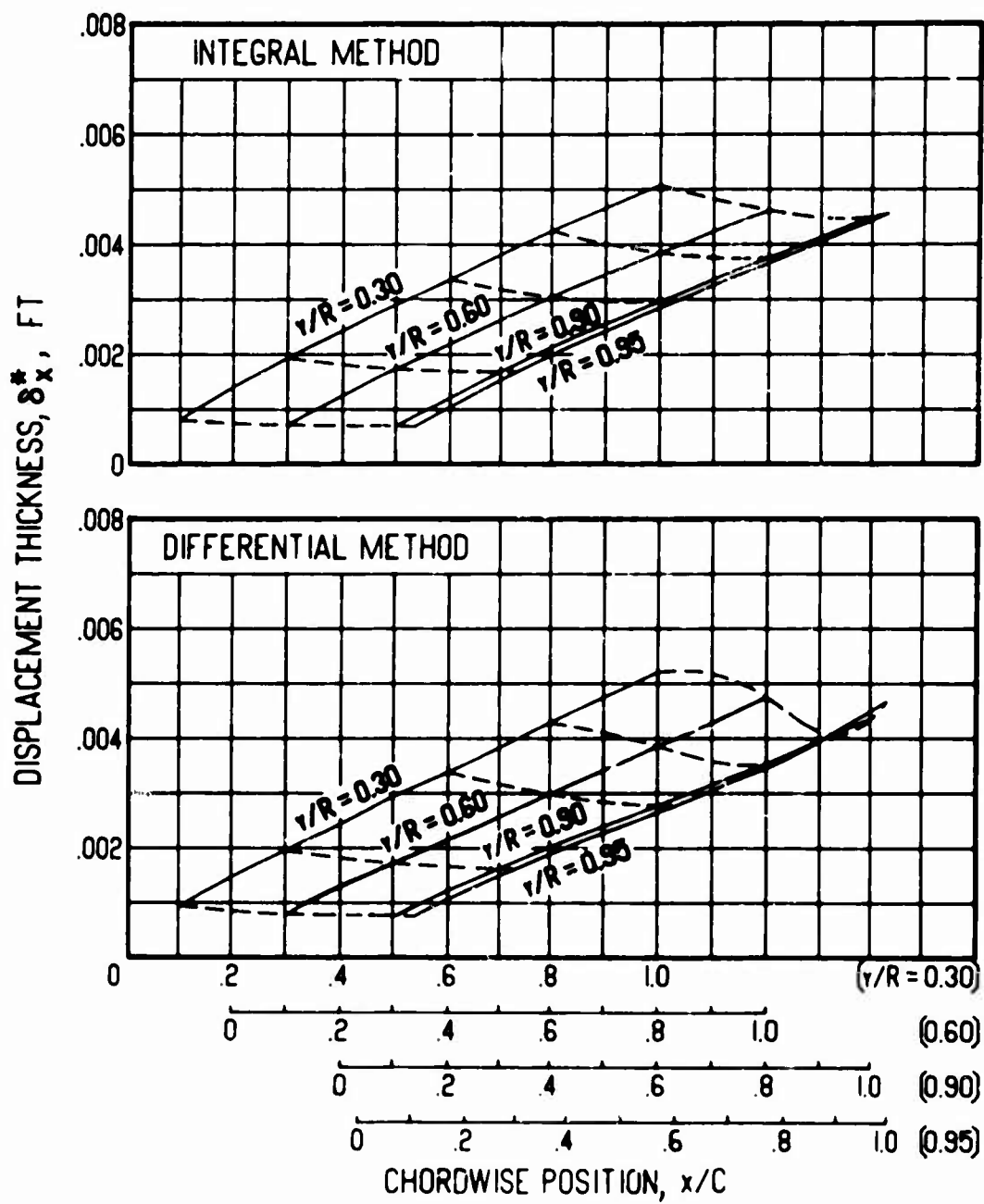
(a) $\Gamma/h = +100$ ft/sec

Figure 8. Displacement Thickness Versus Chordwise Position for
Various Vortex Strengths, Blade Radius = 40 ft,
$\Omega = 15$ rad/sec, $dCp/d(x/C) = 0$, Surface Radius of
Curvature = 8.25 ft.

97
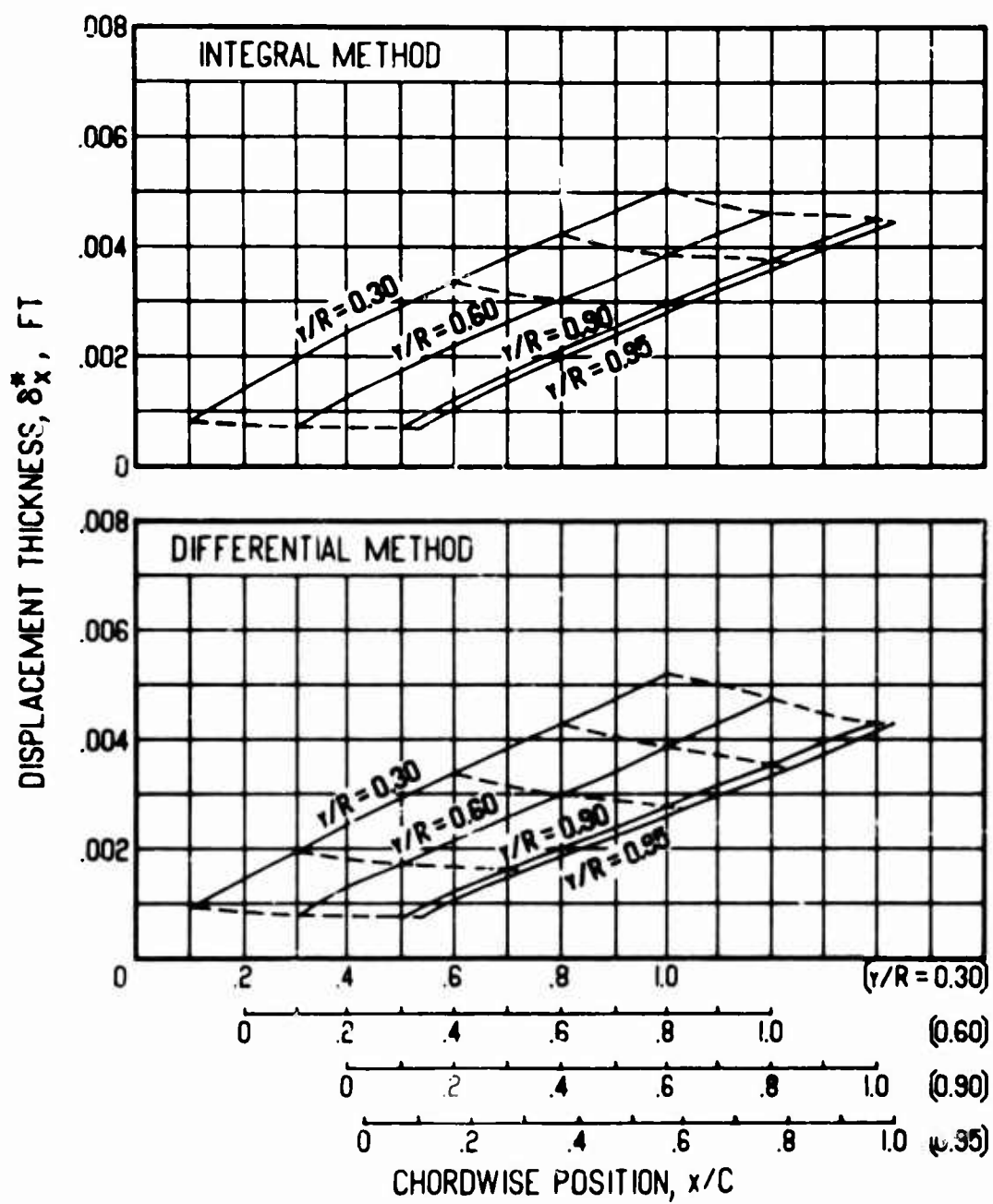
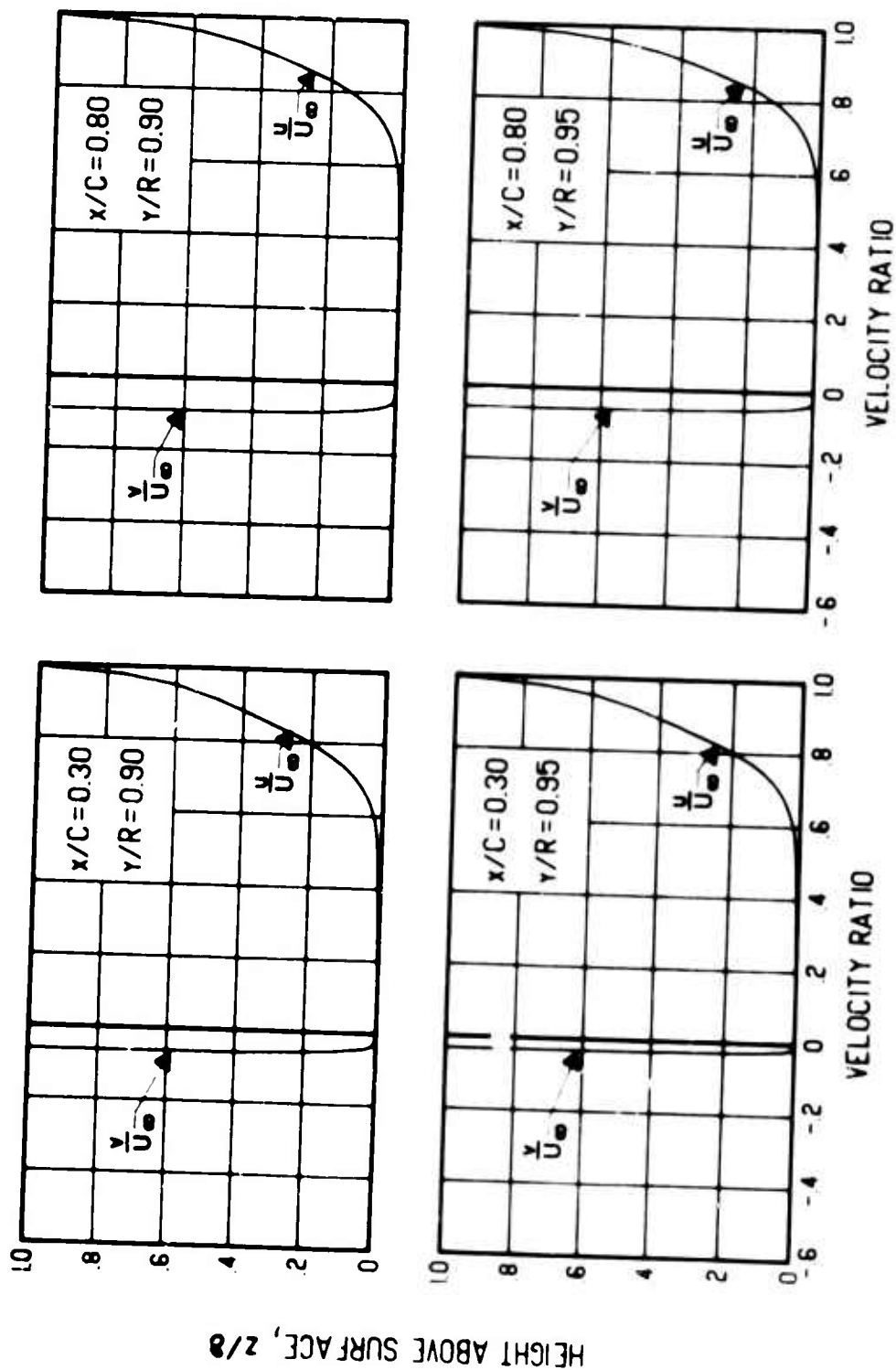(b) $\Gamma/h = -100$ ft/sec

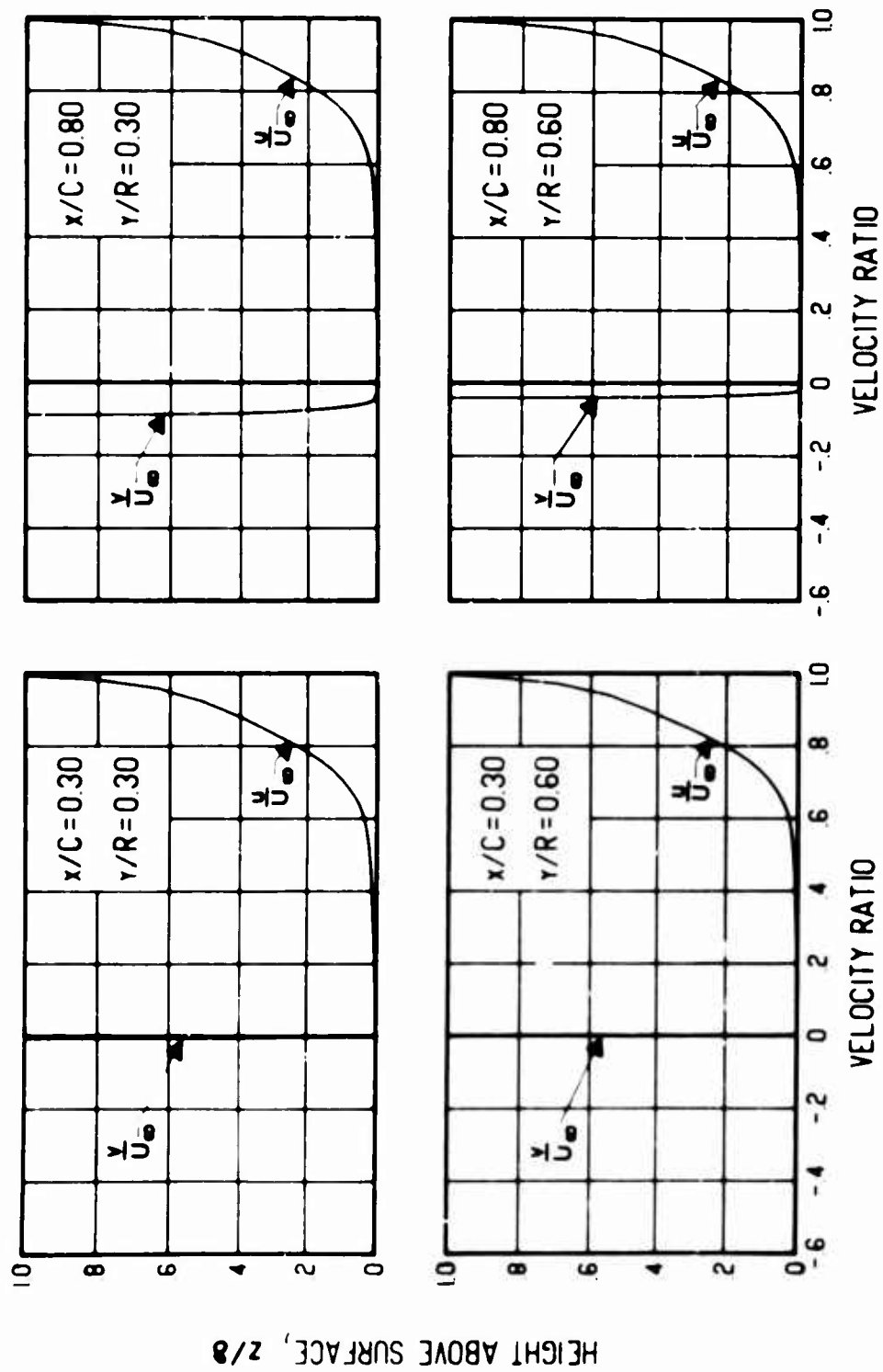Figure 8. Continued.

98

(c) $\Gamma/h = +200$ ft/sec

Figure 8. Continued.

99
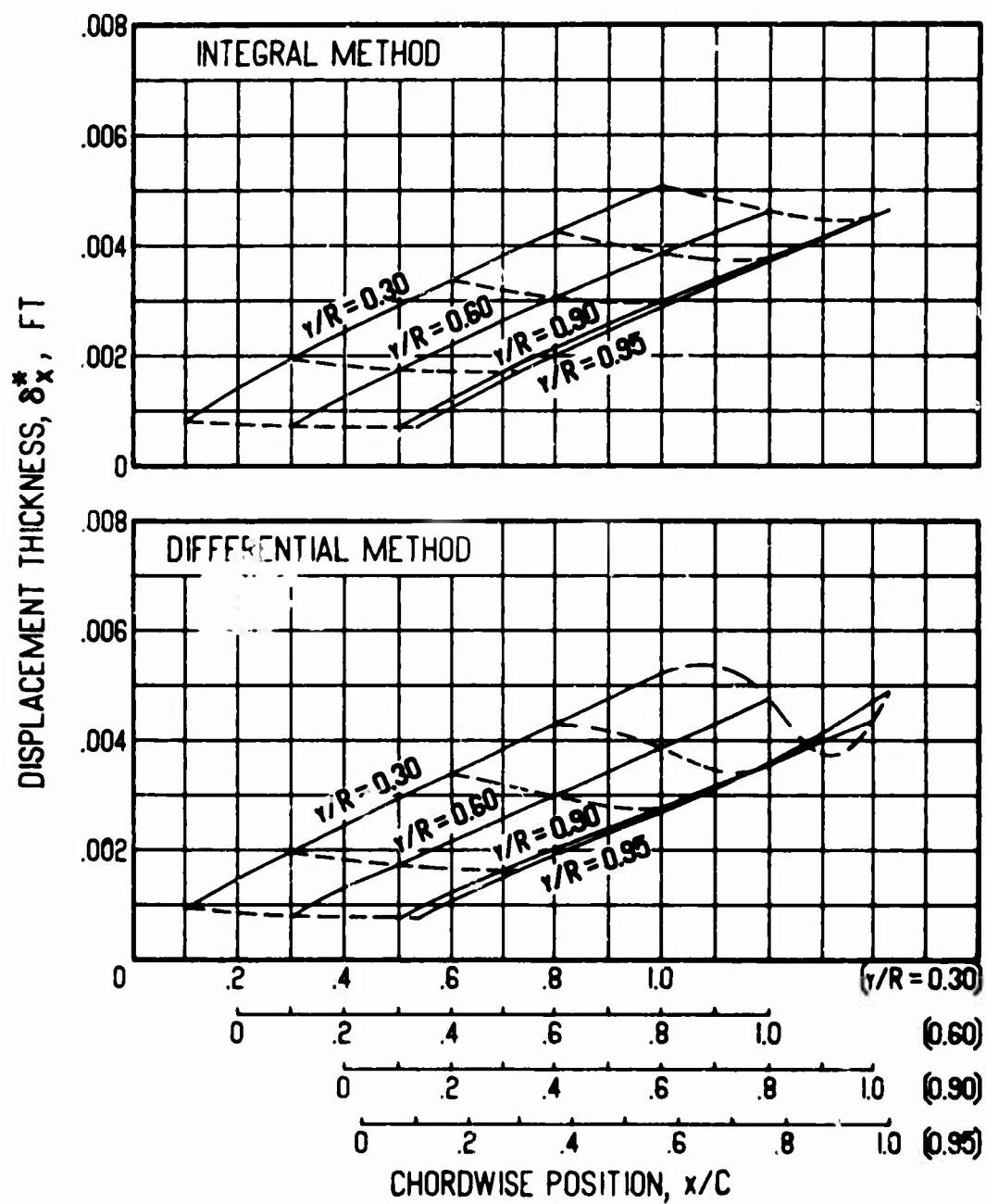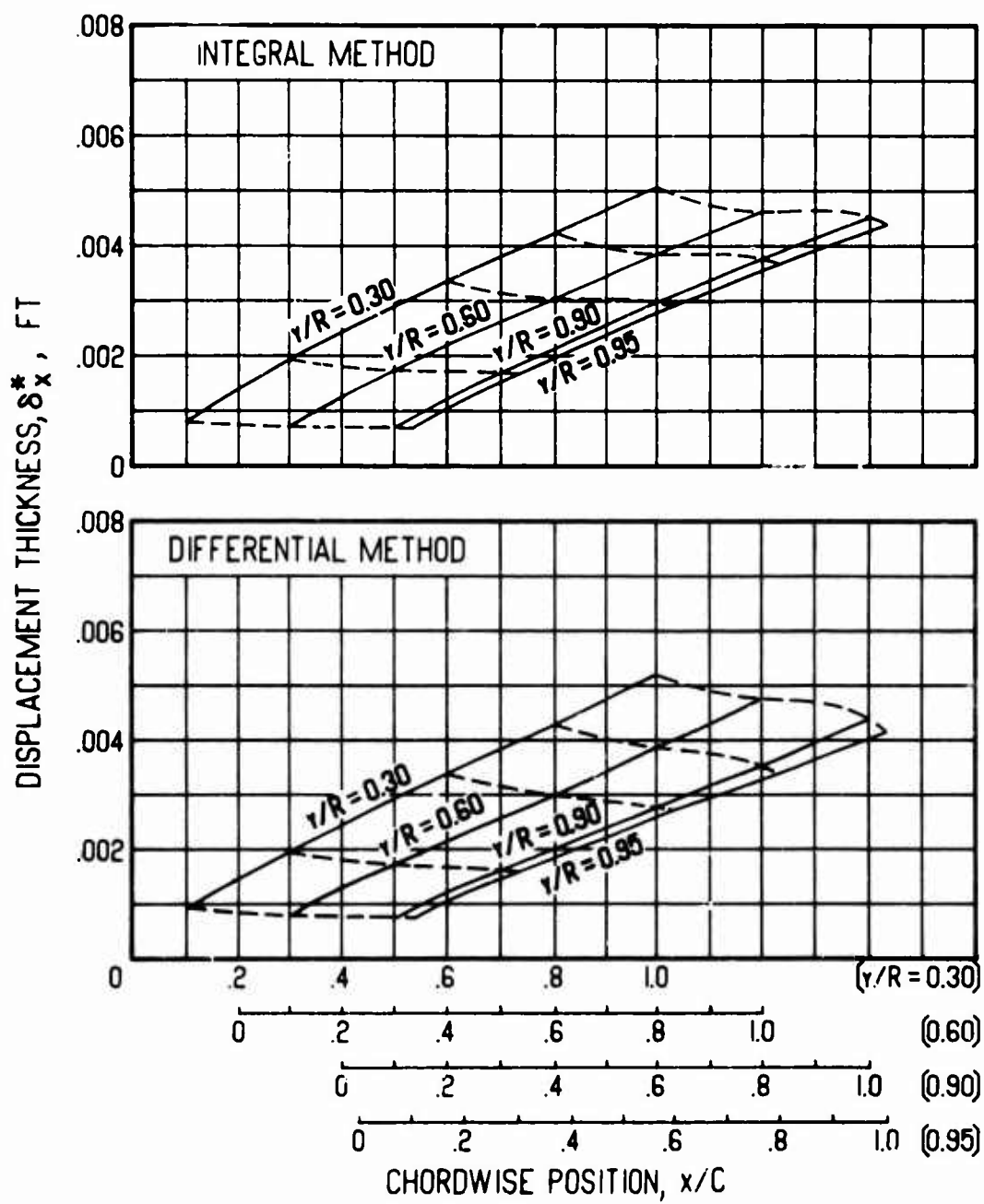
(d) $\Gamma/h = -200$ ft/sec

Figure 8.   Concluded.
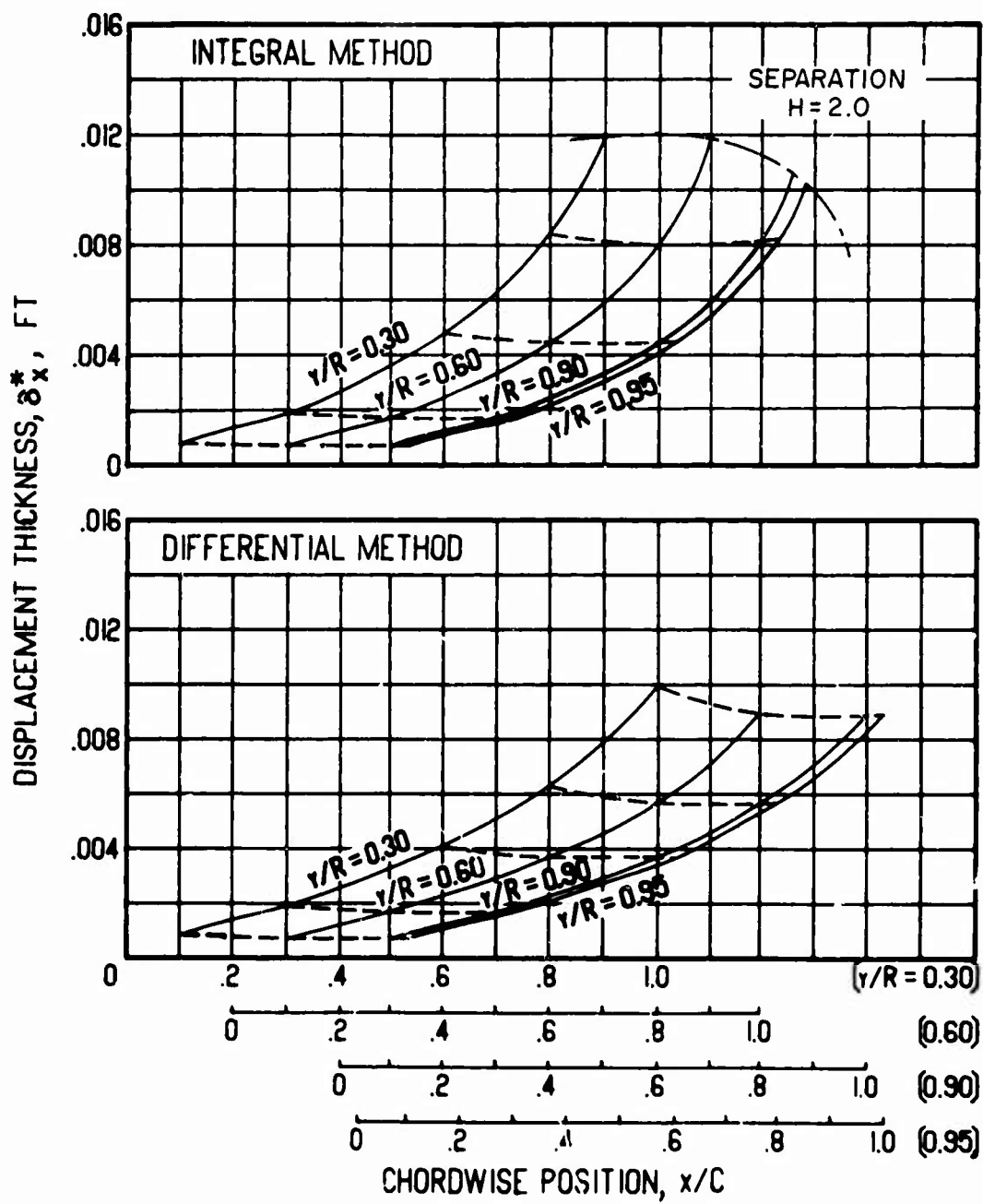
(a) $dCp/d(x/C) = 1$

Figure 9. Displacement Thickness Versus Chordwise Position for
Various Pressure Gradients, Blade Radius = 40 ft,
Ω = 15 rad/sec, Γ/h = 0 ft/sec, Surface Radius of
Curvature = 8.25 ft.

101
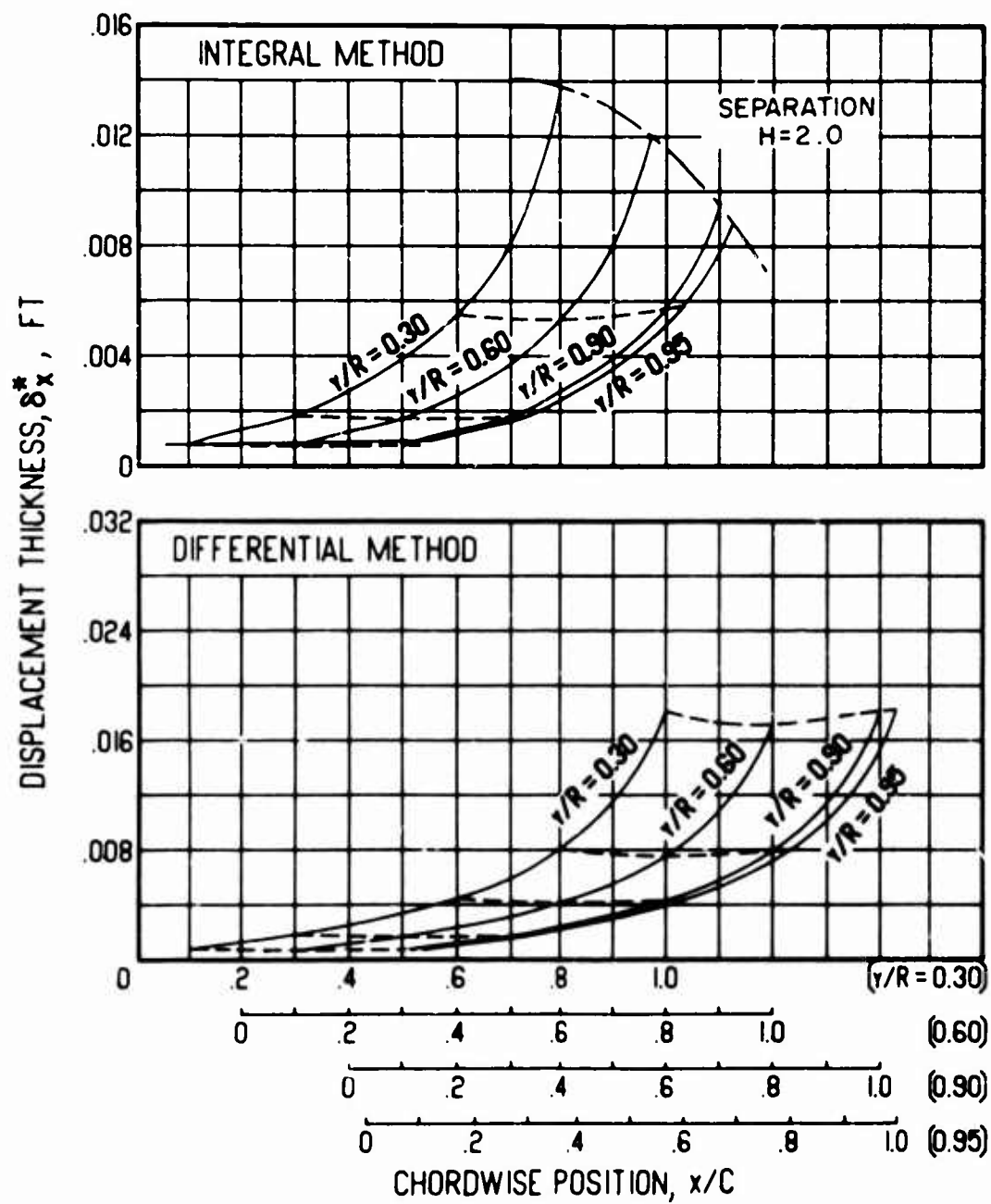
(b) $dCp/d(x/C) = 2$

Figure 9. Concluded.
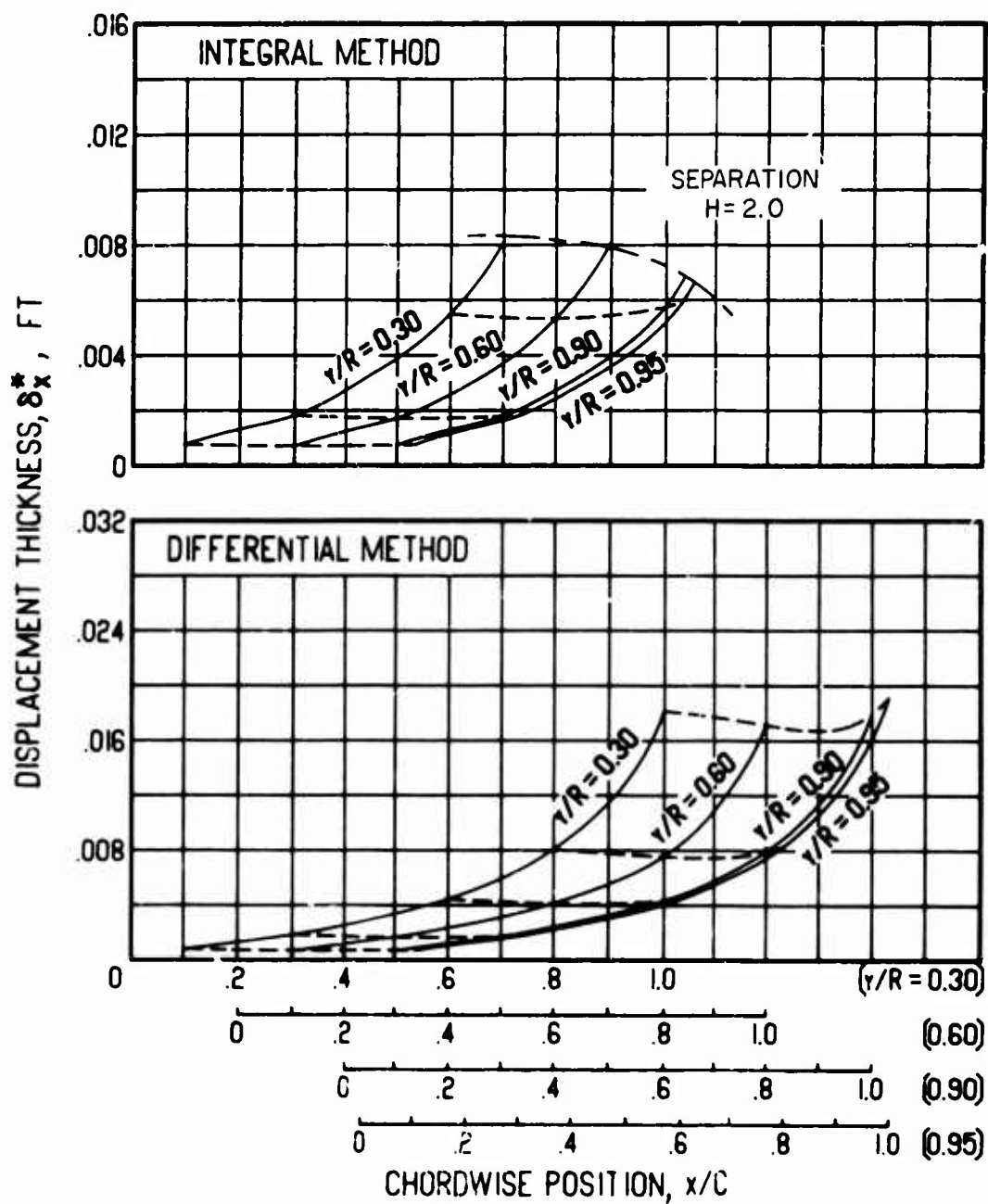
(a) Γ/h = +200 ft/sec

Figure 10. Displacement Thickness Versus Chordwise Position for
Various Vortex Strengths, Blade Radius = 40 ft,
Ω = 15 rad/sec, dCp/d(x/C) = 2, Surface Radius of
Curvature = 8.25 ft.

103
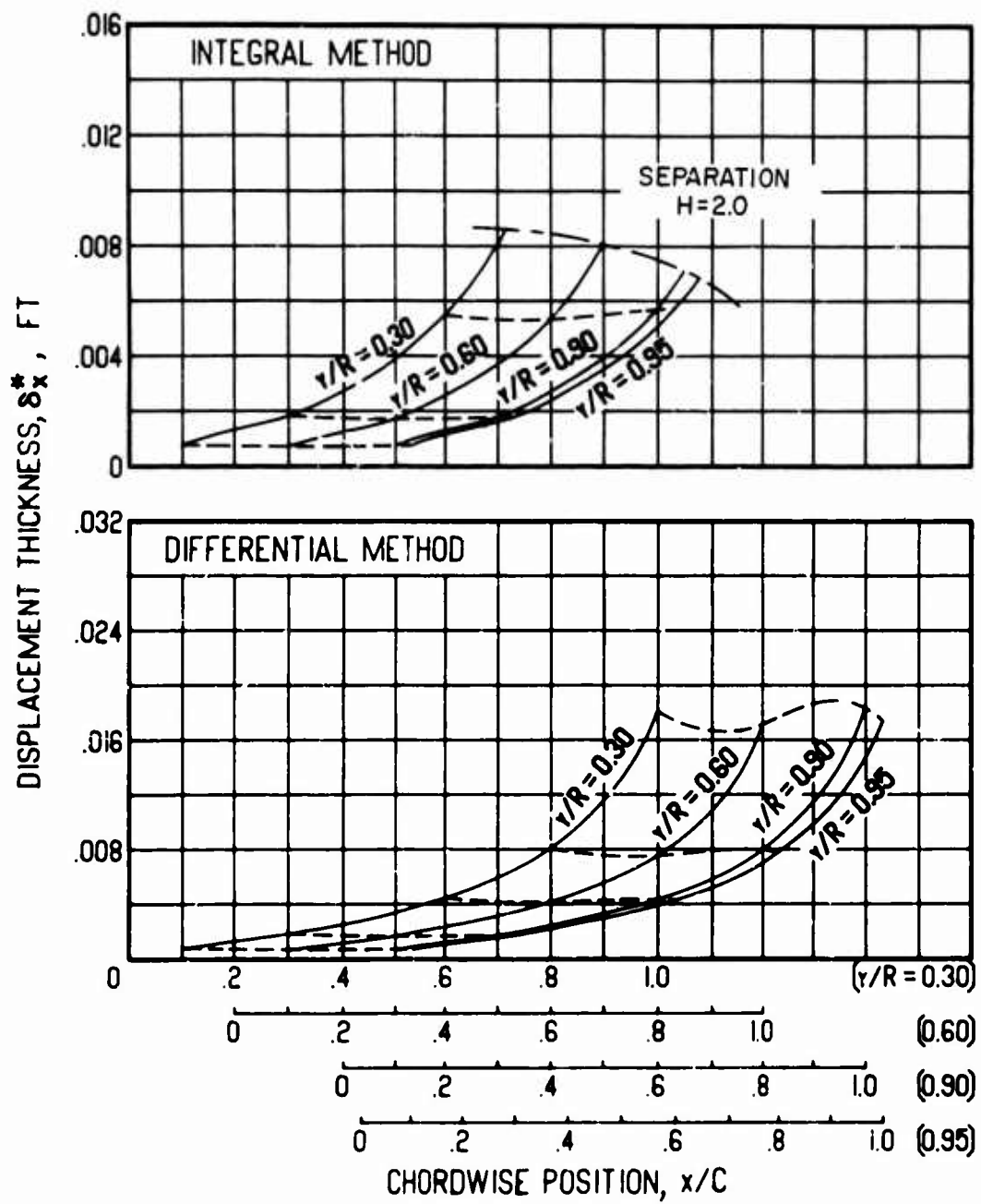
(b) $\Gamma/h = -200$ ft/sec

Figure 10. Concluded.

104
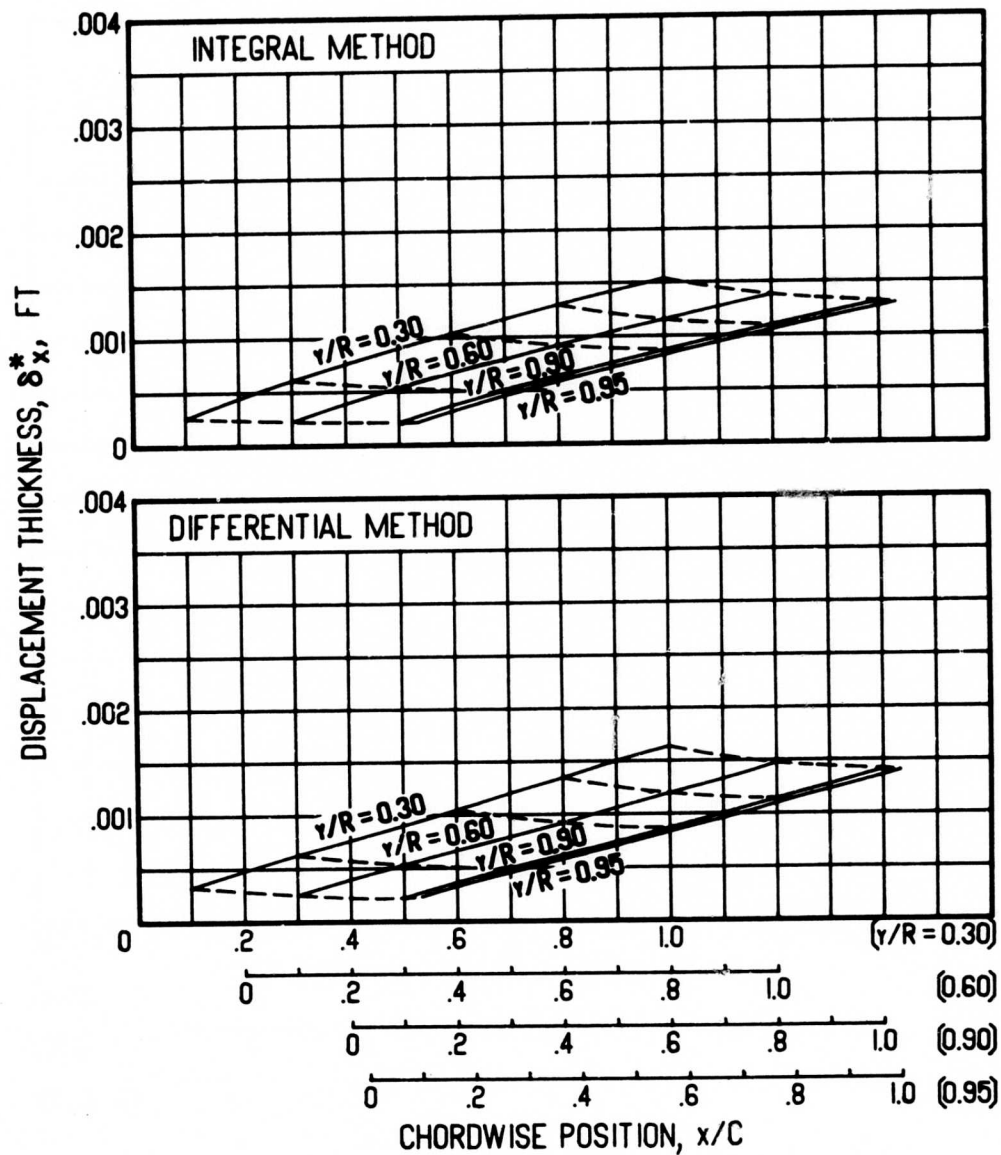
(a) $\Omega = 40$ rad/sec

Figure 11. Displacement Thickness Versus Chordwise Position for Various Angular Velocities, Blade Radius = 10 ft, $\Gamma/h = 0$ ft/sec, $dCp/d(x/C) = 0$, Flat Surface.

105
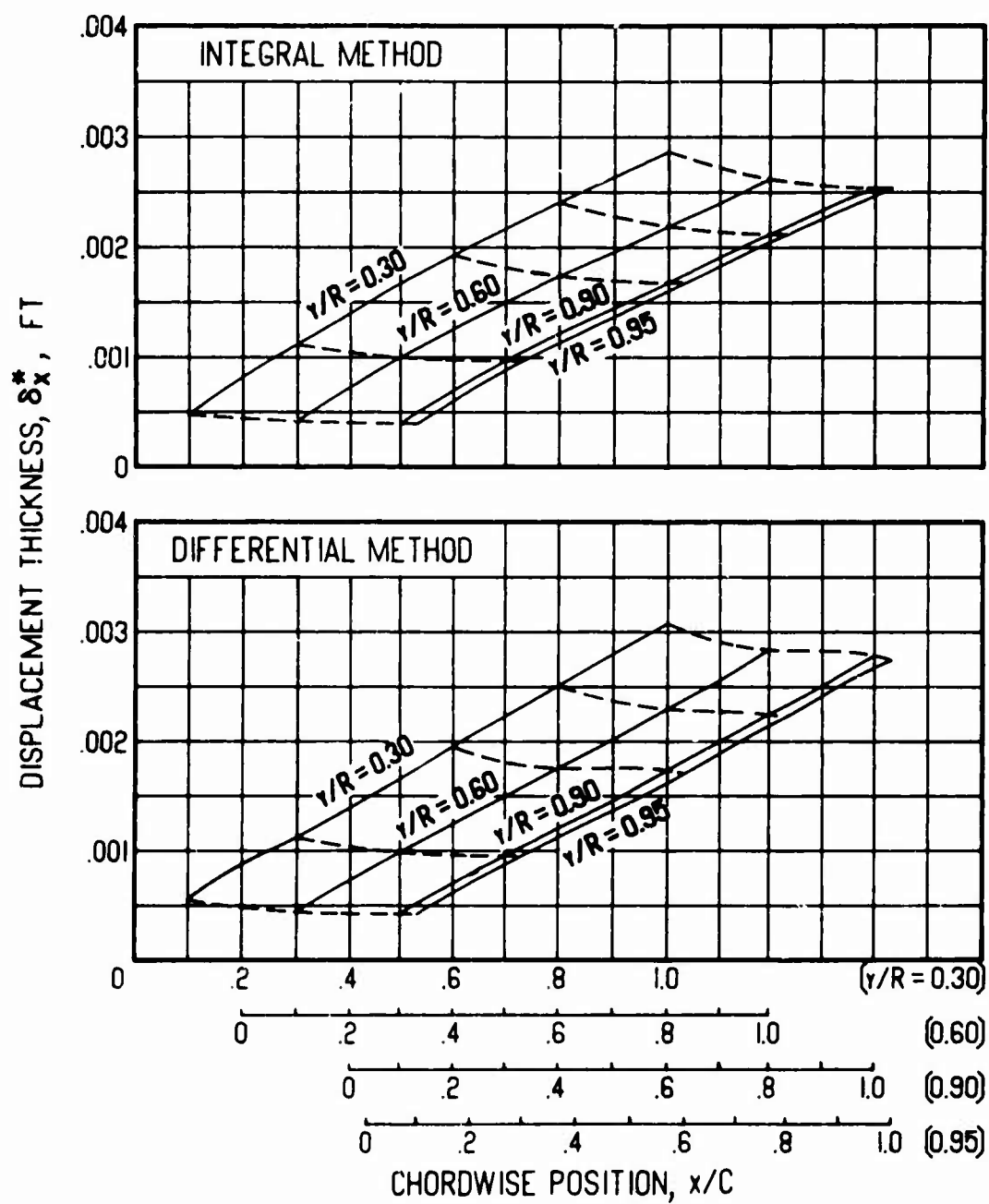
(b) $\Omega = 60$ rad/sec

Figure 11. Continued.
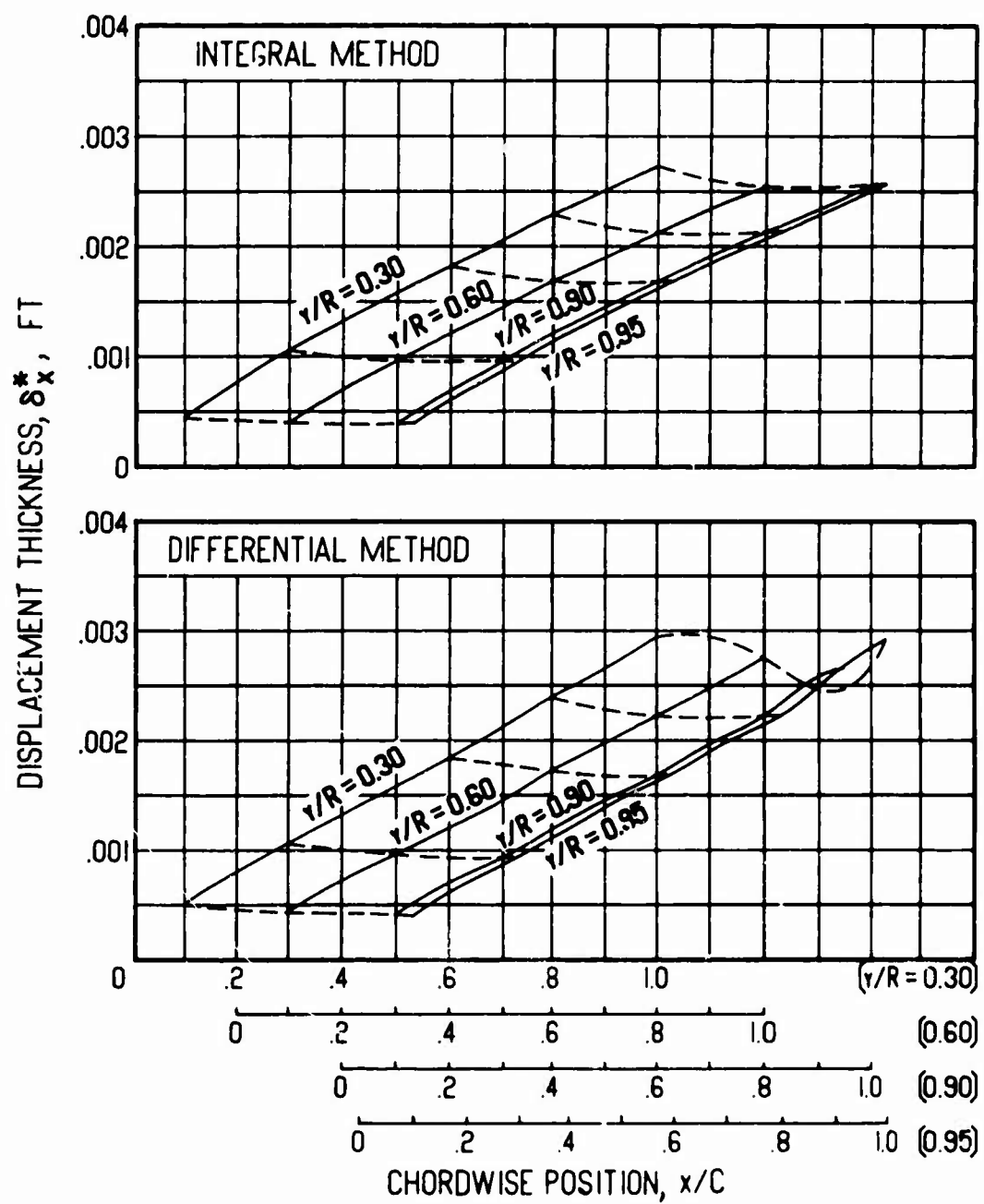
(c) $\Omega = 80$ rad/sec

Figure 11. Concluded.

107
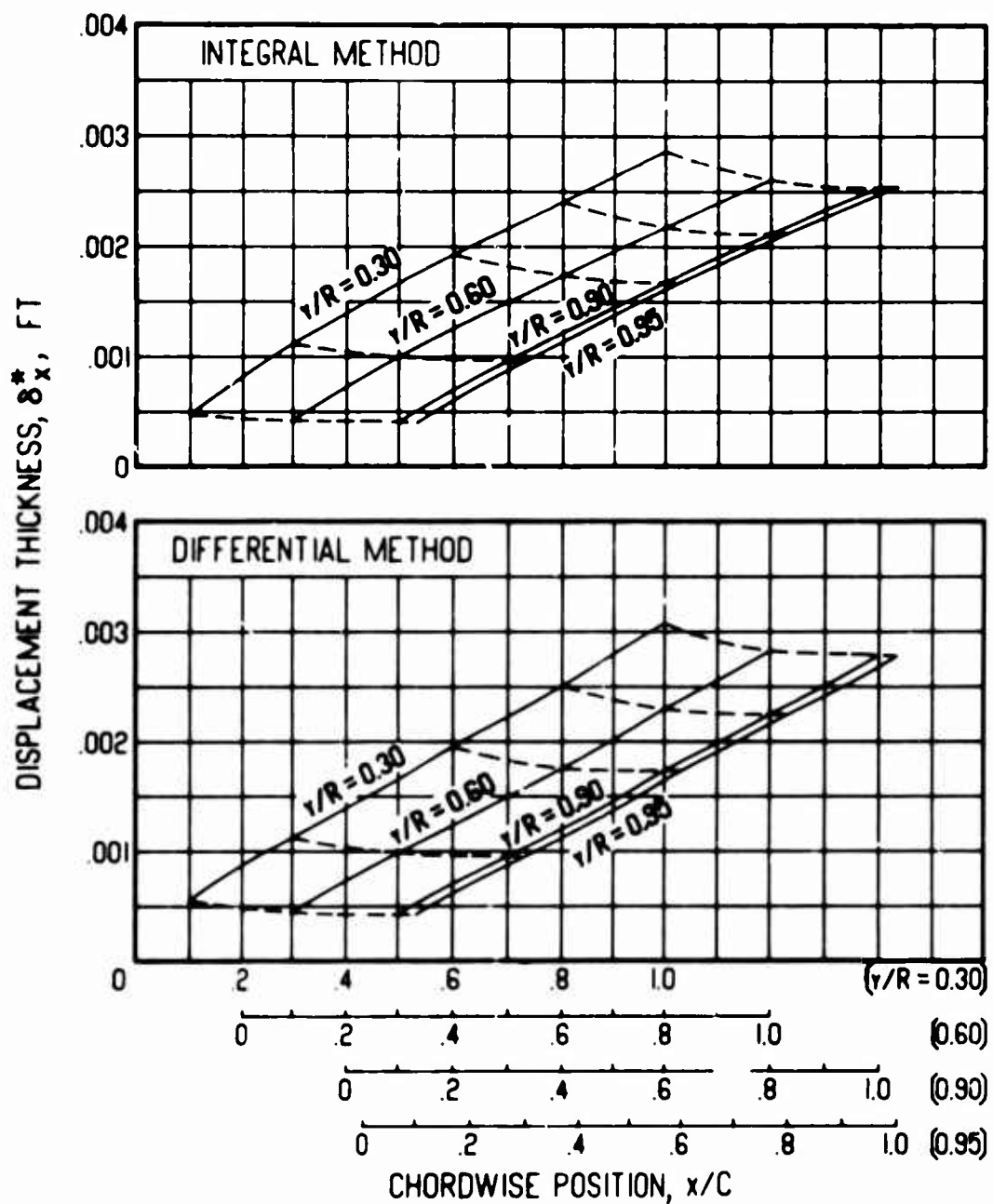
(a) $\Gamma/h = +25$ ft/sec

Figure 12. Displacement Thickness Versus Chordwise Position for
Various Vortex Strengths, Blade Radius = 10 ft,
$\Omega = 60$ rad/sec, $dCp/d(x/C) = 0$, Flat Surface.

108
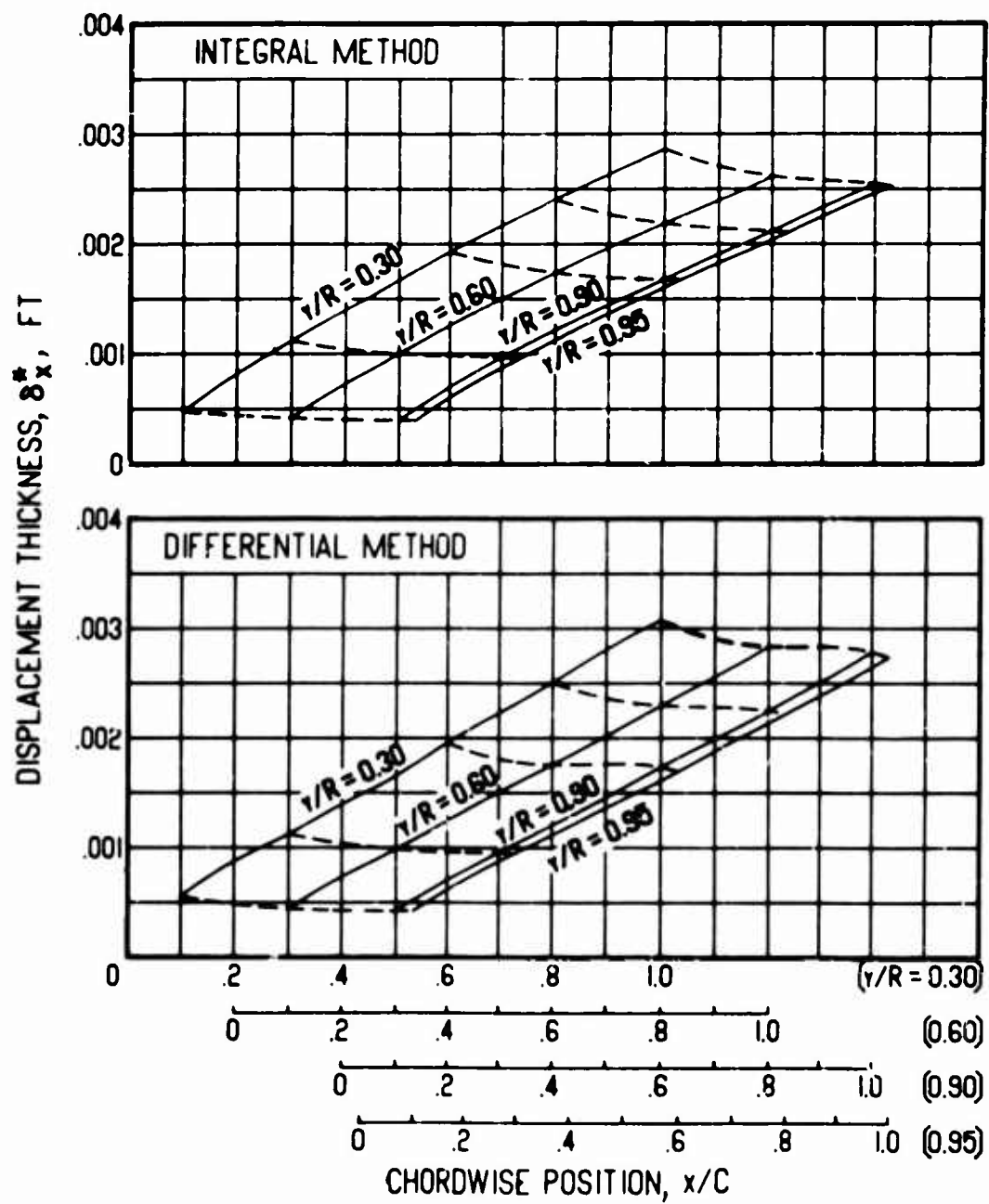
(b) $\Gamma/h = -25$ ft/sec

Figure 12. Continued.

(c) Γ/h = +50 ft/sec

Figure 12. Continued.

110
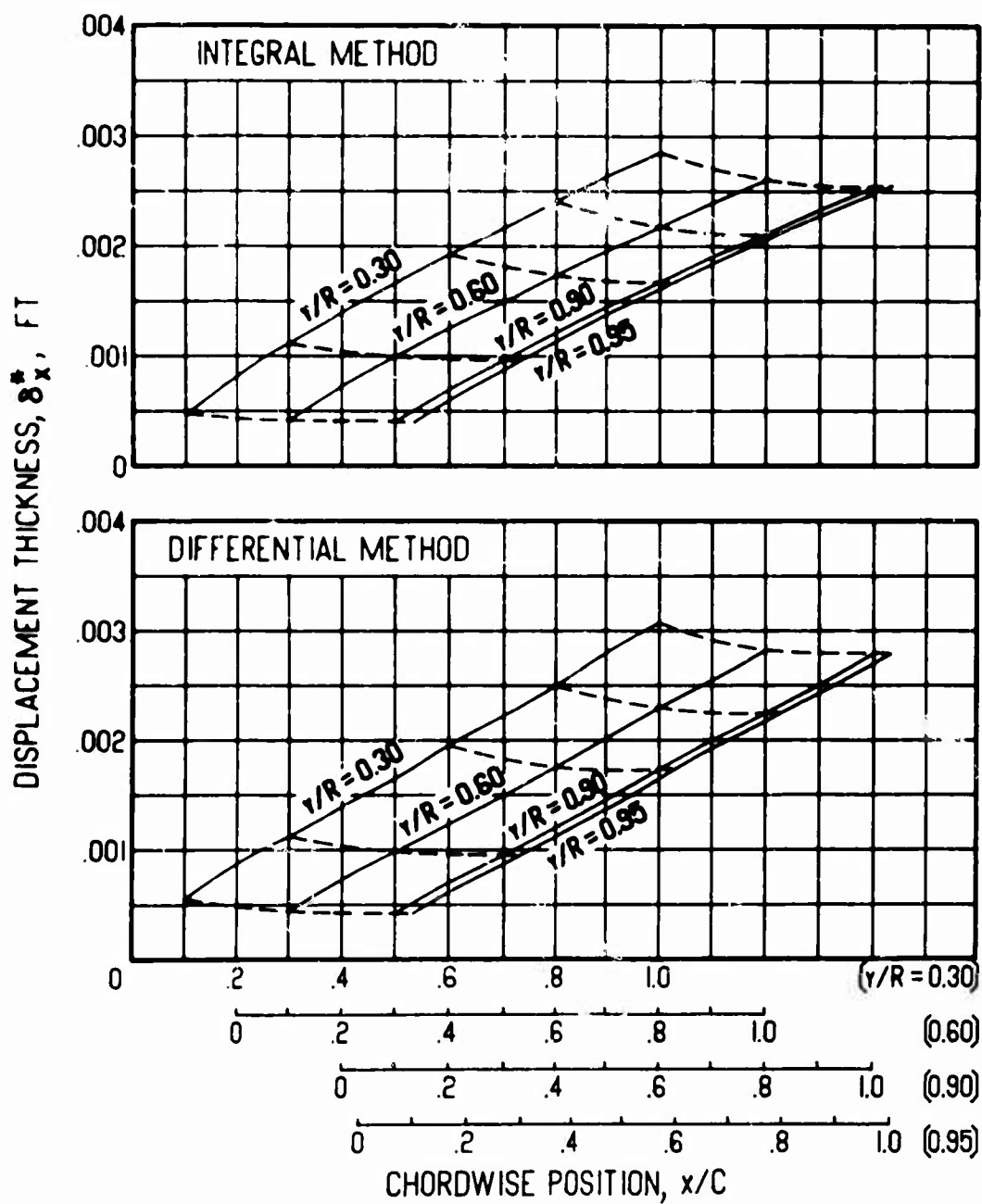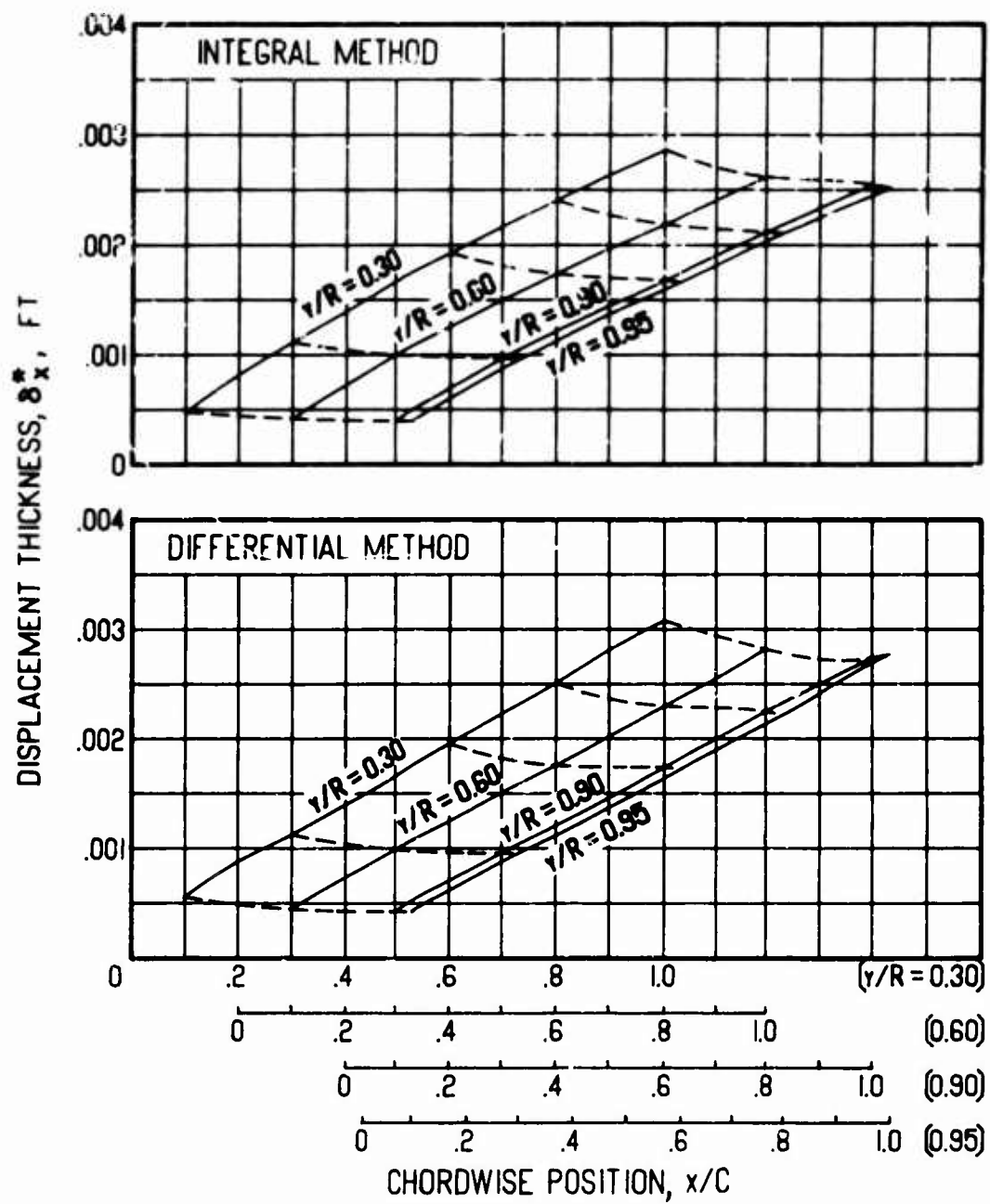
(d) $\Gamma/h = -50$ ft/sec

Figure 12. Concluded.
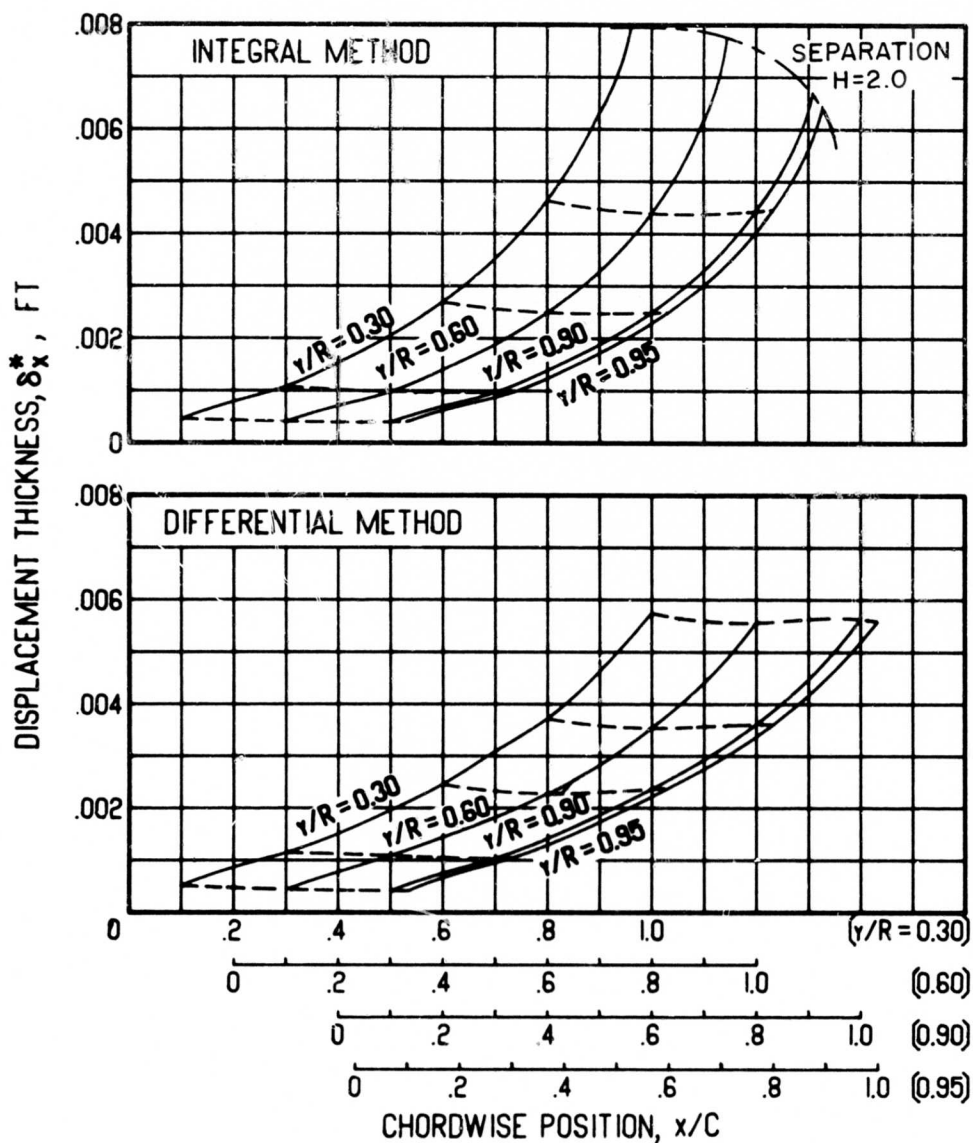
(a) $dCp/d(x/C) = 1$

Figure 13.   Displacement Thickness Versus Chordwise Position for
Various Pressure Gradients, Blade Radius = 10 ft,
$\Omega = 60$ rad/sec, $\Gamma/h = 0$ ft/sec, Flat Surface.

112
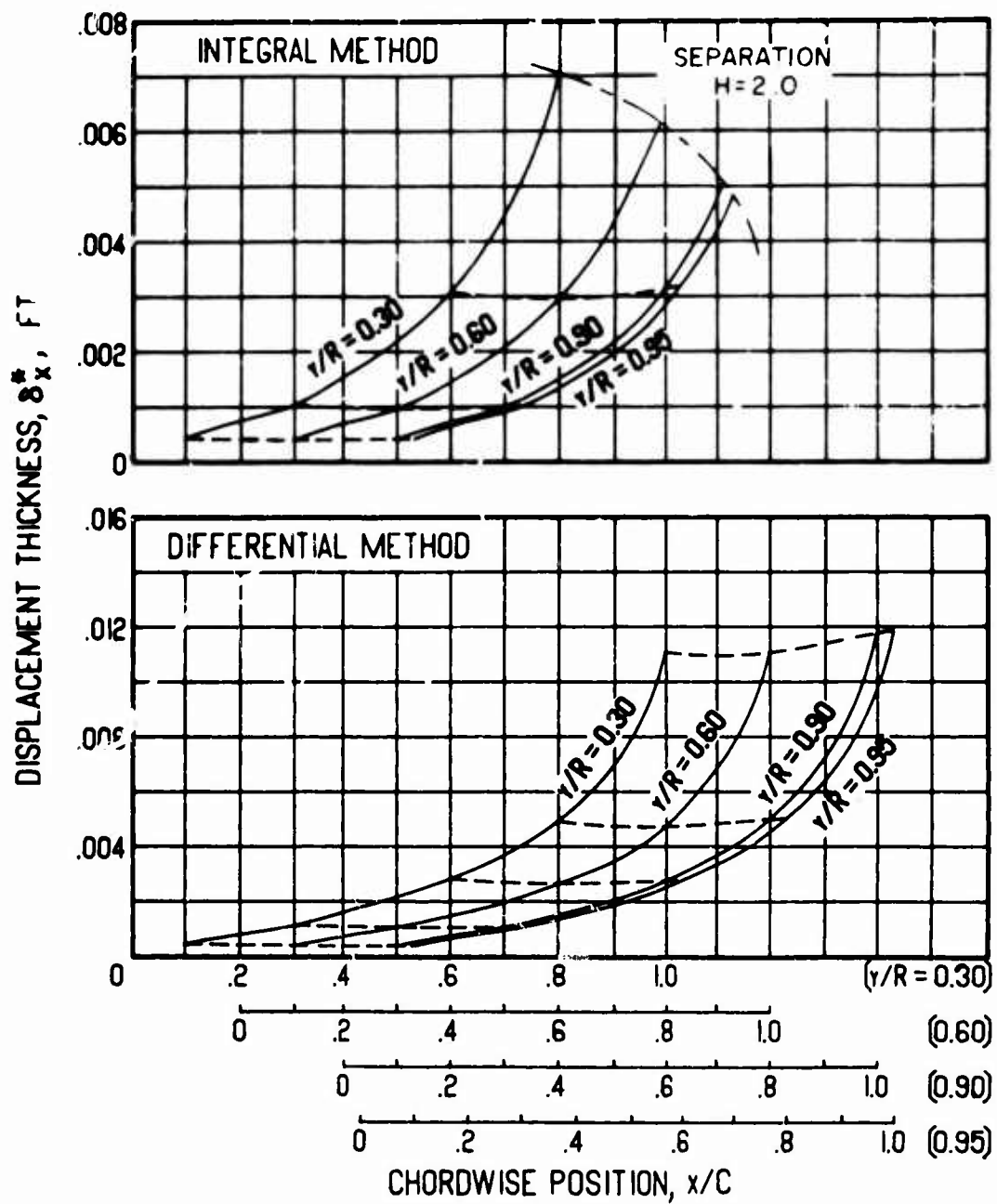
(b) $dCp/d(x/C) = 2$

Figure 13. Concluded.

113
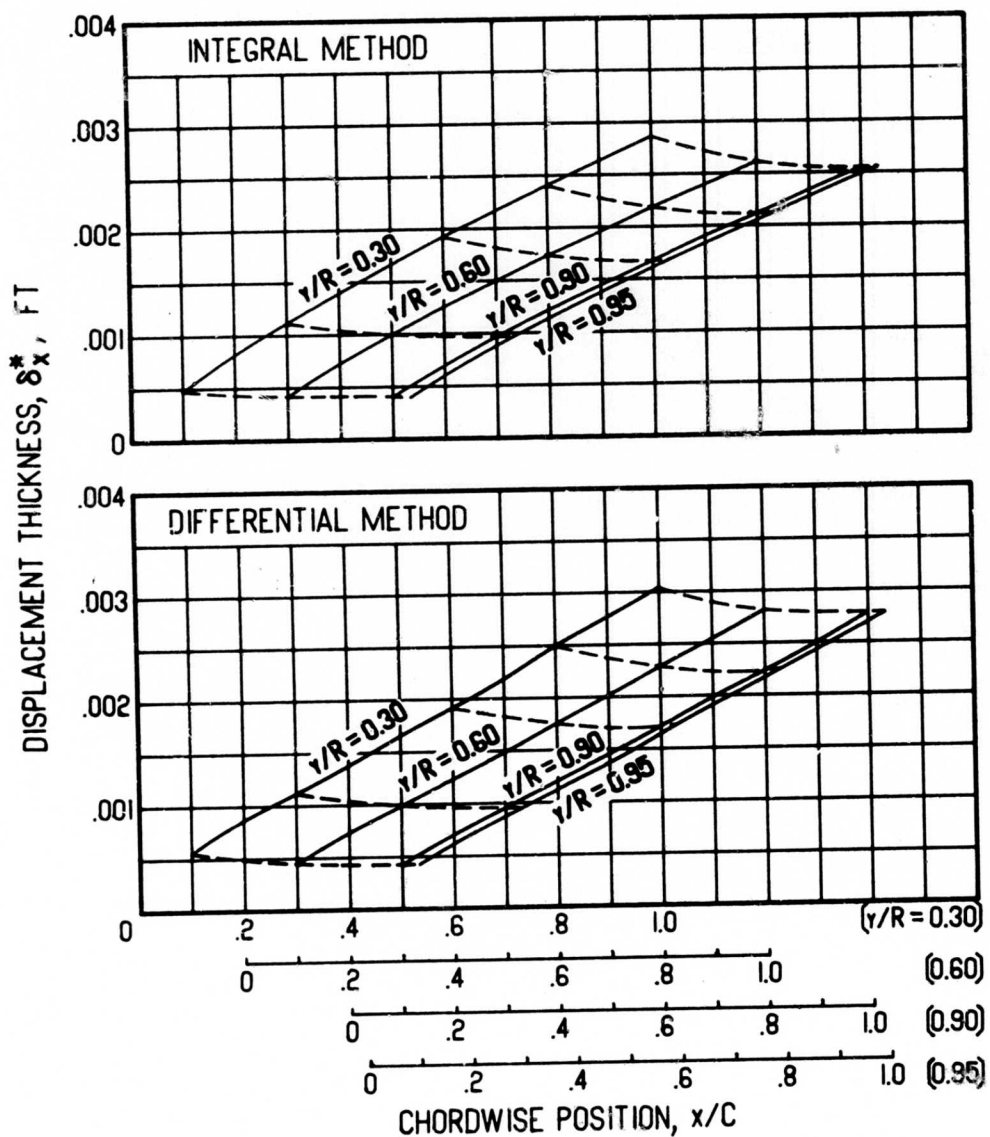
(a) $\Gamma/h = +25$ ft/sec

Figure 14. Displacement Thickness Versus Chordwise Position for
Various Vortex Strengths, Blade Radius = 10 ft,
$\Omega = 60$ rad/sec, $dCp/d(x/C) = 0$, Surface Radius of
Curvature = 4.125 ft.

114
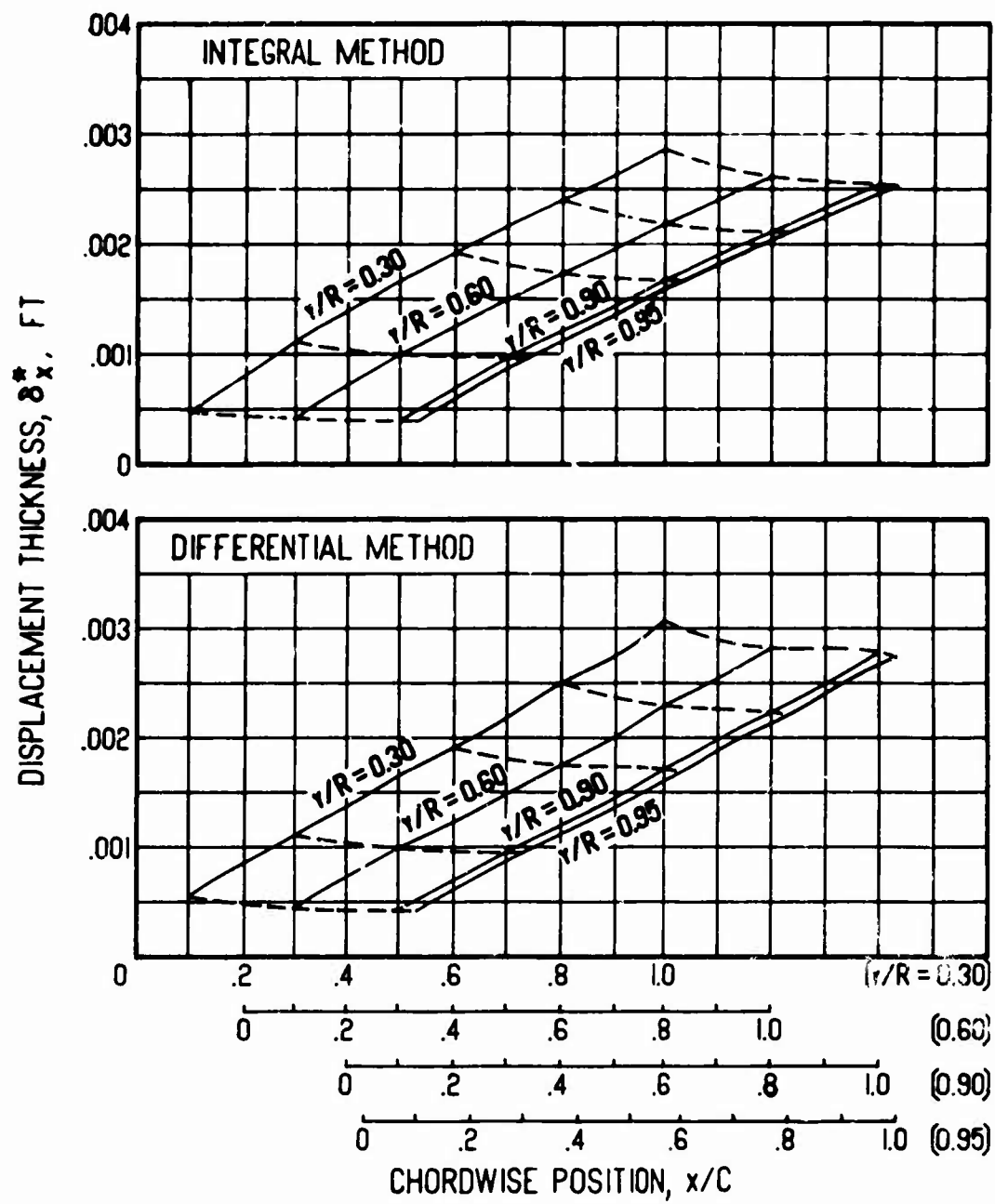
(b) $\Gamma/h = -25$ ft/sec

Figure 14. Continued.
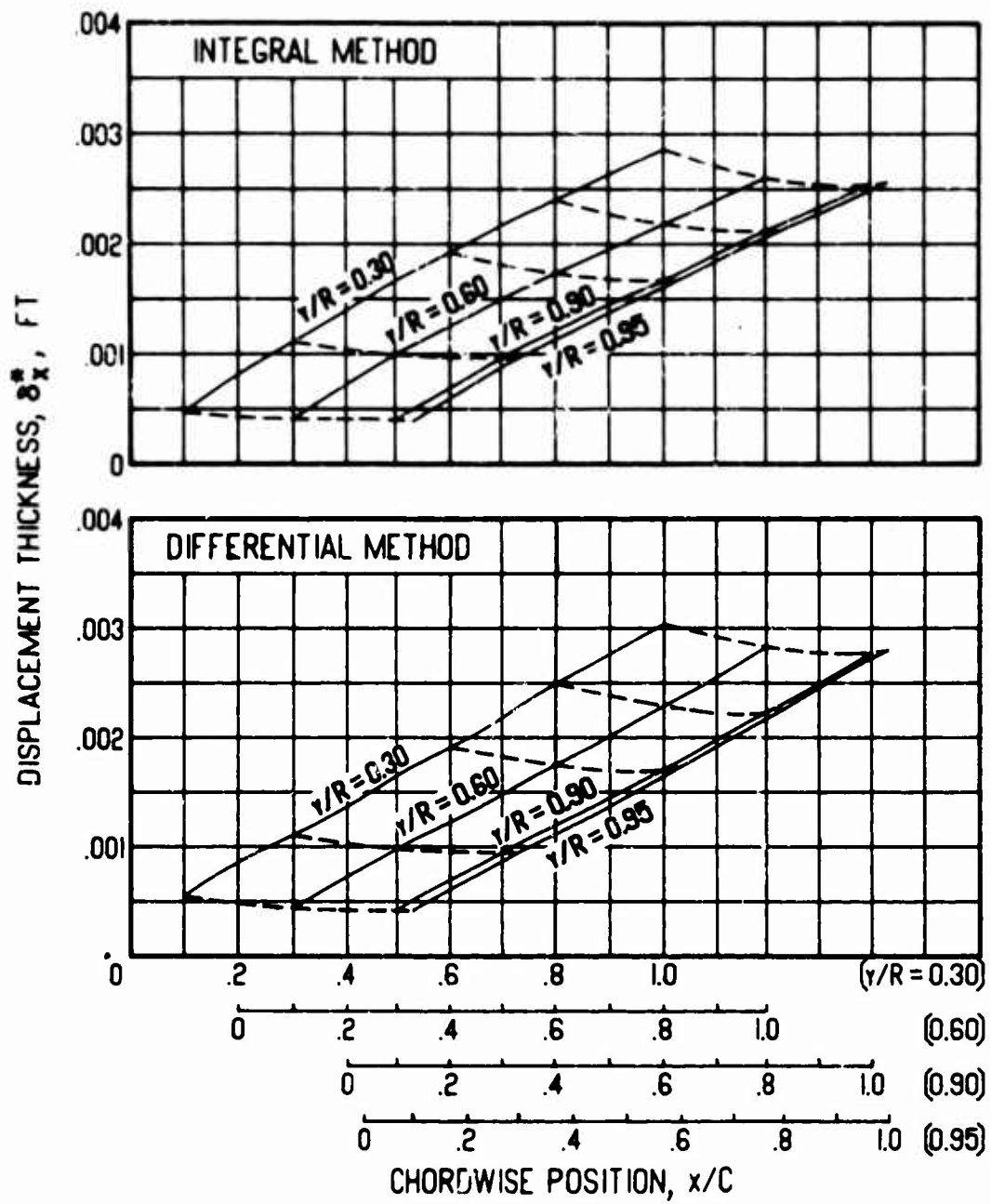
(c) $\Gamma/h = +50$ ft/sec

Figure 14. Continued.

116
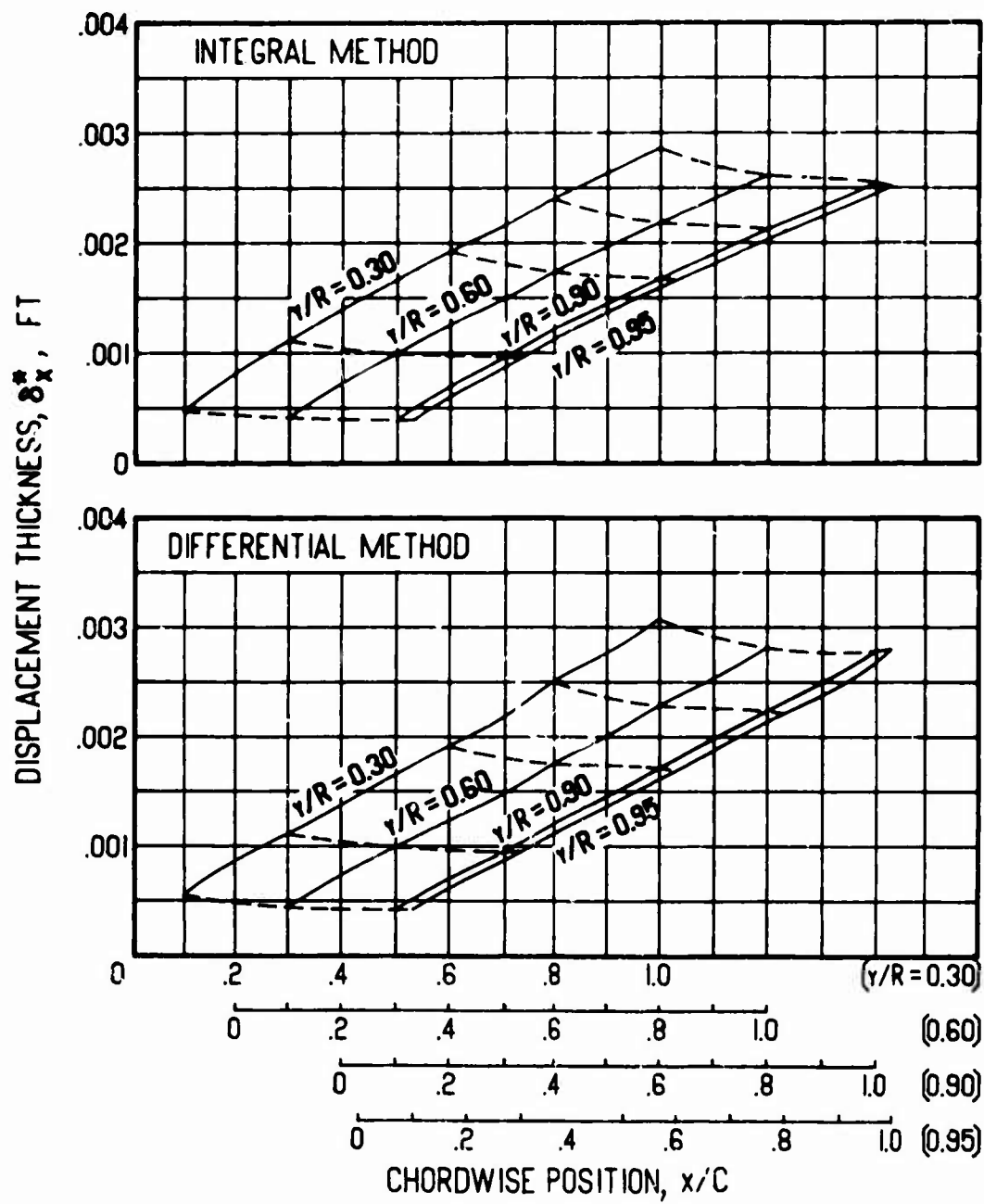
(d) Γ/h = -50 ft/sec

Figure 14. Concluded.

117
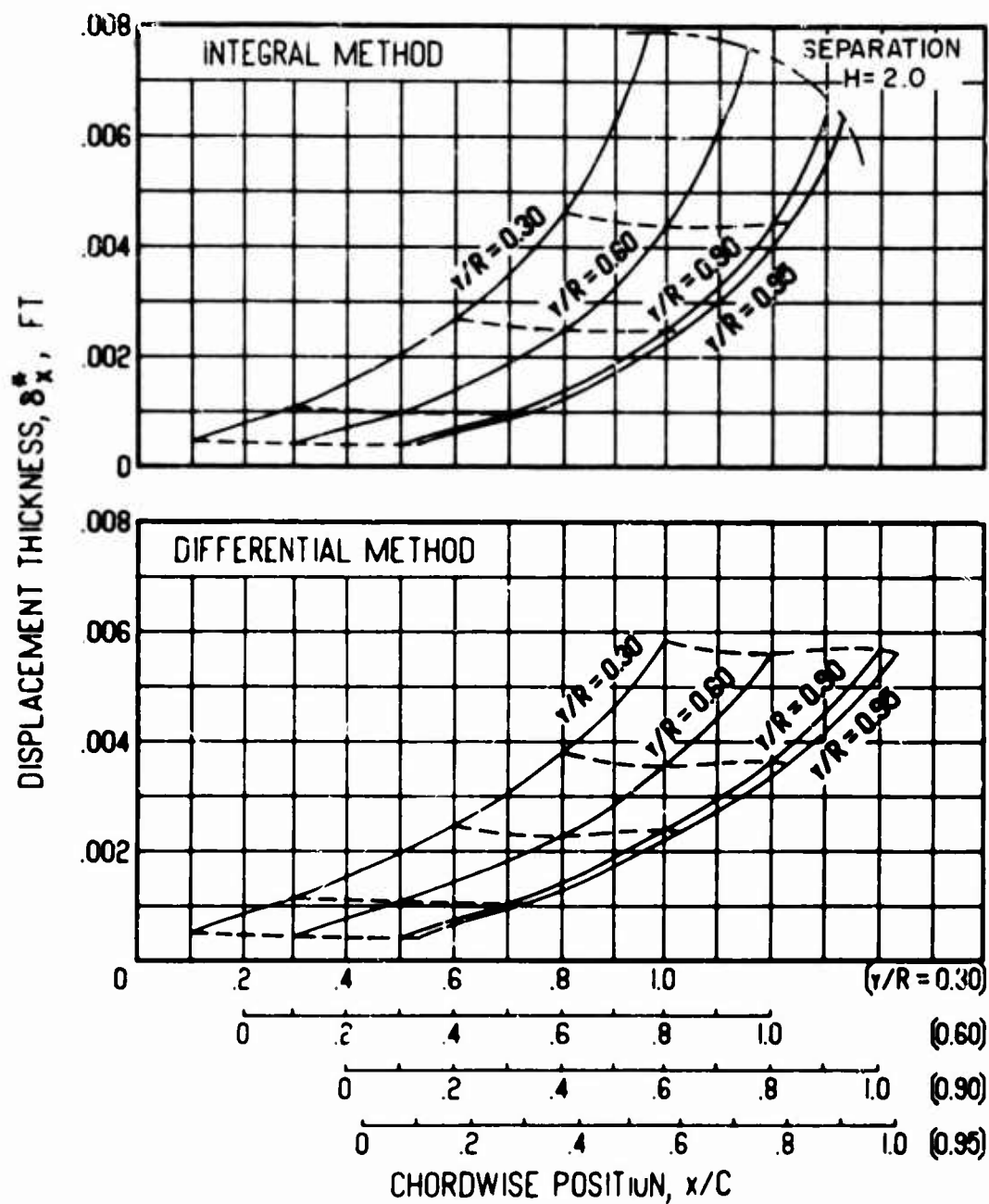
(a) $dCp/d(x/C) = 1$

Figure 15. Displacement Thickness Versus Chordwise Position for
Various Pressure Gradients, Blade Radius = 10 ft,
$\Omega = 60$ rad/sec, $\Gamma/h = 0$ ft/sec, Surface Radius of
Curvature = 4.125 ft.

118
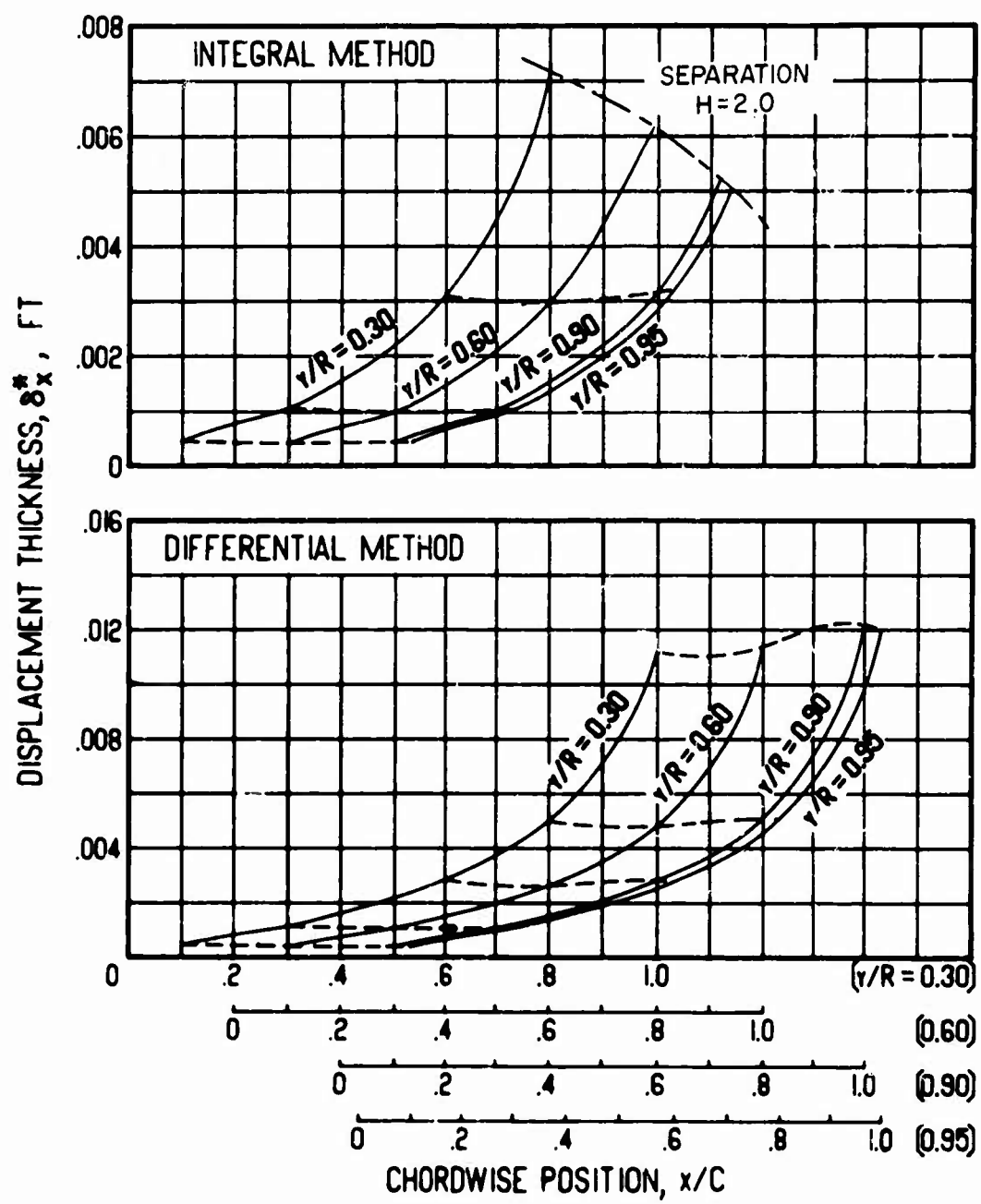
(b) $dCp/d(x/C) = 2$

Figure 15. Concluded.

119
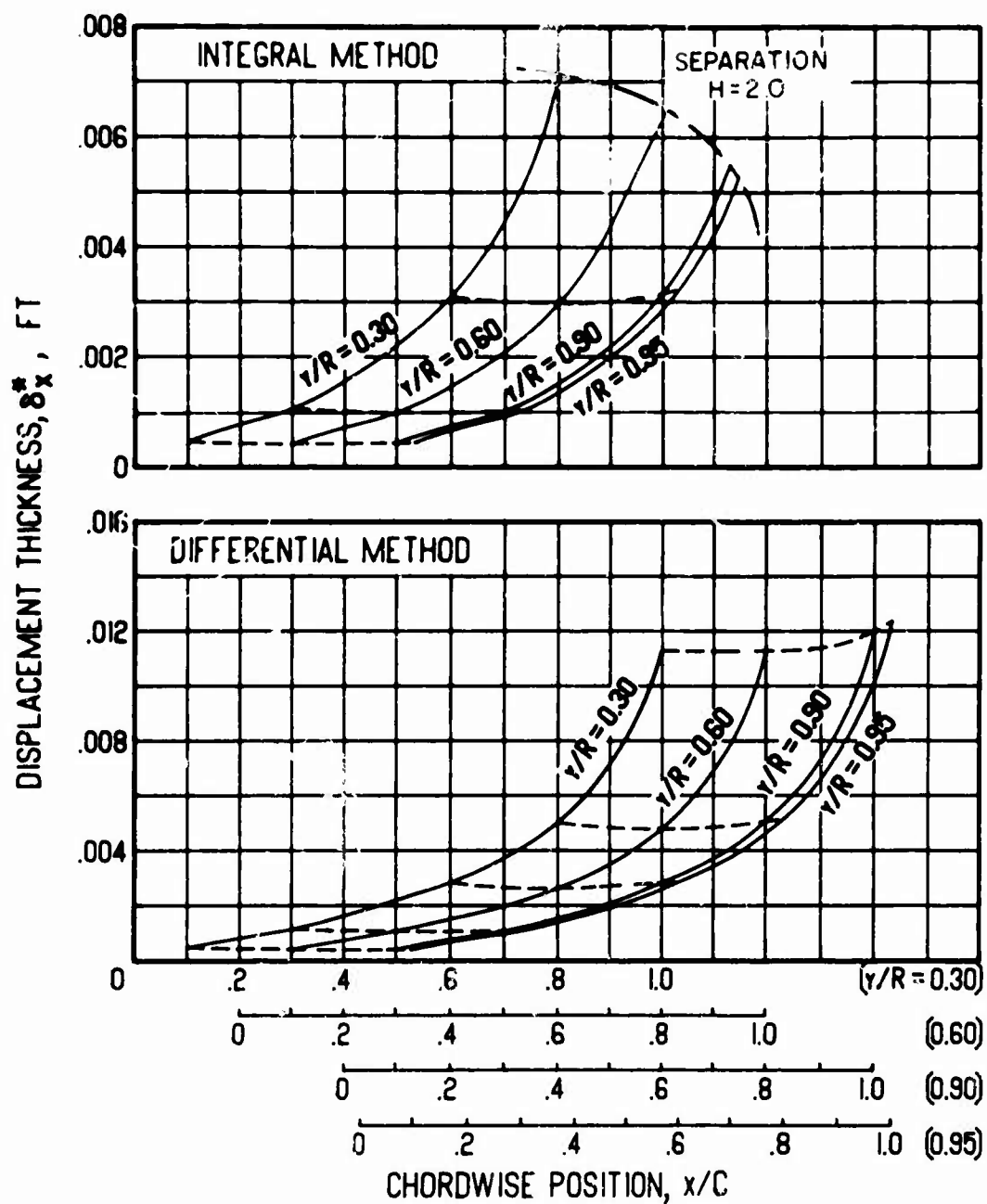
(a) $\Gamma/h = +50$ ft/sec

Figure 16. Displacement Thickness Versus Chordwise Position for Various Vortex Strengths, Blade Radius = 10 ft, $\Omega = 60$ rad/sec, $dCp/d(x/C) = 2$, Surface Radius of Curvature = 4.125 ft.

120
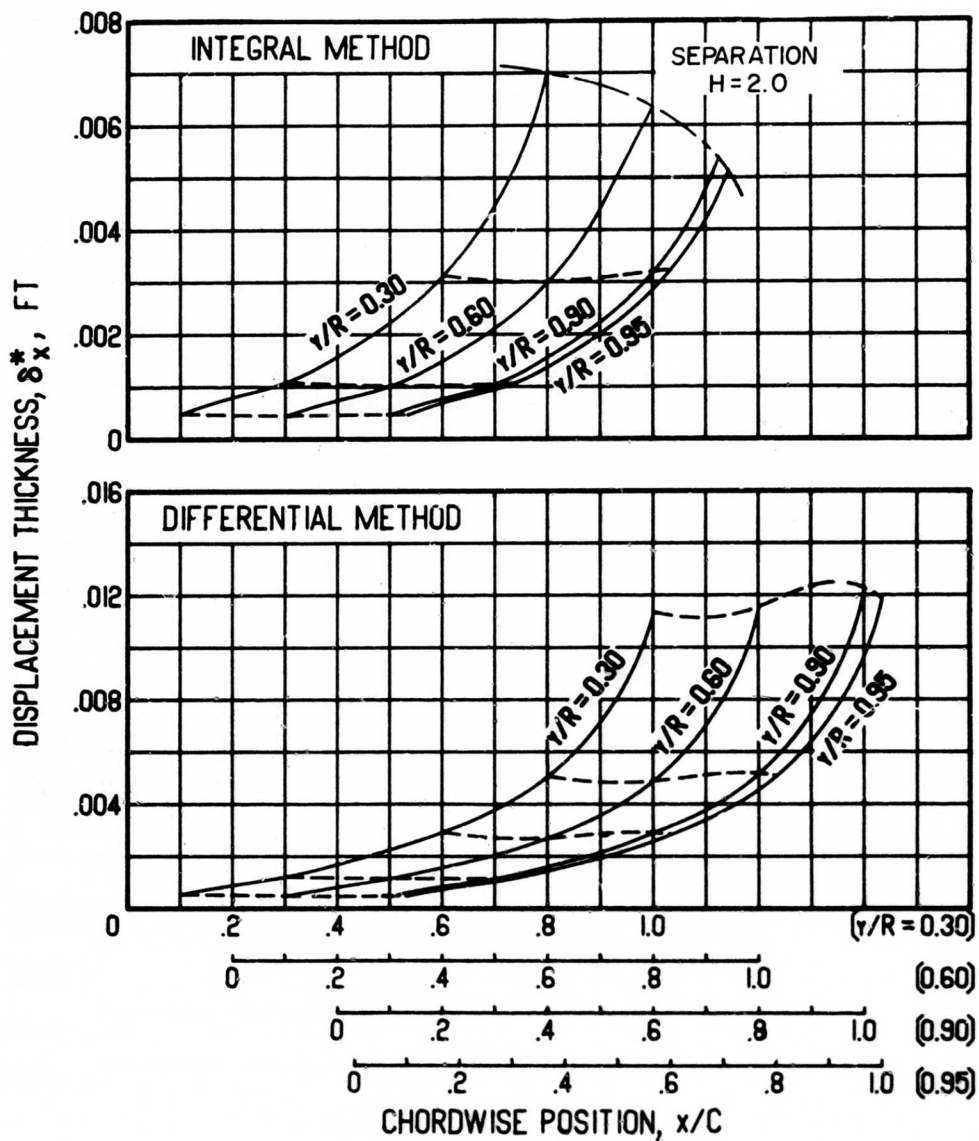
(b) $\Gamma/h = -50$ ft/sec

Figure 16. Concluded.

121
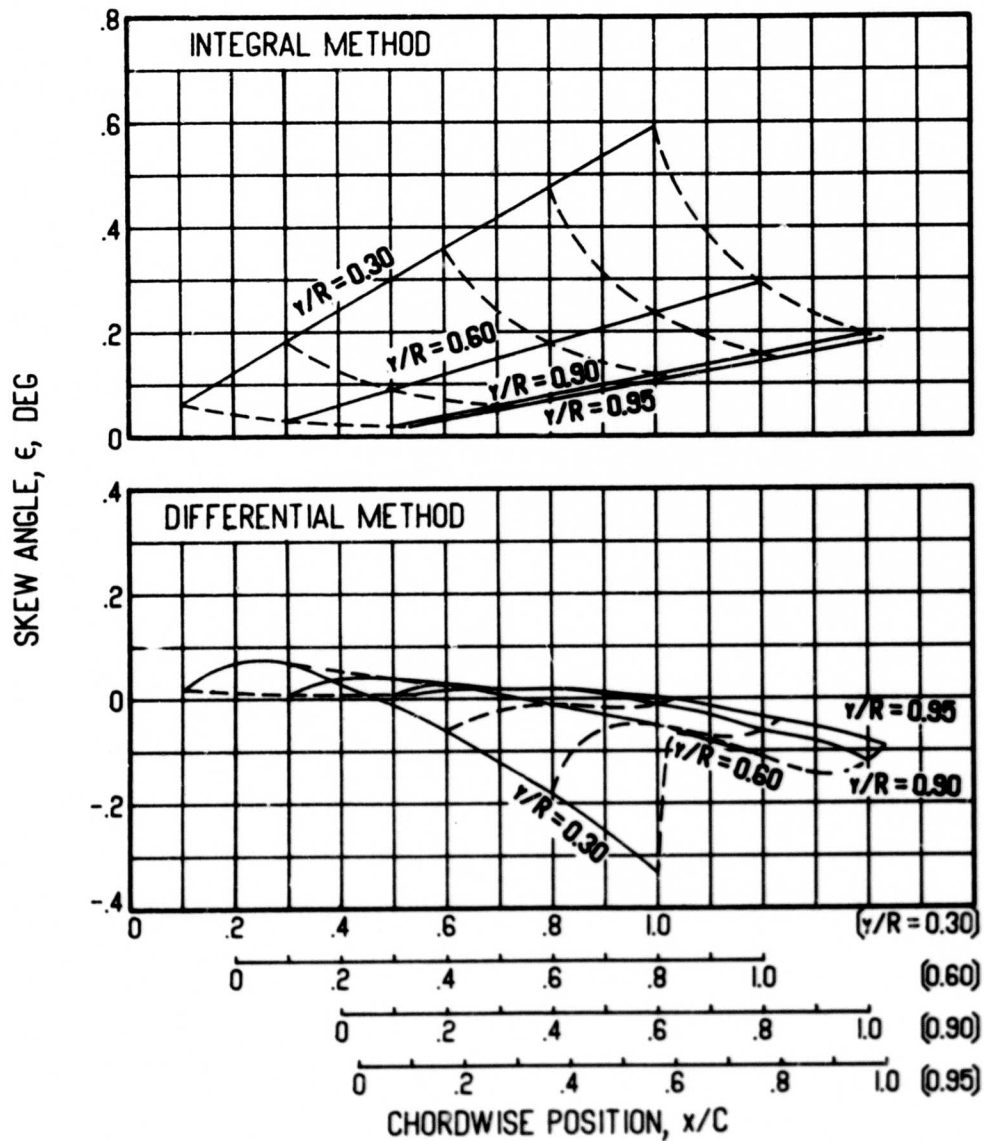
(a) Ω = 10 rad/sec

Figure 17. Skew Angle Versus Chordwise Position for Various
Angular Velocities, Blade Radius = 40 ft,
Γ/h = 0 ft/sec, dCp/d(x/C) = 0, Flat Surface.
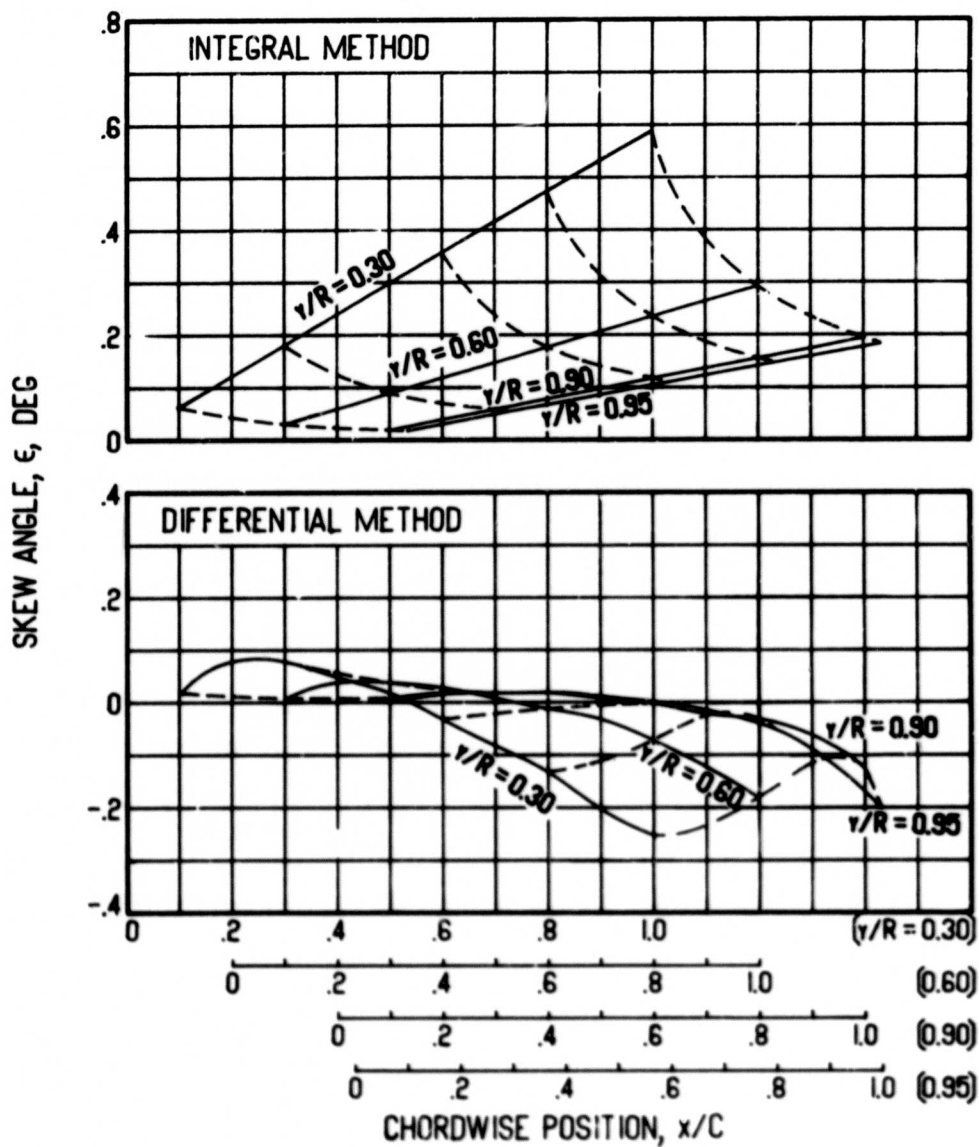
(b) Ω = 15 rad/sec

Figure 17. Continued.

123

(c) Ω = 20 rad/sec
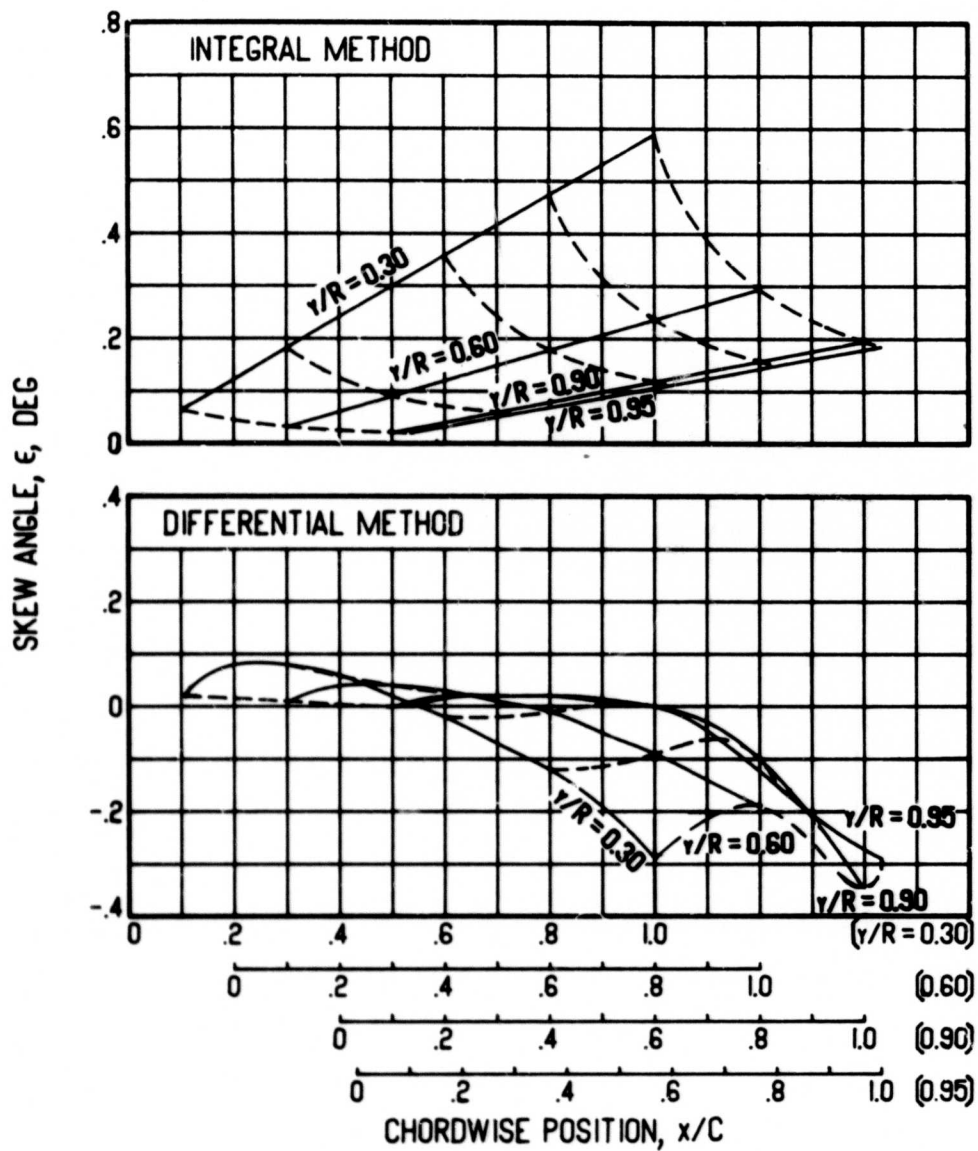
Figure 17. Concluded.

124
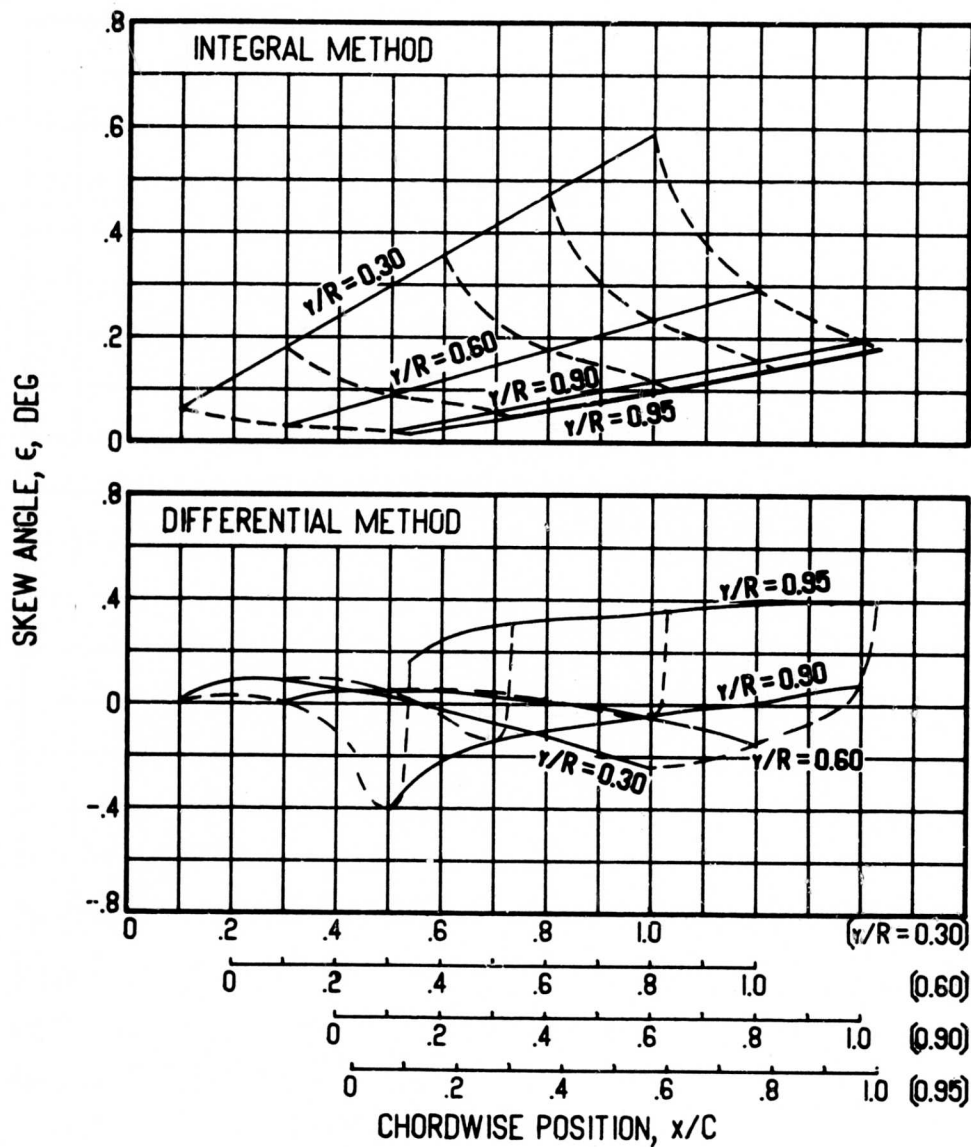
(a) $\Gamma/h = +100$ ft/sec

Figure 18. Skew Angle Versus Chordwise Position for Various
Vortex Strengths, Blade Radius = 40 ft,
$\Omega = 15$ rad/sec, $dCp/d(x/C) = 0$, Flat Surface.

125
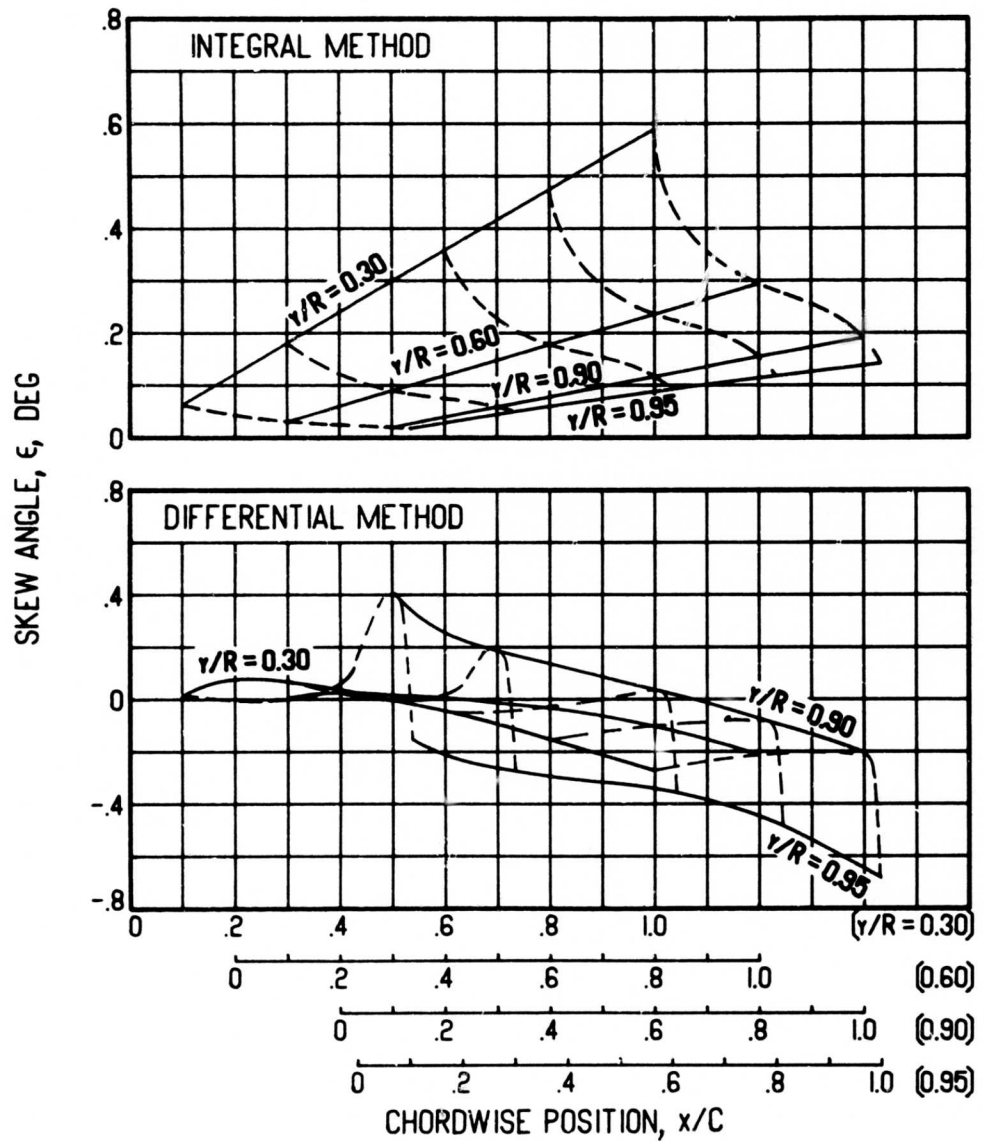
(b) $\Gamma/h = -100$ ft/sec

Figure 18. Continued.

(c) $\Gamma/h = +200$ ft/sec

Figure 18. Continued.

127
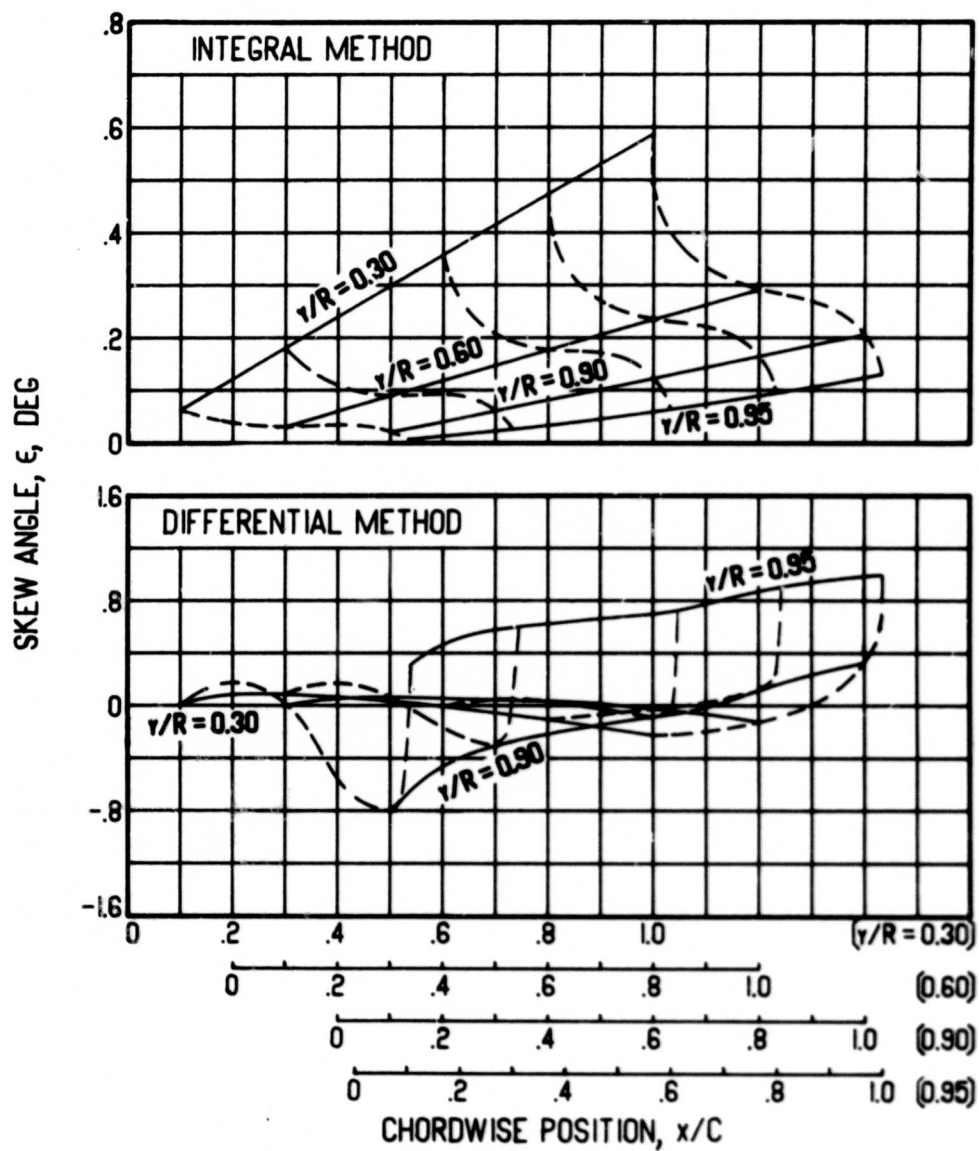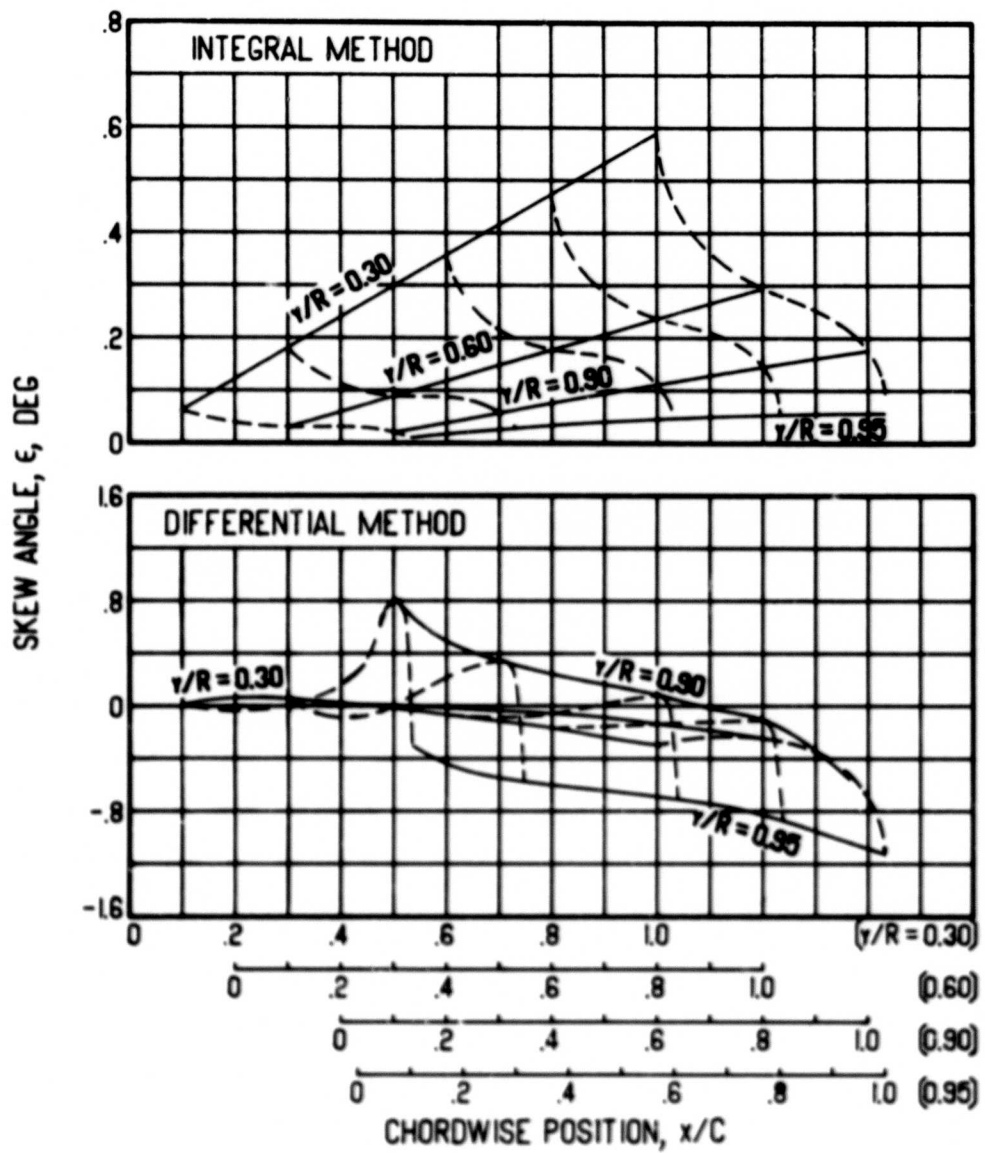
(d) Γ/h = -200 ft/sec

Figure 18. Concluded.
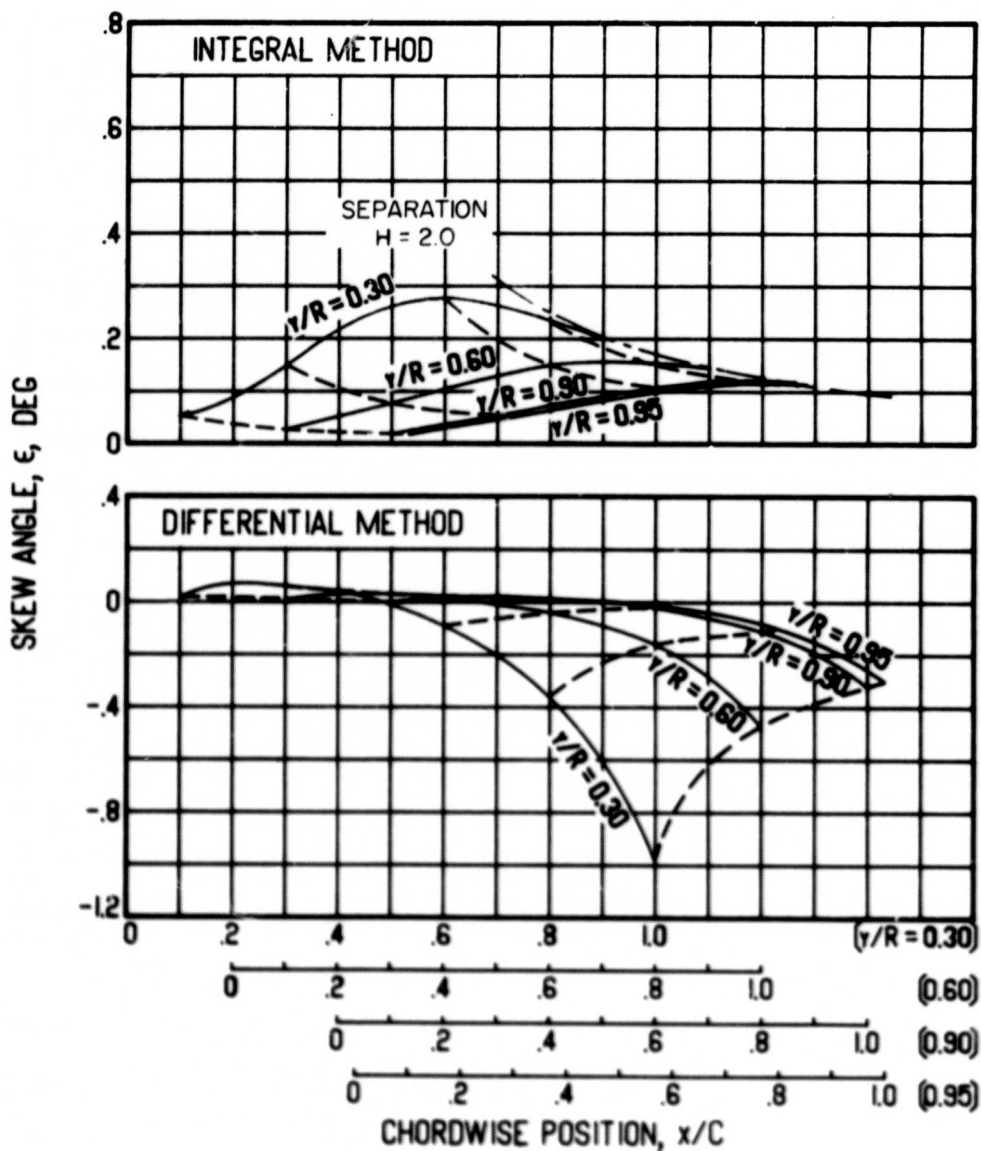
(a) $dCp/d(x/C) = 1$

Figure 19. Skew Angle Versus Chordwise Position for Various
Pressure Gradients, Blade Radius = 40 ft,
Ω = 15 rad/sec, Γ/h = 0 ft/sec, Flat Surface.

(b) dCp/d(x/C) = 2

Figure 19. Concluded.
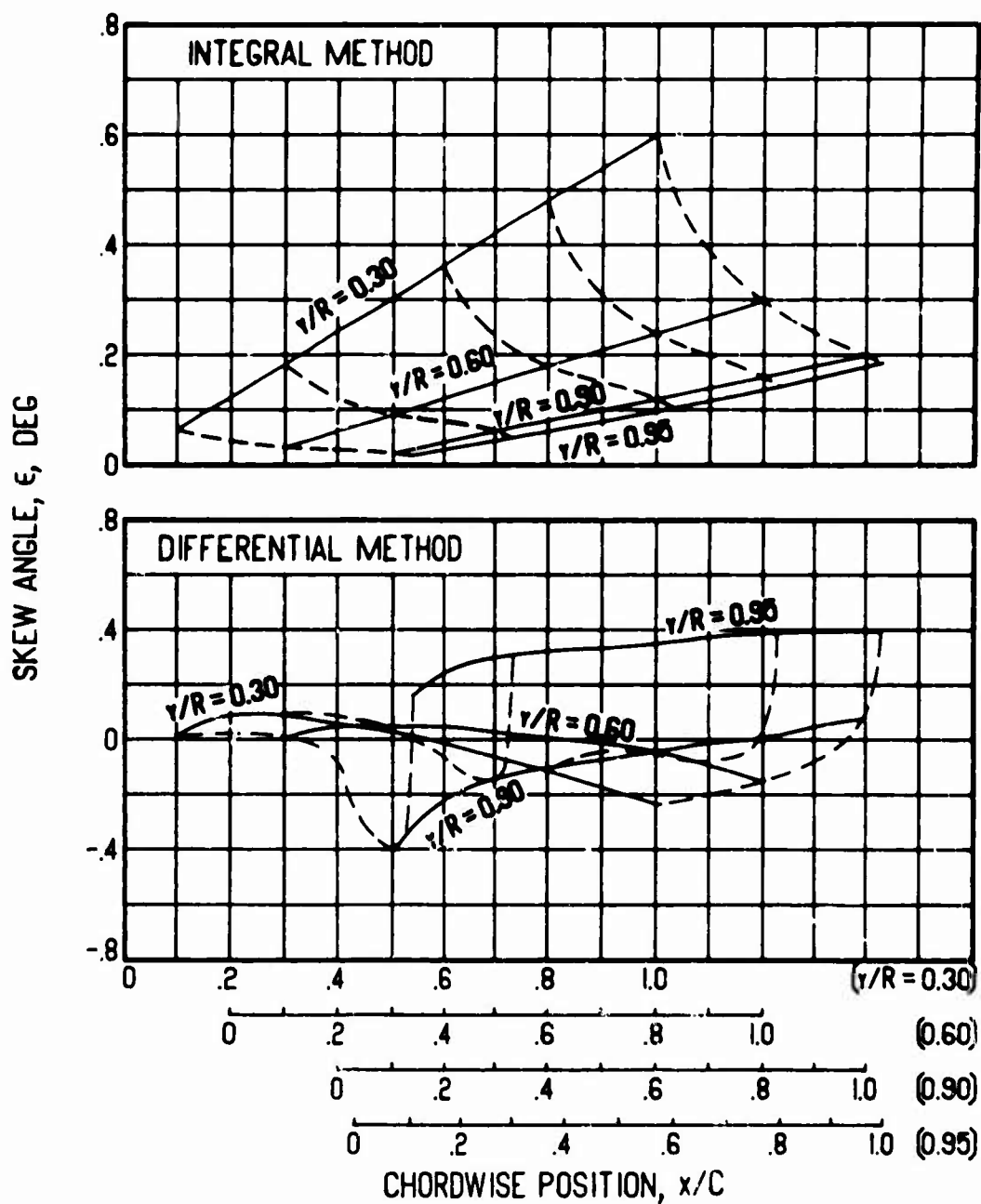
(a) $\Gamma/h = +100$ ft/sec

Figure 20.   Skew Angle Versus Chordwise Position for Various
             Vortex Strengths, Blade Radius = 40 ft,
             $\Omega = 15$ rad/sec, $dCp/d(x/C) = 0$, Surface Radius
             of Curvature = 8.25 ft.

131

(b) $\Gamma/h = -100$ ft/sec

Figure 20. Continued.

132

(c) $\Gamma/h = +200$ ft/sec

Figure 20. Continued.

133
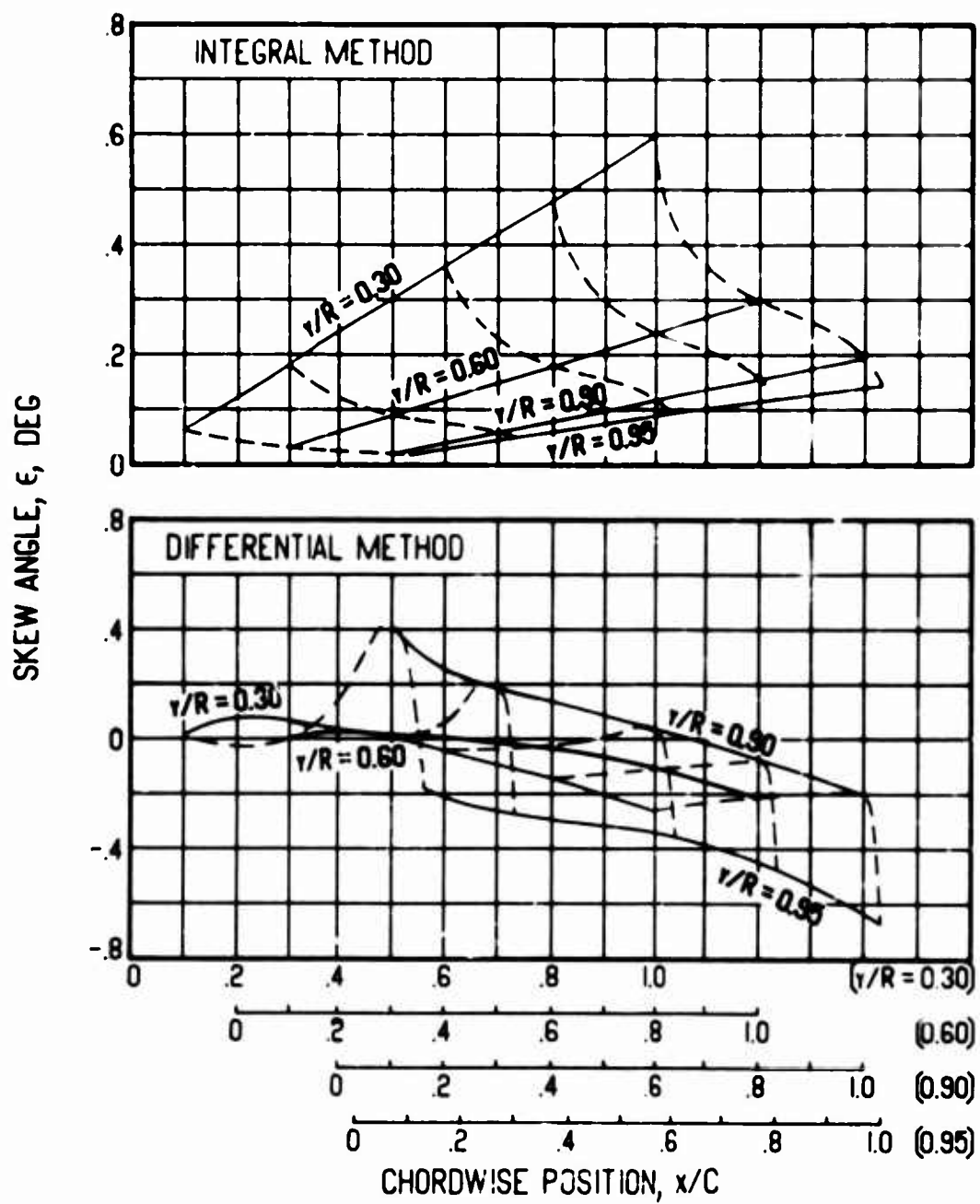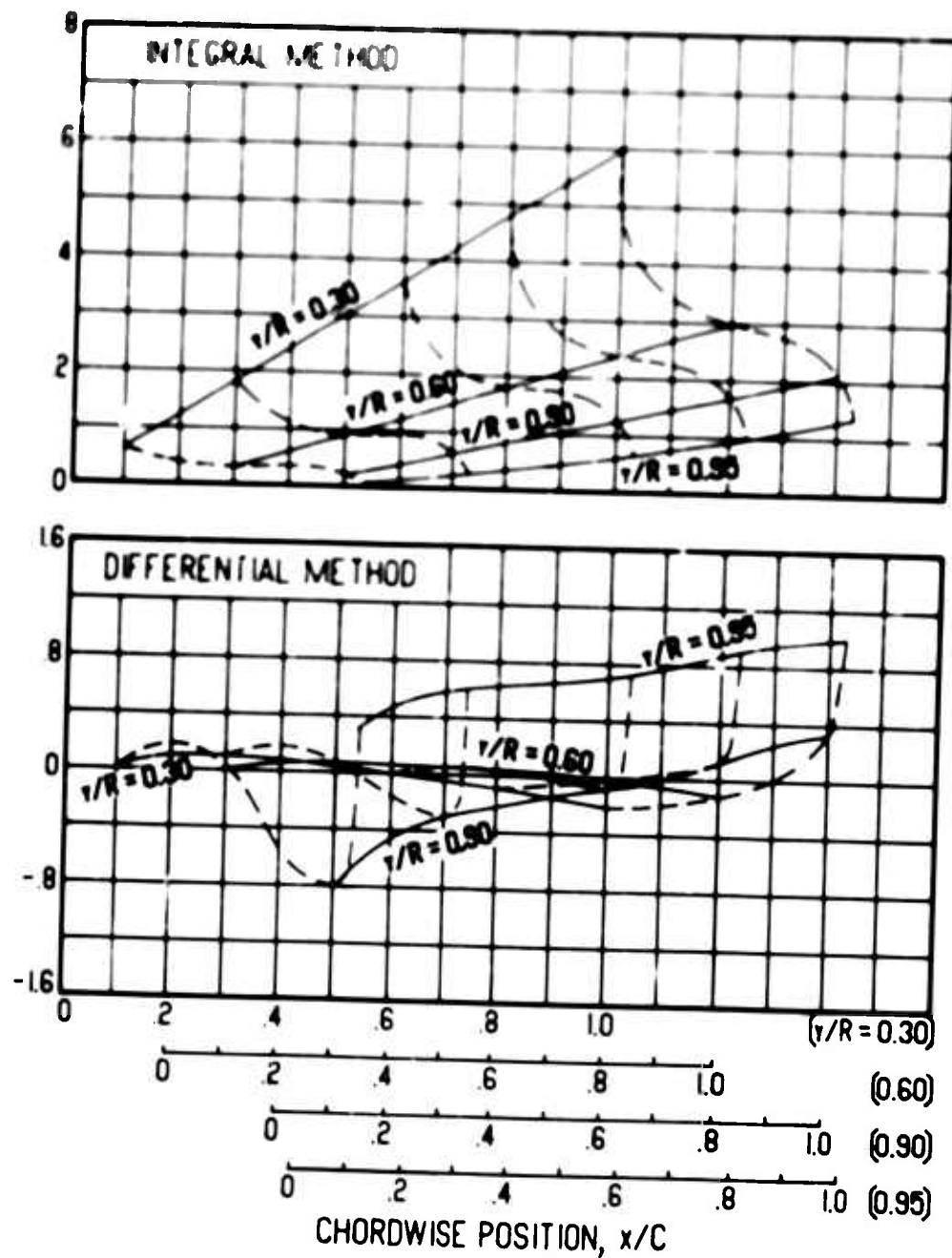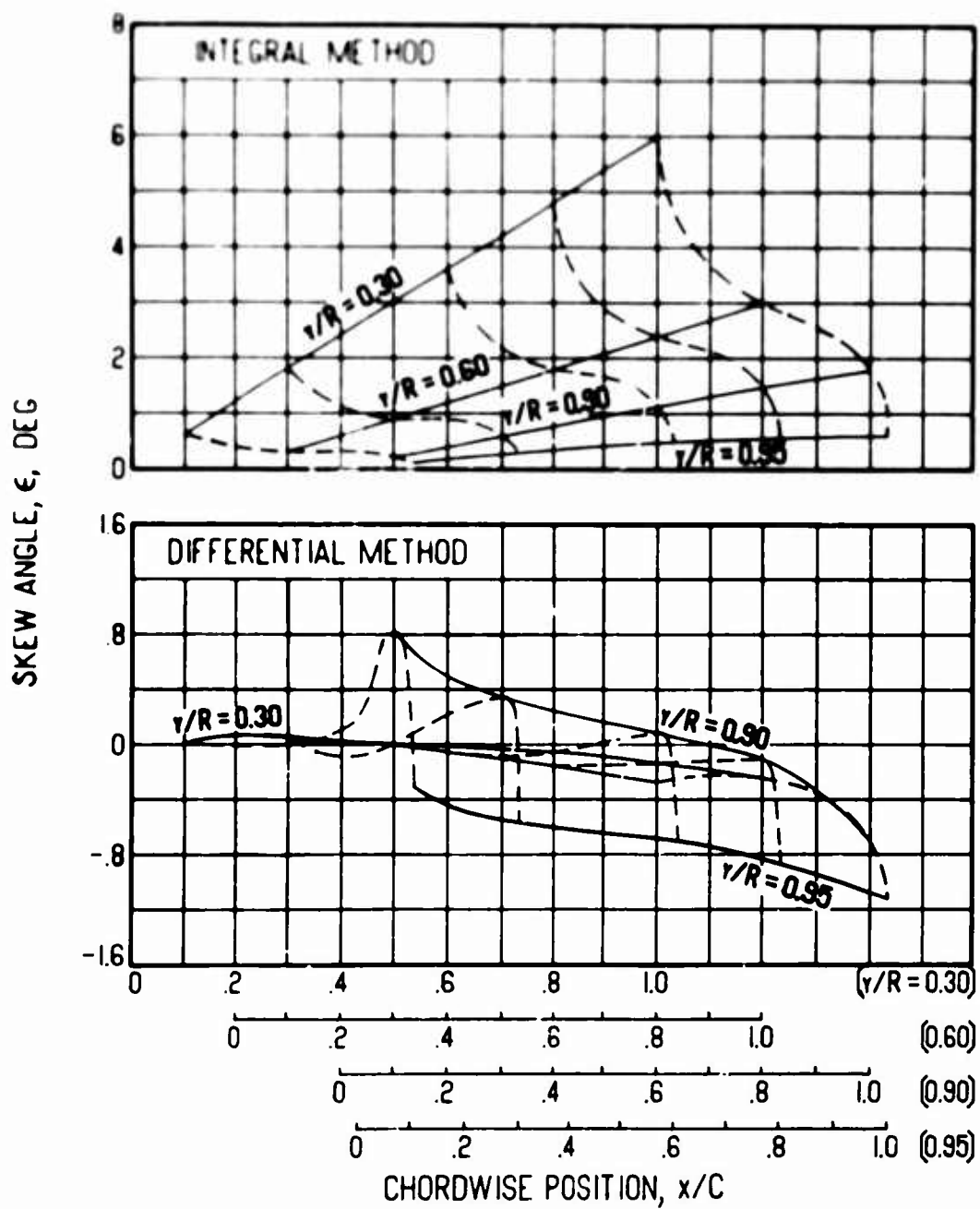
(d) Γ/h = -200 ft/sec

Figure 20. Concluded.
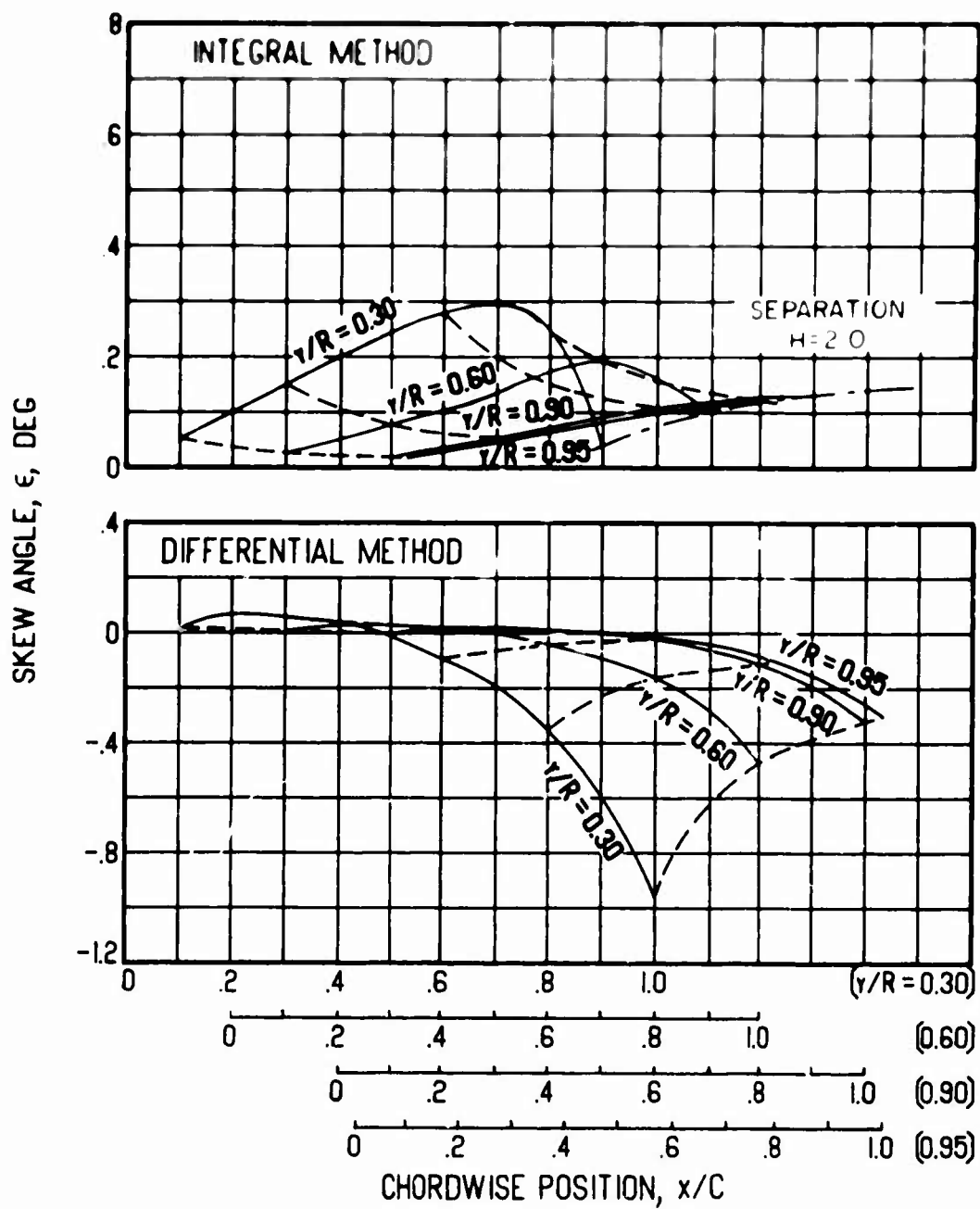
(a) $dCp/d(x/C) = 1$

Figure 21. Skew Angle Versus Chordwise Position for Various
Pressure Gradients, Blade Radius = 40 ft,
$\Omega = 15$ rad/sec, $\Gamma/h = 0$ ft/sec, Surface Radius
of Curvature = 8.25 ft.

135
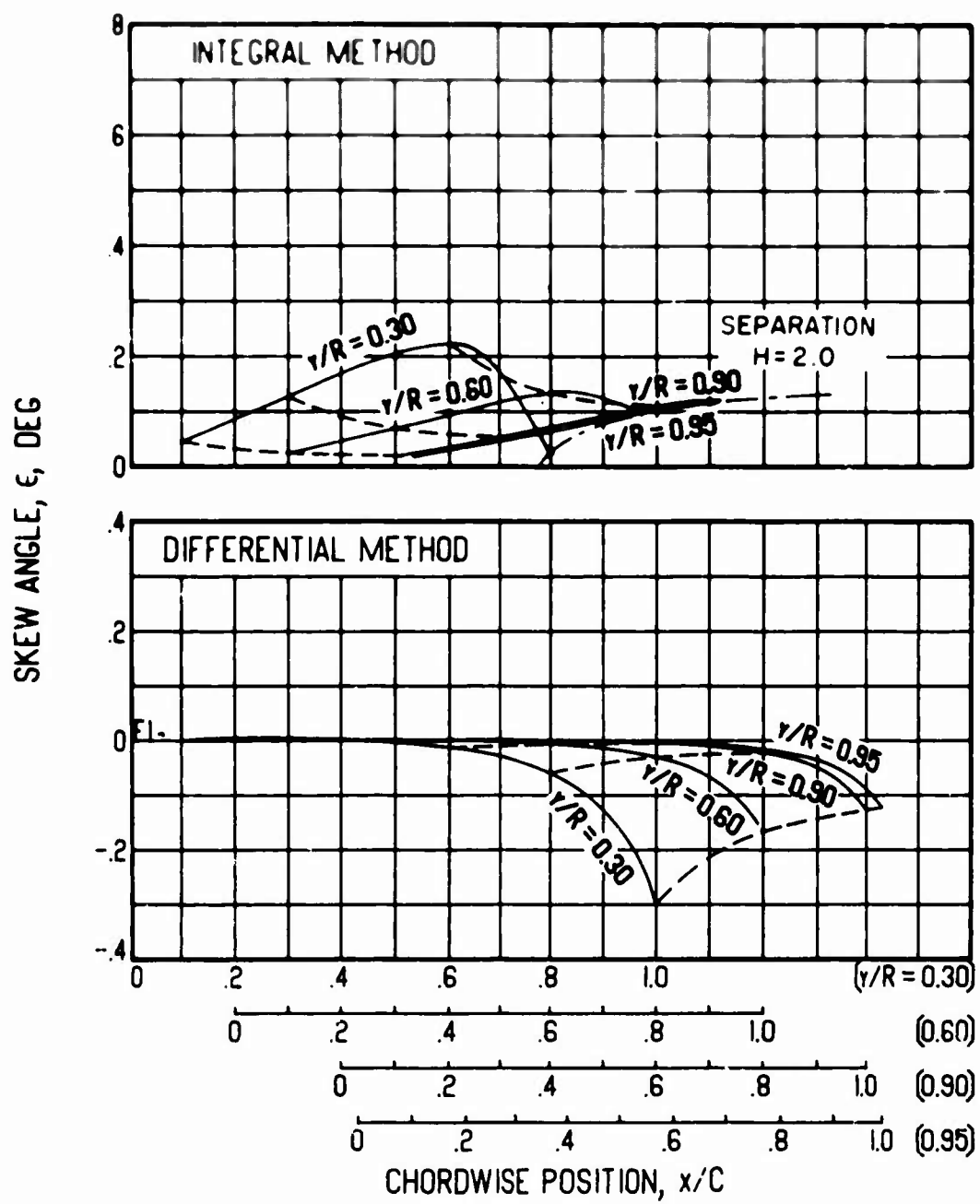
(b) dCp/d(x/C) = 2

Figure 21. Concluded.

136
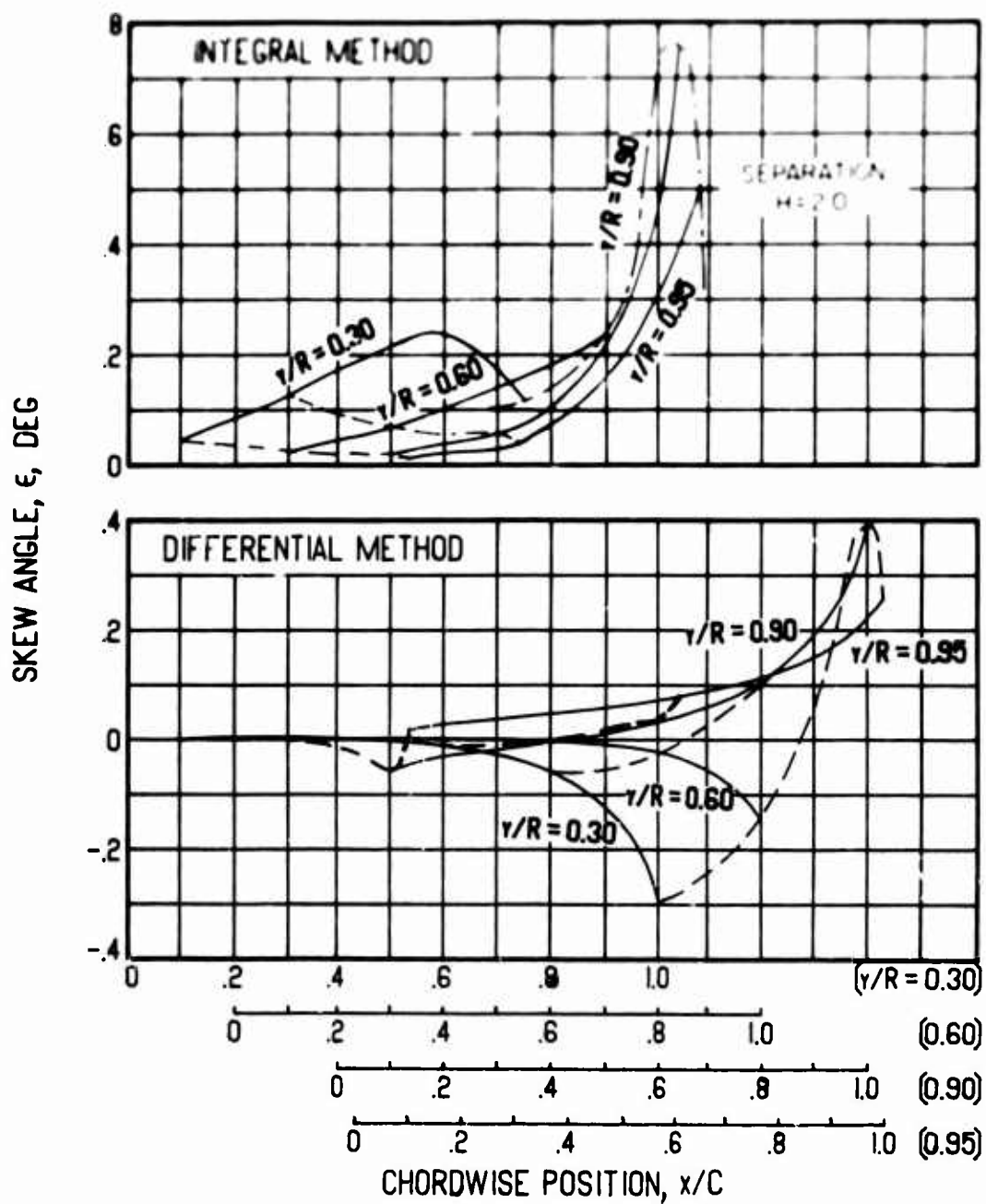
(a) $\Gamma/h = +200$ ft/sec

Figure 22. Skew Angle Versus Chordwise Position for Various
Vortex Strengths, Blade Radius = 40 ft,
$\Omega = 15$ rad/sec, $dC_p/d(x/C) = 2$, Surface Radius
of Curvature = 8.25 ft.

137

(b) $\Gamma/n = -200$ ft/sec

Figure 22.   Concluded.

138
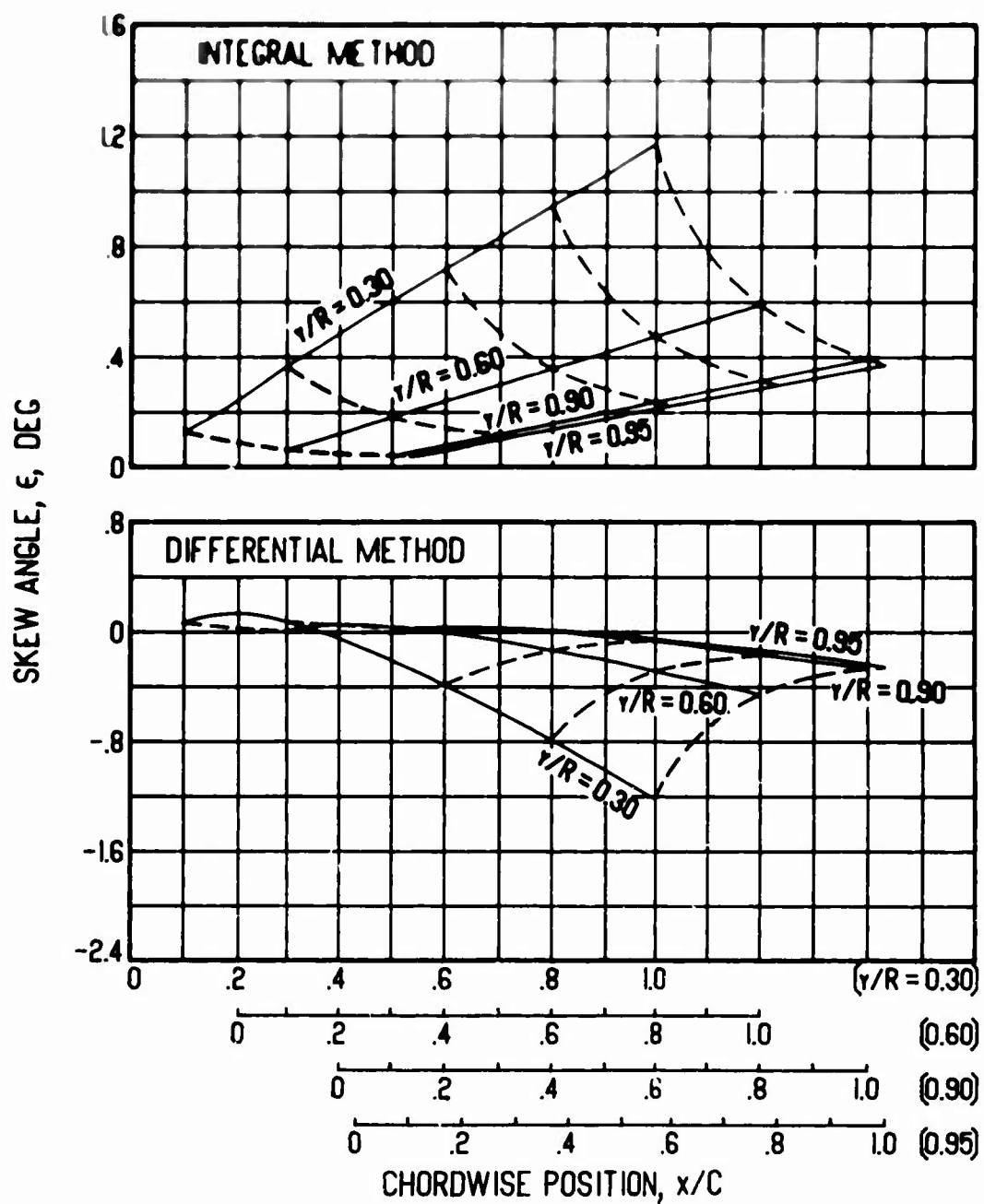
(a) Ω = 40 rad/sec

Figure 23. Skew Angle Versus Chordwise Position for Various
Angular Velocities, Blade Radius = 10 ft,
Γ/h = 0 ft/sec, $dCp/d(x/C)$ = 0, Flat Surface.

139
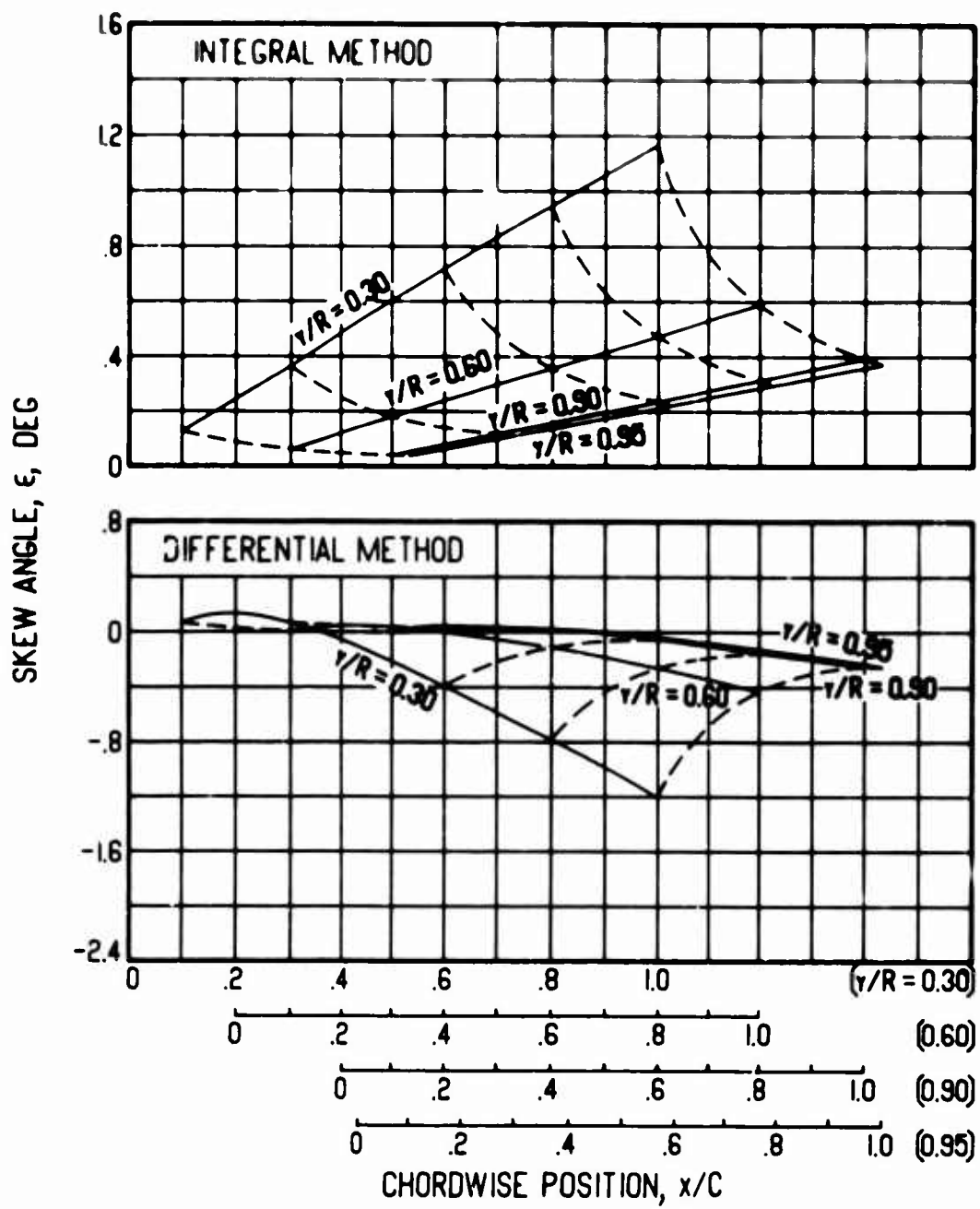
(b) $\Omega = 60$ rad/sec

Figure 23. Continued.

140
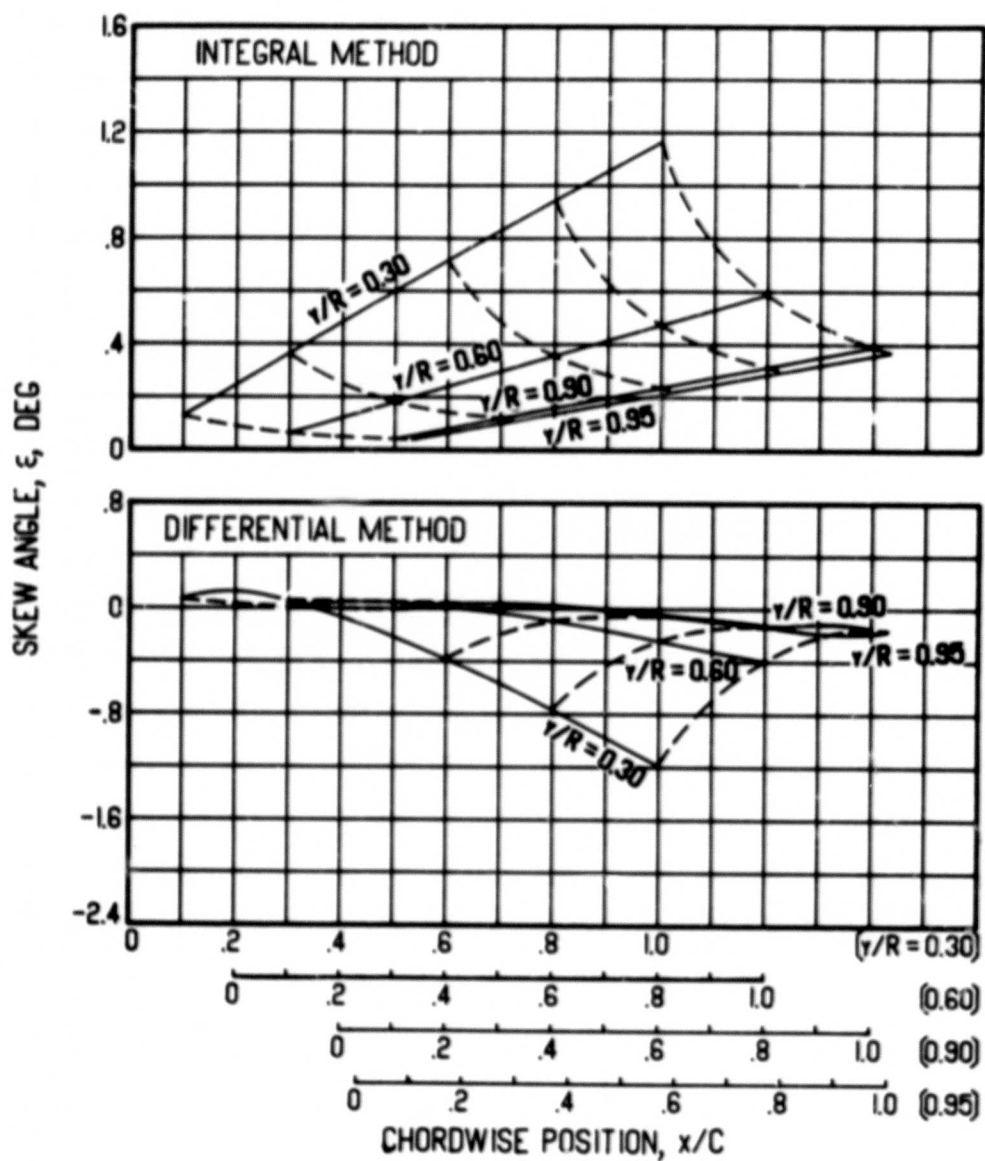
(c) Ω = 80 rad/sec

Figure 23. Concluded.

141
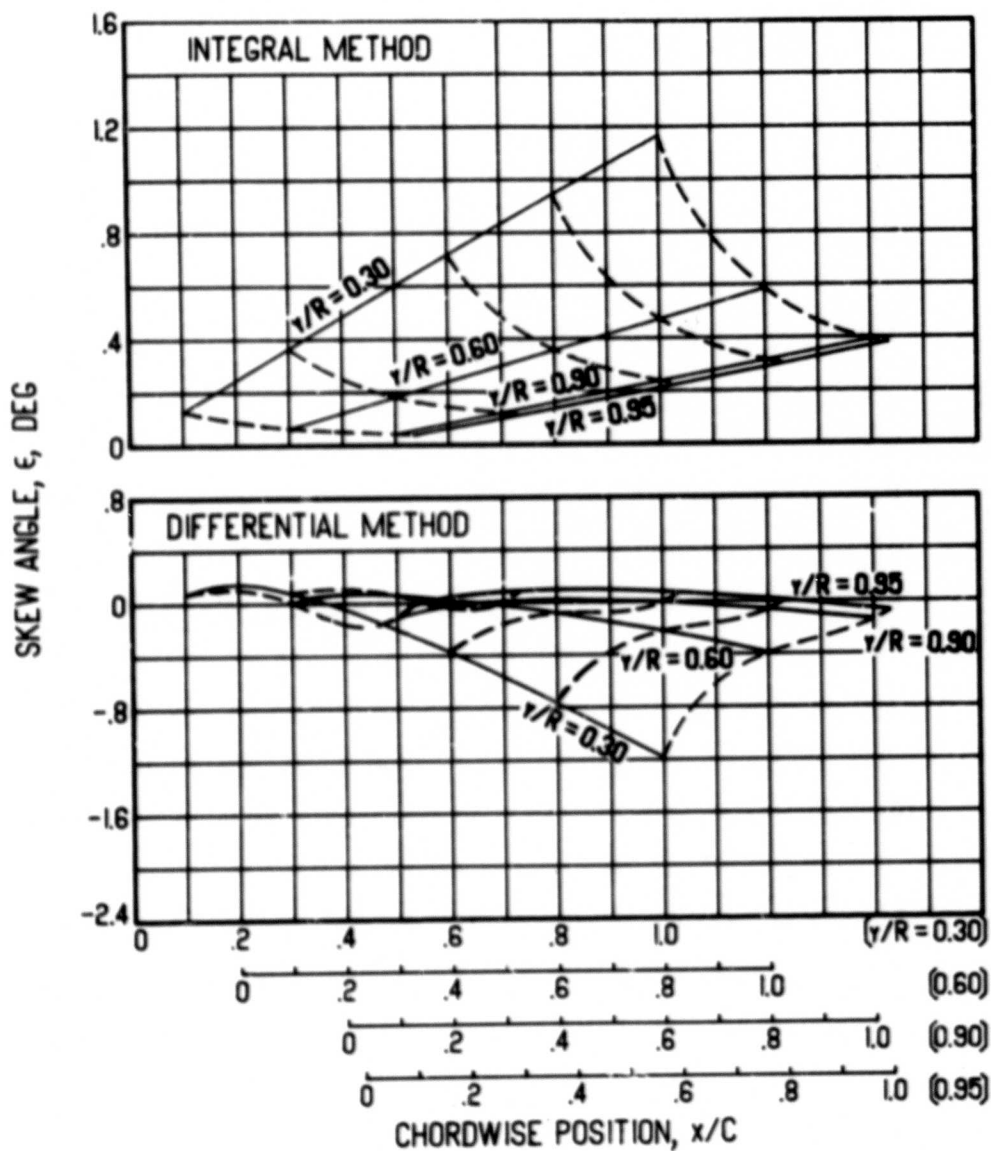
(a) $\Gamma/h = +25$ ft/sec

Figure 24. Skew Angle Versus Chordwise Position for Various
Vortex Strengths, Blade Radius = 10 ft,
$\Omega = 60$ rad/sec, $dCp/d(x/C) = 0$, Flat Surface.

142
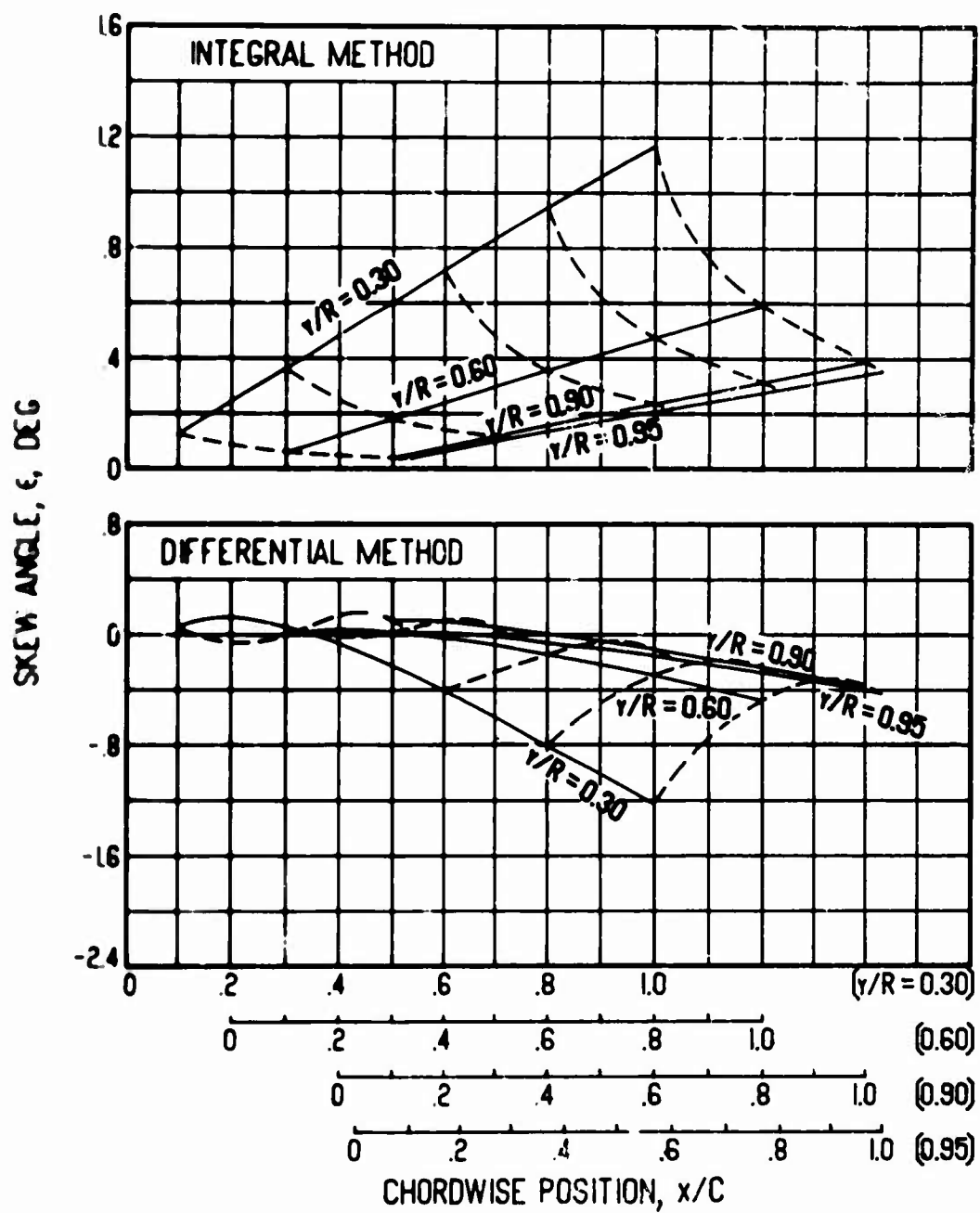
(b) $\Gamma/h = -25$ ft/sec

Figure 24. Continued.
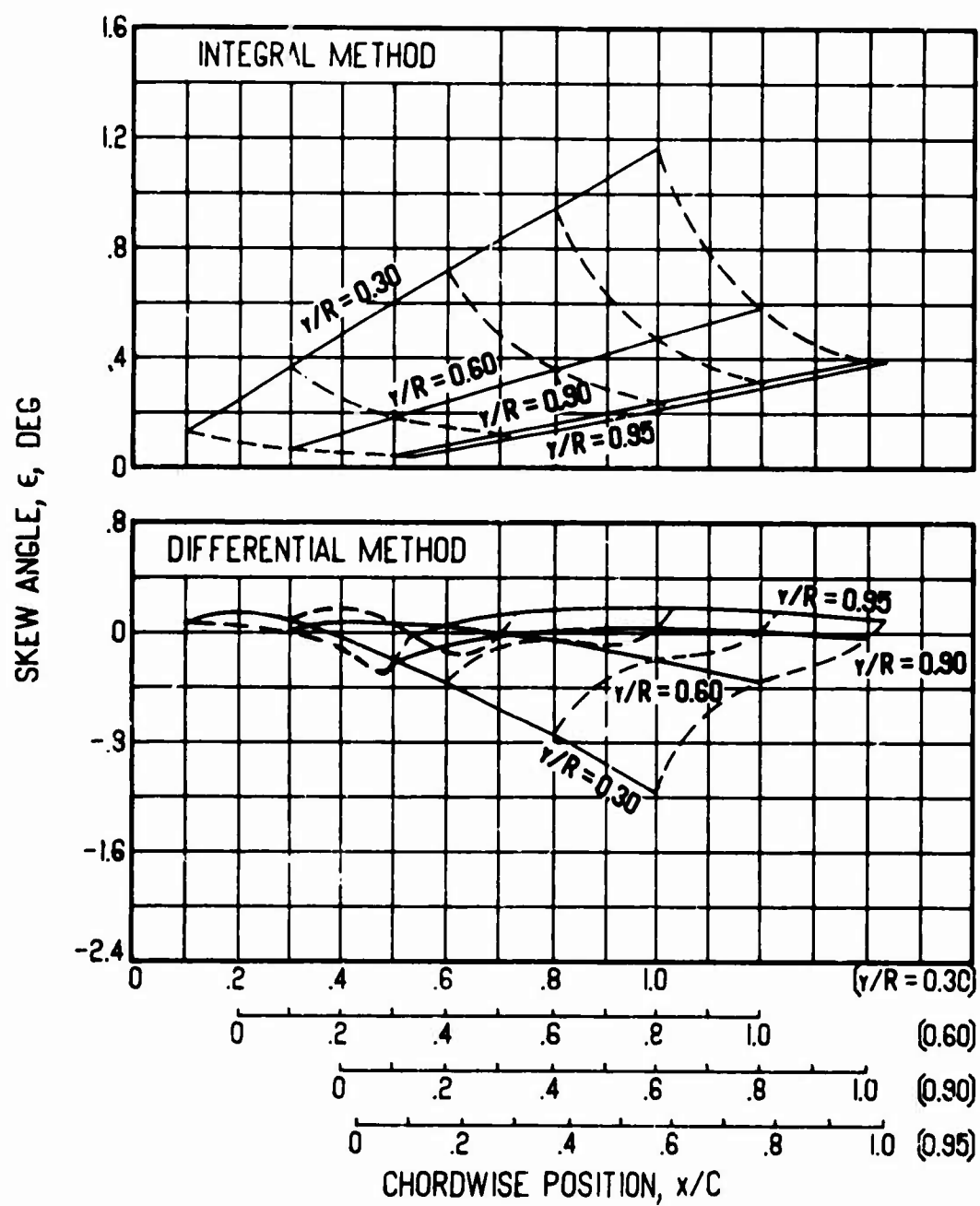
(c) $\Gamma/h = +50$ ft/sec

Figure 24. Continued.
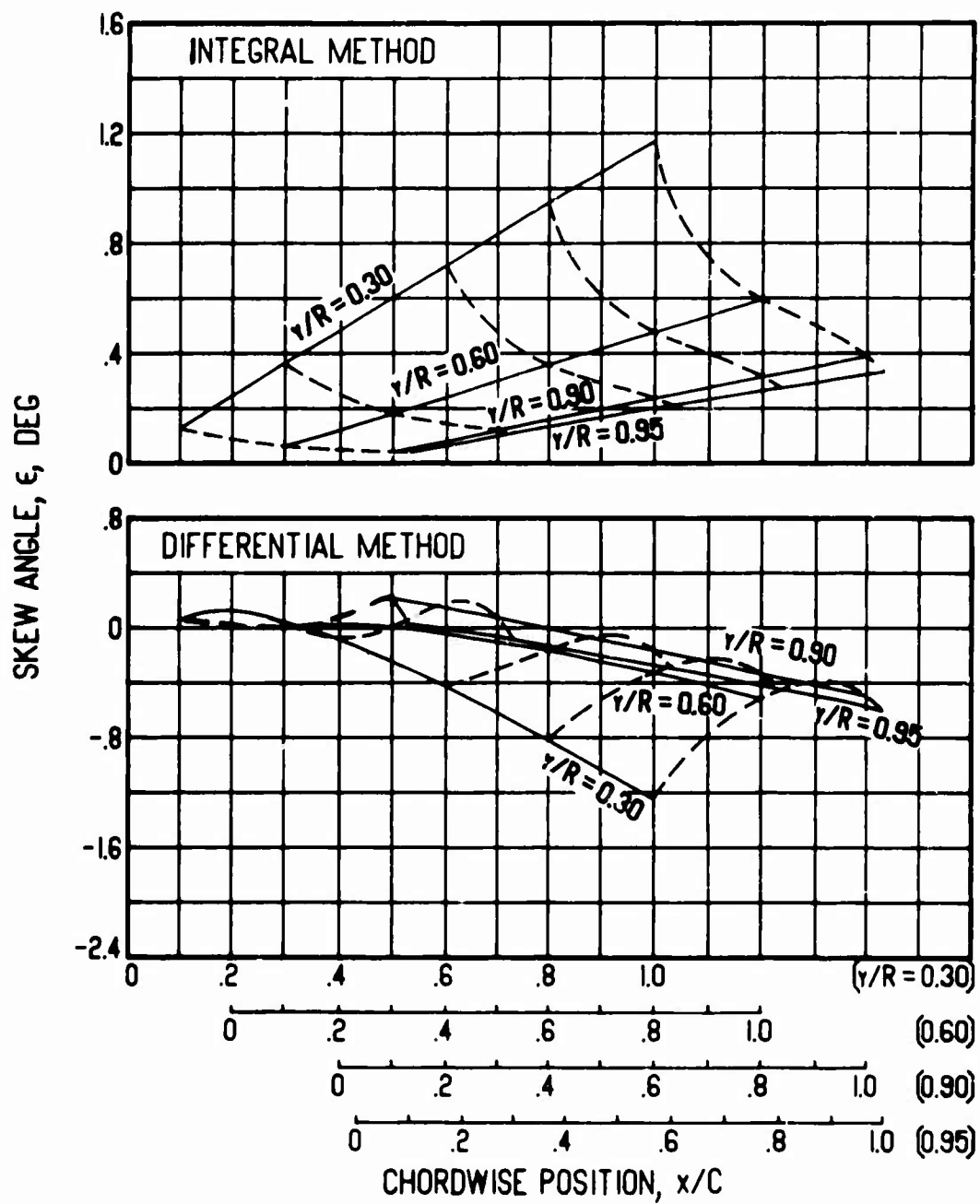
(d) $\Gamma/h = -50$ ft/sec

Figure 24. Concluded.
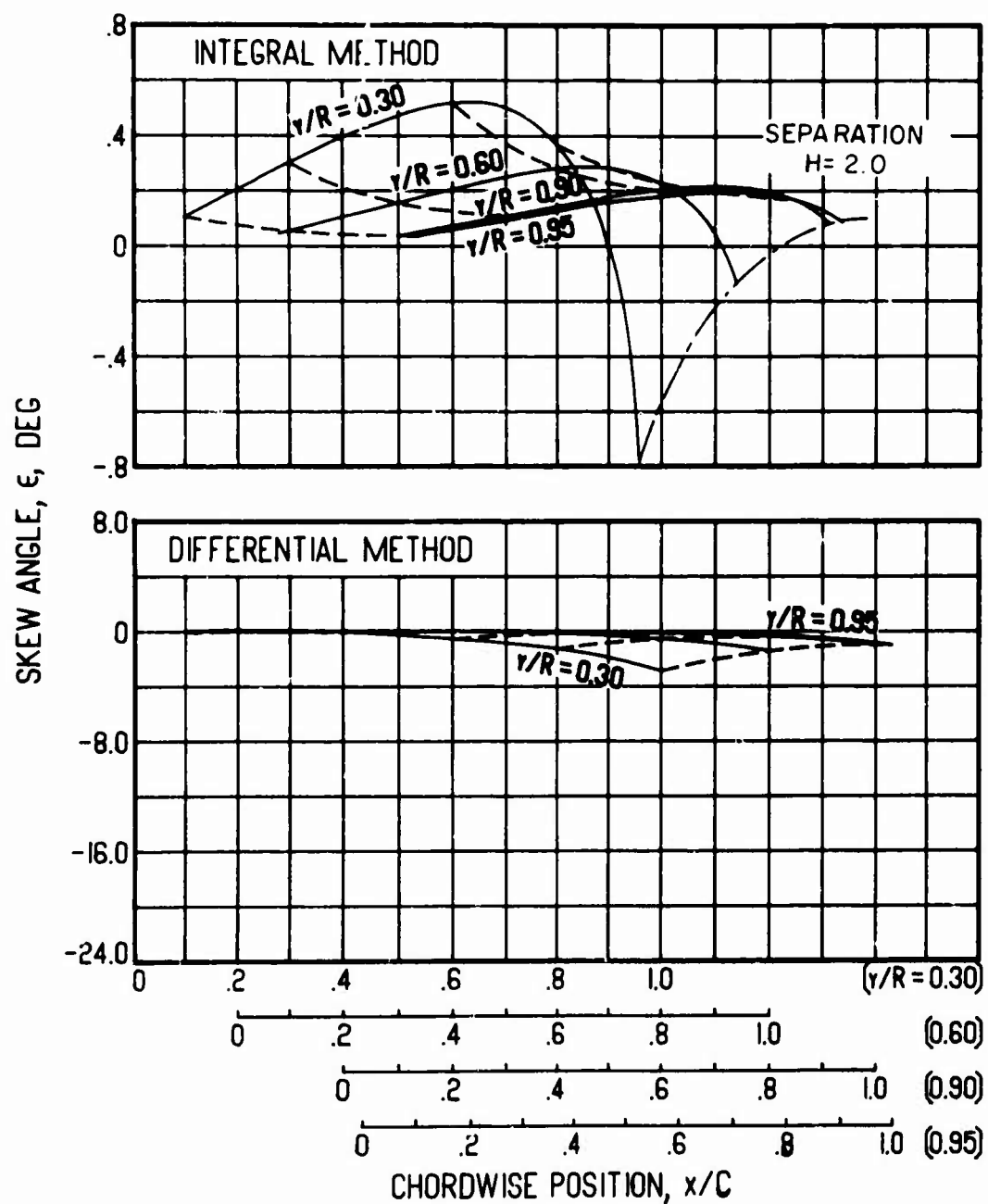
(a) $dCp/d(x/C) = 1$

Figure 25. Skew Angle Versus Chordwise Position for Various
Pressure Gradients, Blade Radius = 10 ft,
Ω = 60 rad/sec, Γ/h = 0 ft/sec, Flat Surface.

146
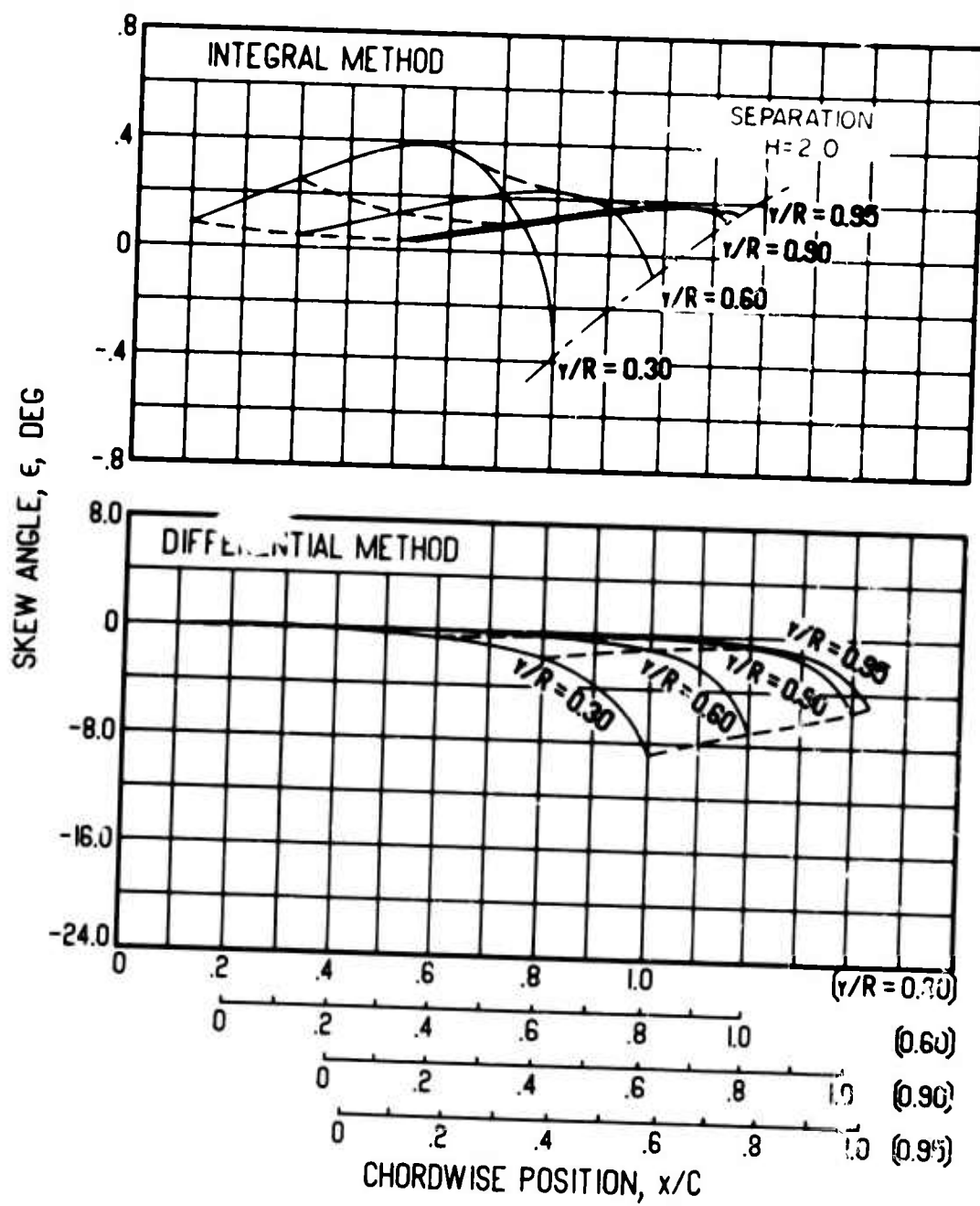
(b) $dC_p/d(x/C) = 2$

Figure 25. Concluded.

147
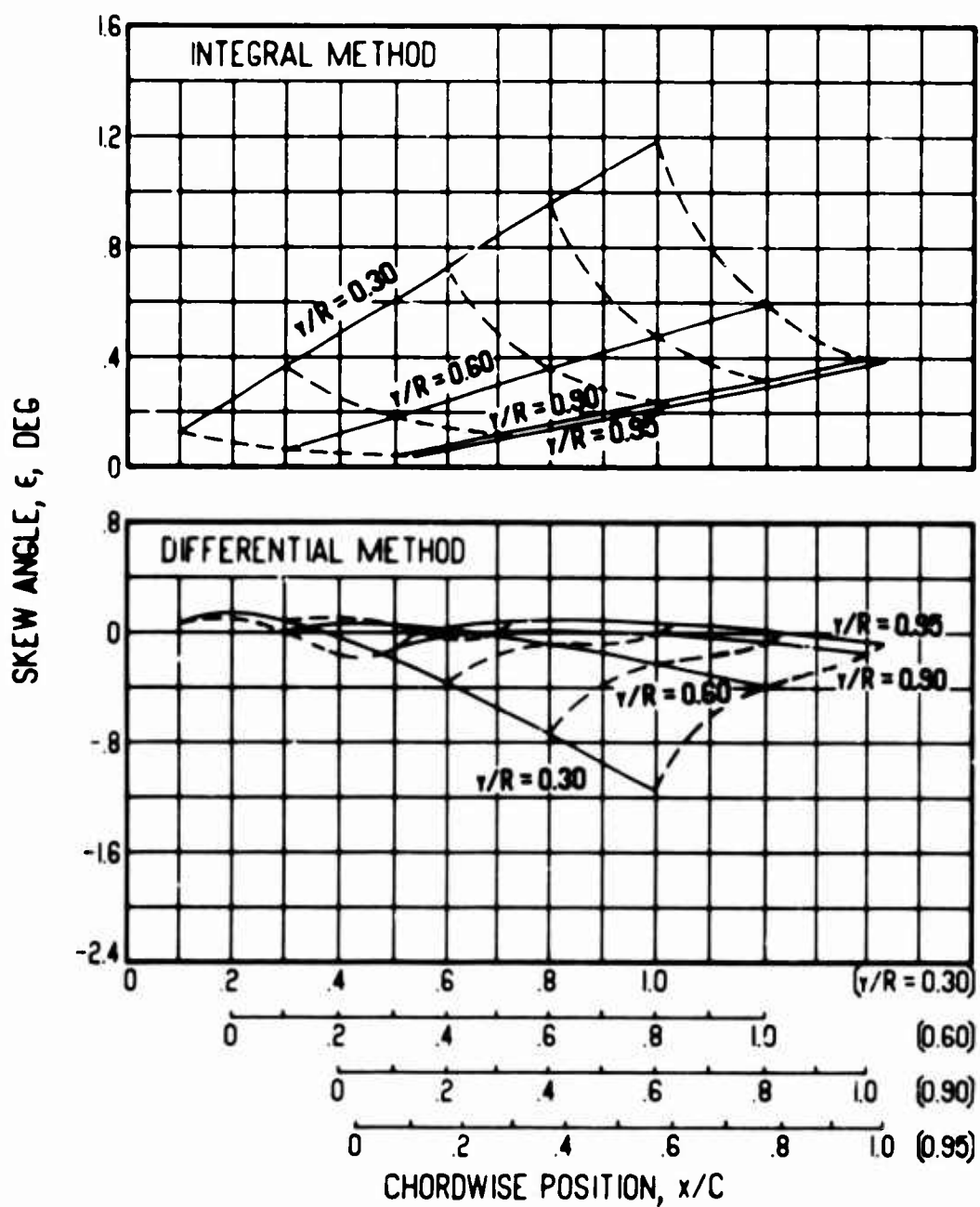
(a) $\Gamma/h = +25$ ft/sec

Figure 26. Skew Angle Versus Chordwise Position for Various
Vortex Strengths, Blade Radius = 10 ft,
$\Omega = 60$ rad/sec, $dCp/d(x/C) = 0$, Surface Radius
of Curvature = 4.125 ft.

148
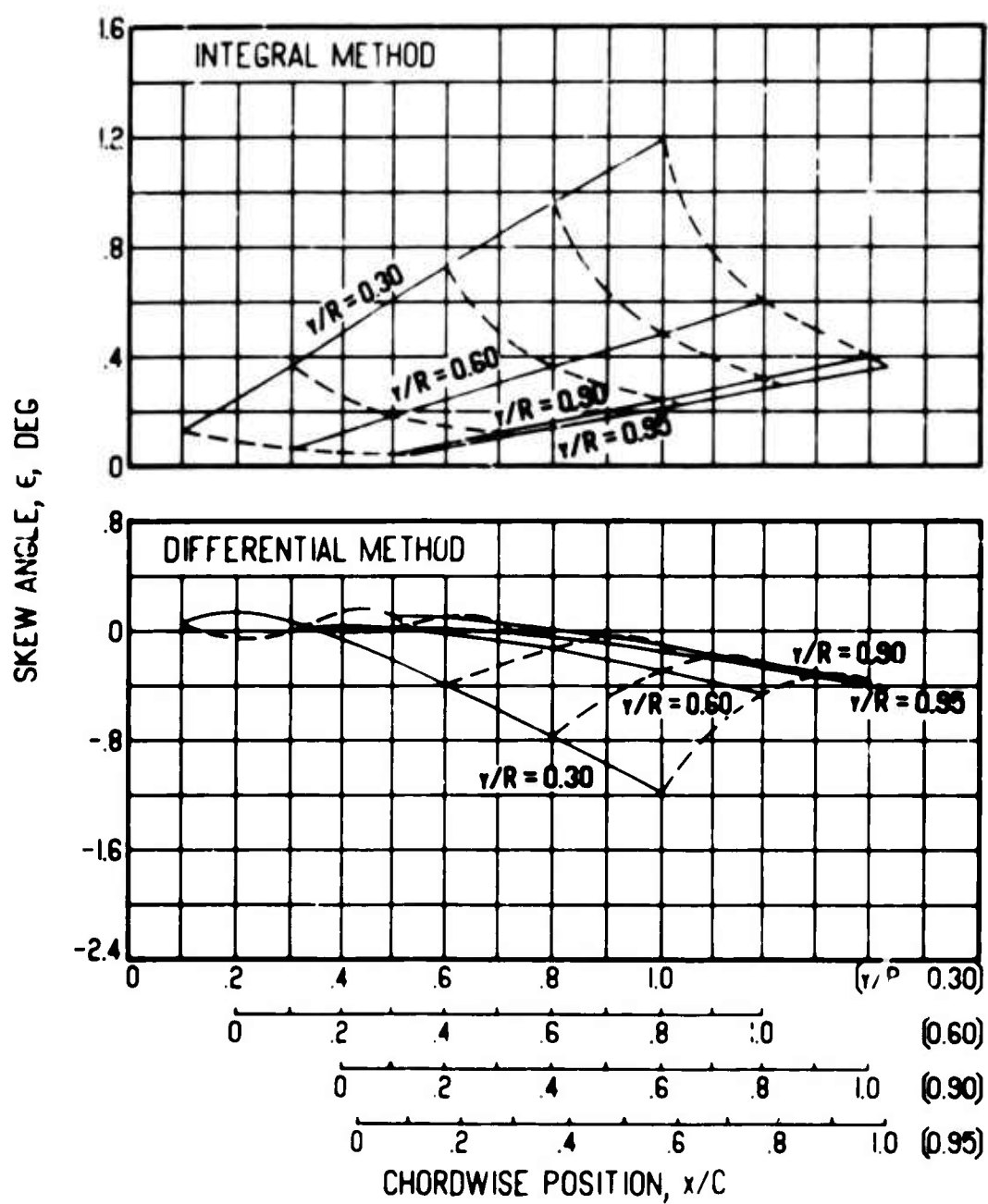
(b) $\Gamma/h = -25$ ft/sec

Figure 26. Continued.

(c) $\Gamma/h = +50$ ft/sec

Figure 26. Continued.

150
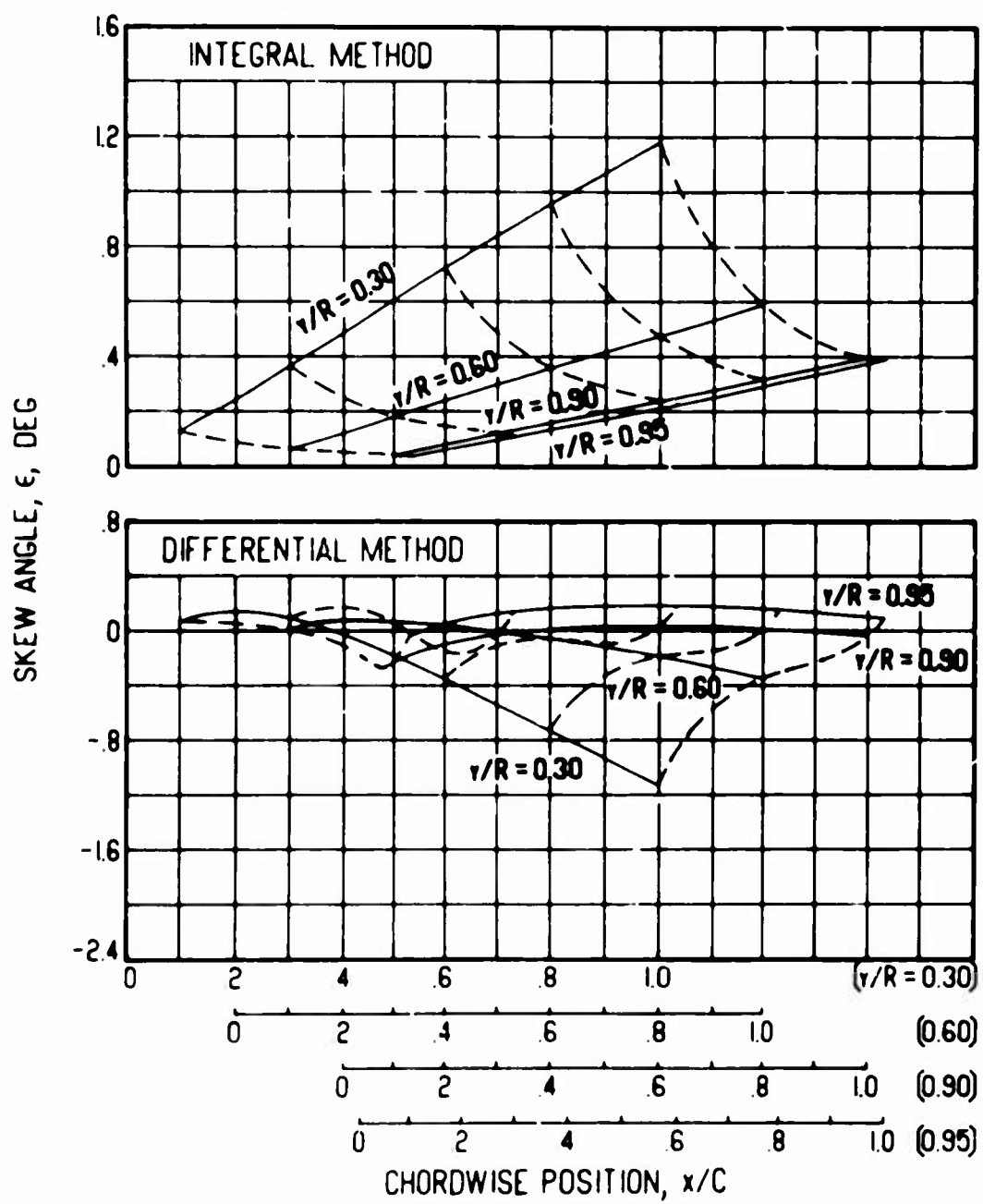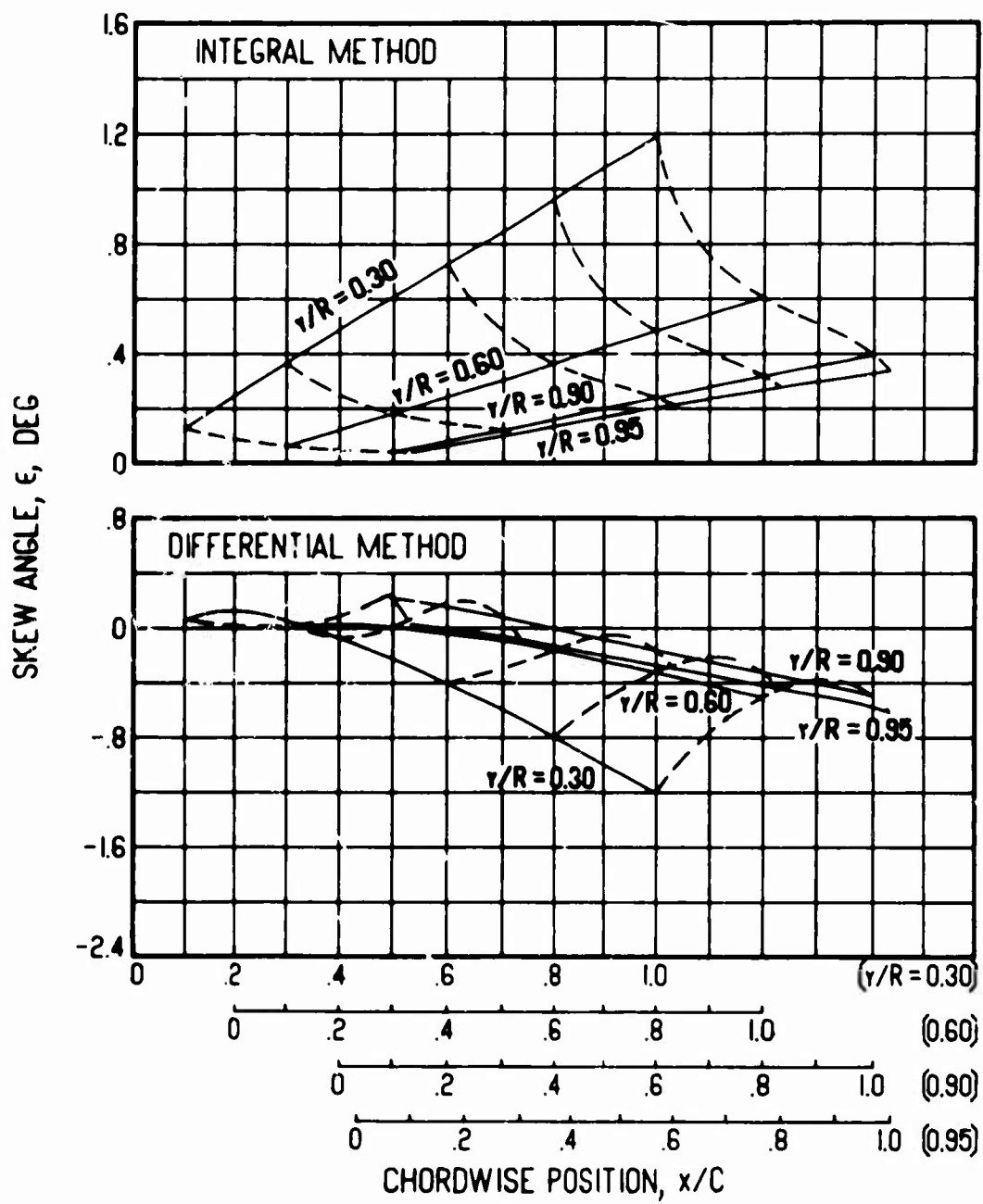
(d) $\Gamma/h = -50$ ft/sec

Figure 26. Concluded.

151
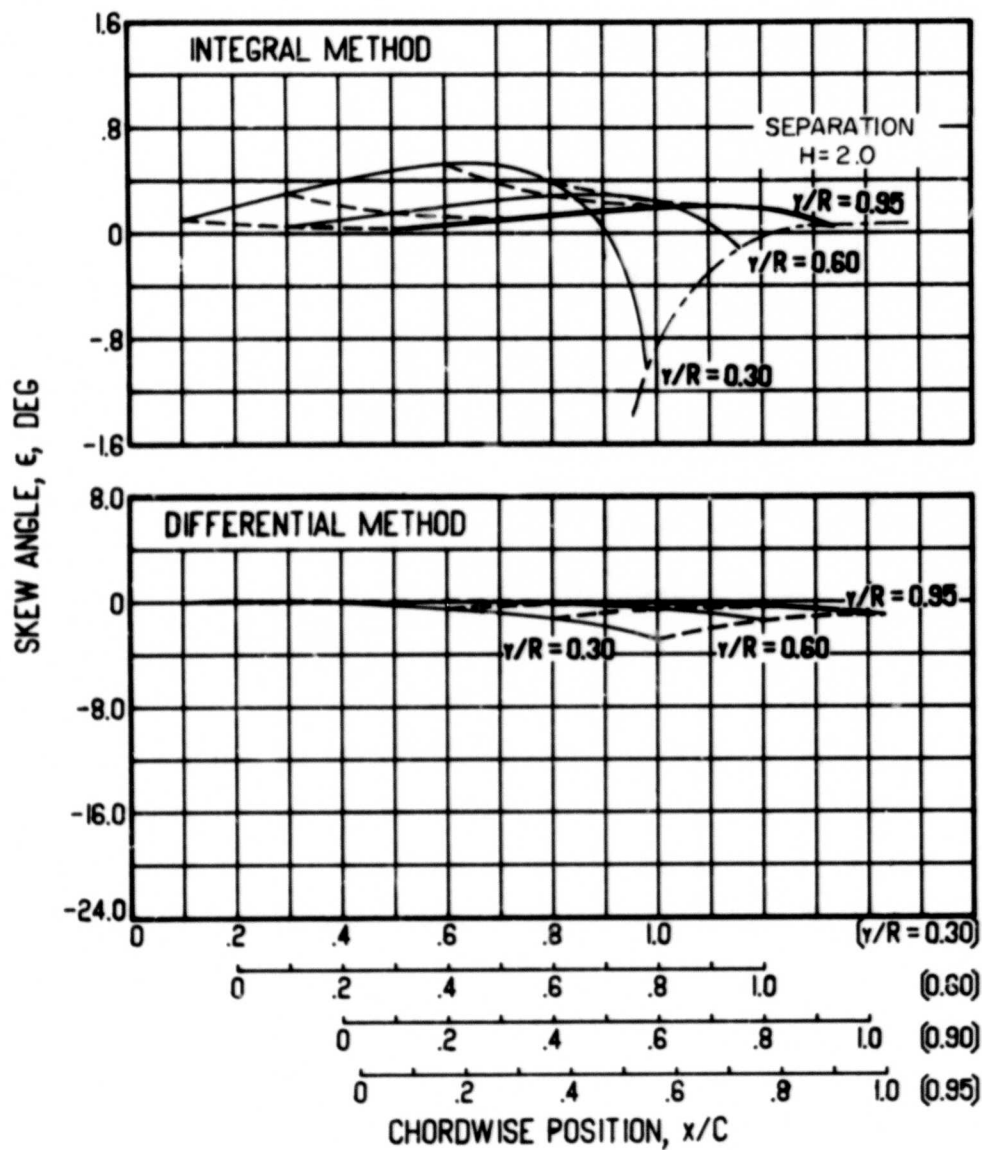
(a) $dCp/d(x/C) = 1$

Figure 27. Skew Angle Versus Chordwise Position for Various
Pressure Gradients, Blade Radius = 10 ft,
Ω = 60 rad/sec, Γ/h = 0 ft/sec, Surface Radius
of Curvature = 4.125 ft.

152
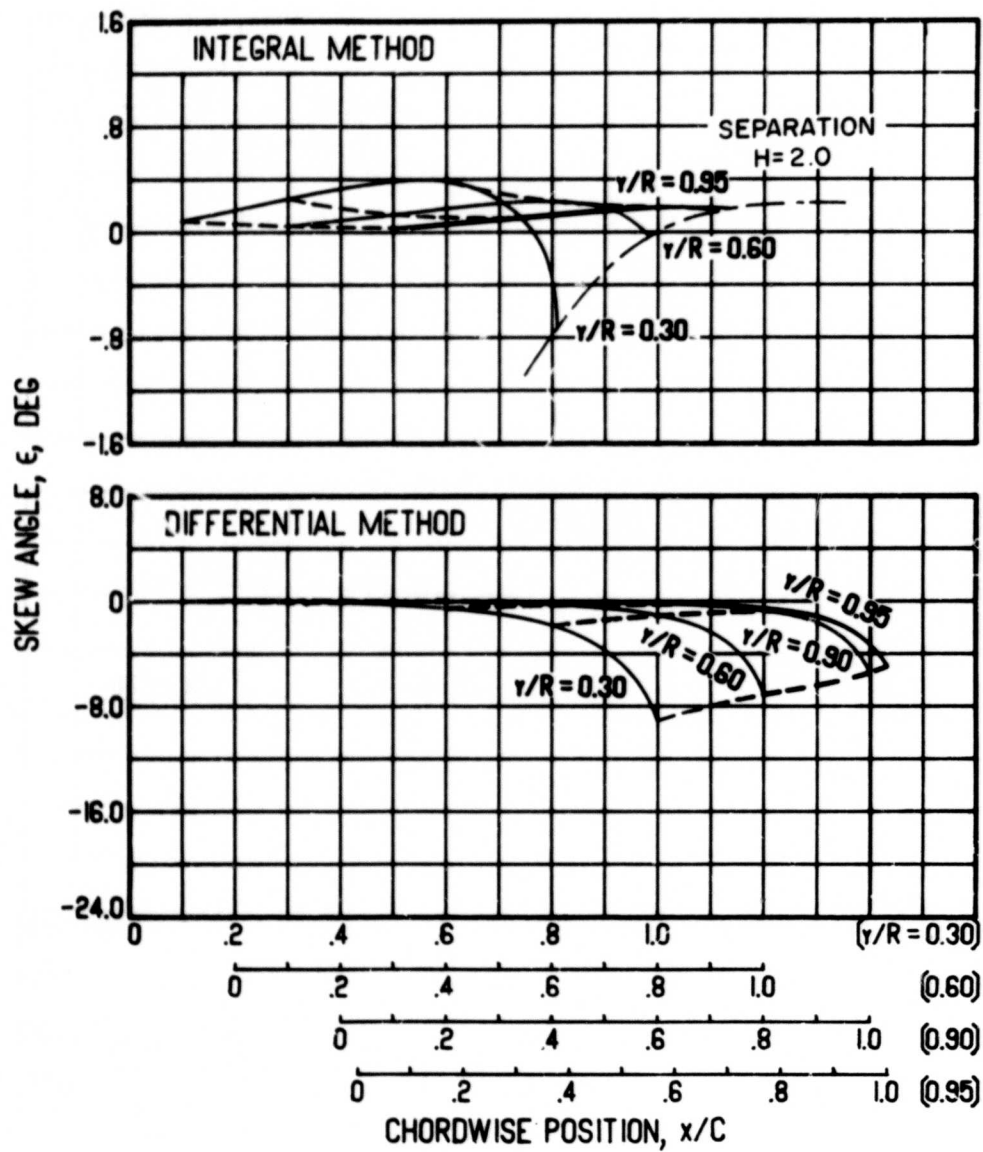
(b) $dCp/d(x/C) = 2$

Figure 27. Concluded.

153
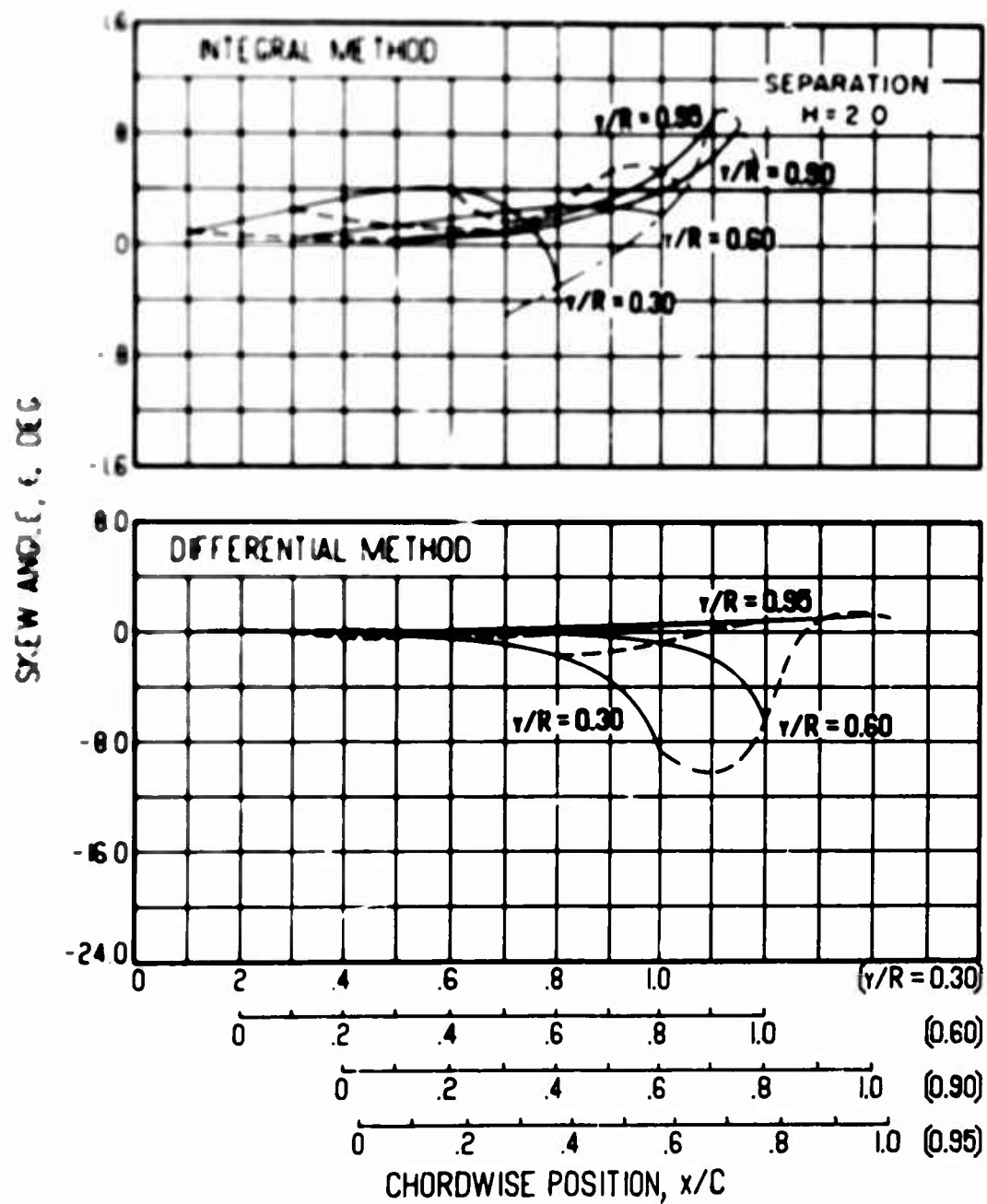
(a) Γ/h = +50 ft/sec

Figure 28. Skew Angle Versus Chordwise Position for Various
Vortex Strengths, Blade Radius = 10 ft,
Ω = 60 rad/sec, dCp/d(x/C) = 2, Surface Radius
of Curvature = 4.125 ft.

154
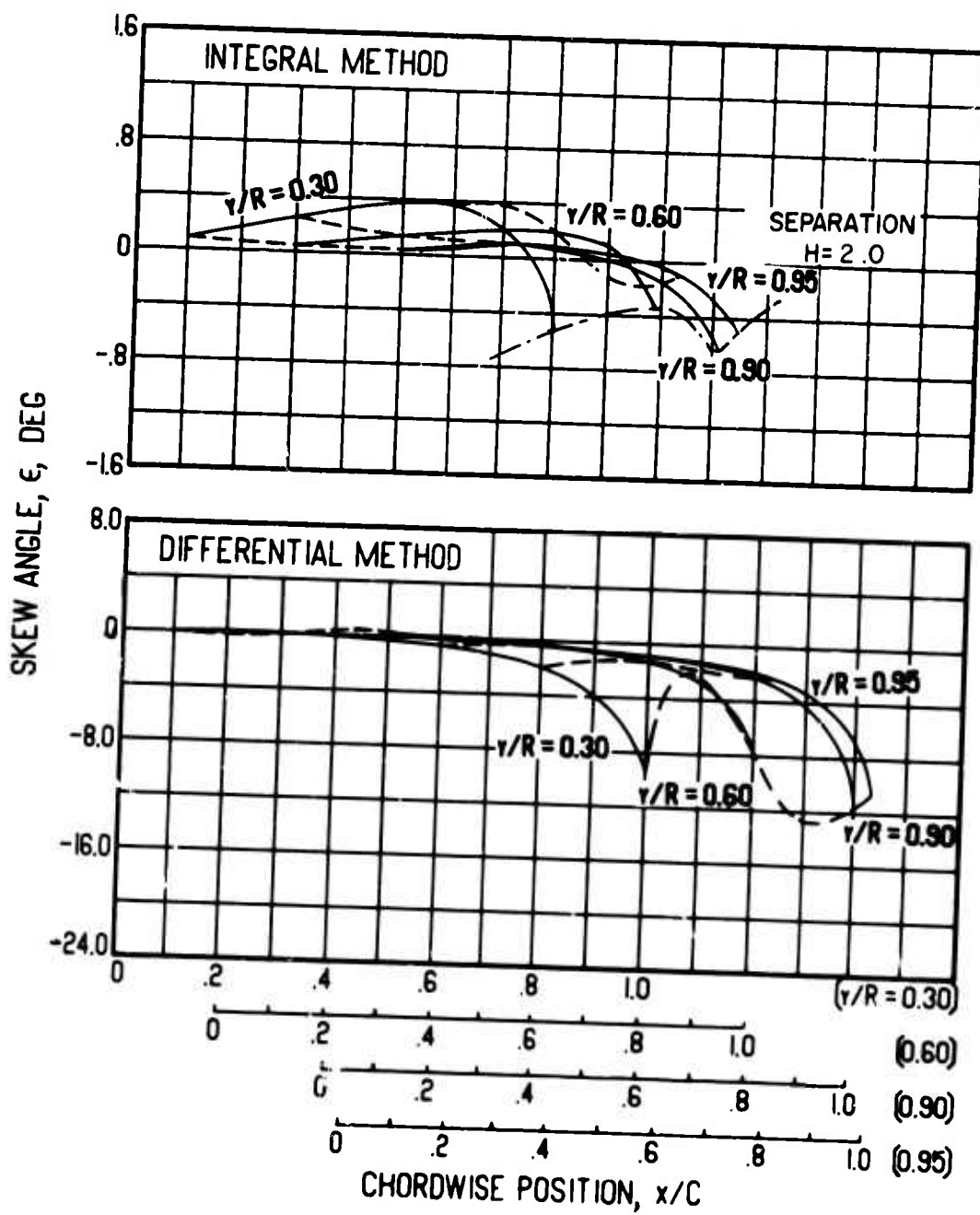
(b) $\Gamma/h = -50$ ft/sec

Figure 28. Concluded.
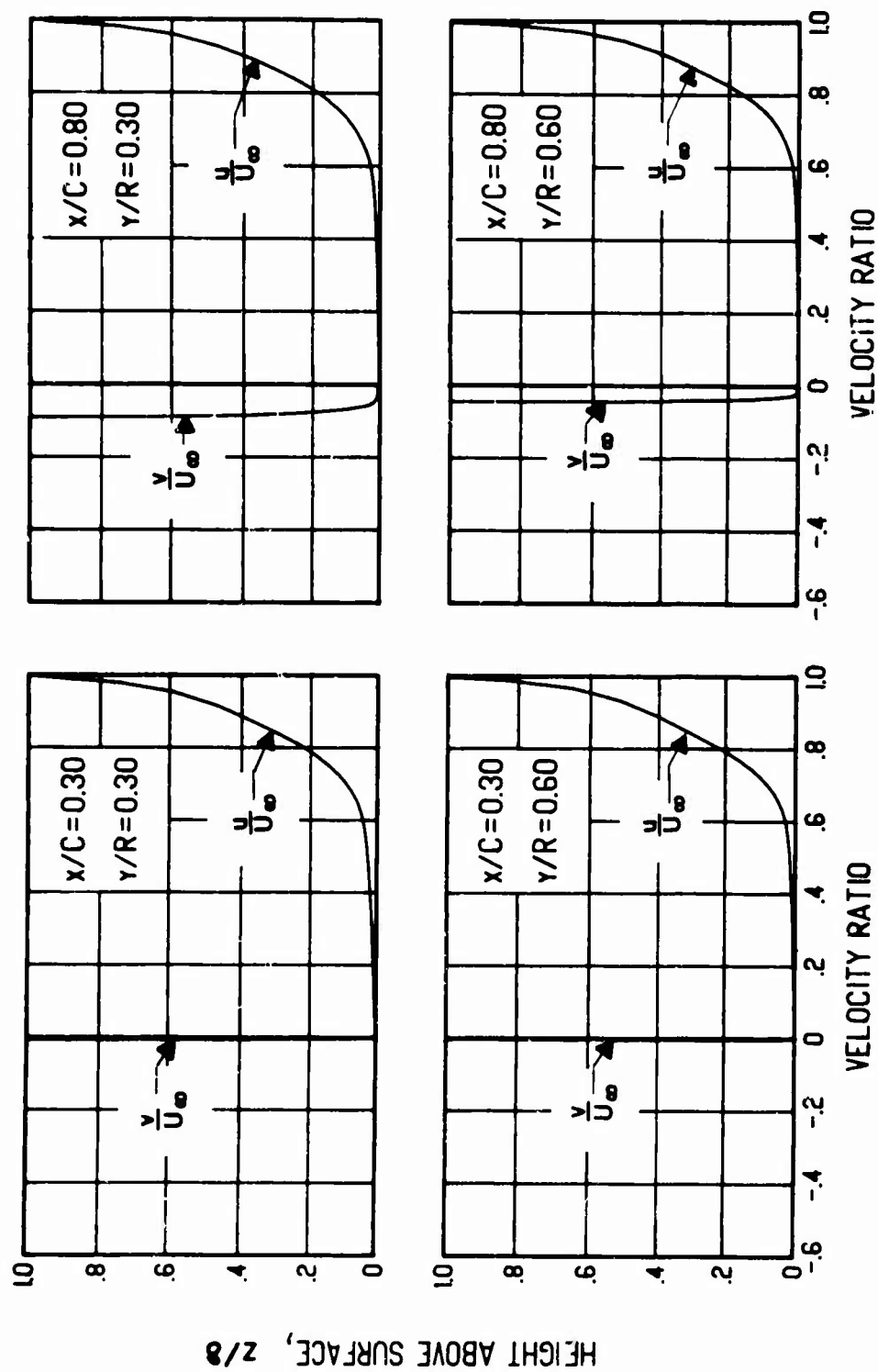
Figure 29. Chordwise and Spanwise Velocity Profiles for Various Angular Velocities, Blade Radius = 40 ft, Γ/h = 0 ft/sec, $dCp/d(x/C)$ = 0, Flat Surface.

(a) Ω = 10 rad/sec
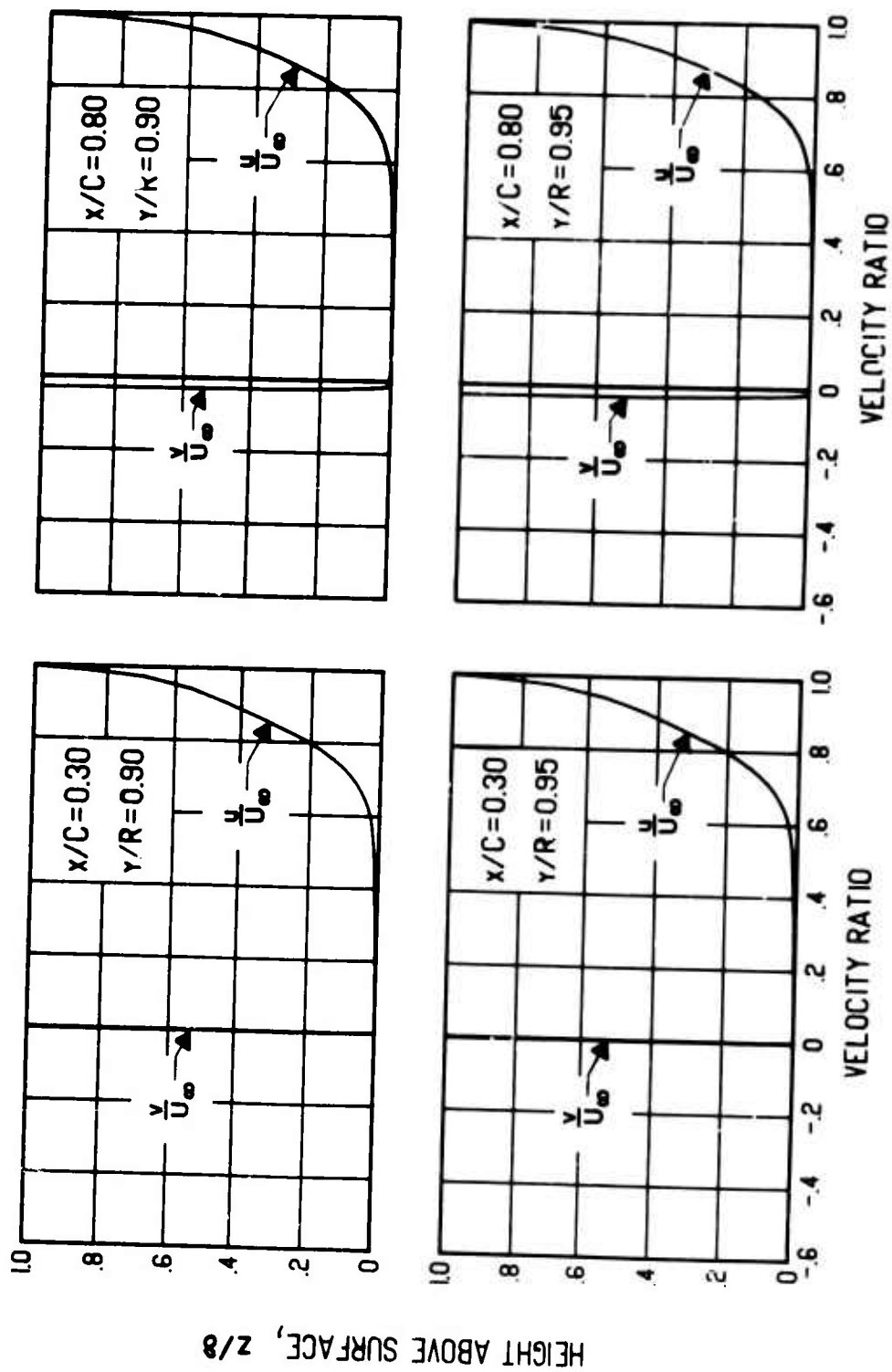
(a) Concluded.

Figure 29. Continued.
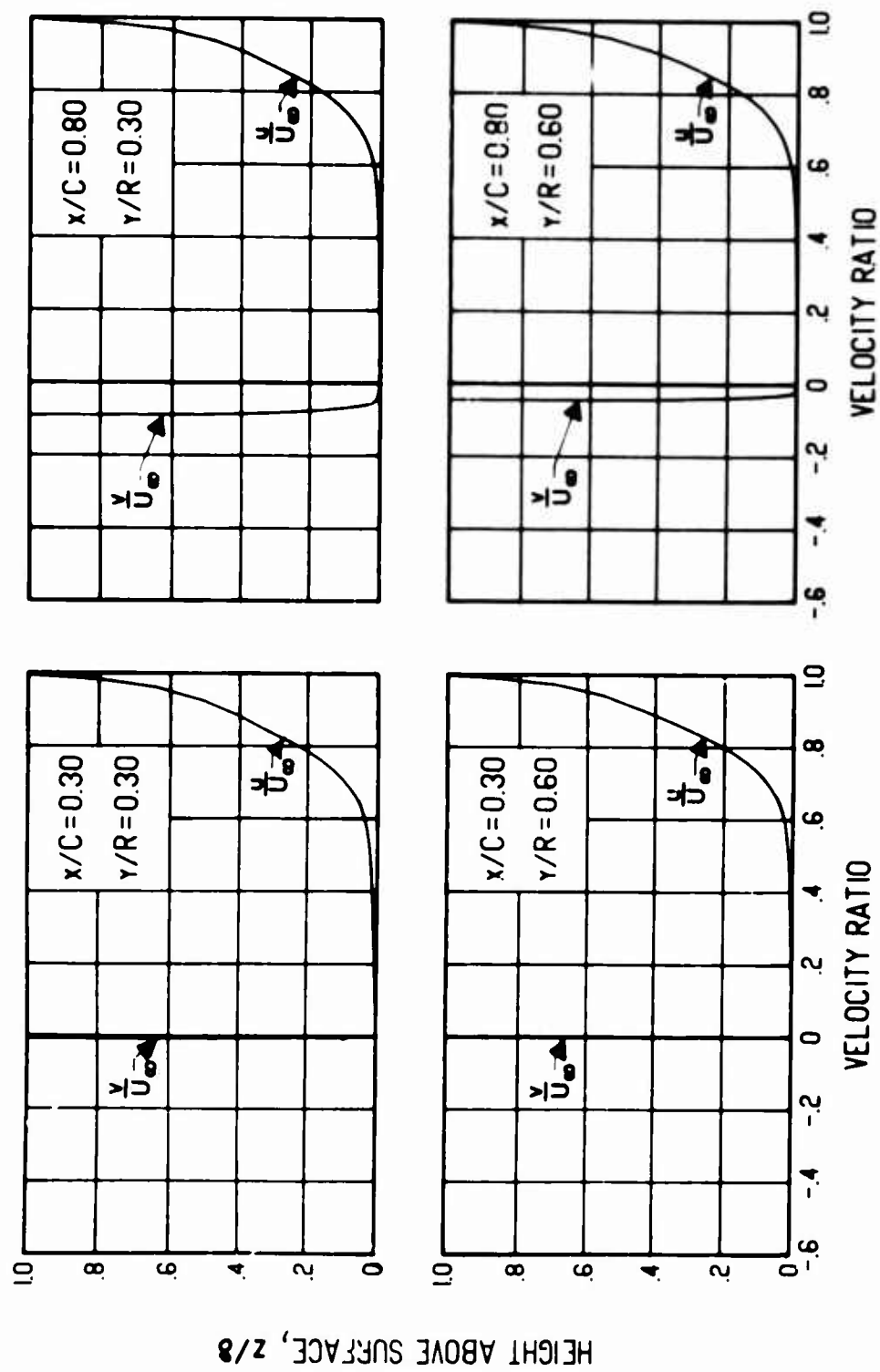
(b) $\Omega = 15$ rad/sec

Figure 29. Continued.

158

(b) Concluded.

Figure 29. Continued.

159
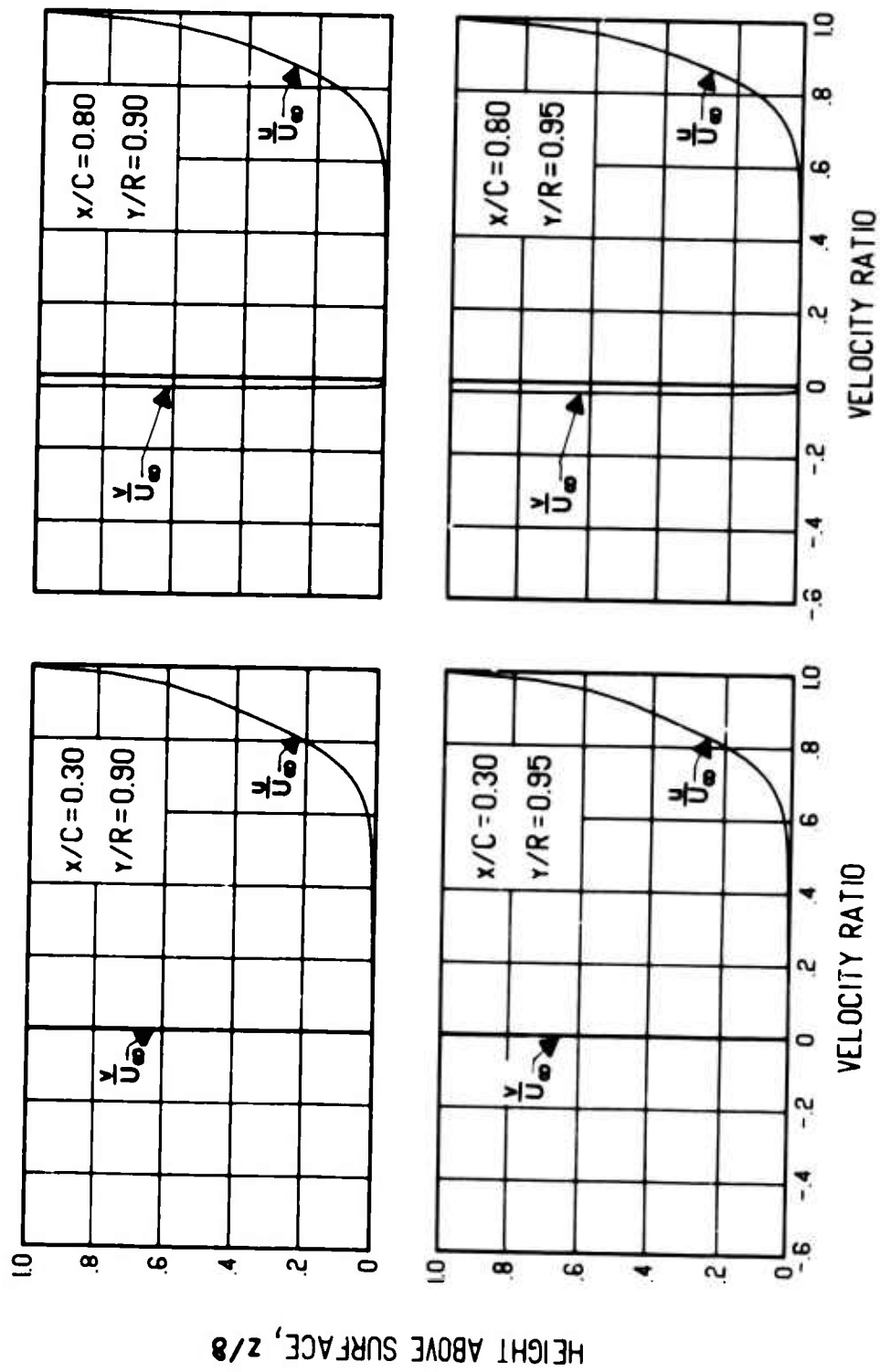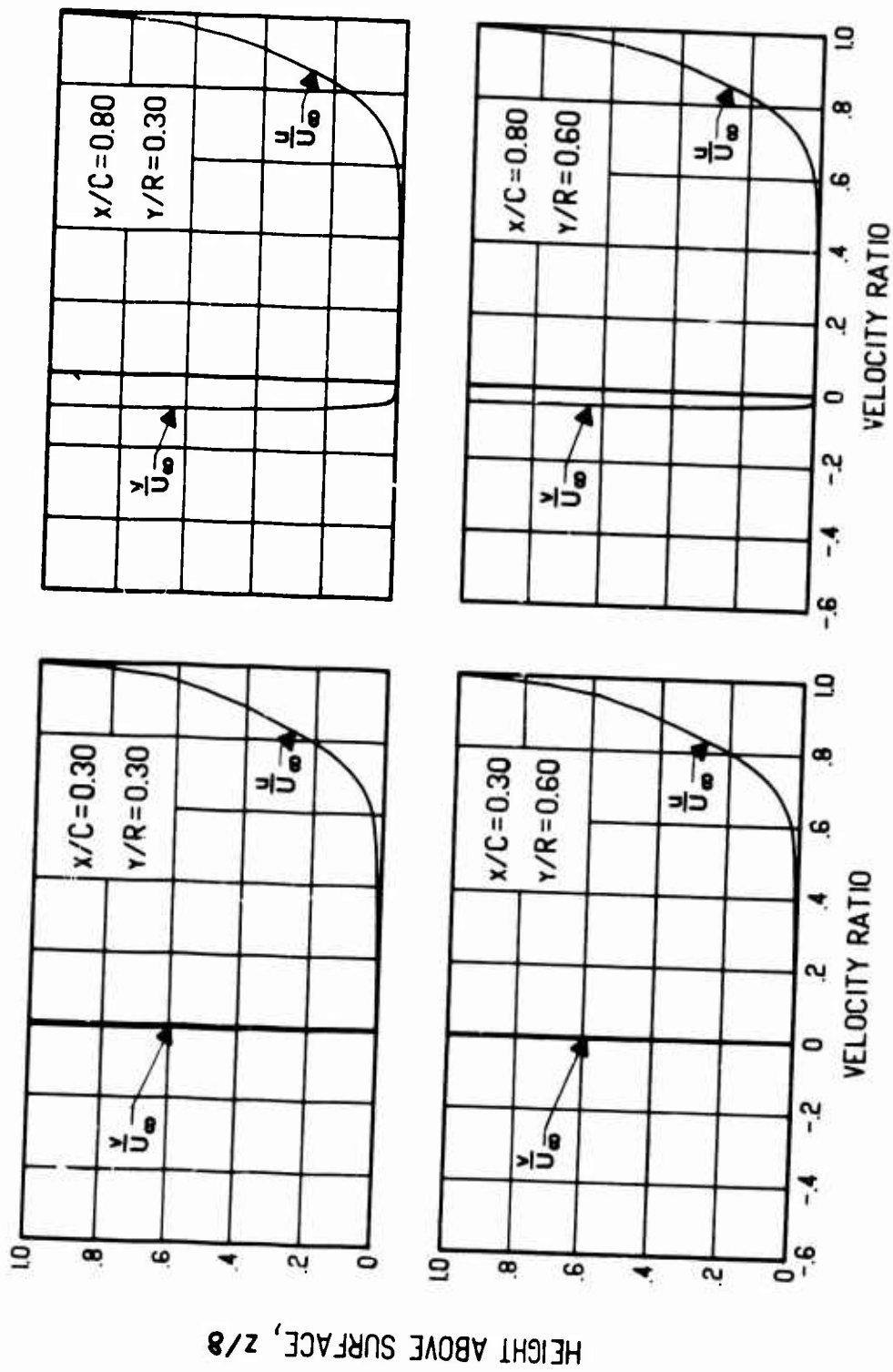
(c) $\Omega = 20$ rad/sec
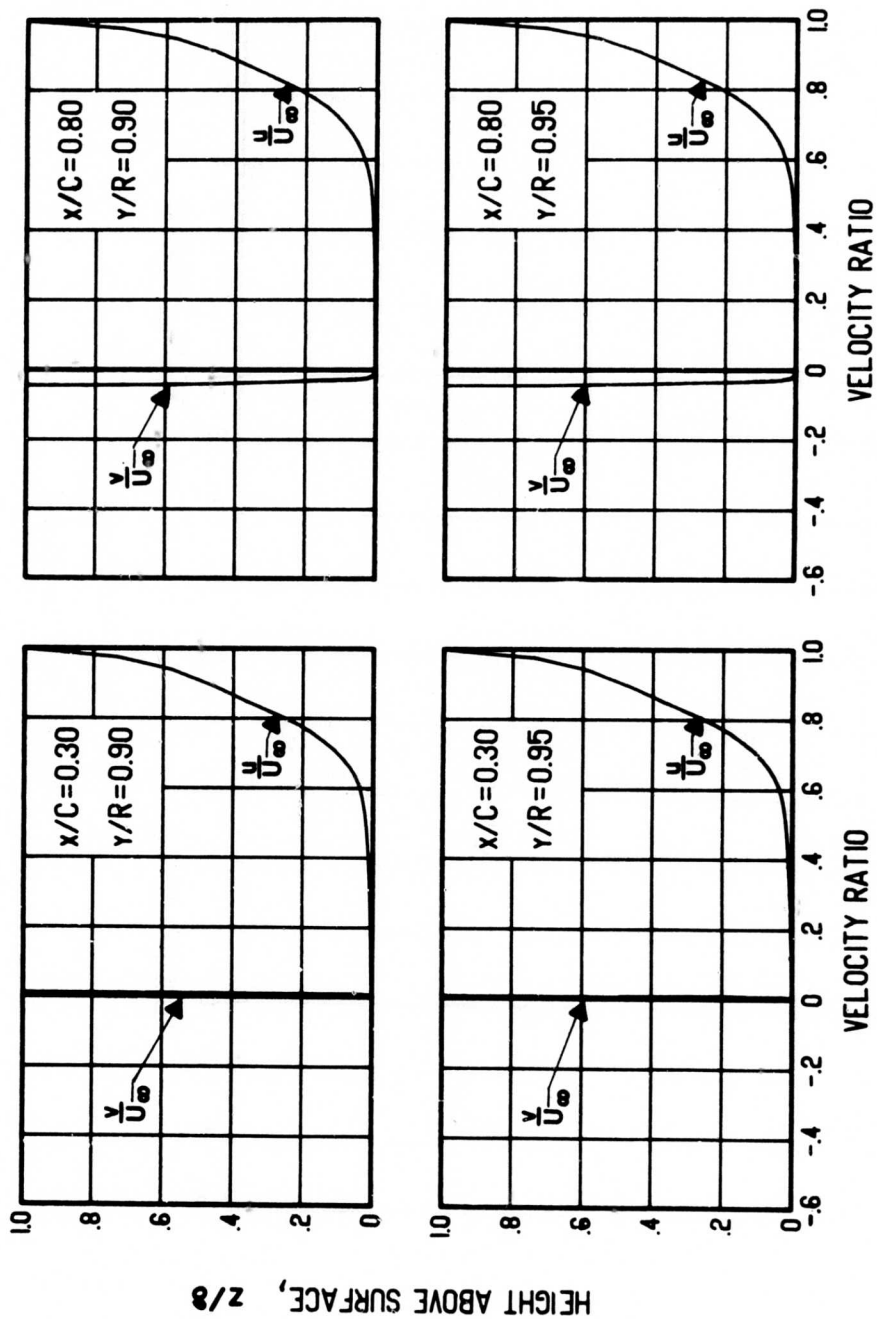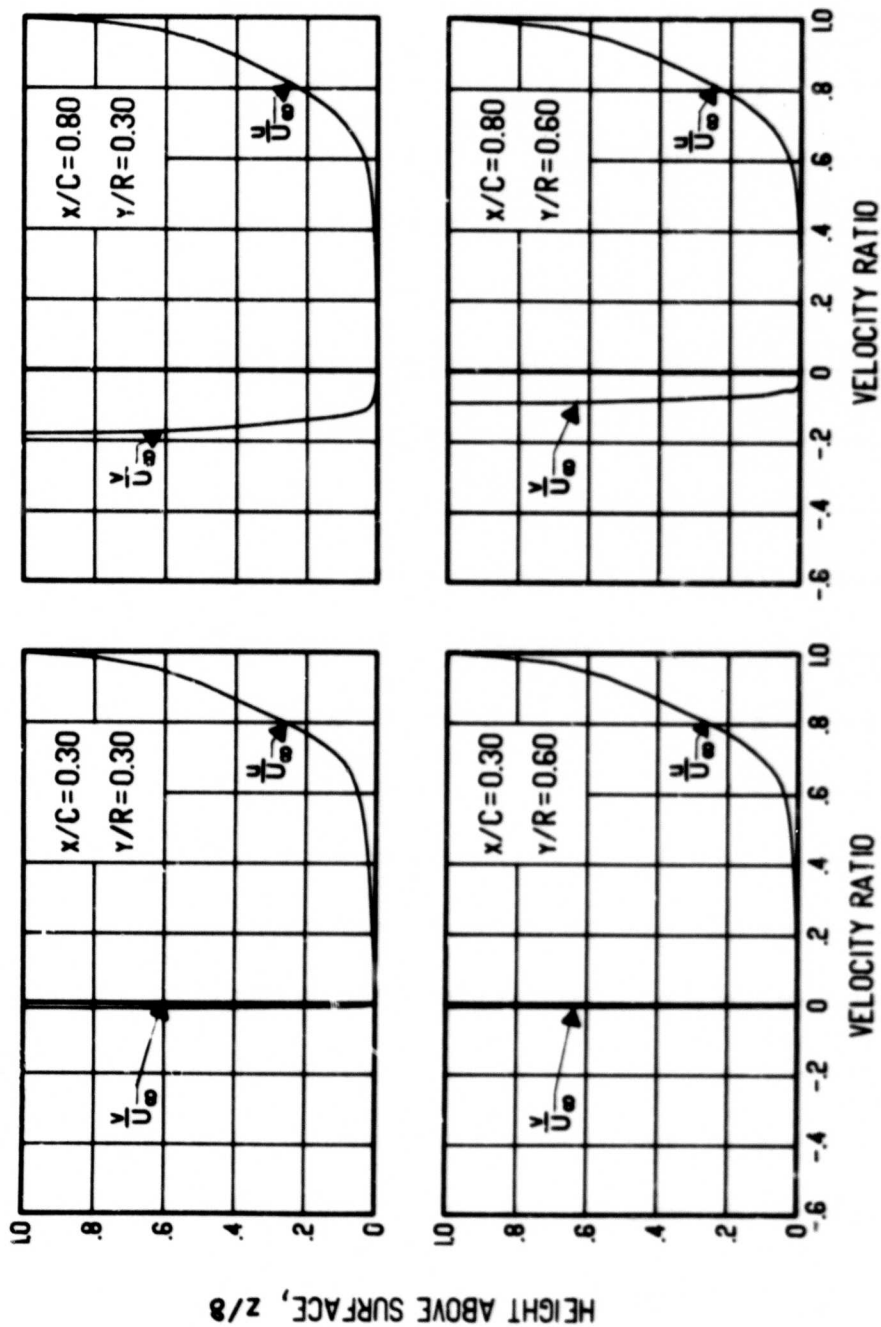
Figure 29. Continued.
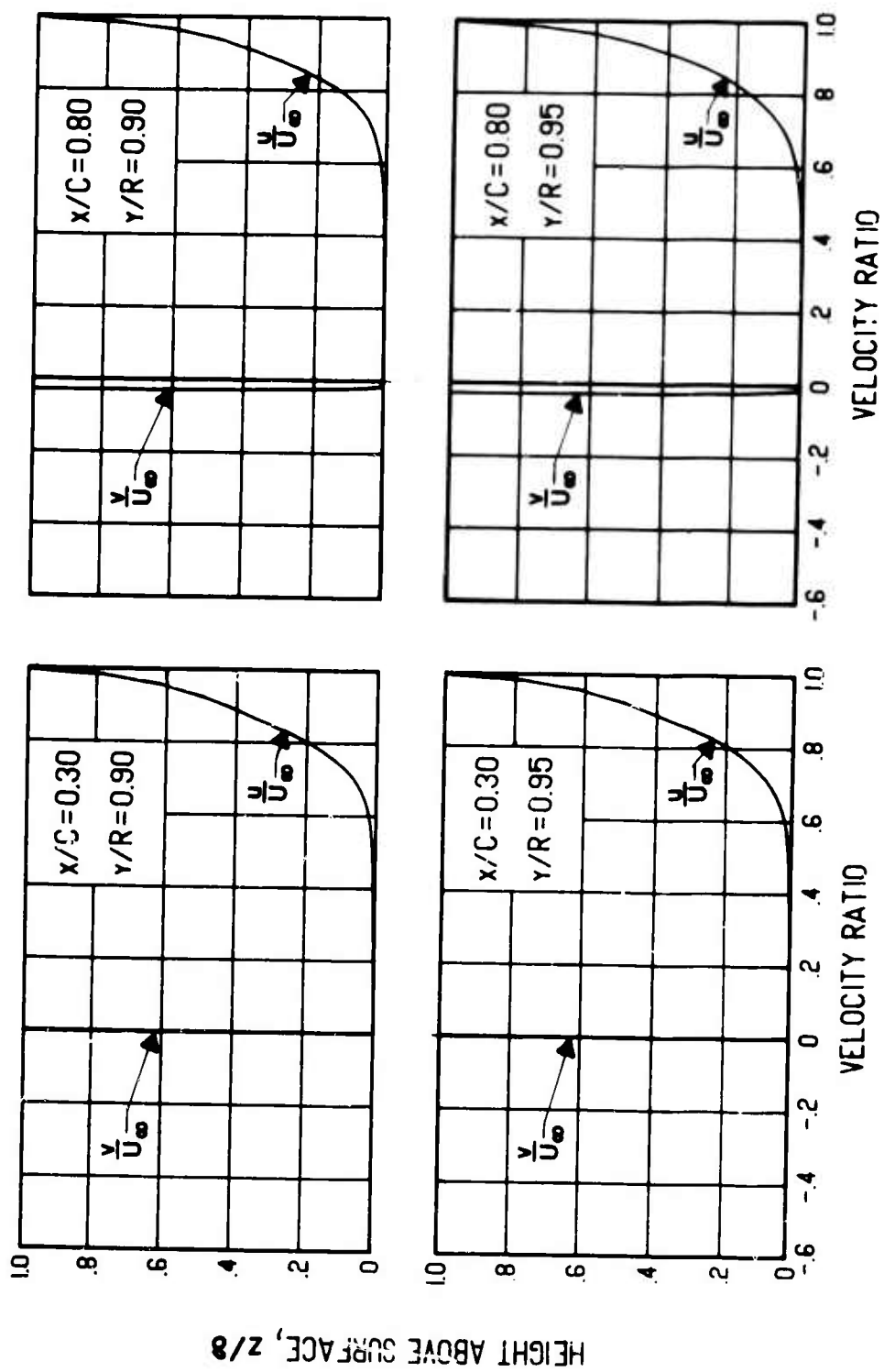
(c) Concluded.

Figure 29. Concluded.

161
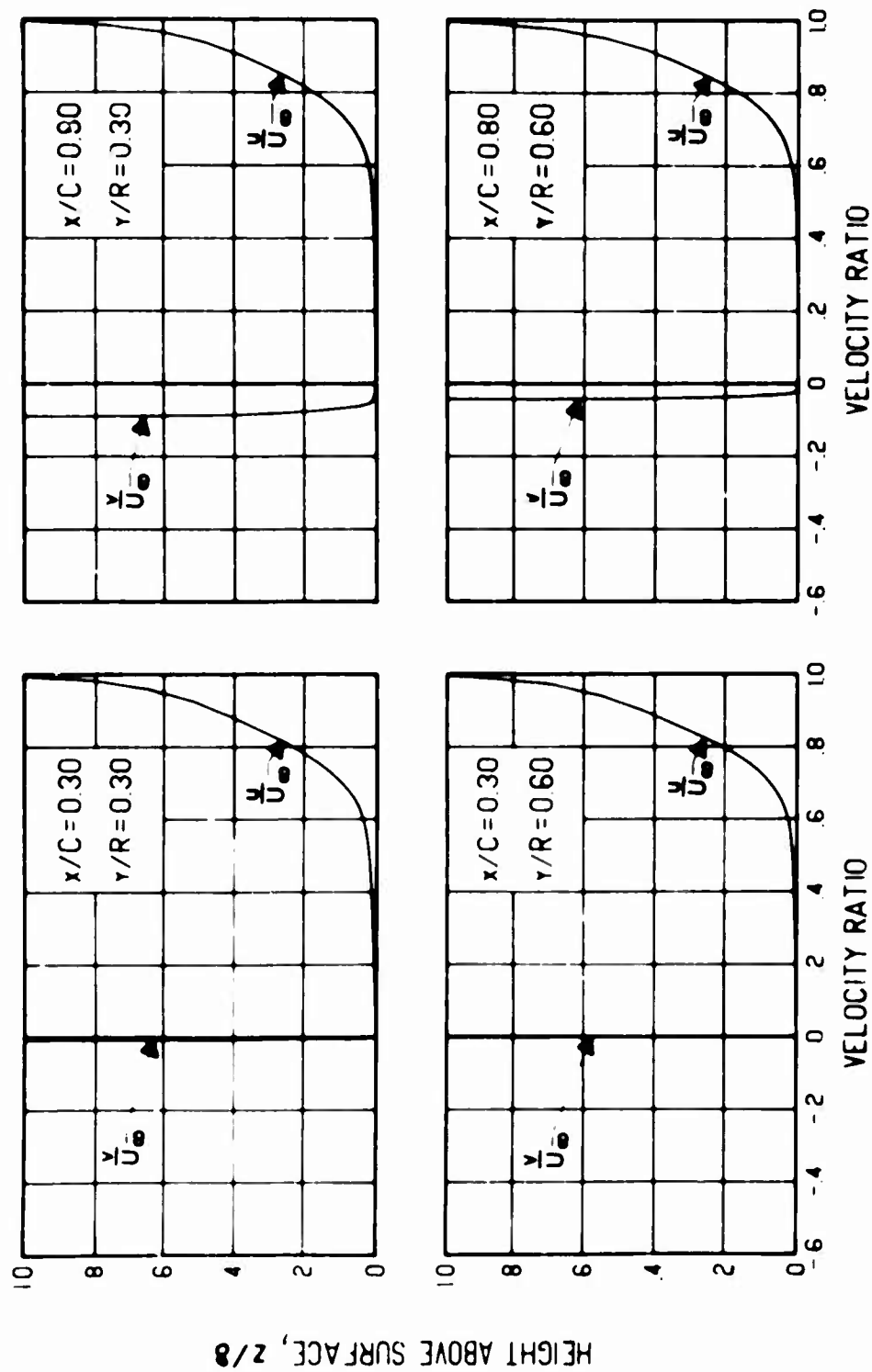
Figure 30. Chordwise and Spanwise Velocity Profiles for Various Vortex Strengths, Blade Radius = 40 ft, Ω = 15 rad/sec, dCp/d(x/C) = 0, Flat Surface.

(a) Γ/h = +100 ft/sec

162

(a) Concluded.

Figure 30. Continued.

163
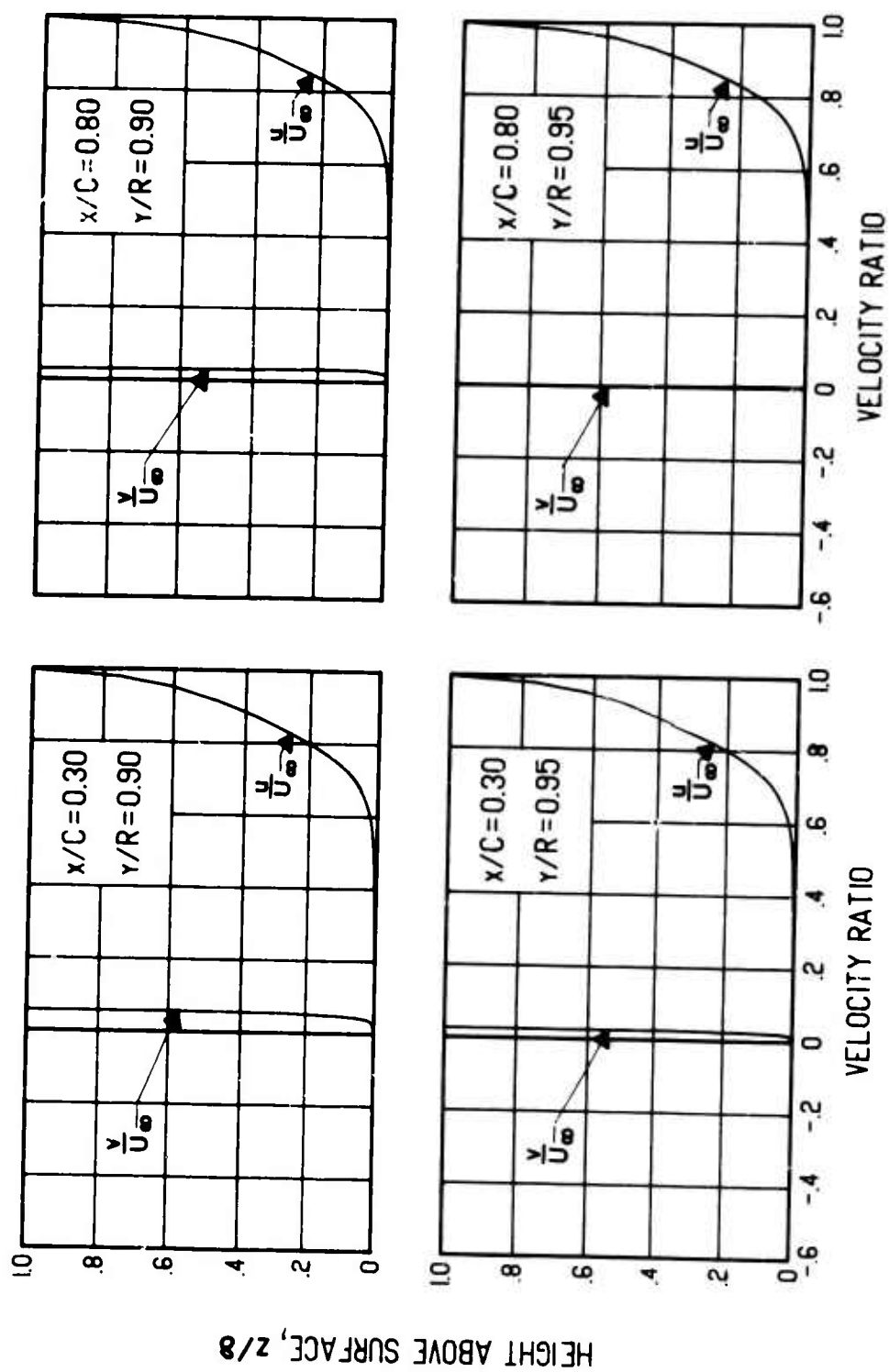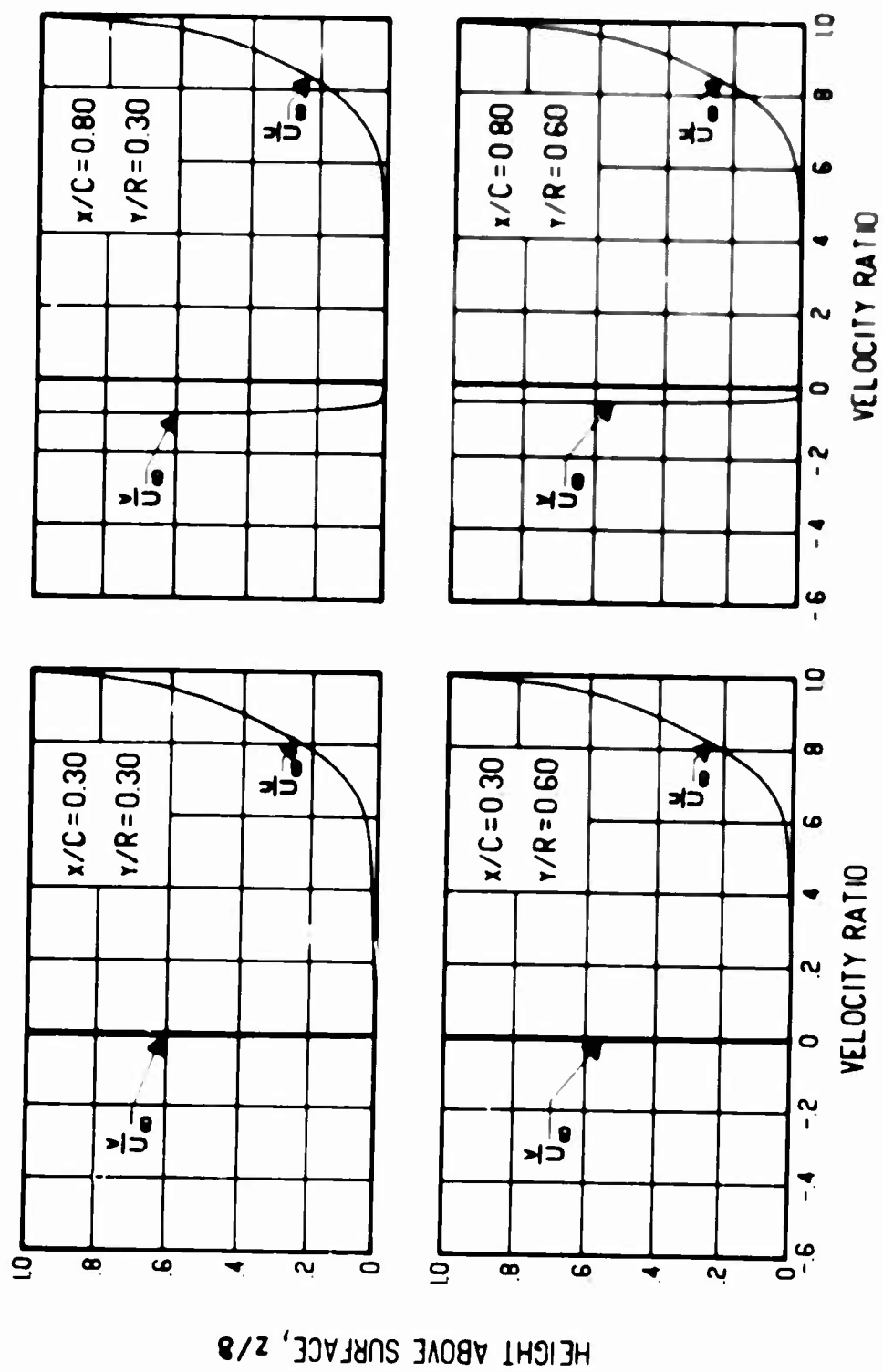
(b) $\Gamma/h = -100$ ft/sec

Figure 30. Continued.
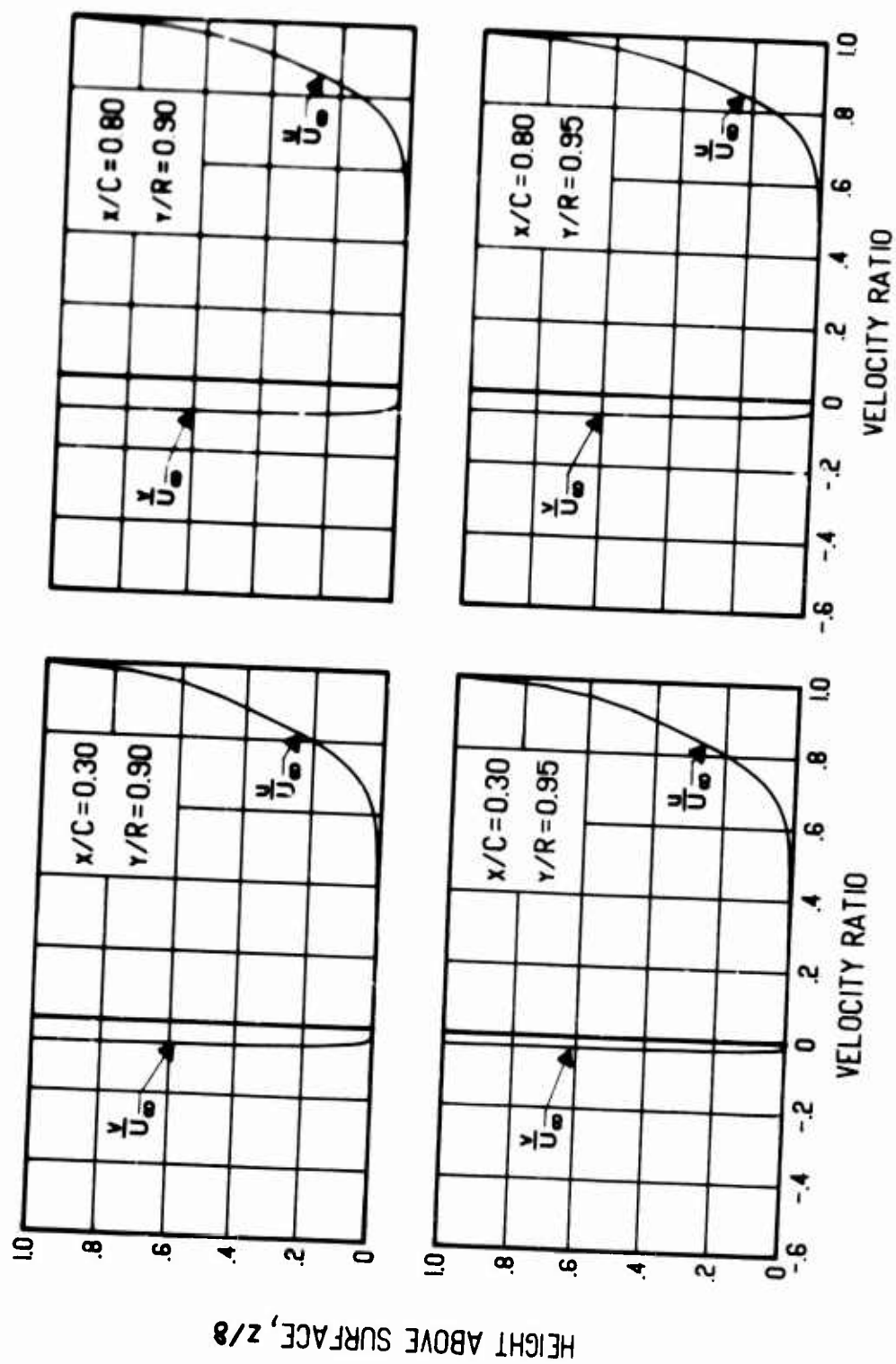
(b) Concluded.

Figure 30. Continued.

(c) $\Gamma/h = +200$ ft/sec

Figure 30. Continued.

166
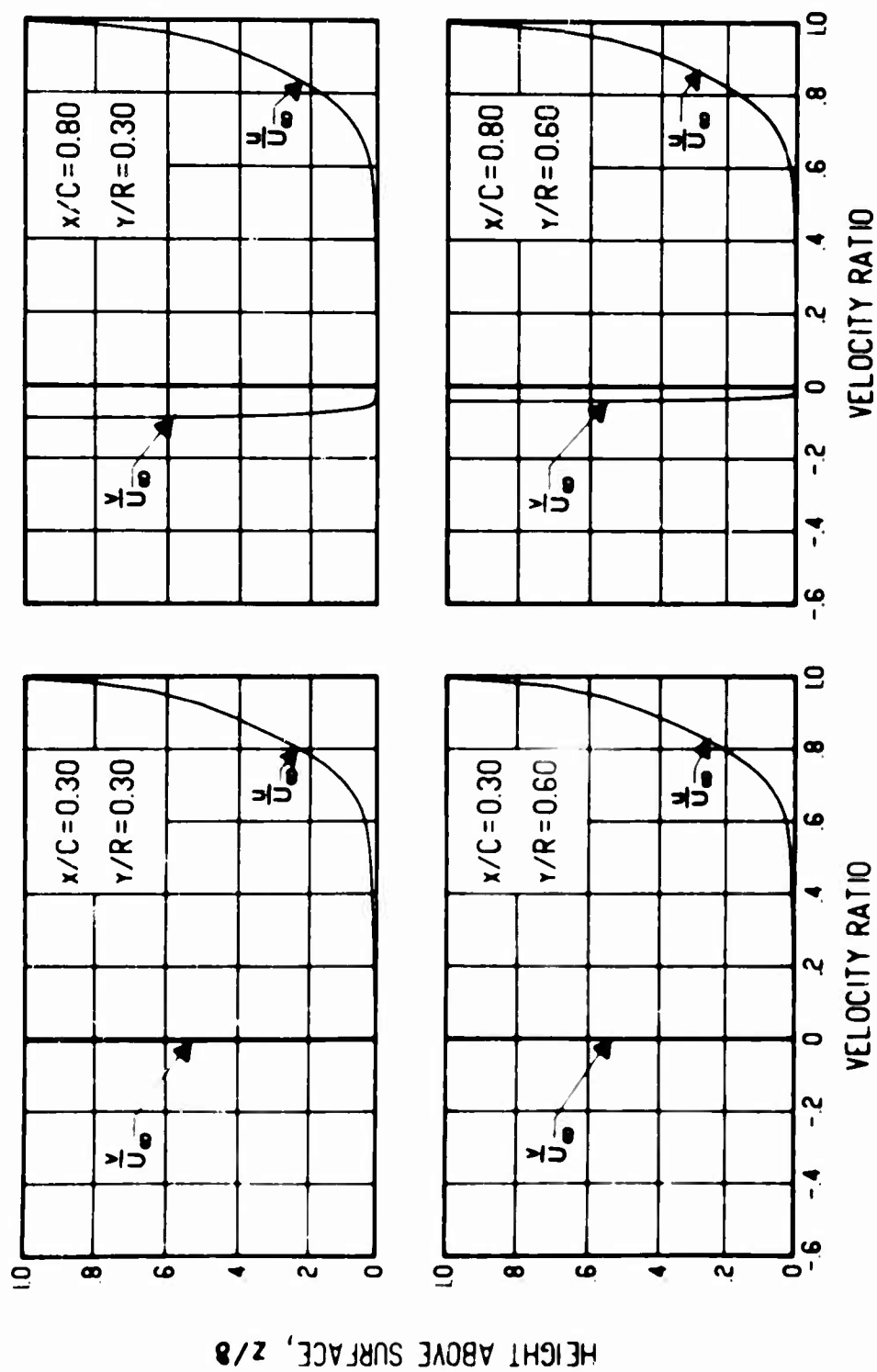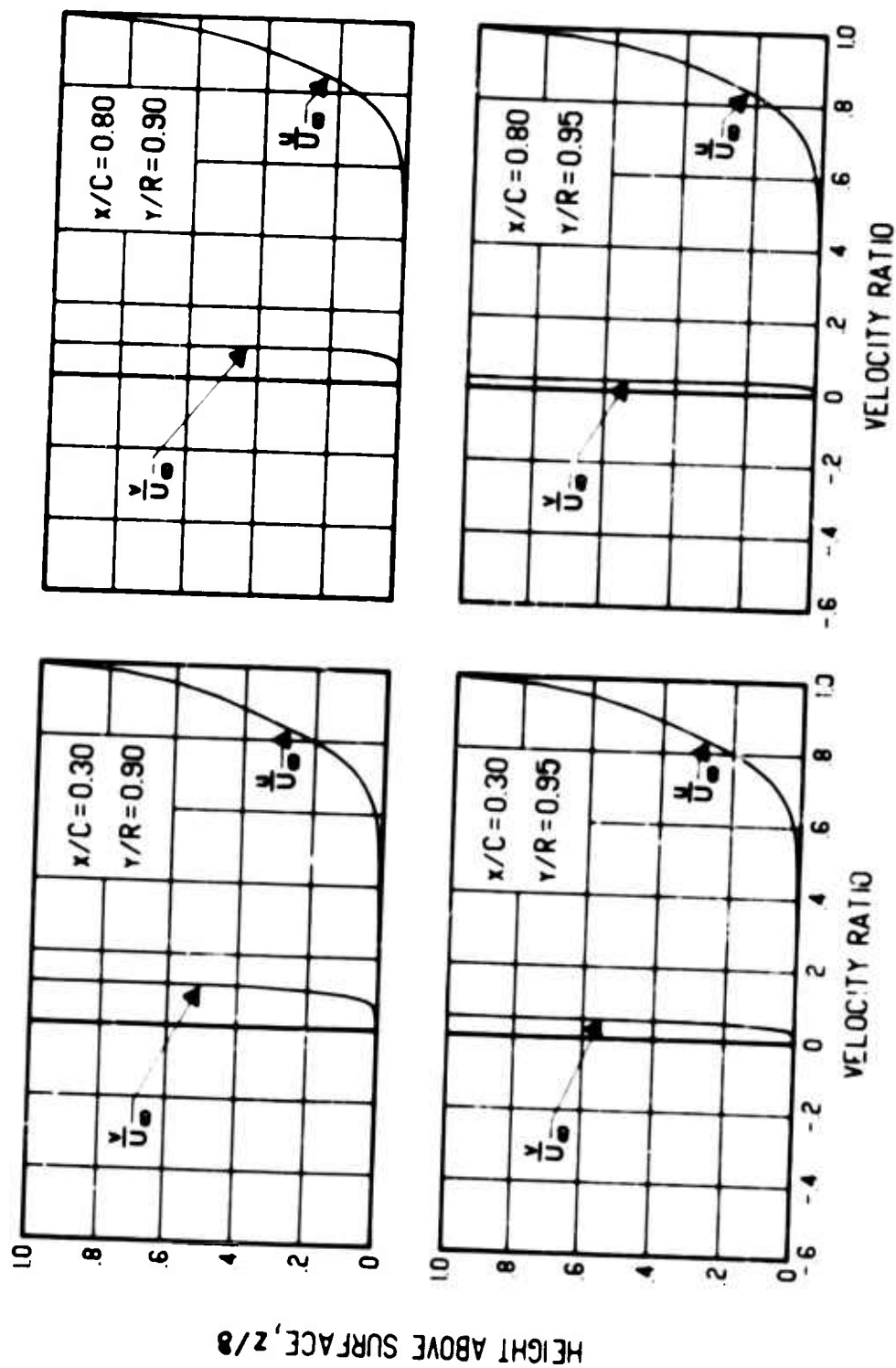
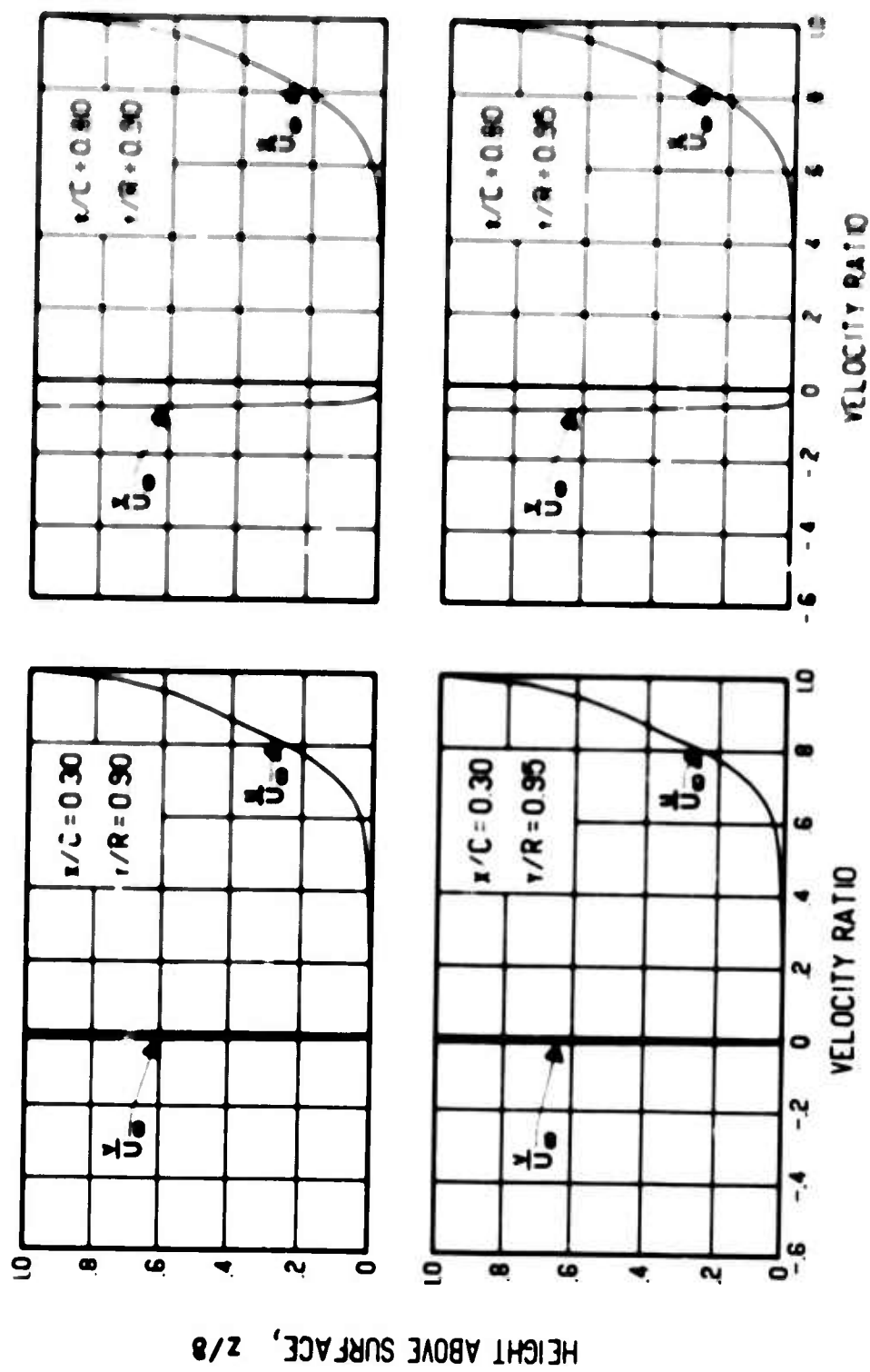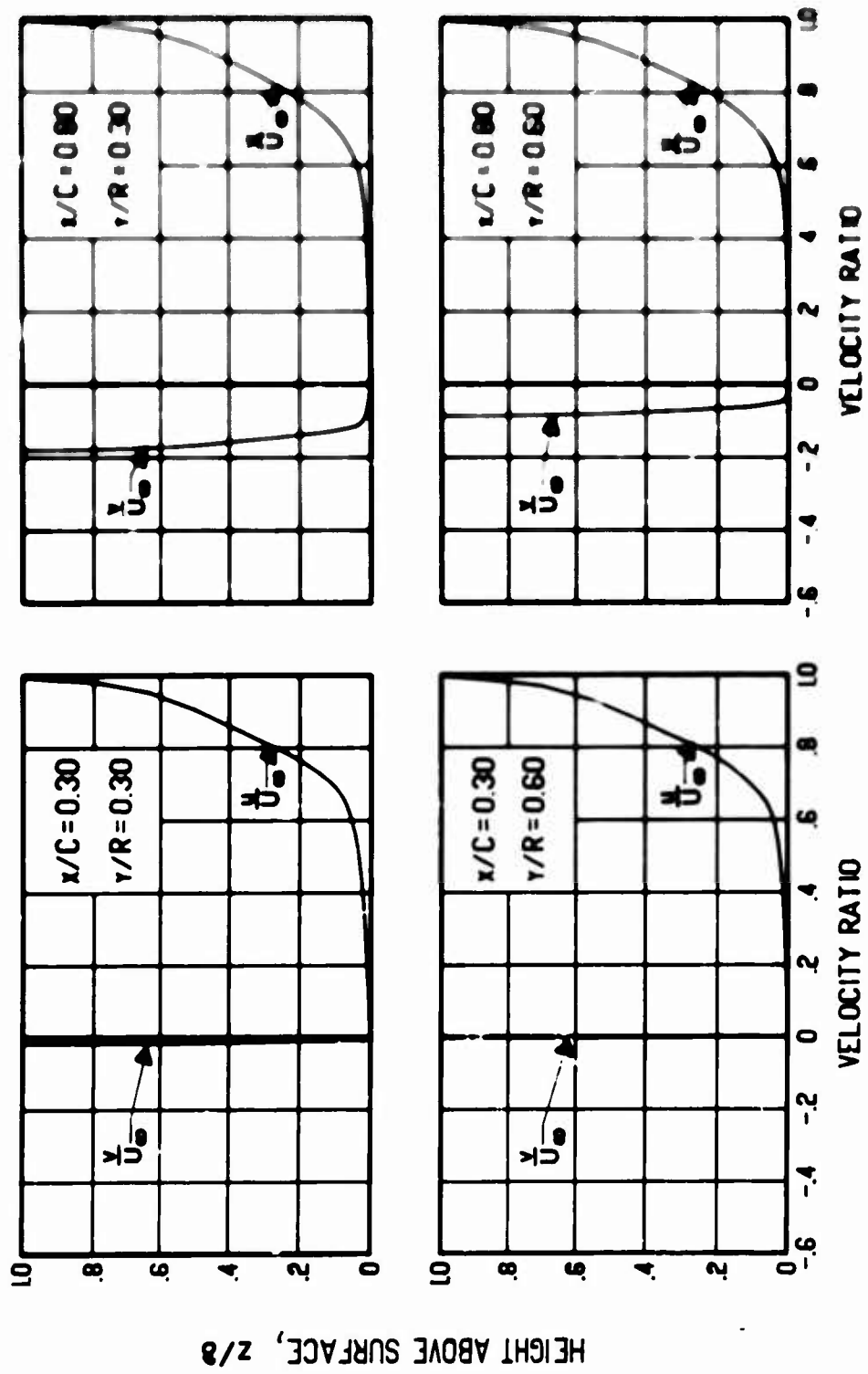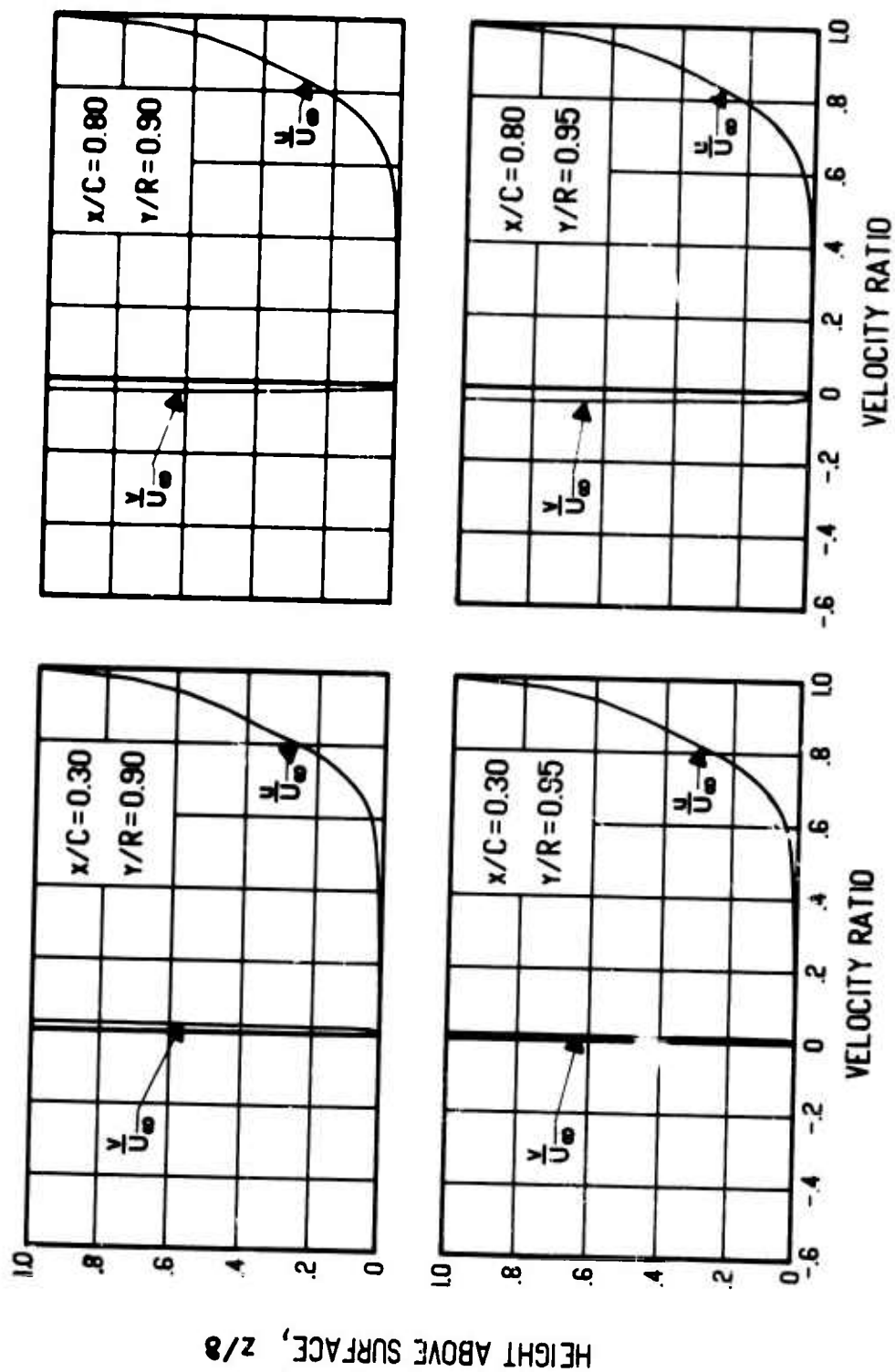(c) Concluded.

Figure 30. Continued.
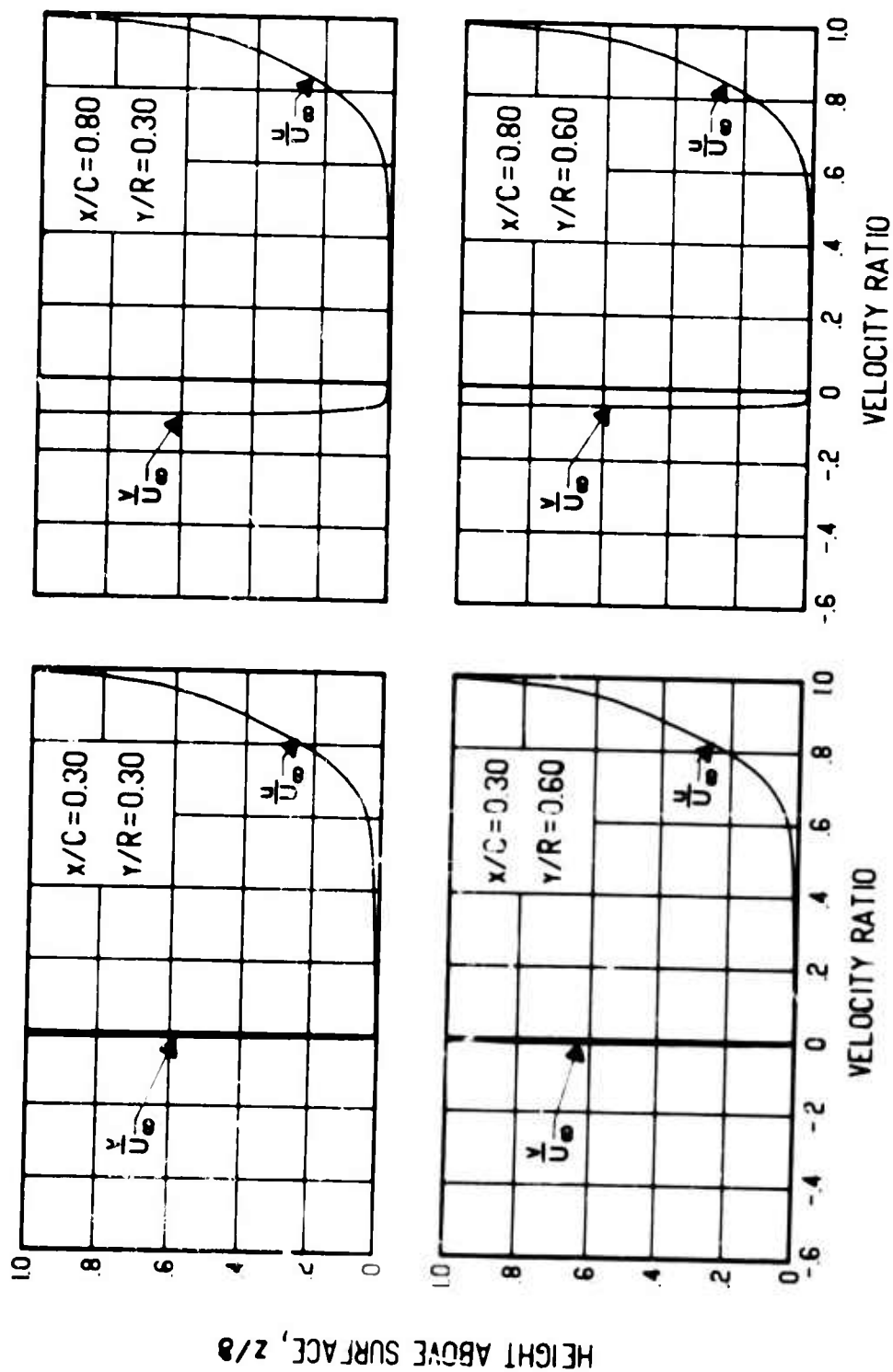
(d, $\Gamma/h = -200$ ft/sec

Figure 30. Continued.
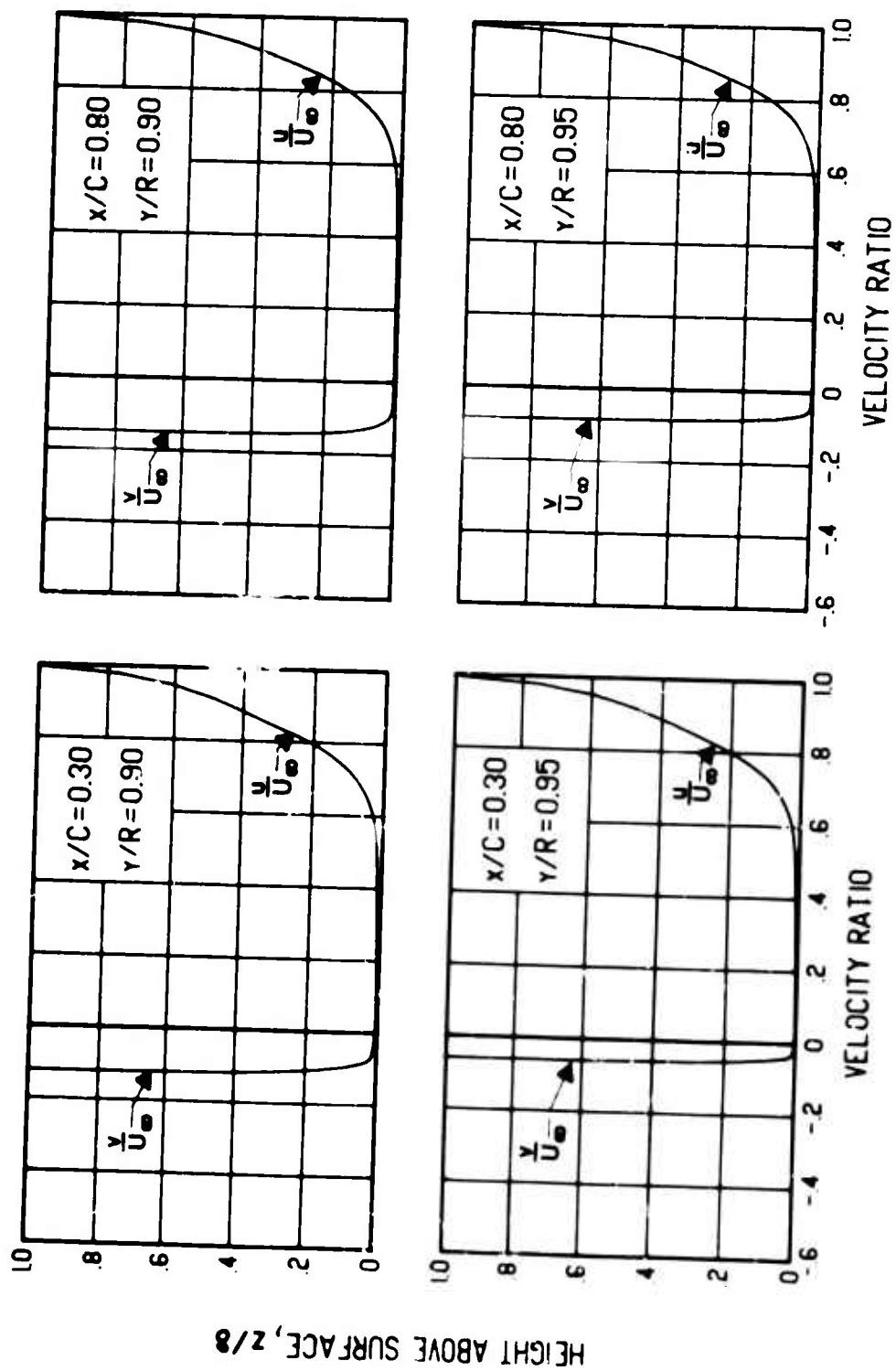
(d) Concluded.

Figure 30. Concluded.
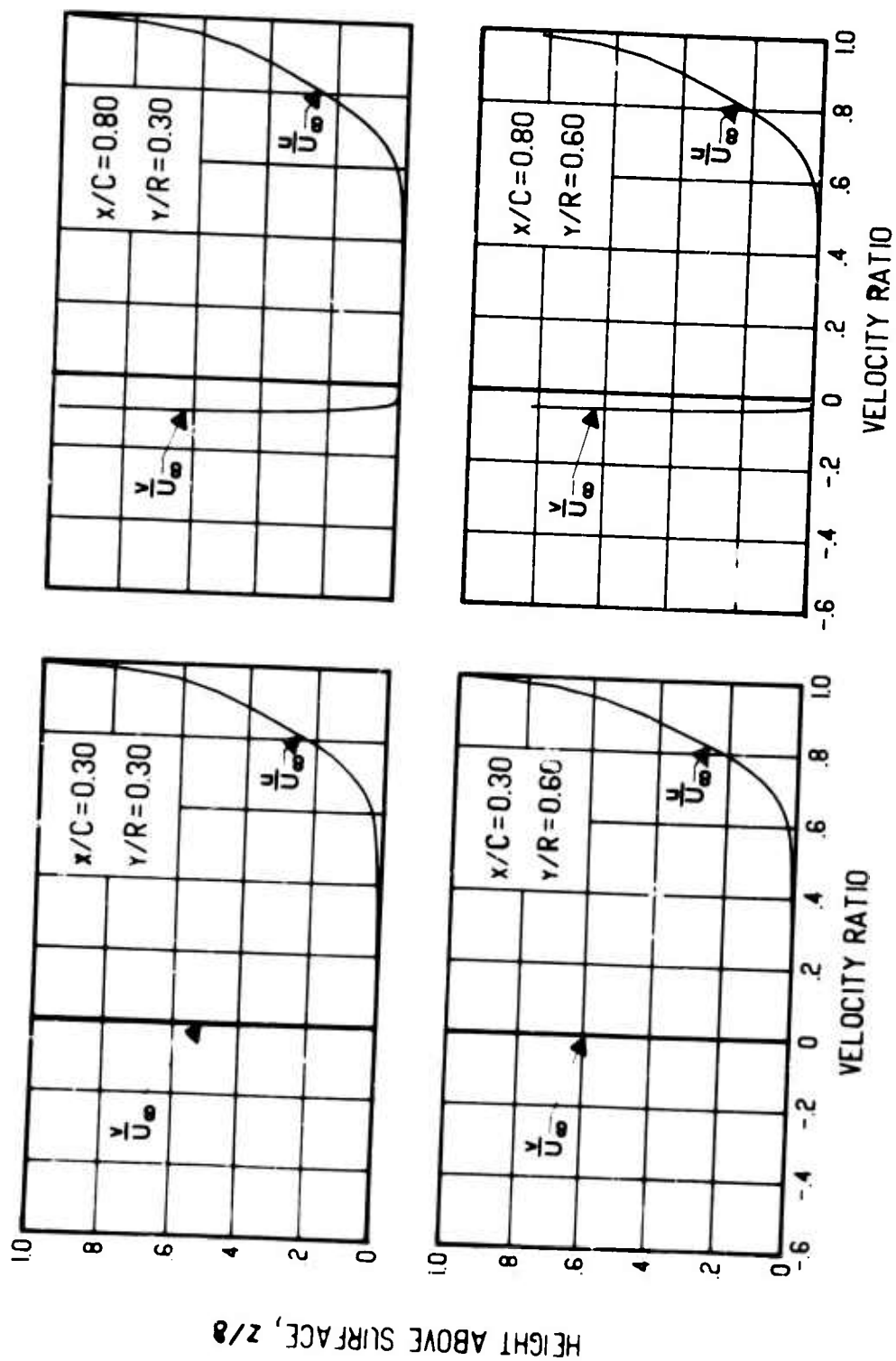
Figure 31. Chordwise and Spanwise Velocity Profiles for Various Pressure Gradients, Blade Radius = 40 ft, Ω = 15 rad/sec, Γ/h = 0 ft/sec, Flat Surface.
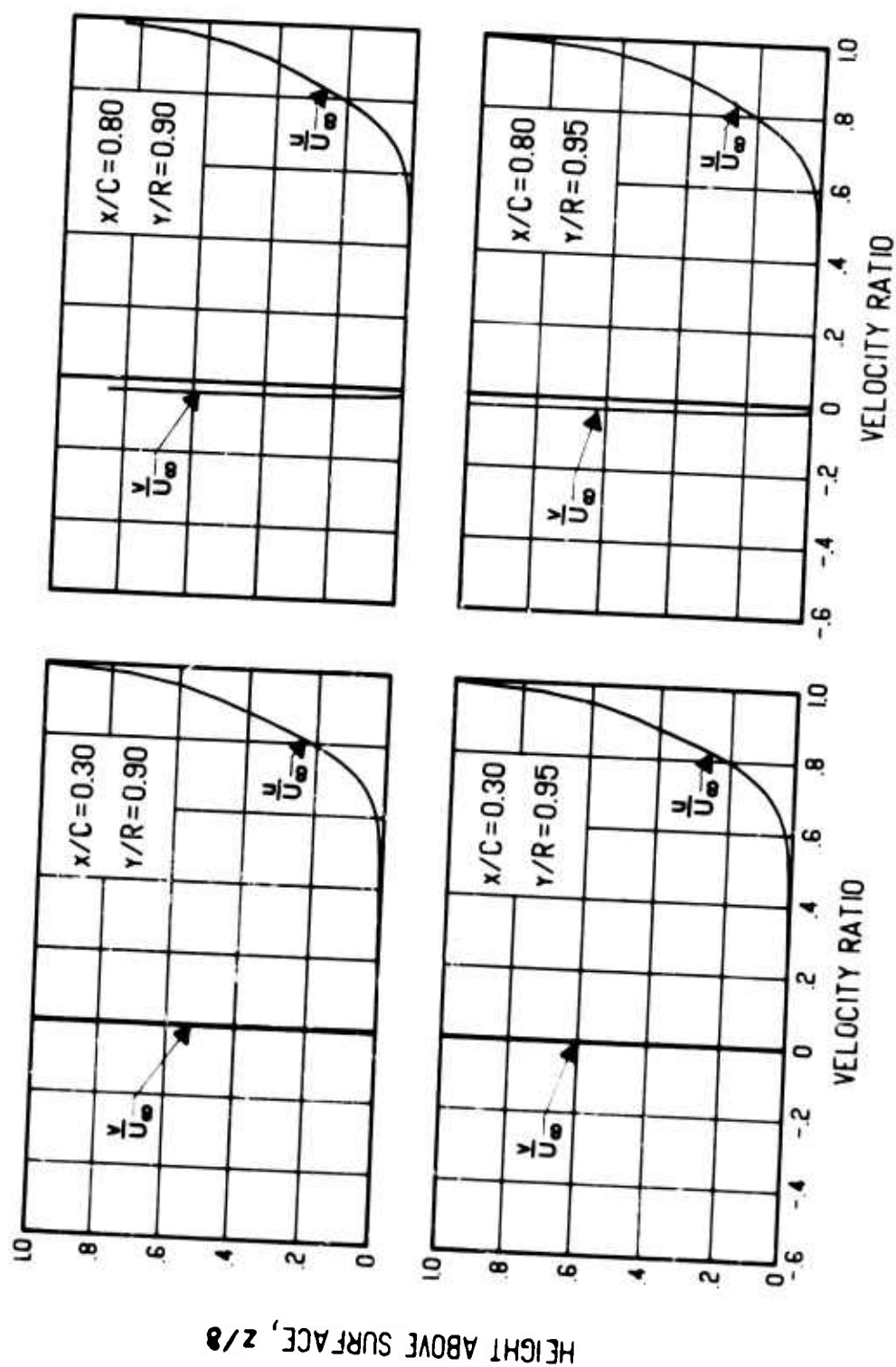
(a) $dCp/d(x/C) = 1$

(a) Concluded.

Figure 31. Continued.

171
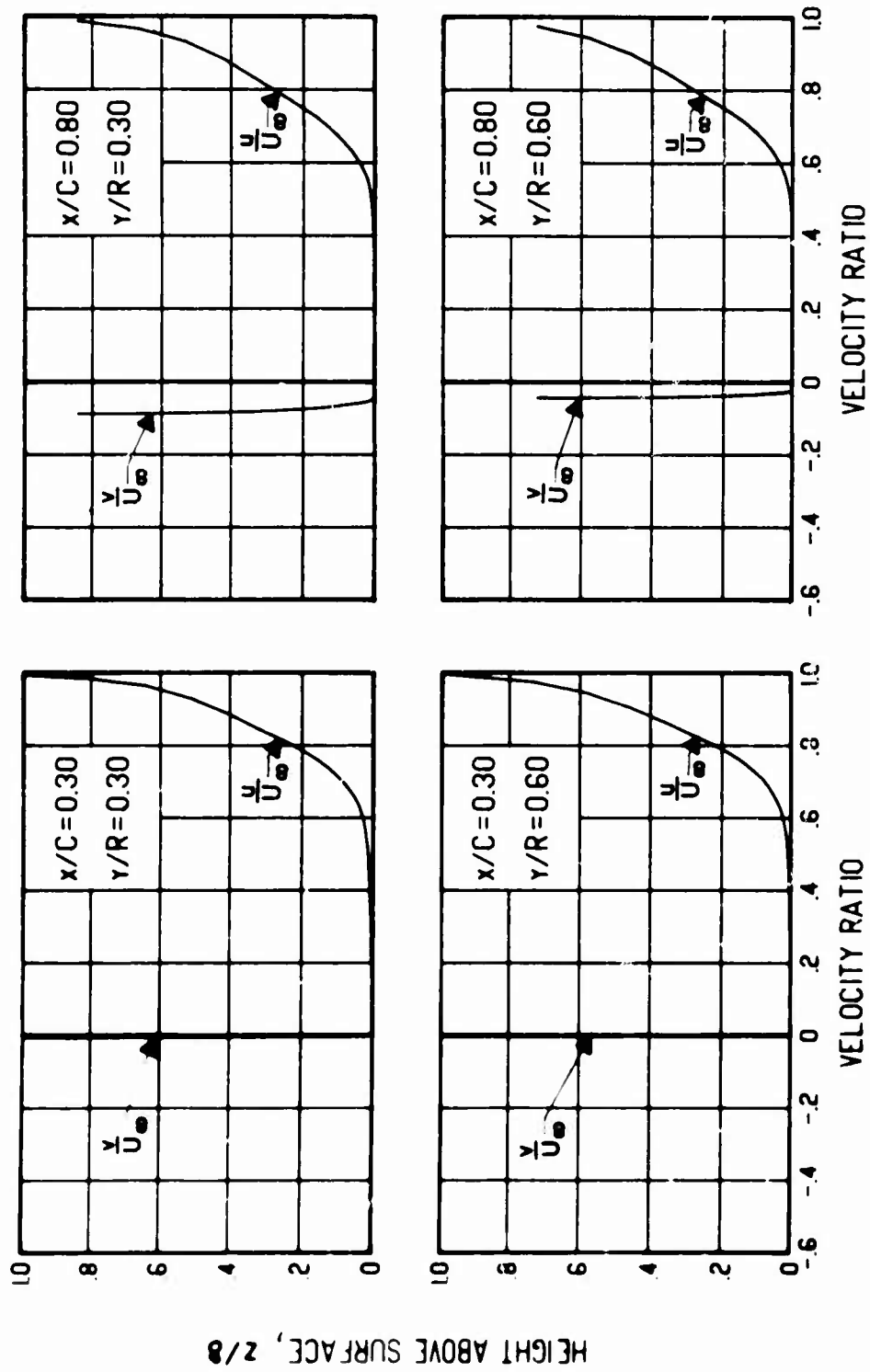
(b) $\partial Cp/\partial(x/C) = 2$

Figure 31. Continued.
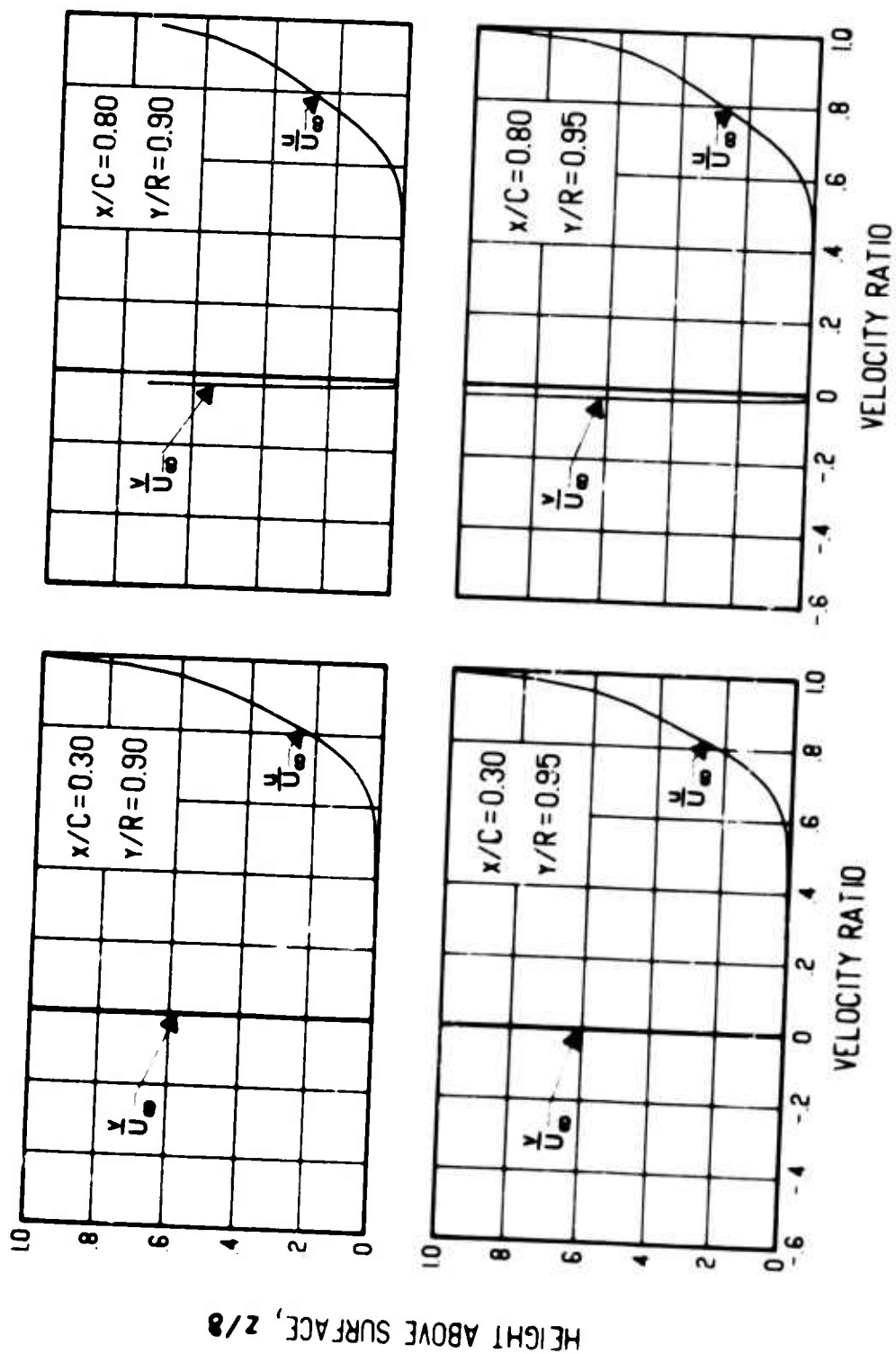
(b) Concluded.

Figure 31. Concluded.
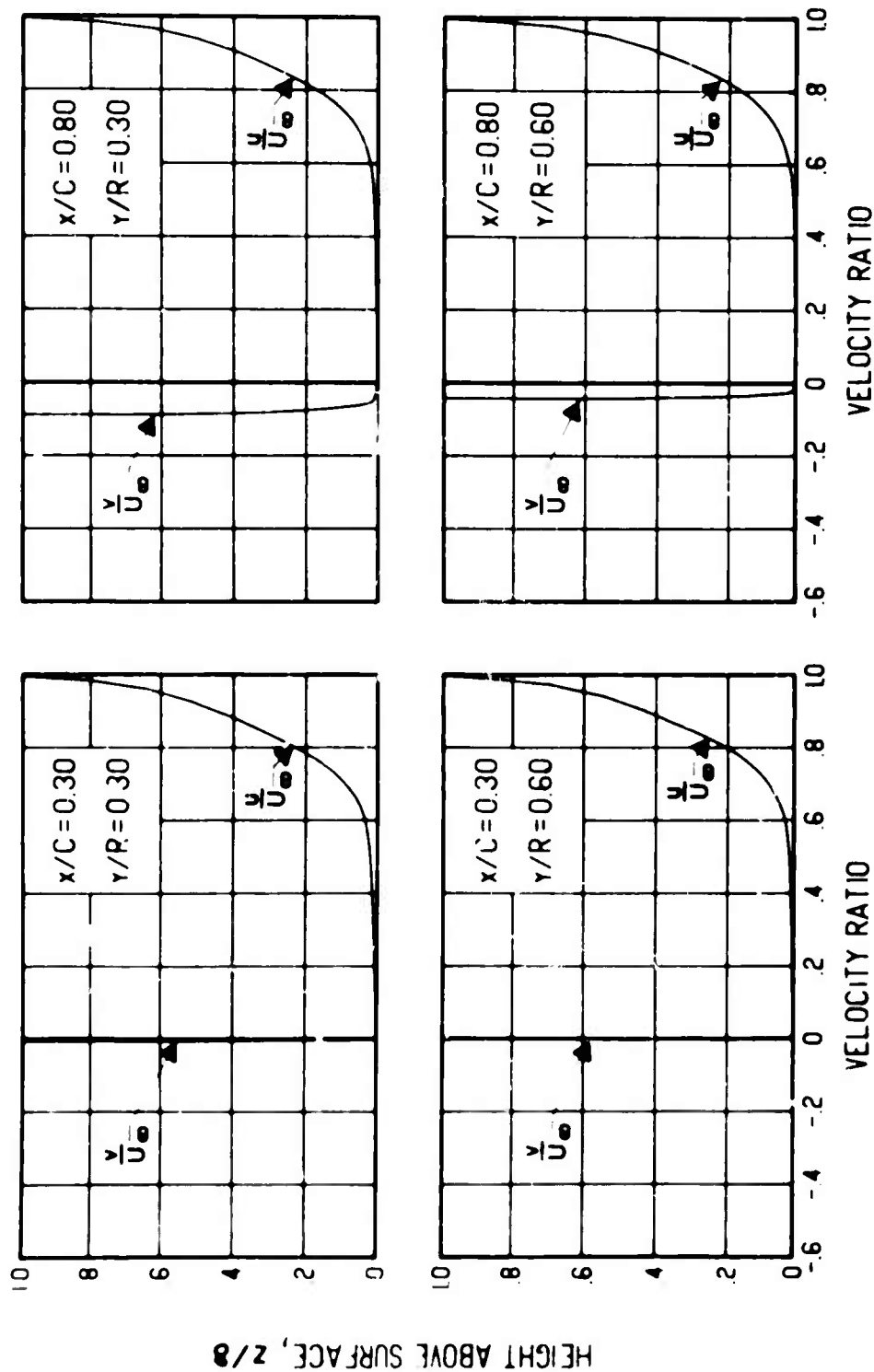
Figure 32. Chordwise and Spanwise Velocity Profiles for Various Vortex Strengths, Blade Radius = 40 ft, Ω = 15 rad/sec, $dCp/d(x/C)$ = 0, Surface Radius of Curvature = 8.25 ft.

(a) Γ/h = +100 ft/sec

174
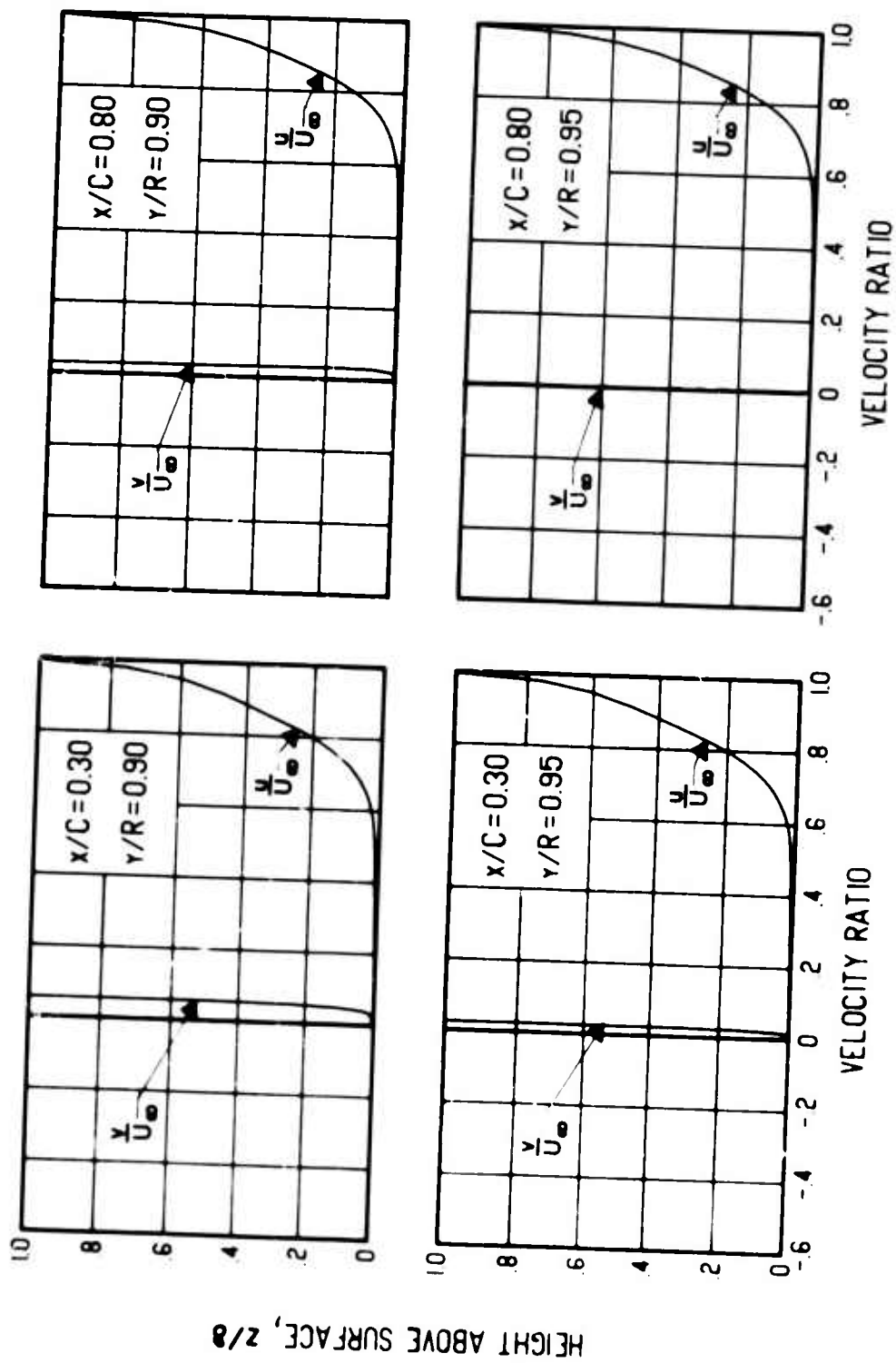
(a) Concluded.

Figure 32. Continued.

(b) $\Gamma/h = -100$ ft/sec

Figure 32. Continued.

176

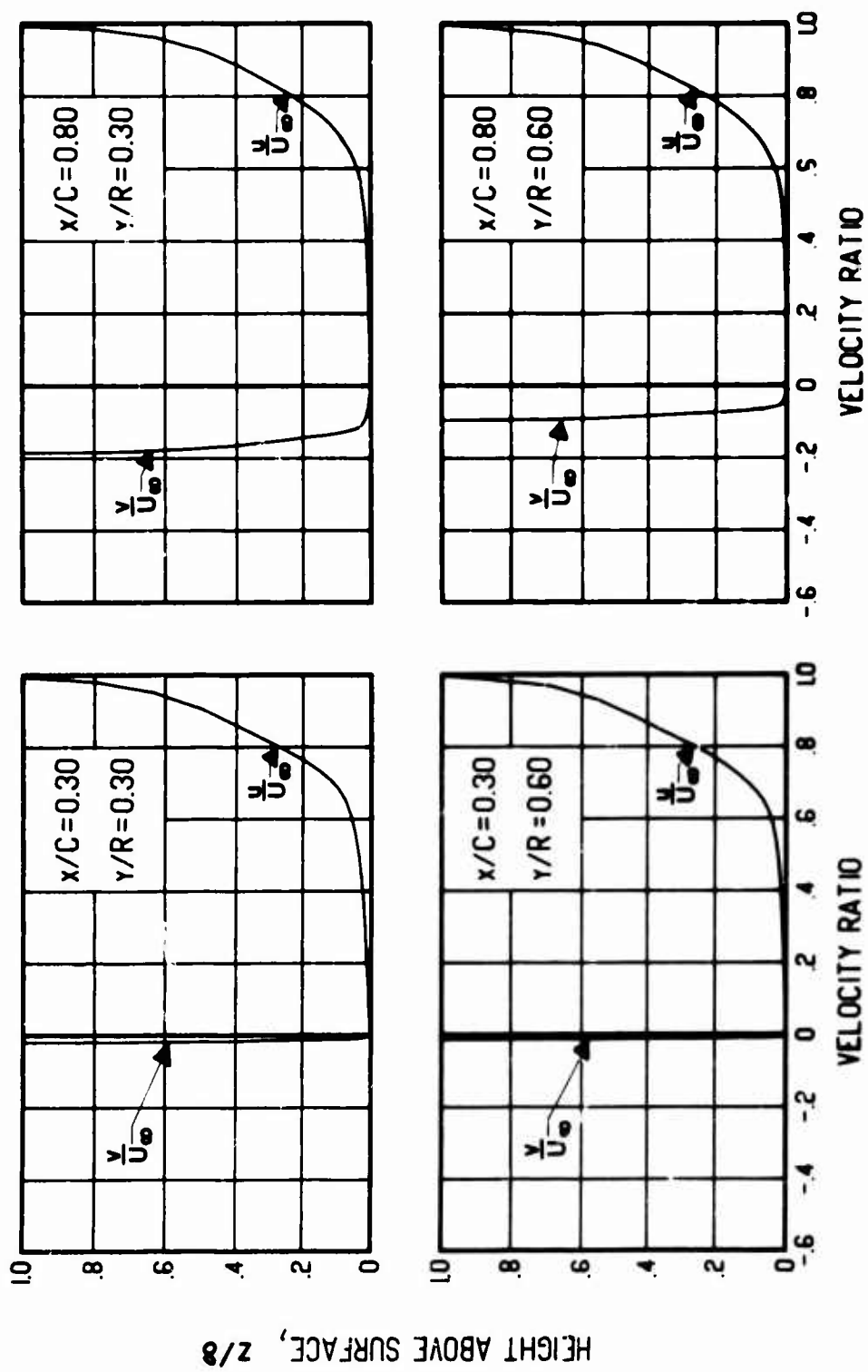(b) Concluded.

Figure 32. Continued.

177

(c) $\Gamma/h = +200$ ft/sec

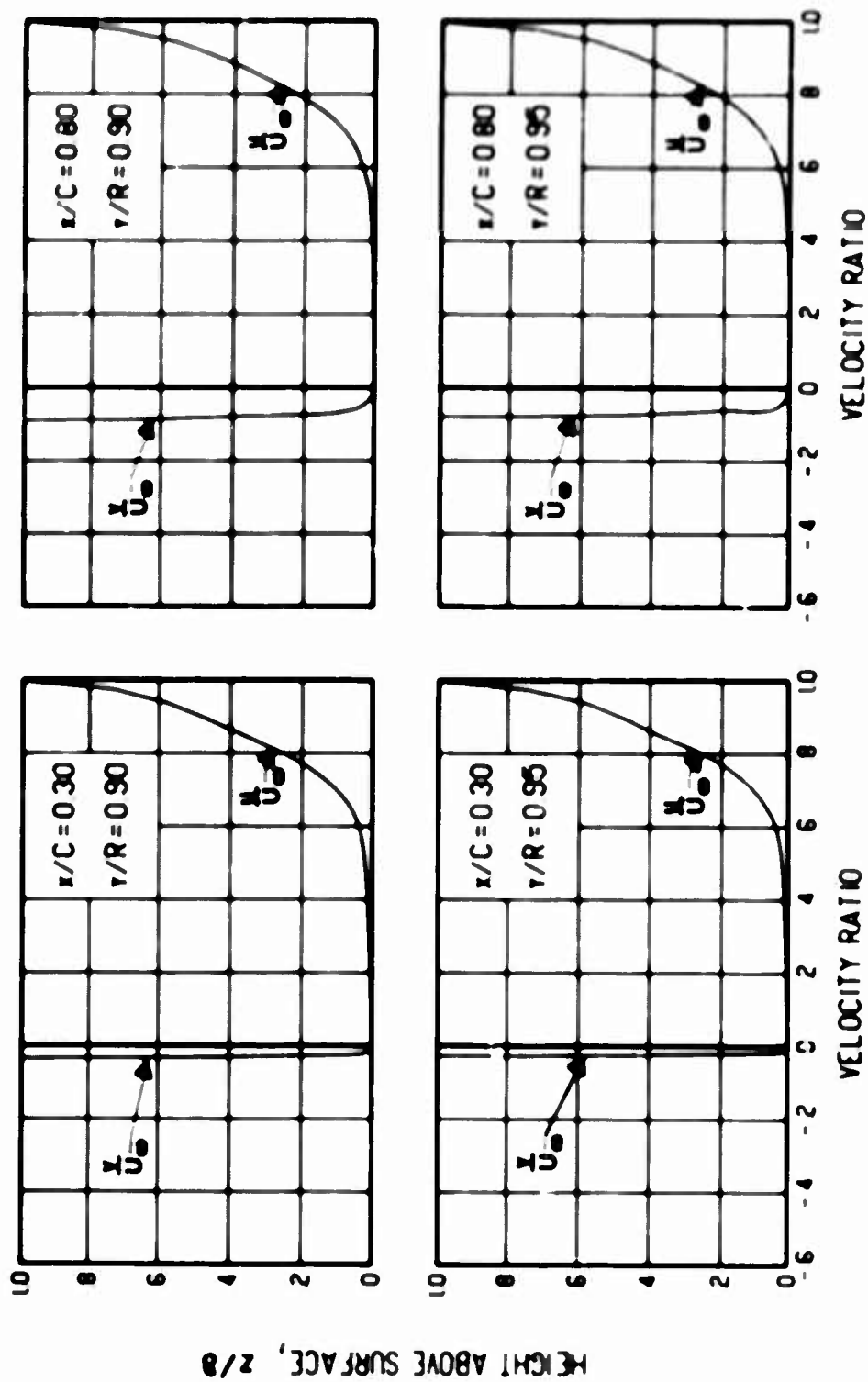Figure 32. Continued.

178
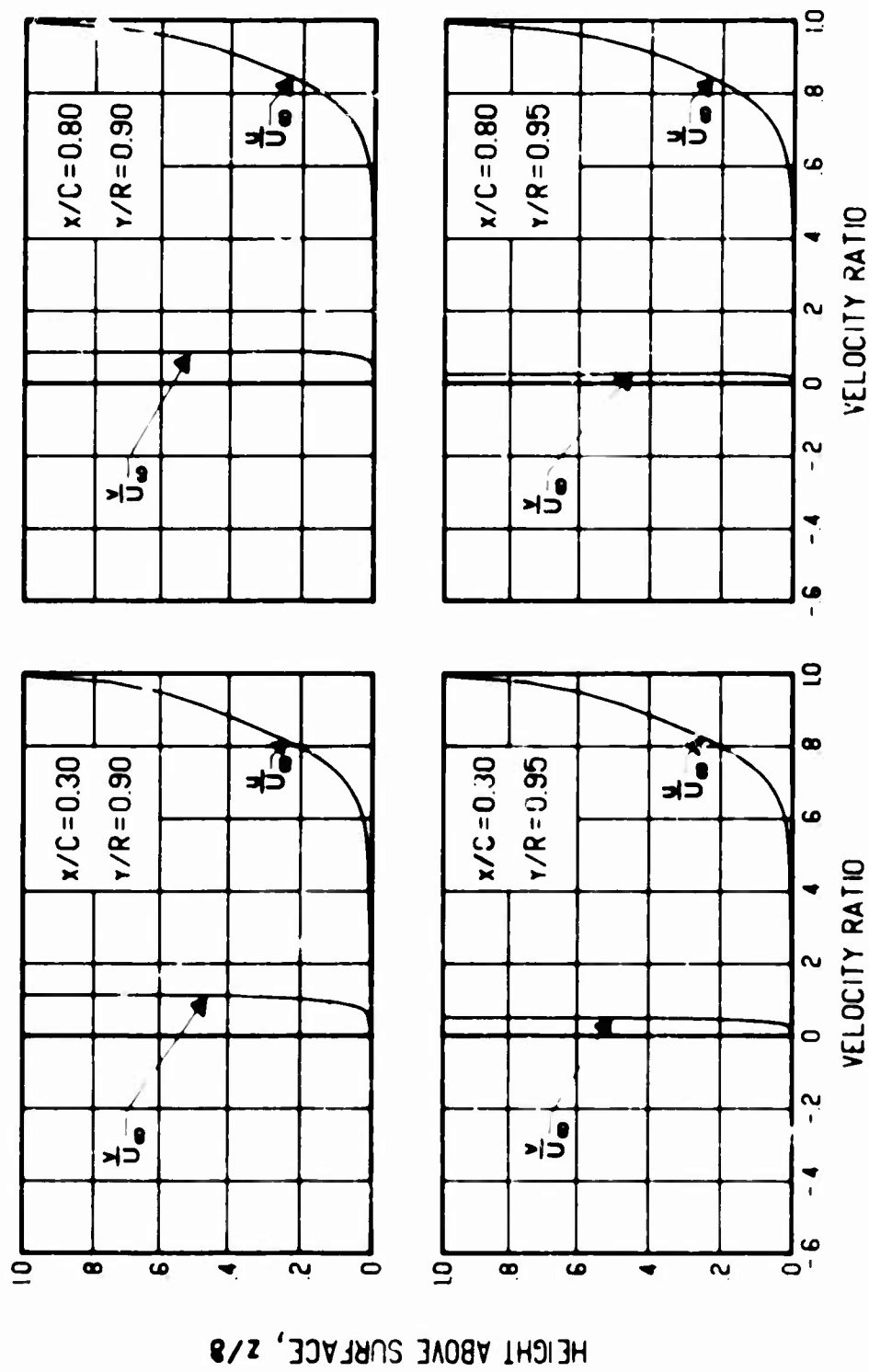
(c) Concluded.

Figure 32. Continued.
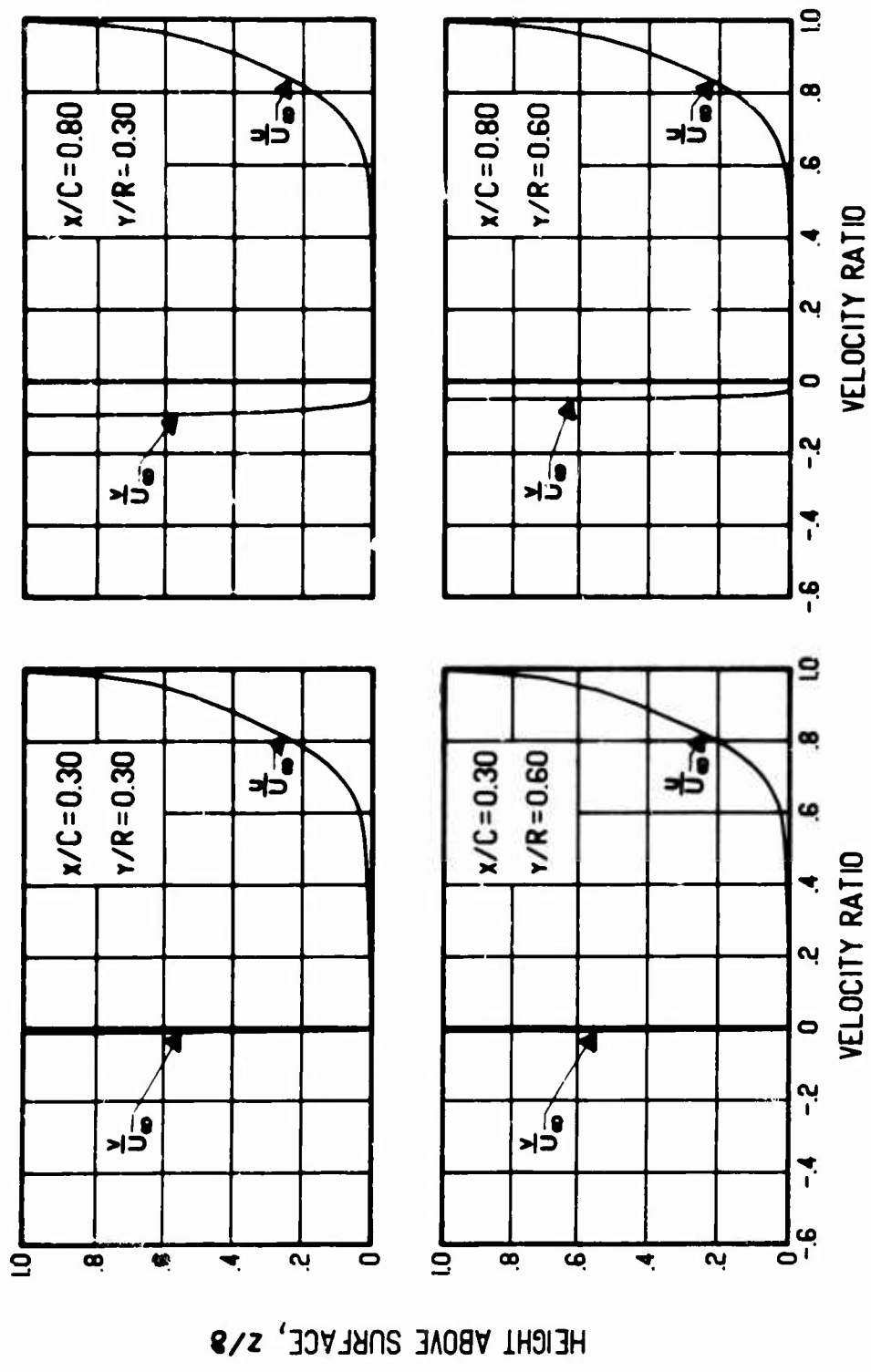
(d) Γ/h = -200 ft/sec

Figure 32. Continued.
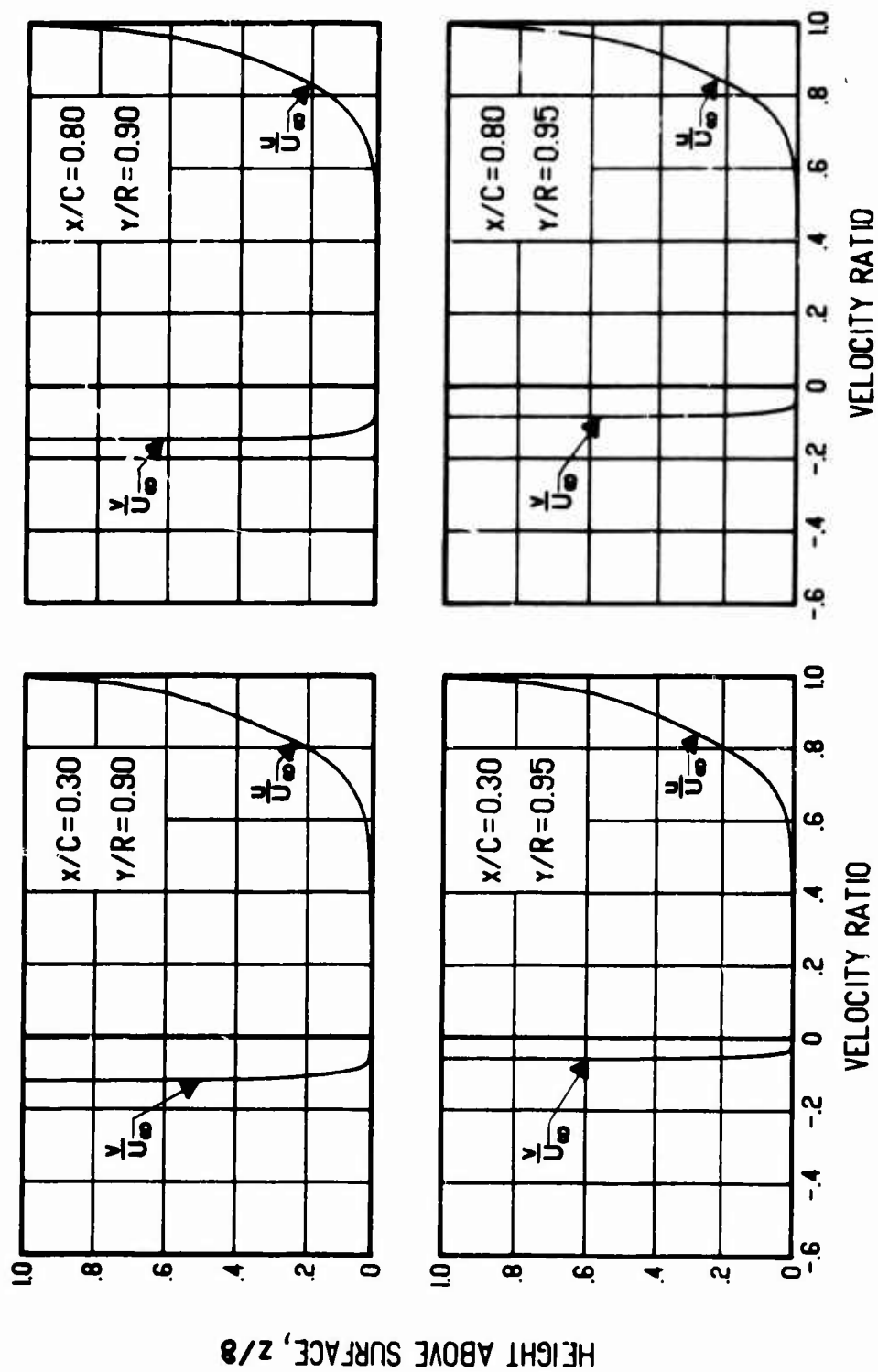
(d) Concluded.

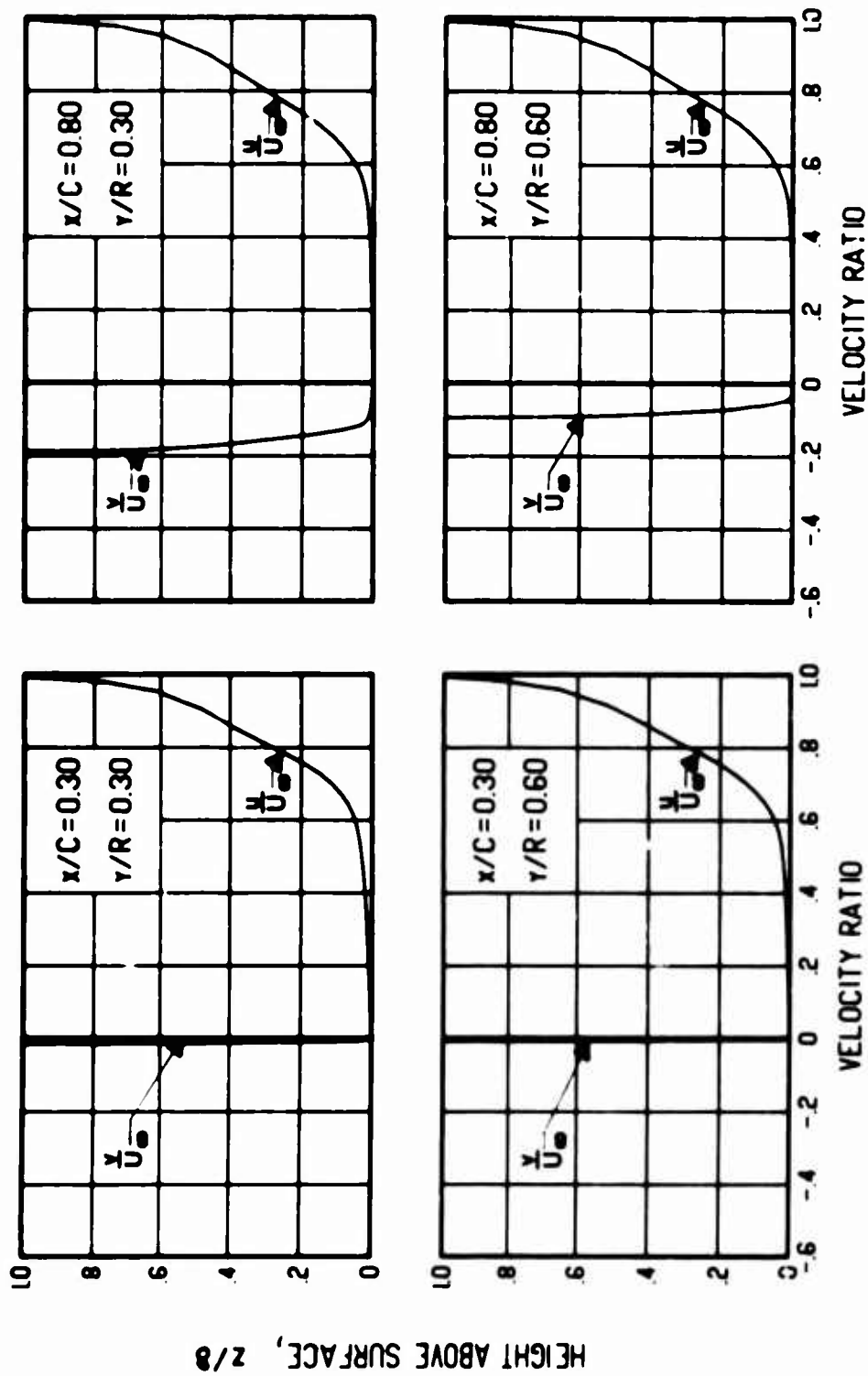Figure 32. Concluded.
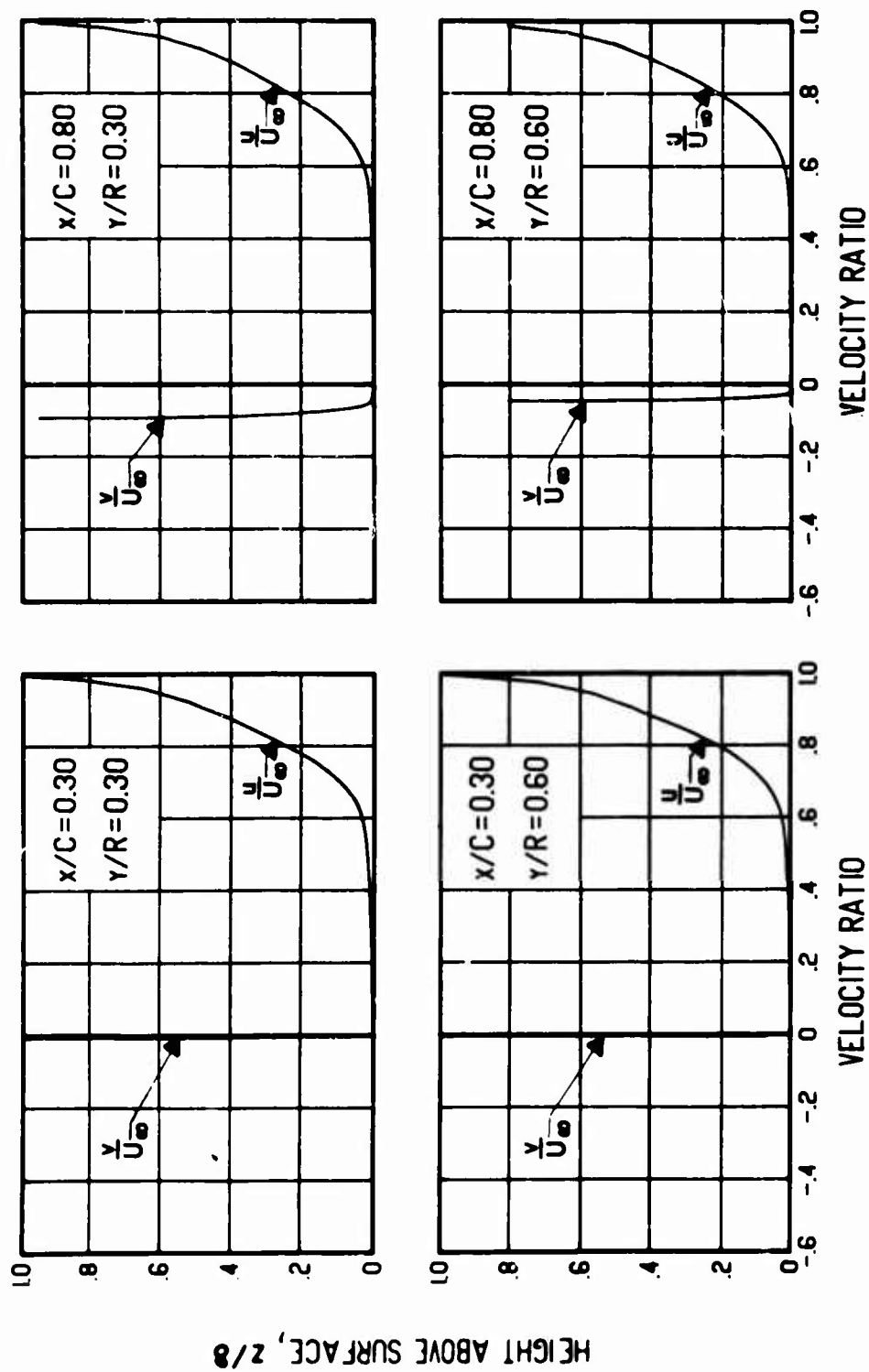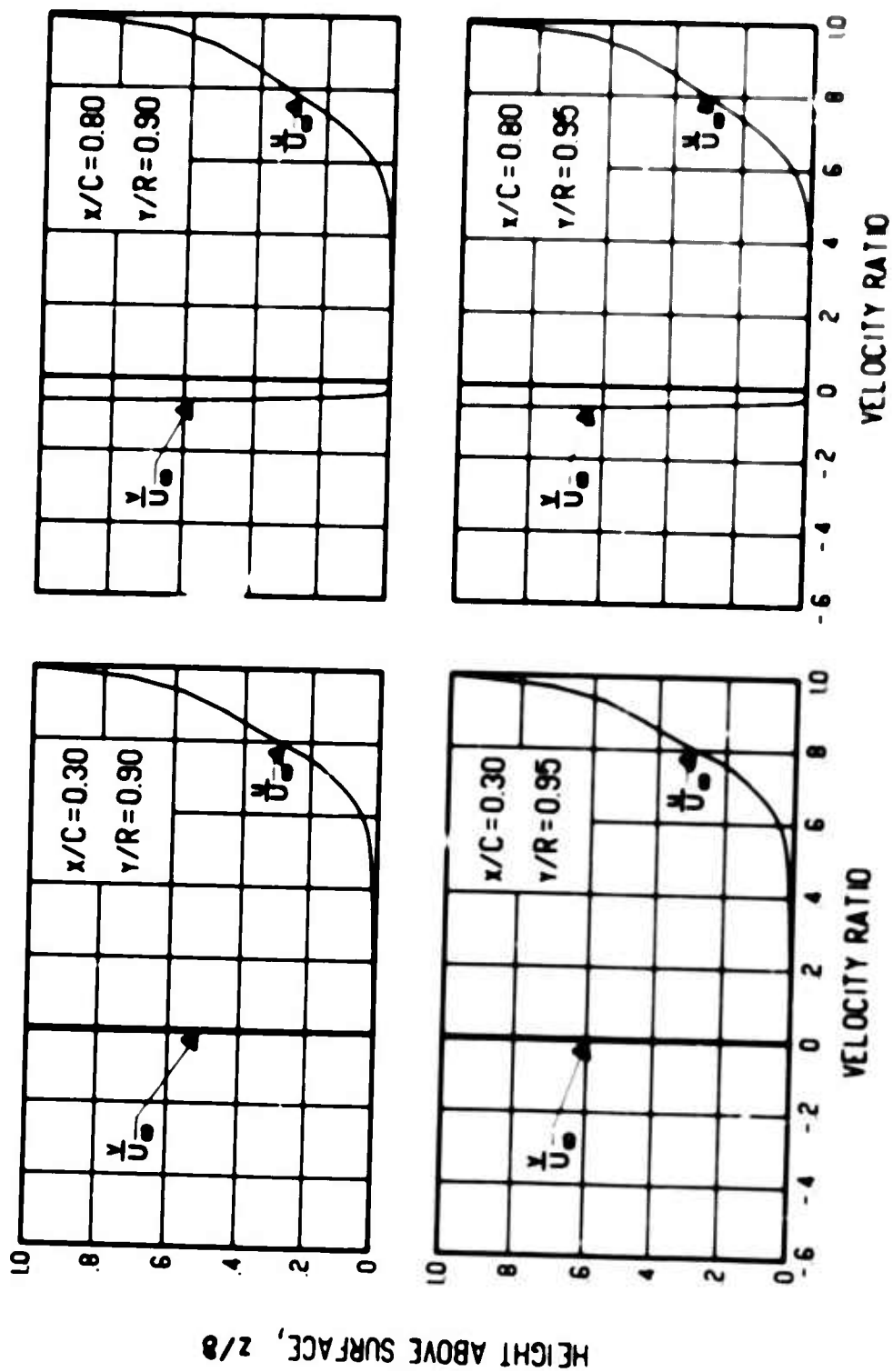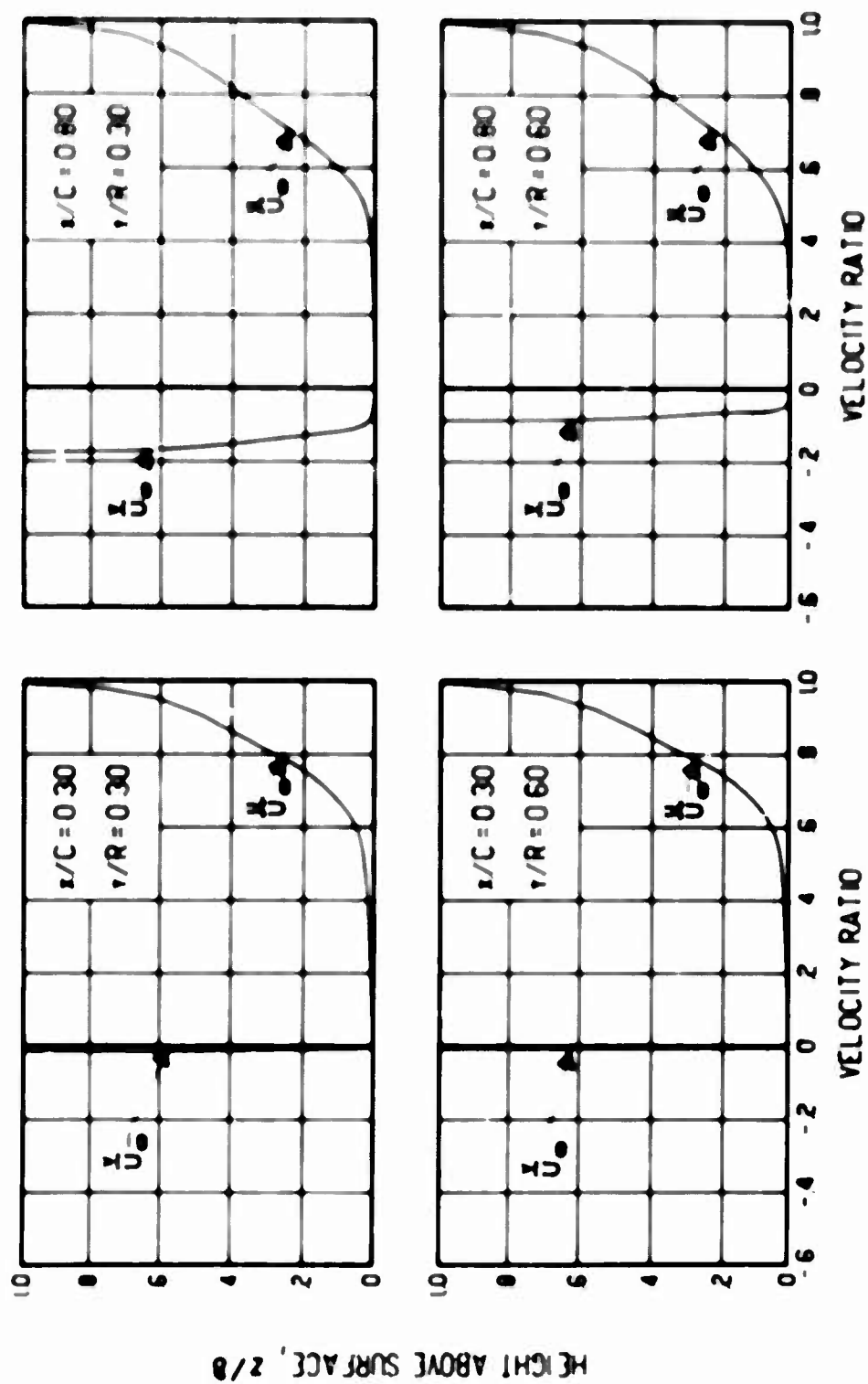
(a) $dCp/d(x/C) = 1$

Figure 33. Chordwise and Spanwise Velocity Profiles for Various Pressure
Gradients, Blade Radius = 40 ft, Ω = 15 rad/sec,
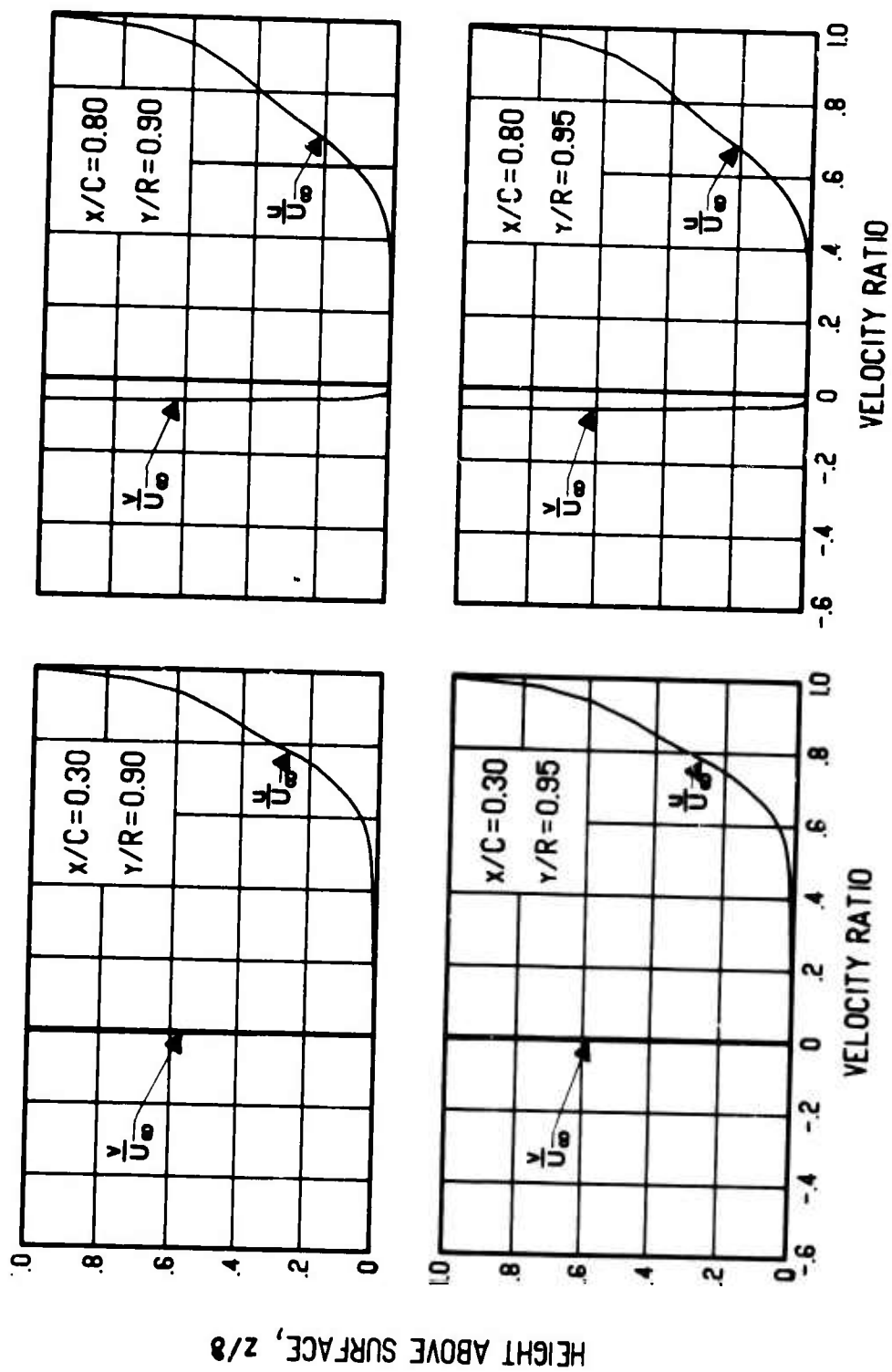Γ/h = 0 ft/sec, Surface Radius of Curvature = 8.25 ft.
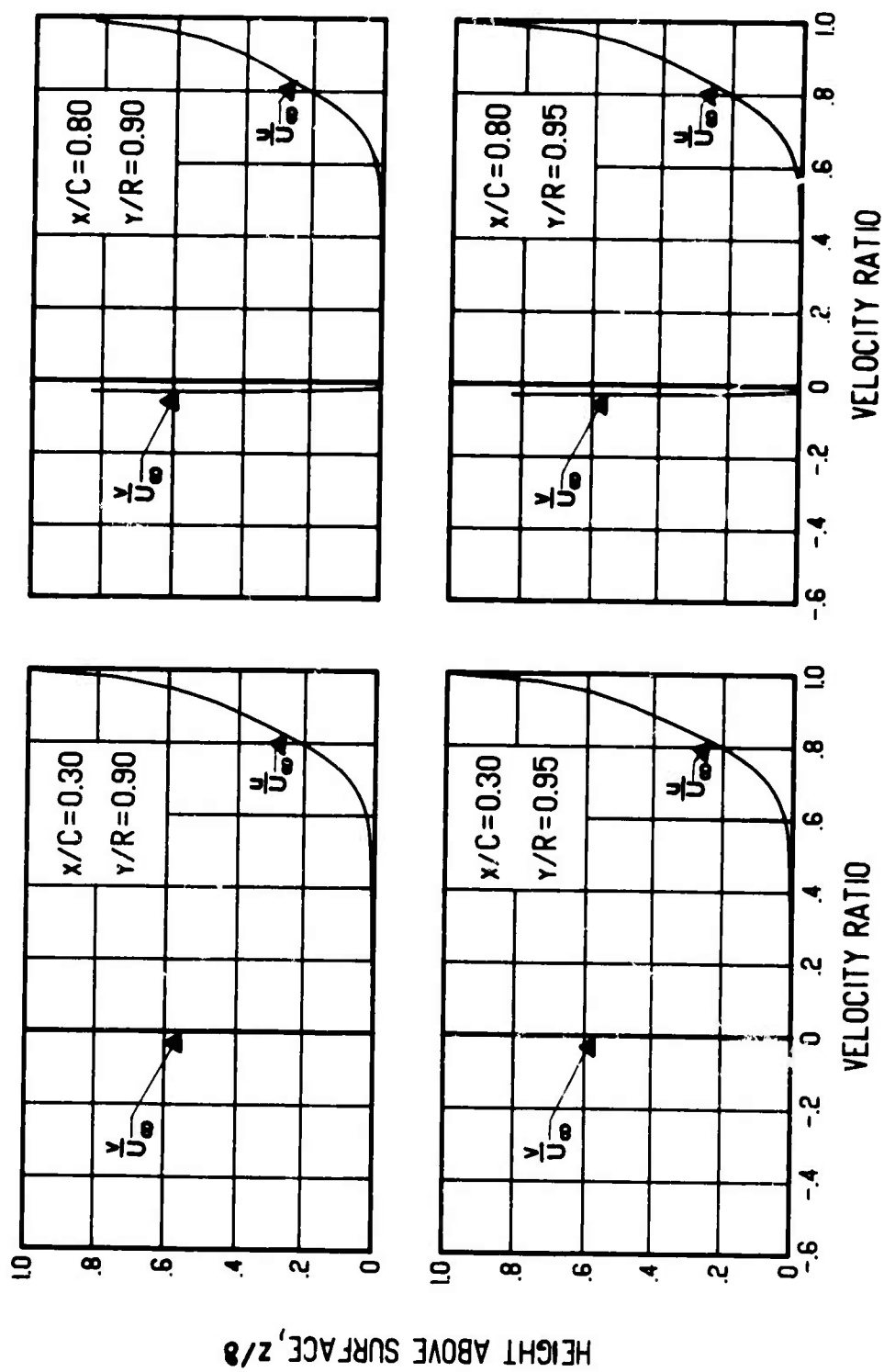
(a) Concluded.

Figure 33. Continued.

183
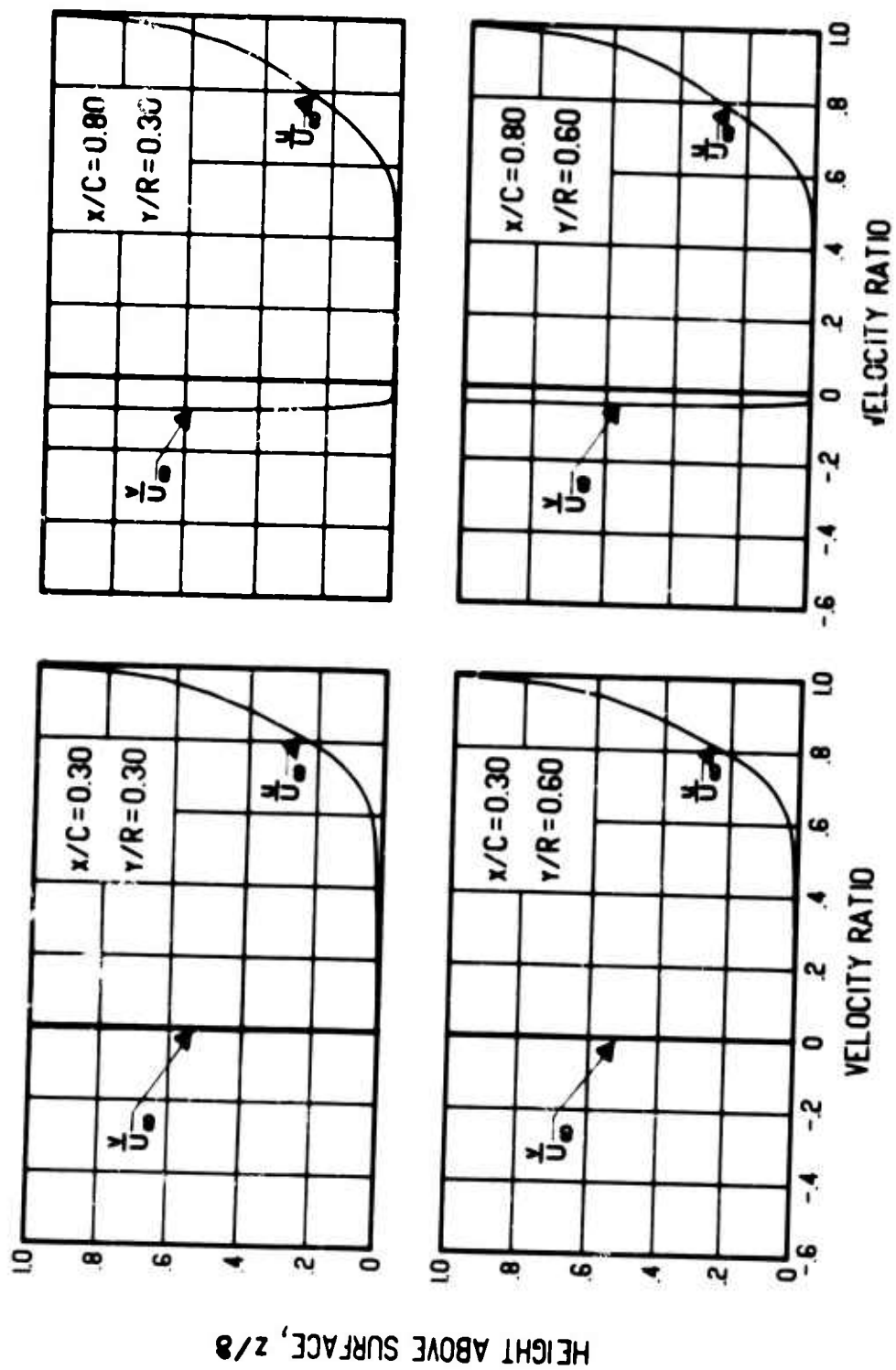
(b) $dCp/d(x/C) = 2$

Figure 33. Continued.

184
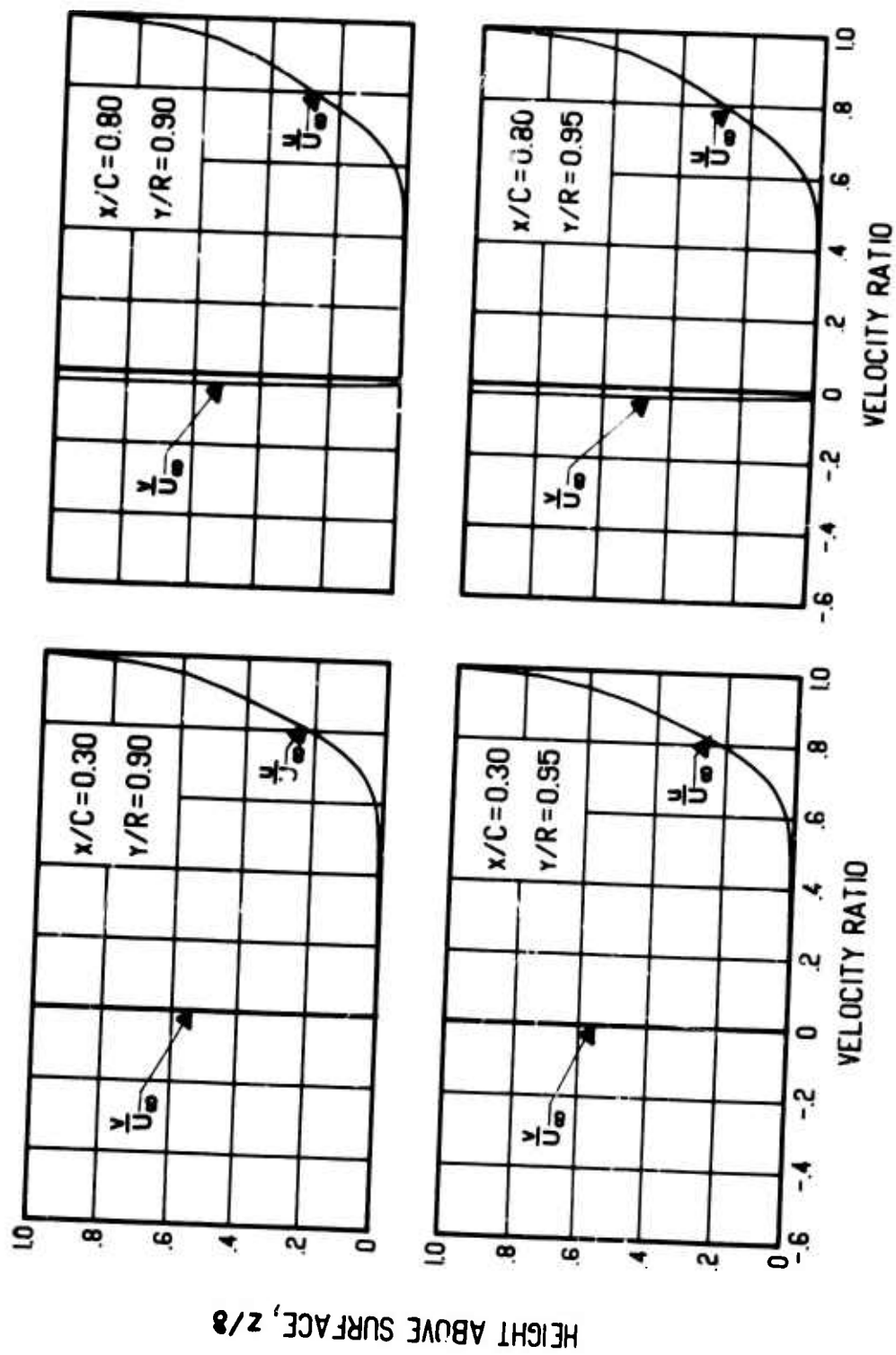
(b) Concluded.

Figure 33. Concluded.
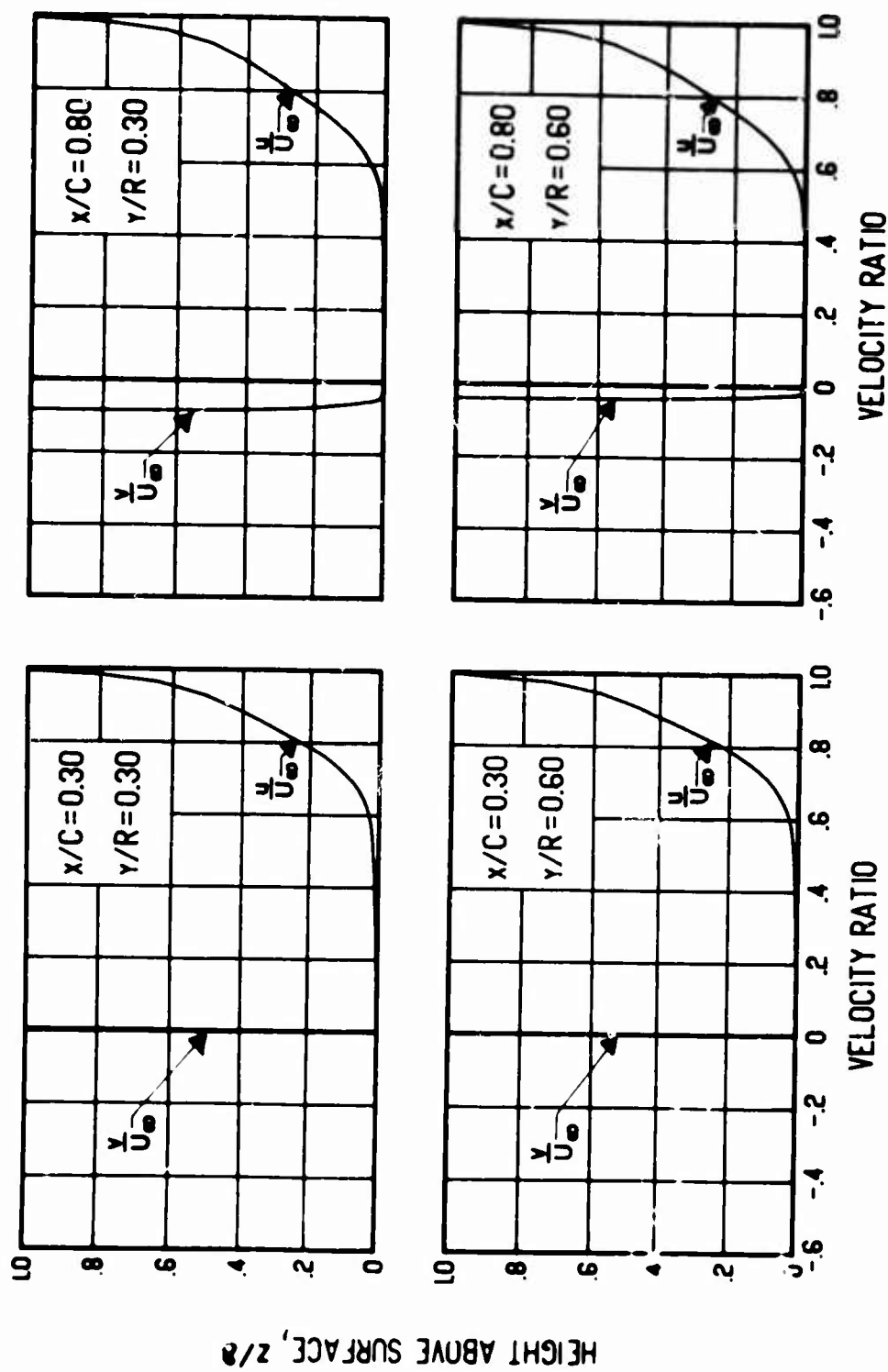
Figure 34. Chordwise and Spanwise Velocity Profiles for Various Vortex
Strengths, Blade Radius = 40 ft, Ω = 15 rad/sec,
$dCp/d(x/C)$ = 2, Surface Radius of Curvature = 8.25 ft.
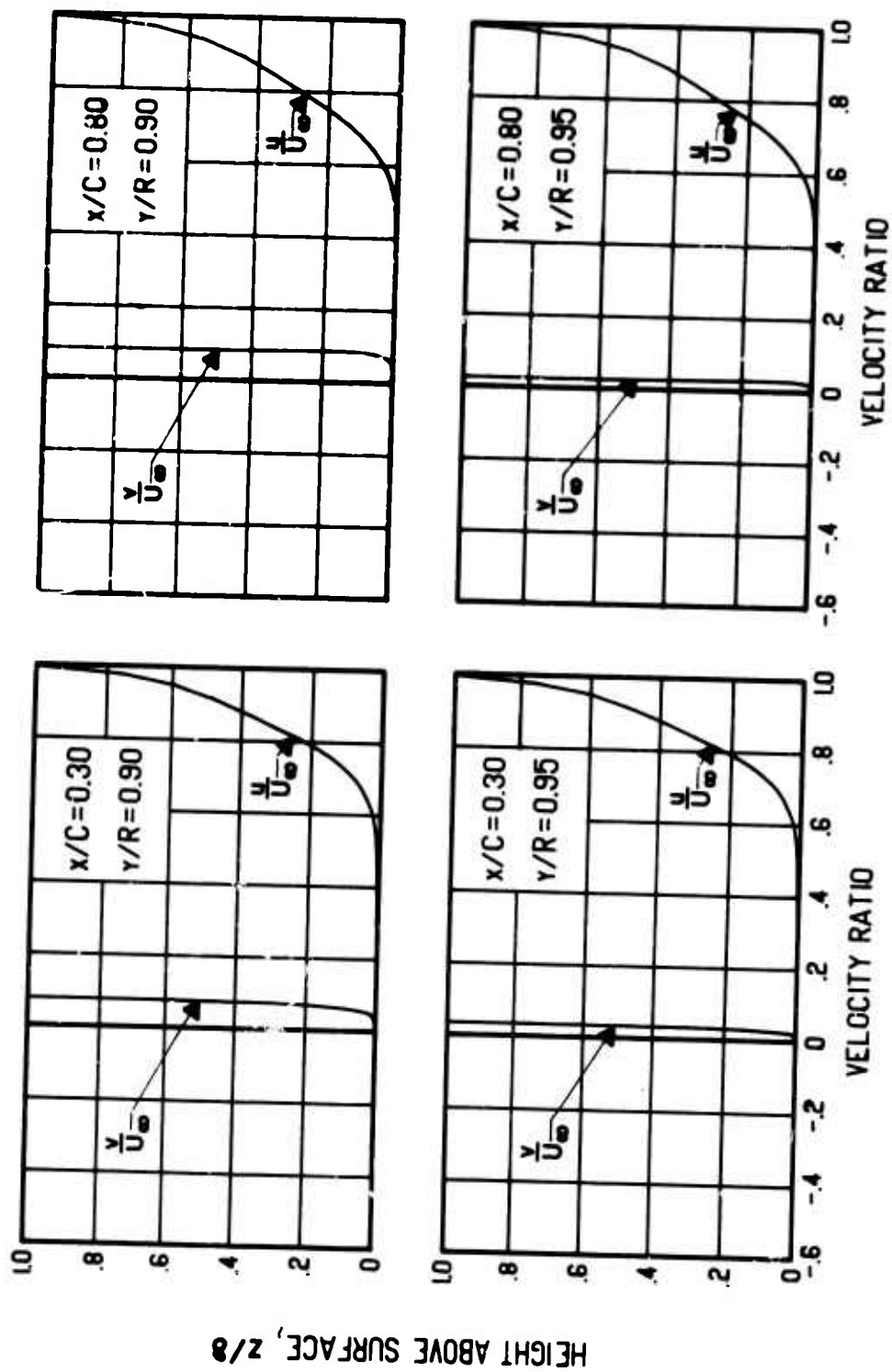
(a) Γ/h = +200 ft/sec

(a) Concluded.

Figure 34. Continued.

187
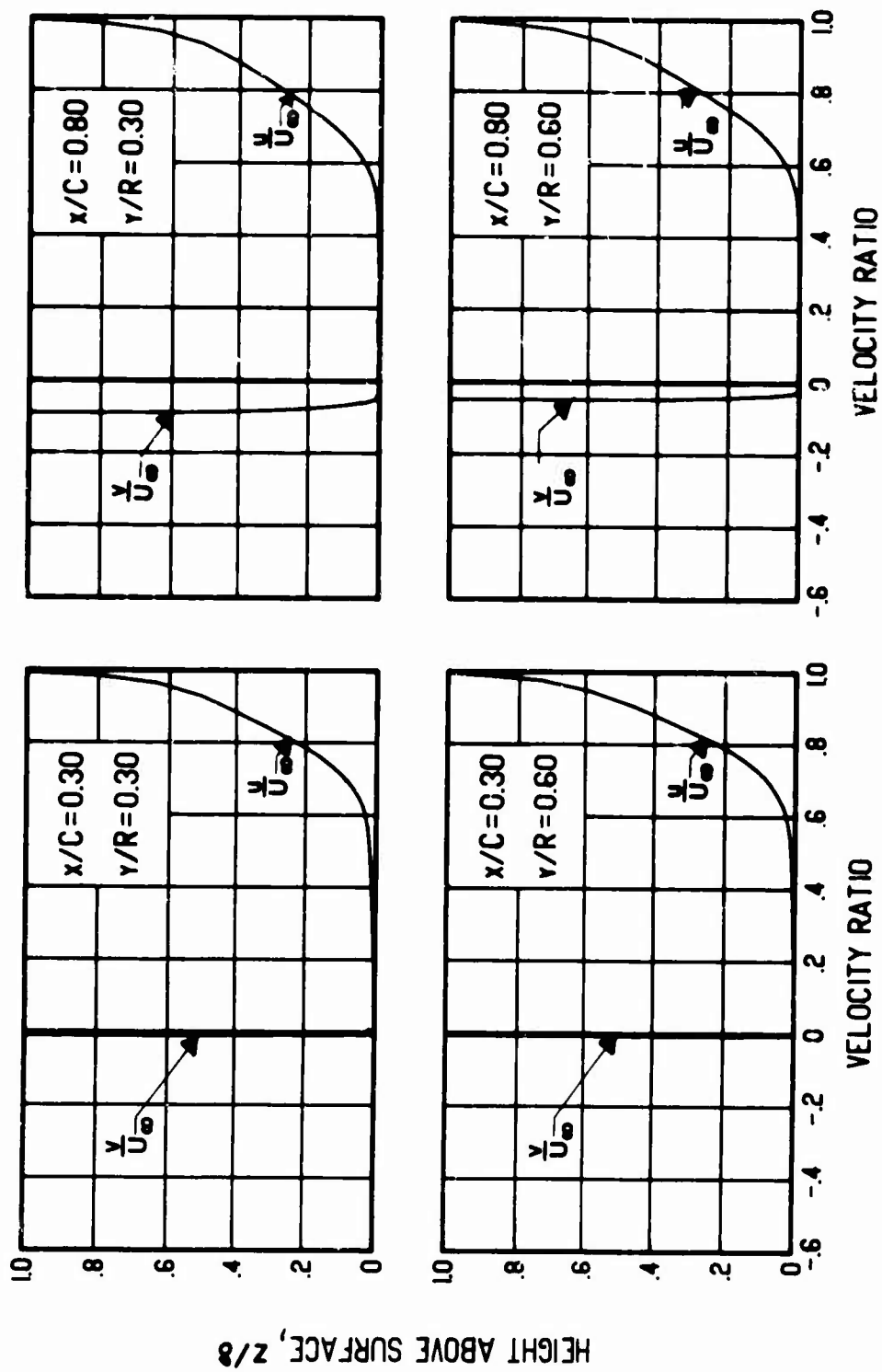
(b) $\Gamma/h = -200$ ft/sec

Figure 34. Continued.

188
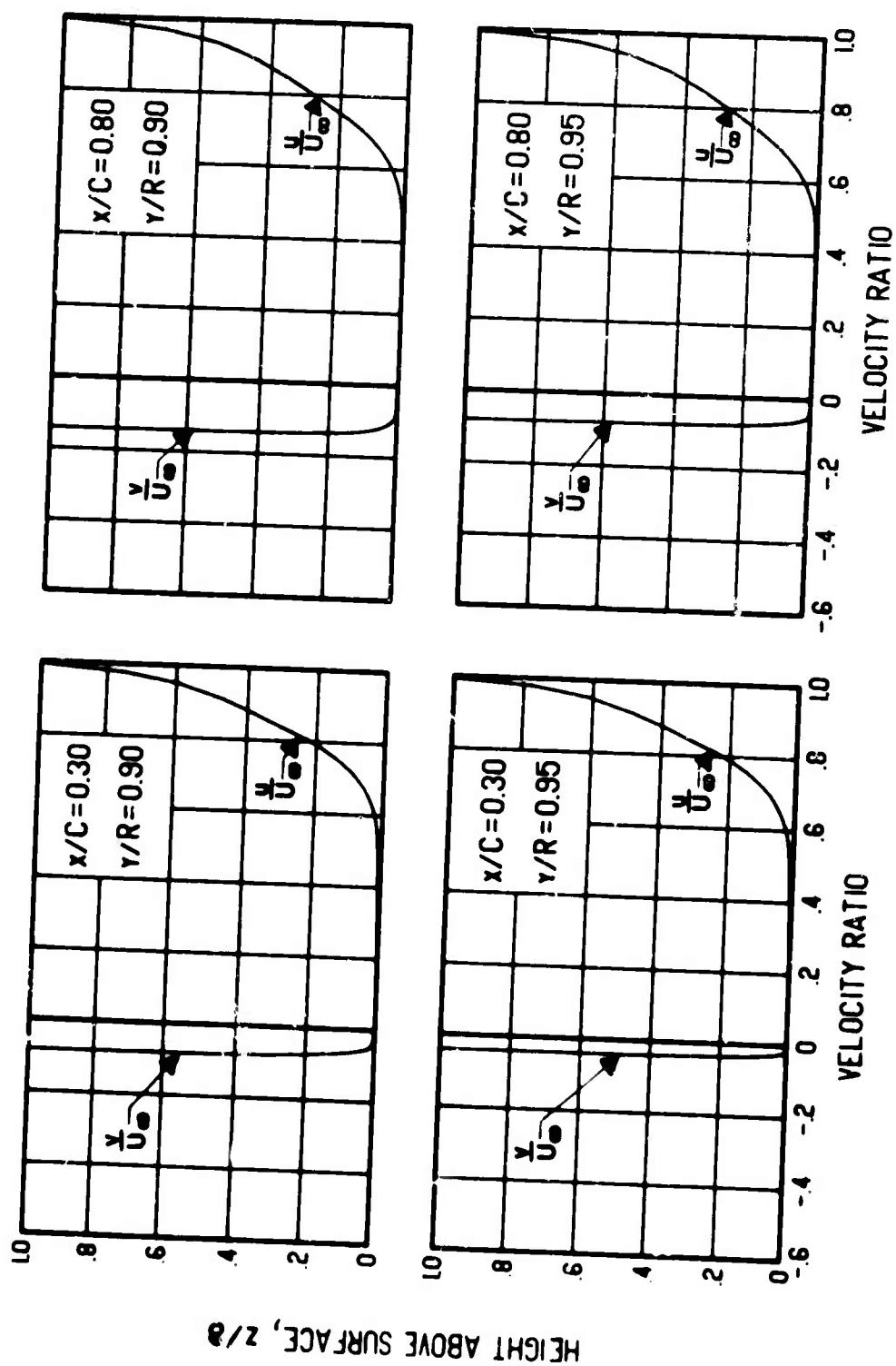
(b) Concluded.

Figure 34. Concluded.

189
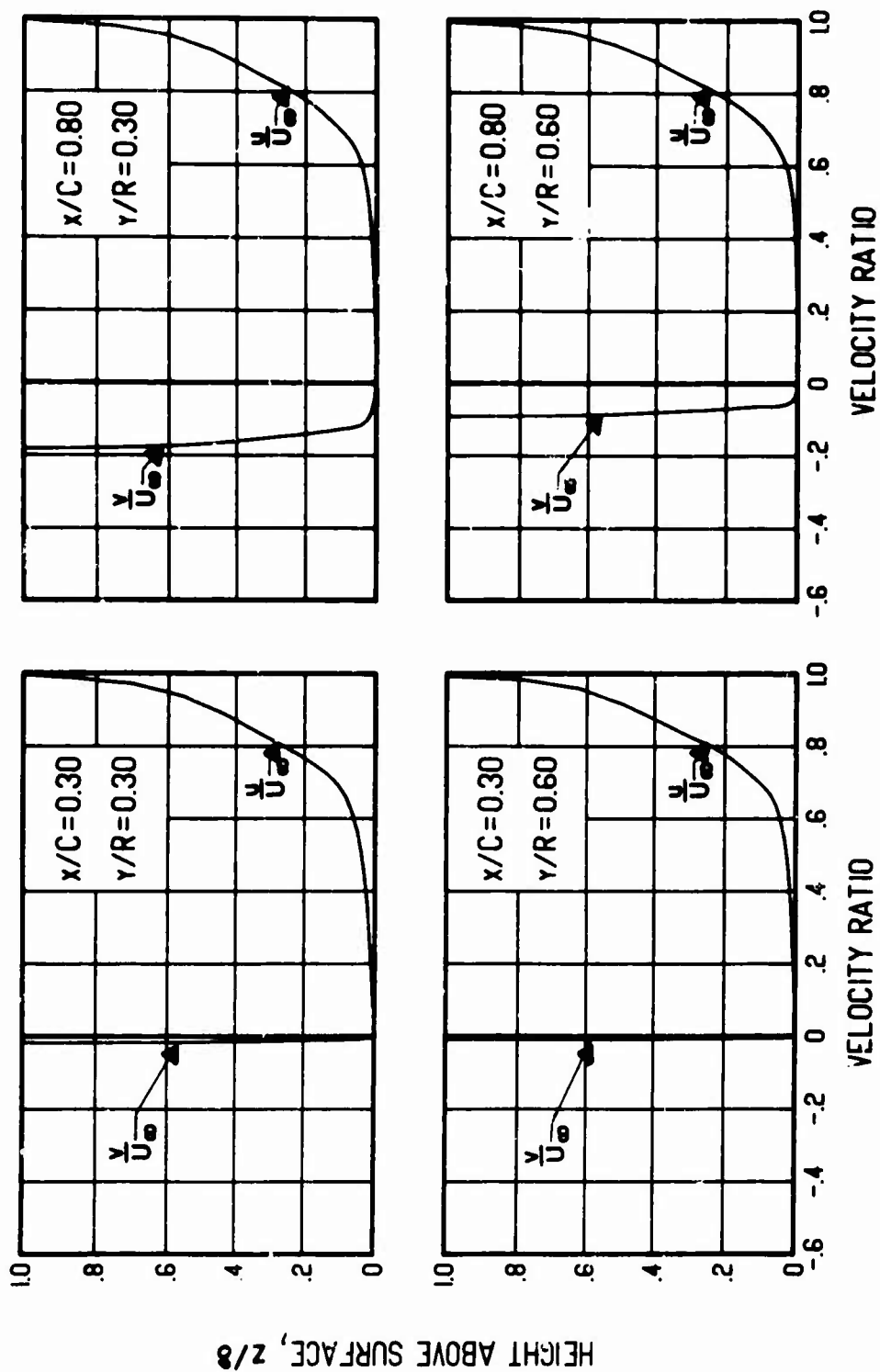
Figure 35. Chordwise and Spanwise Velocity Profiles for Various Angular Velocities, Blade Radius = 10 ft, $\Gamma/h = 0$ ft/sec, $dCp/d(x/C) = 0$, Flat Surface.
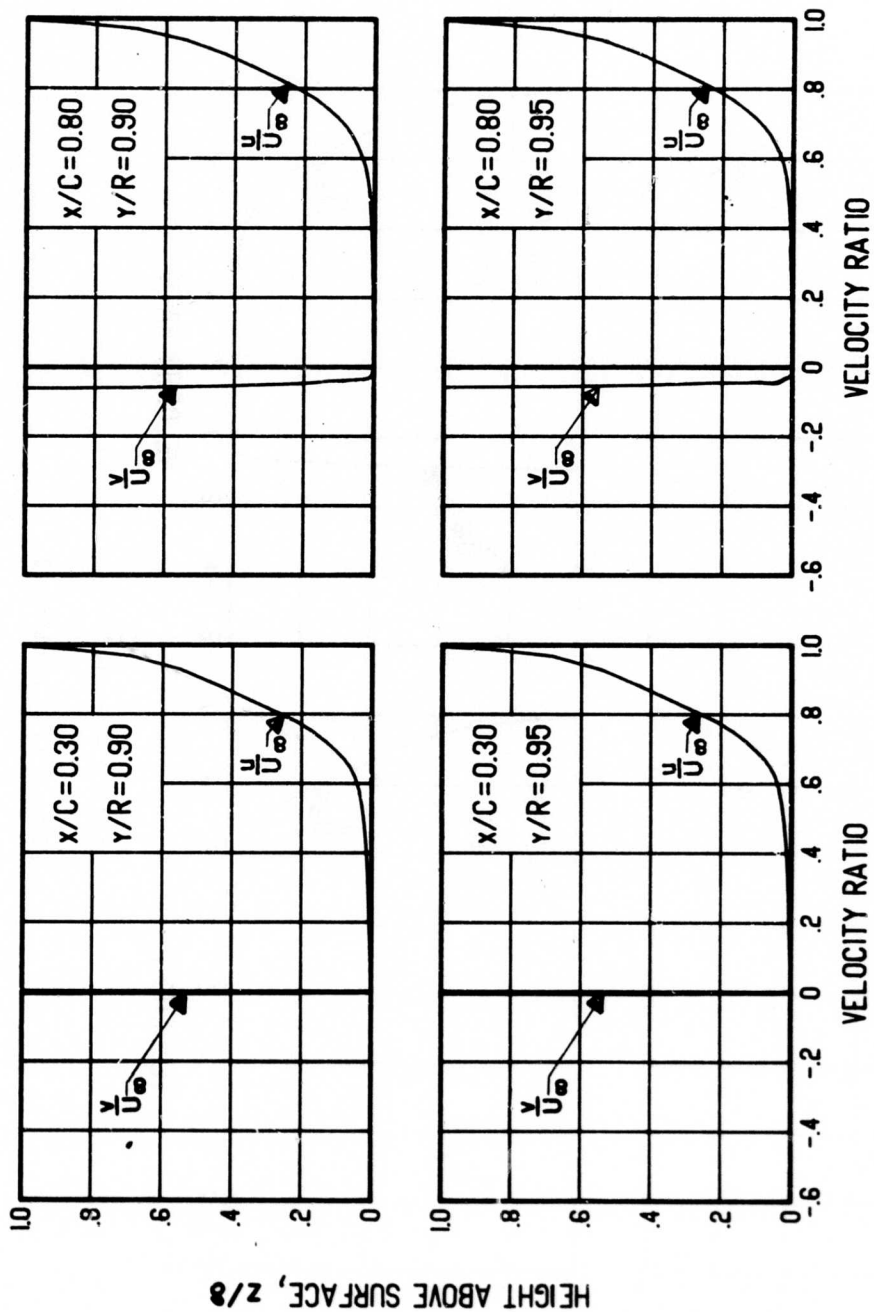
(a) $\Omega = 40$ rad/sec

(a) Concluded.

Figure 35. Continued.
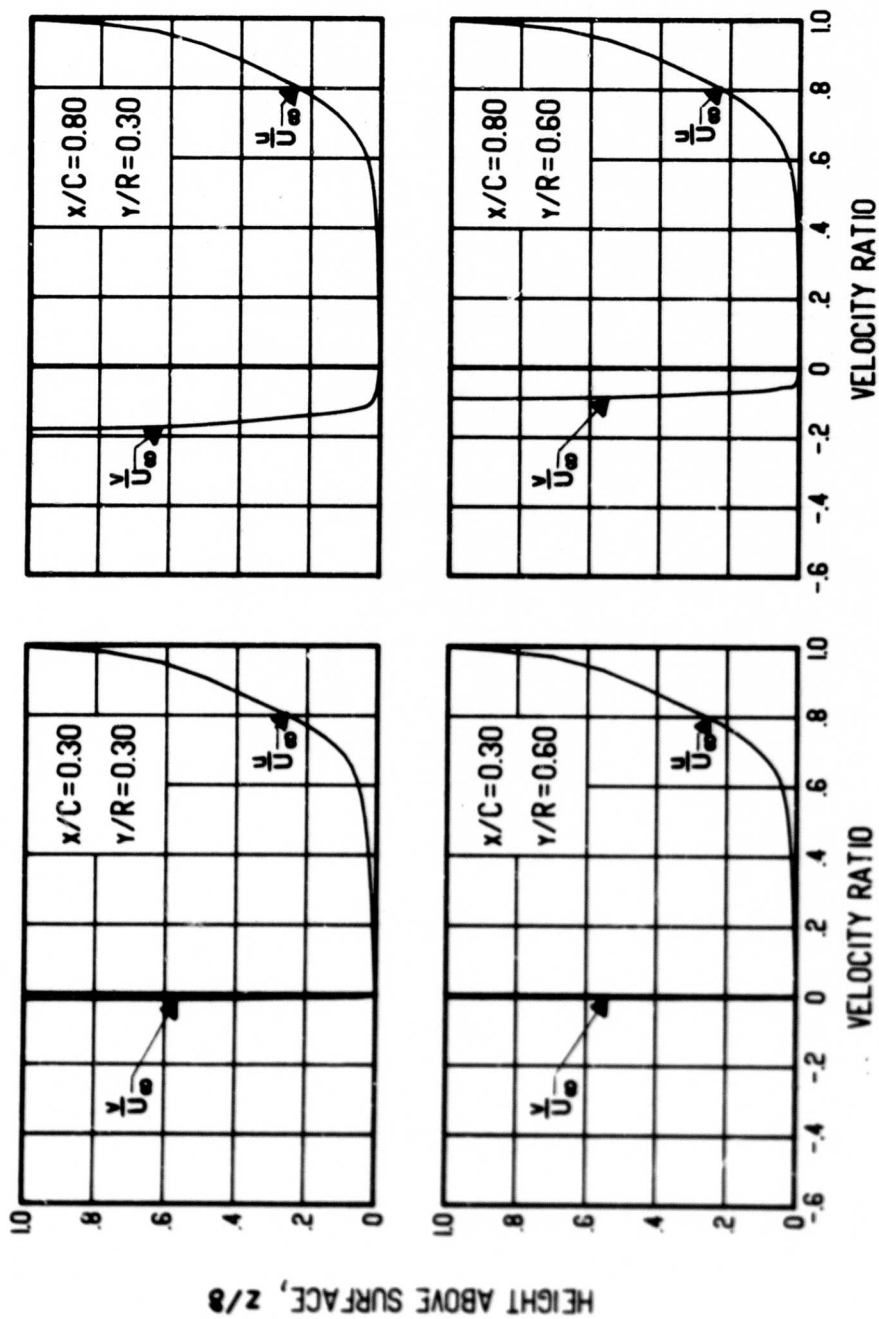
(b) $\Omega = 60$ rad/sec

Figure 35. Continued.
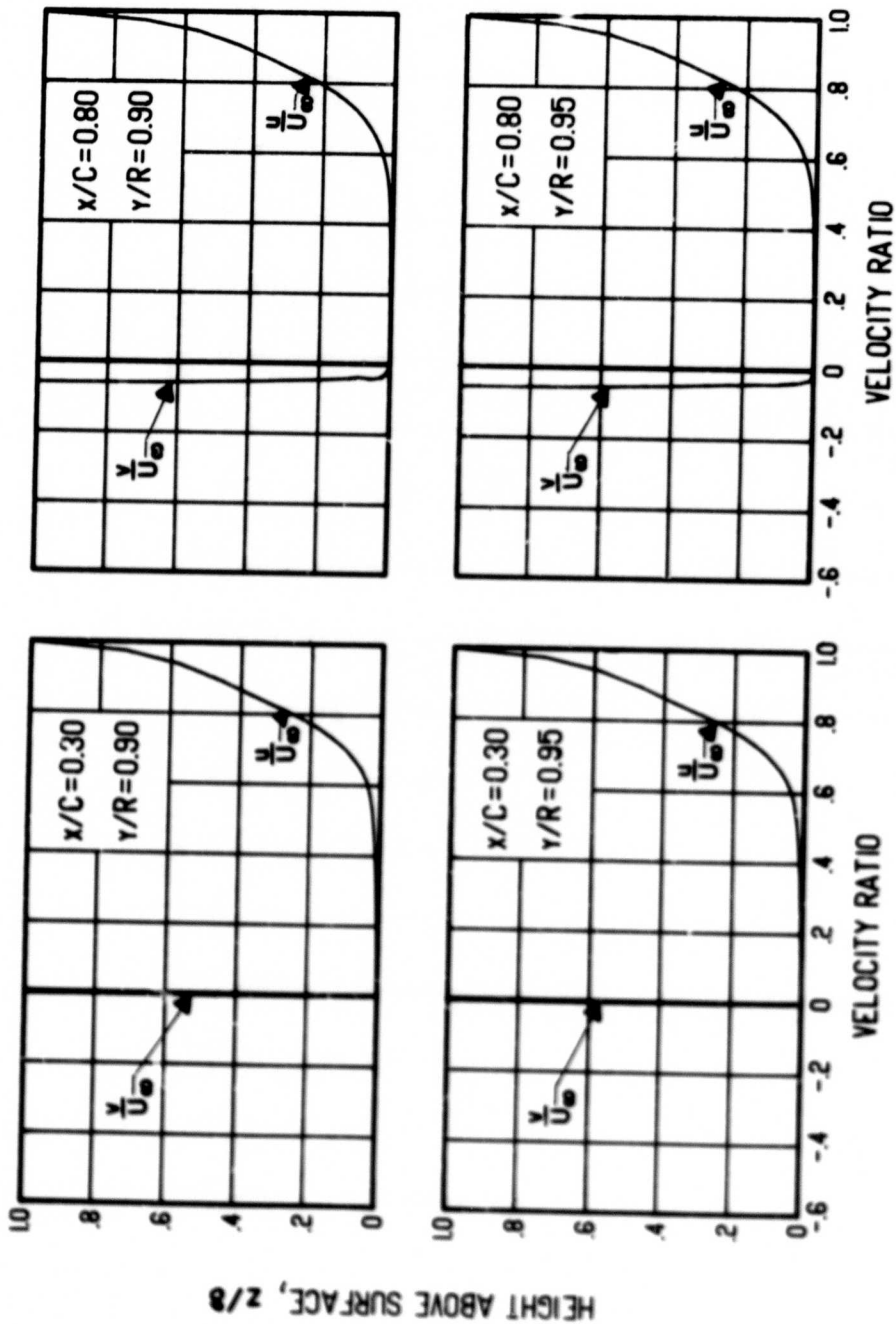
(b) Concluded.

Figure 35. Continued.
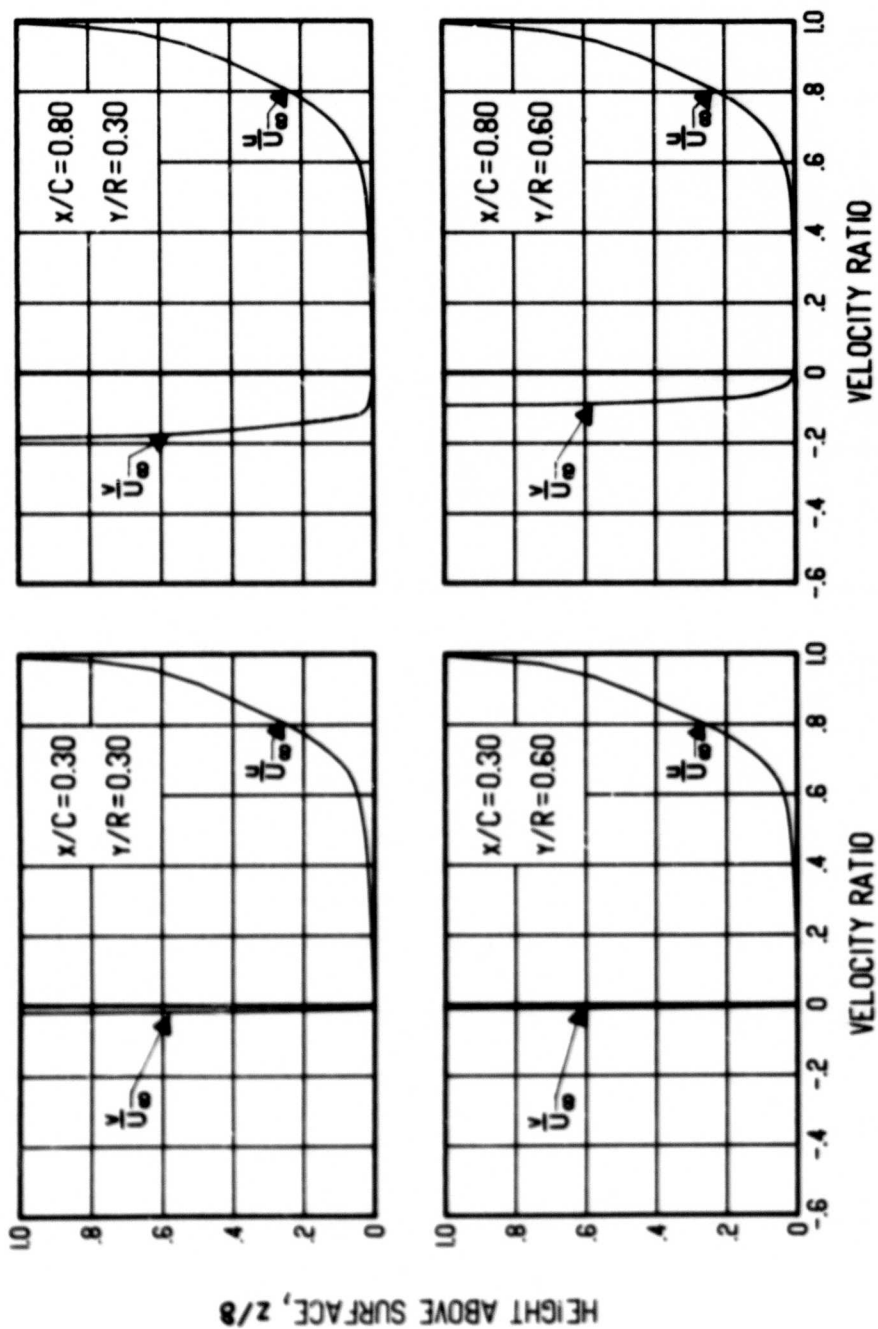
(c) Ω = 80 rad/sec

Figure 35. Continued.
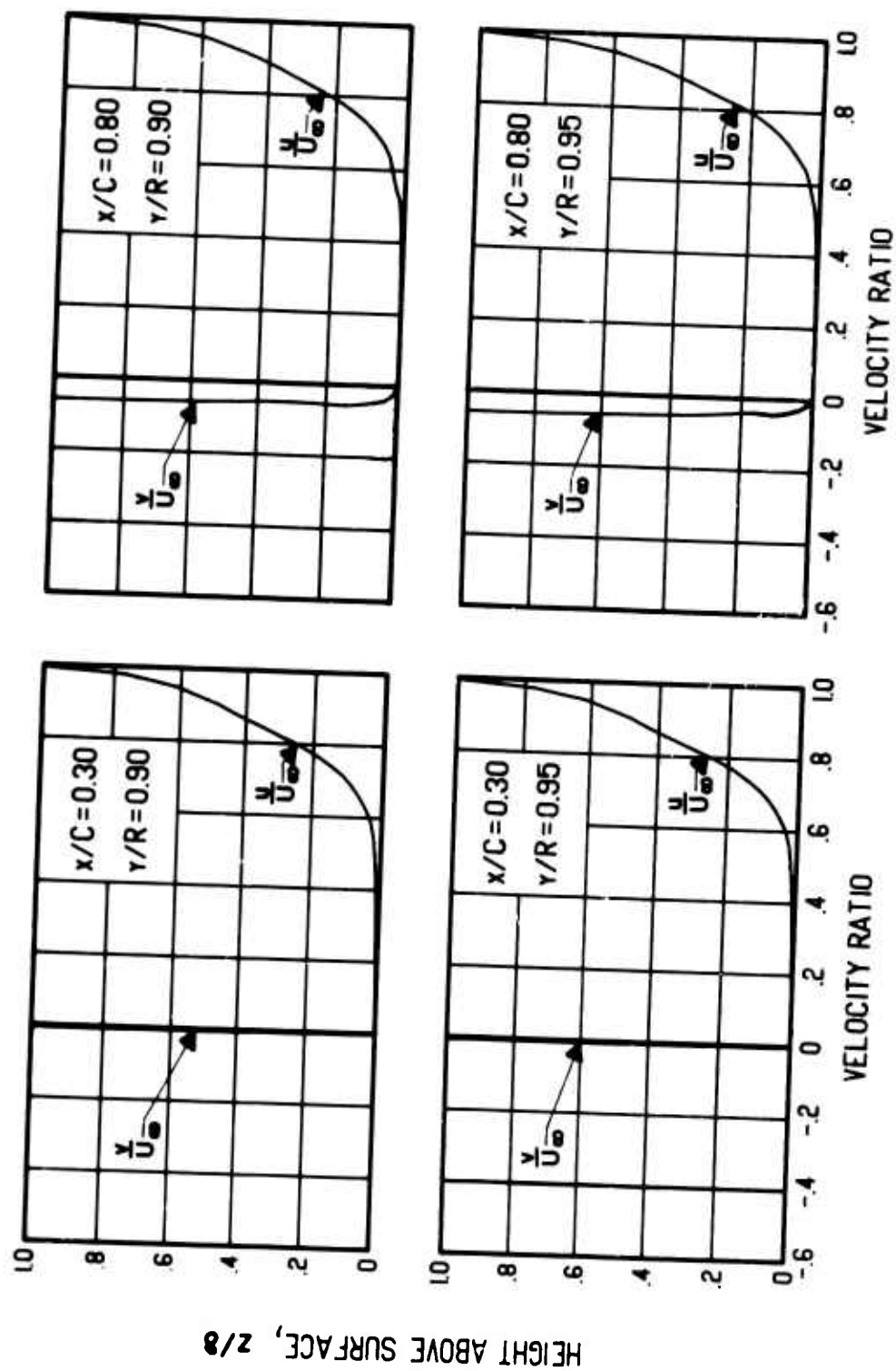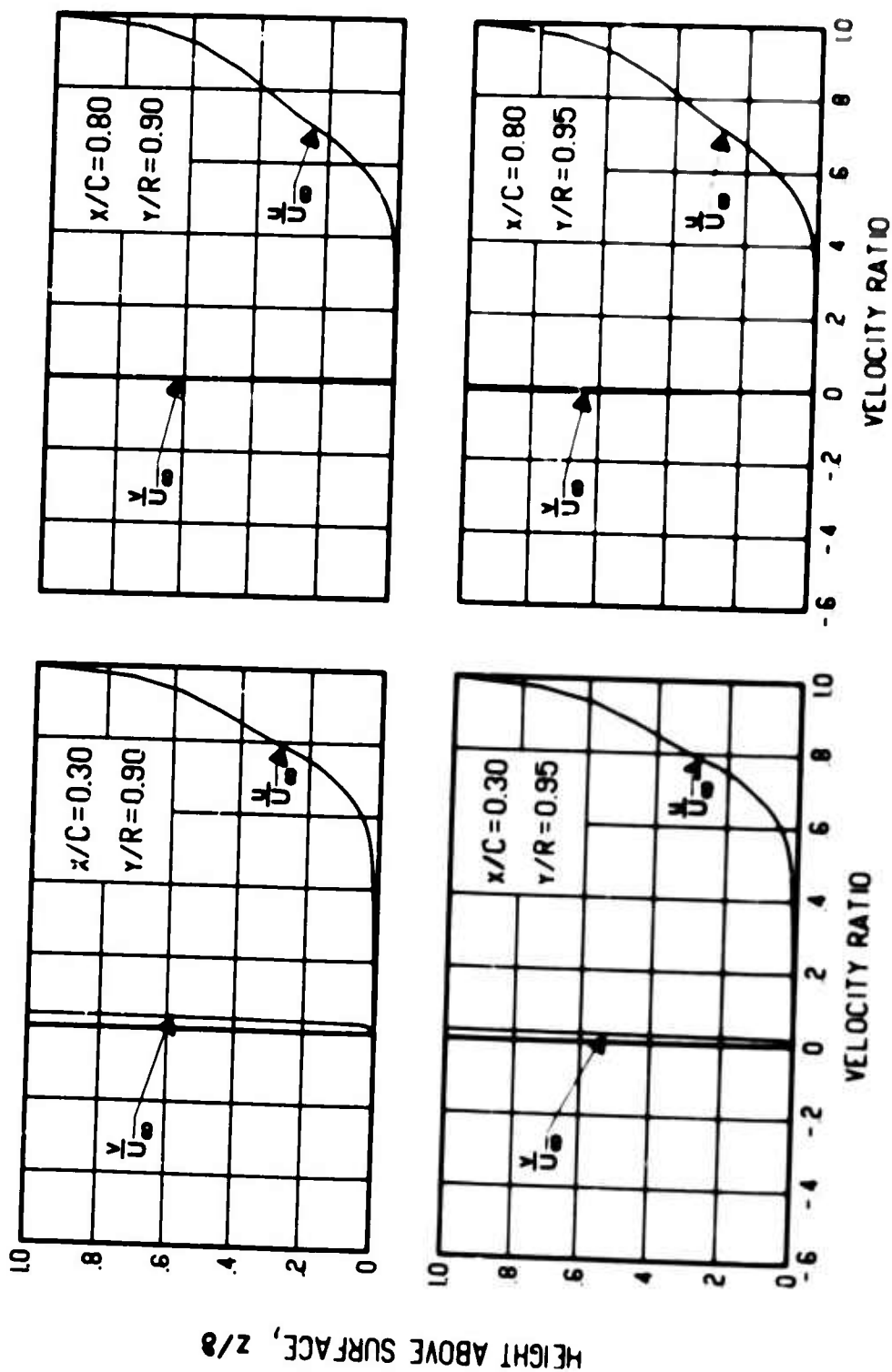
(c) Concluded.

Figure 35. Concluded.
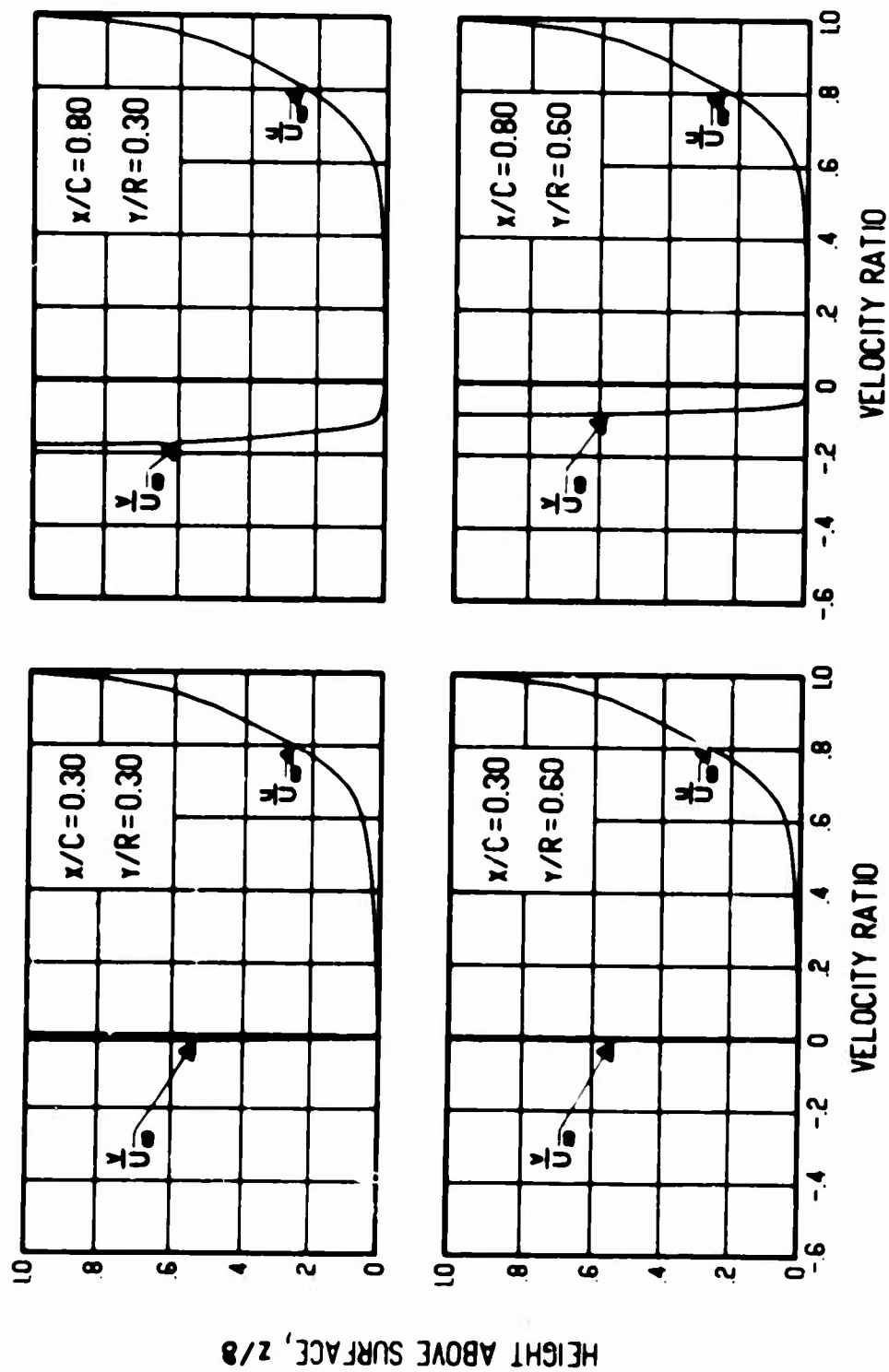
Figure 36. Chordwise and Spanwise Velocity Profiles for Various Vortex Strengths, Blade Radius = 10 ft, Ω = 60 rad/sec, dCp/d(x/C) = 0, Flat Surface.
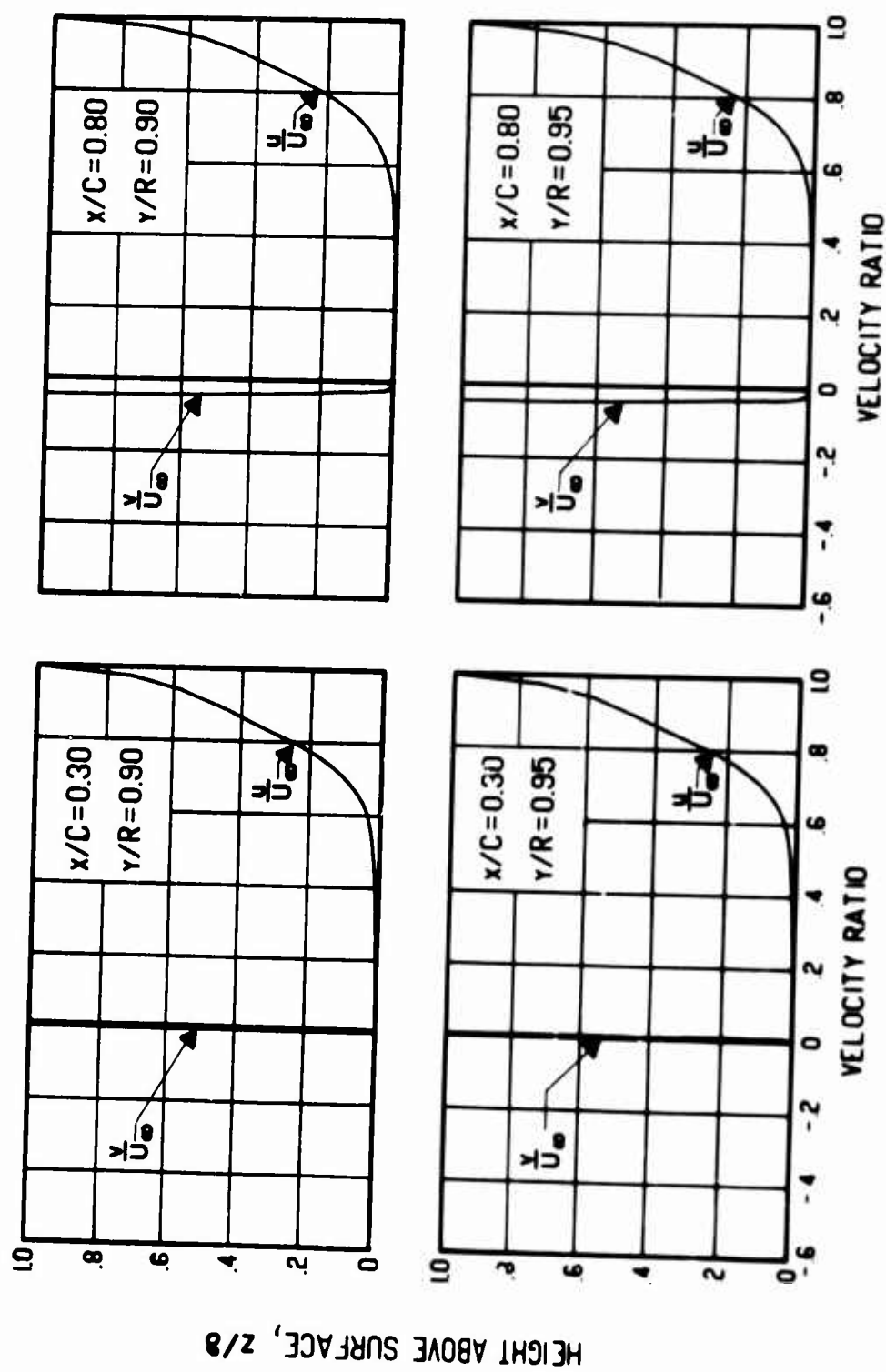
(a) Γ/h = +25 ft/sec
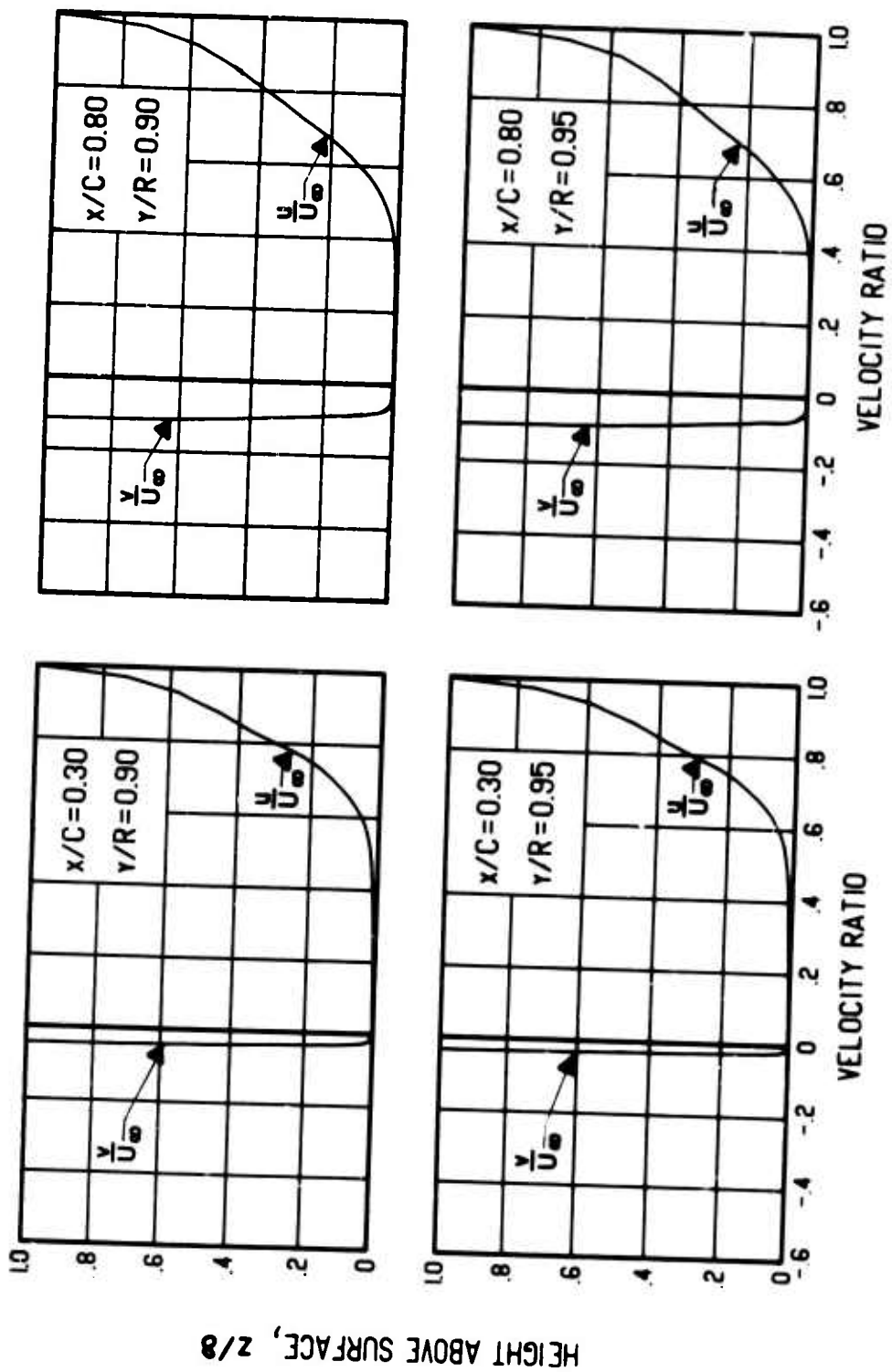
(a) Concluded.

Figure 36. Continued.
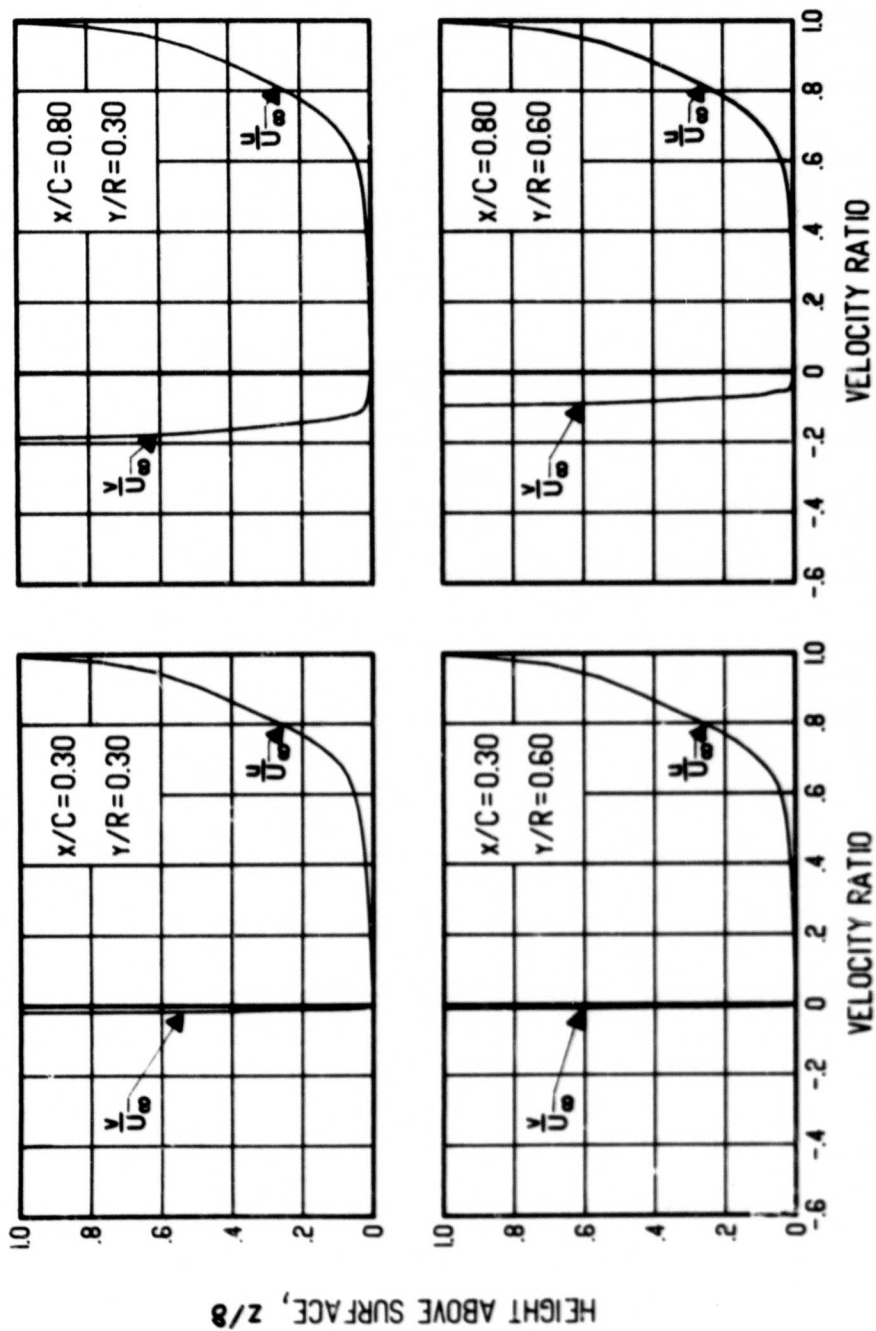
(b) $\Gamma/h = -25$ ft/sec

Figure 36. Continued.
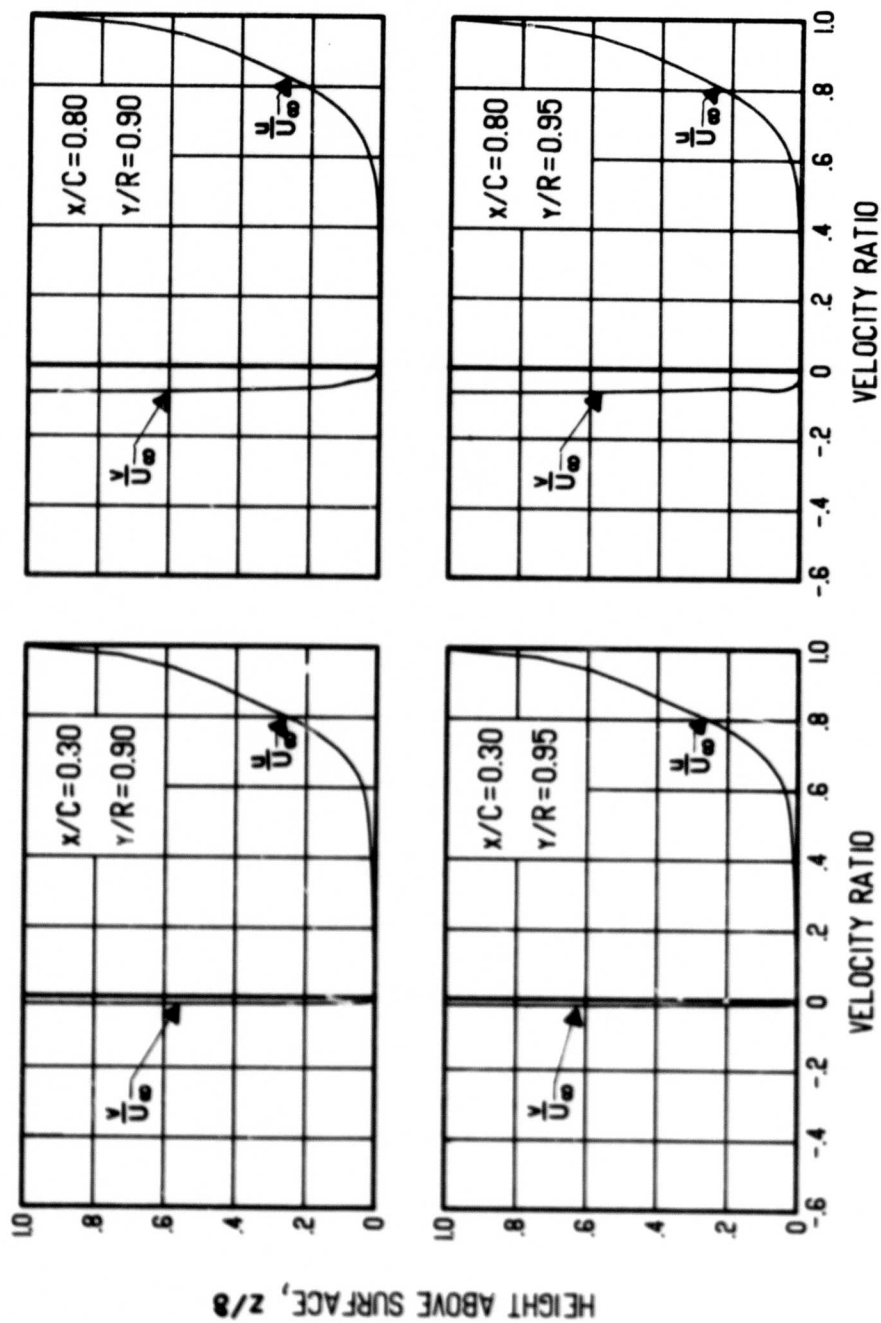
(b) Concluded.

Figure 36. Continued.

199

(c) $\Gamma/h = +50$ ft/sec

Figure 36. Continued.

200

(c) Concluded.

Figure 36. Continued.

201
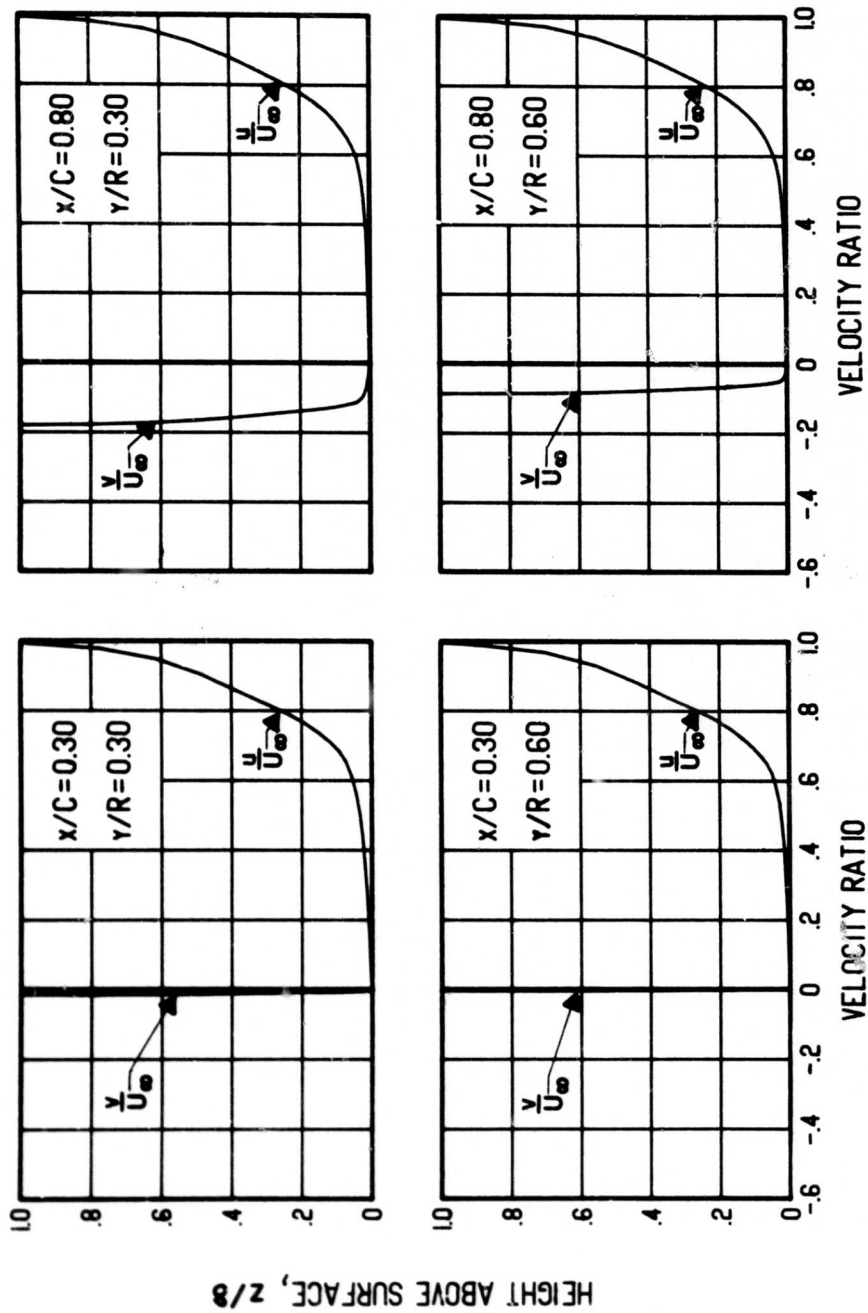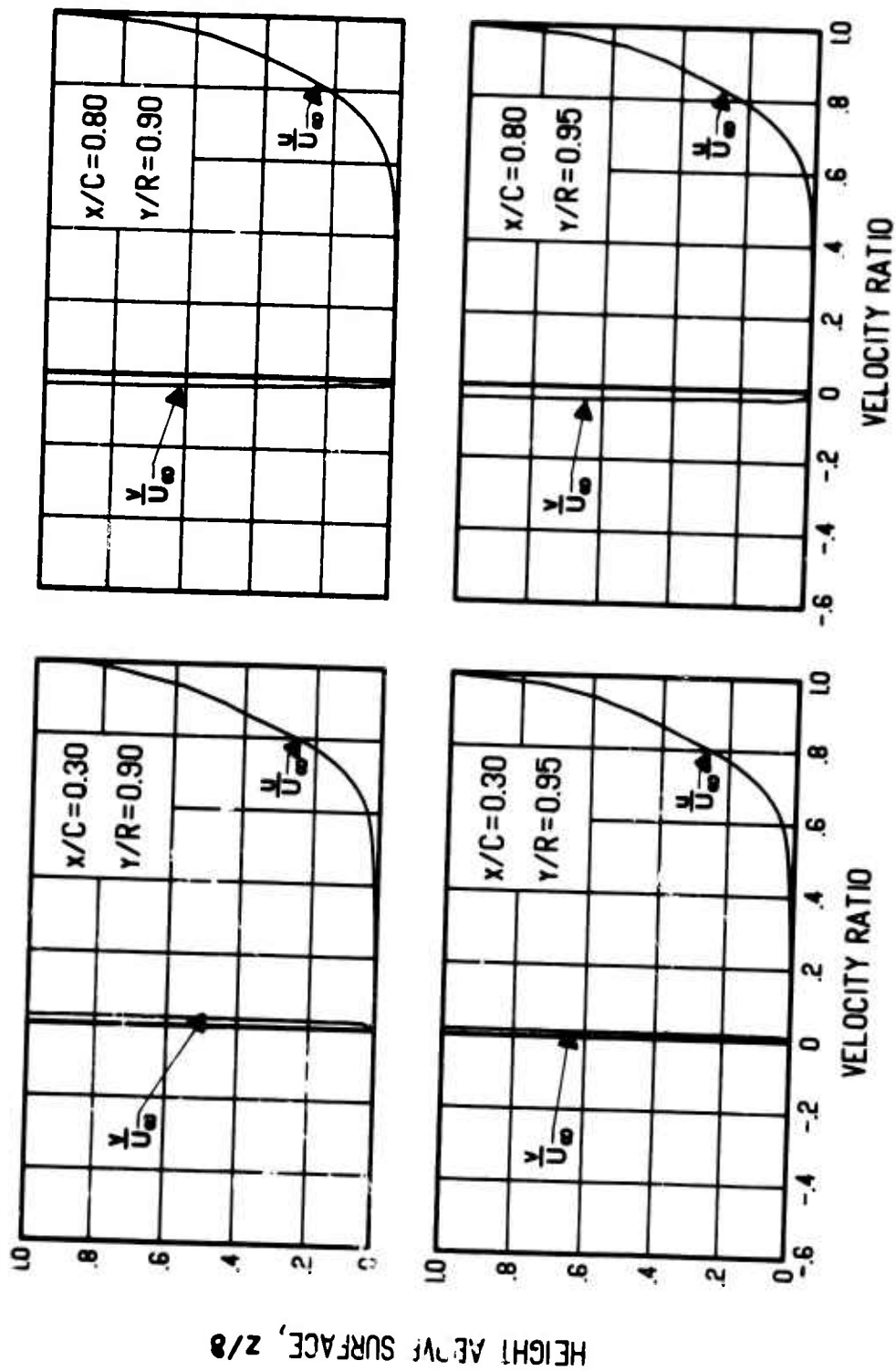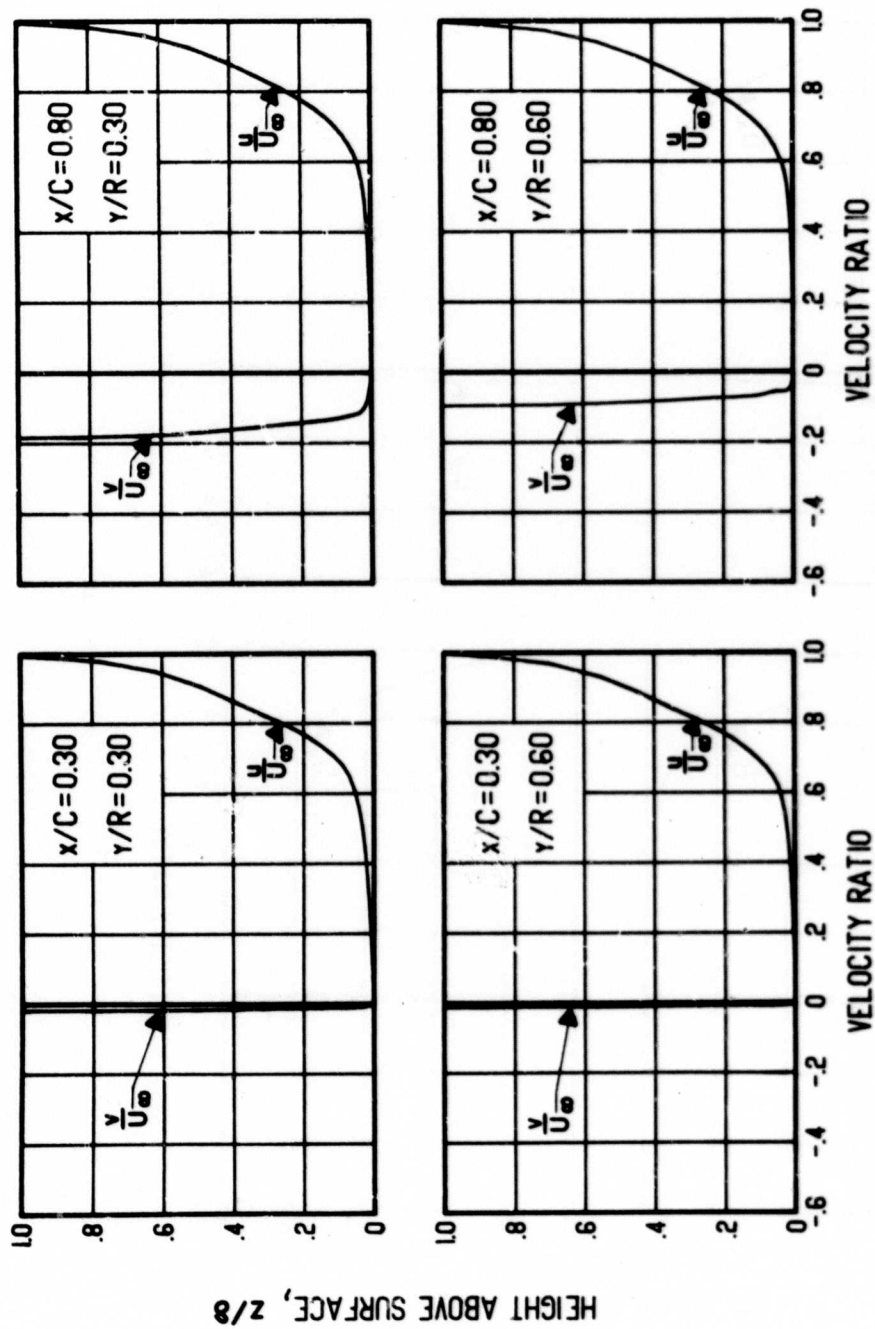
(d) $\Gamma/h = -50$ ft/sec

Figure 36. Continued.
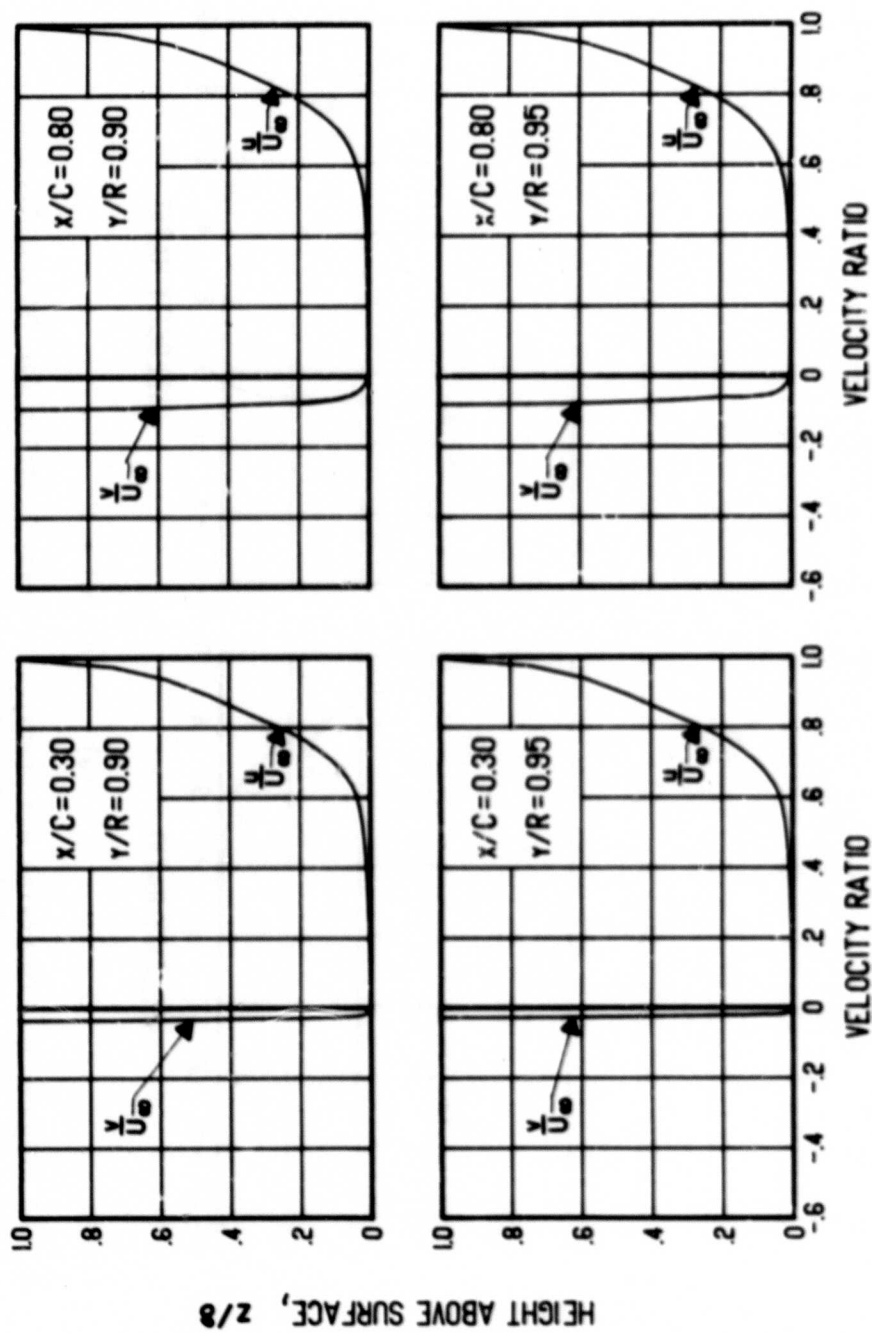
(d) Concluded.

Figure 36. Concluded.
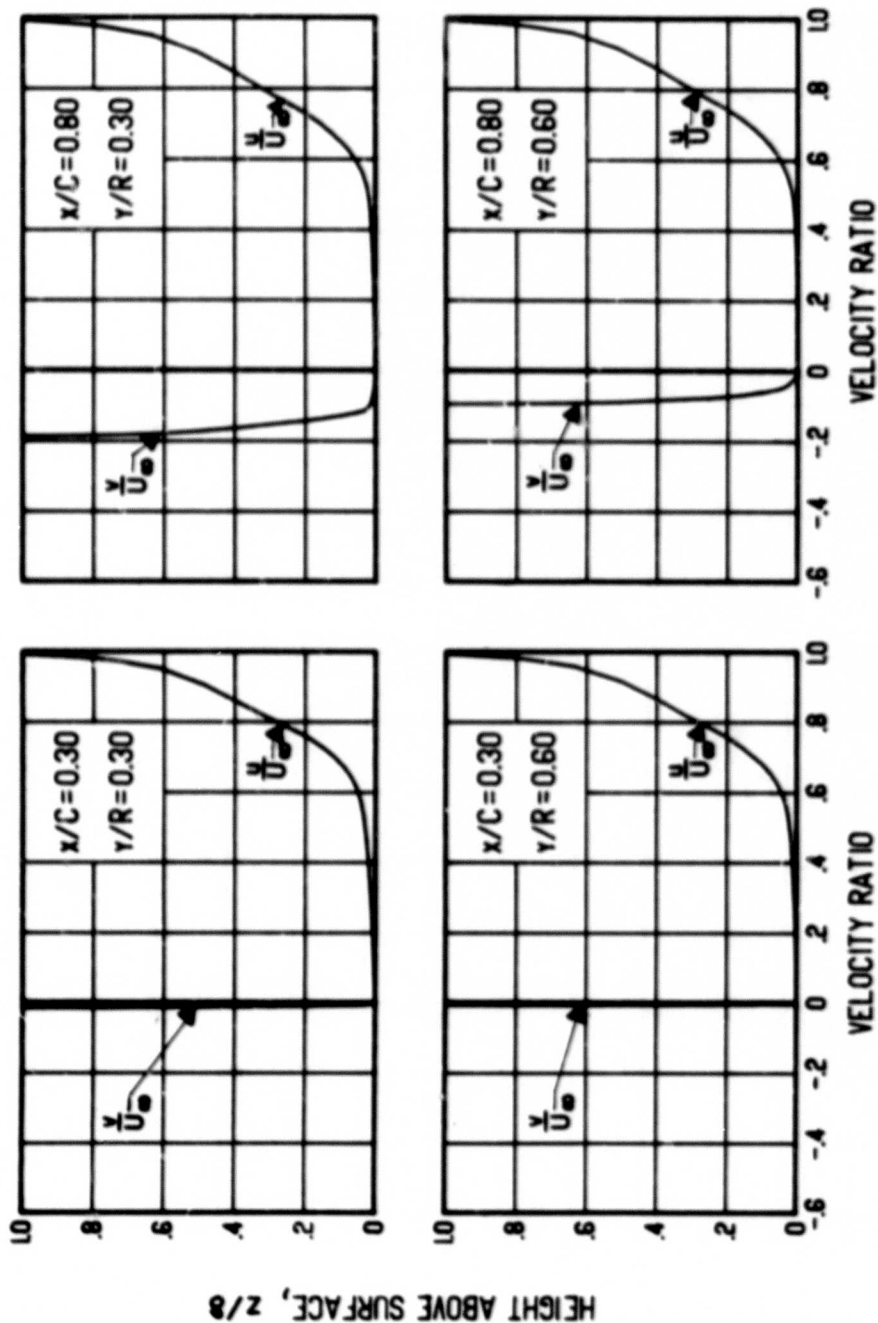
Figure 37. Chordwise and Spanwise Velocity Profiles for Various Pressure
Gradients, Blade Radius = 10 ft, Ω = 60 rad/sec,
Γ/h = 0 ft/sec, Flat Surface.

(a) $dCp/d(x/C) = 1$

204
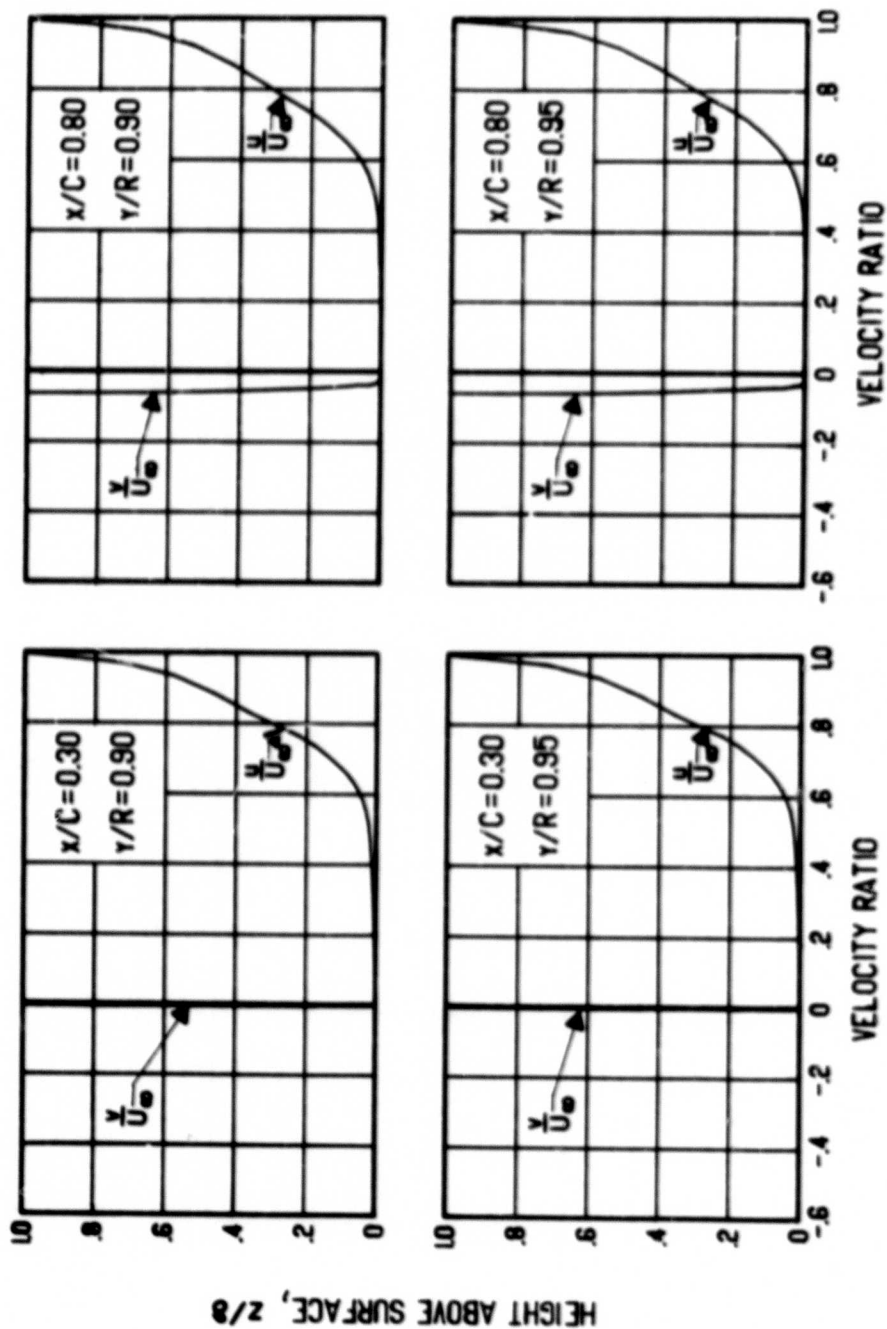
(a) Concluded.

Figure 37. Continued.
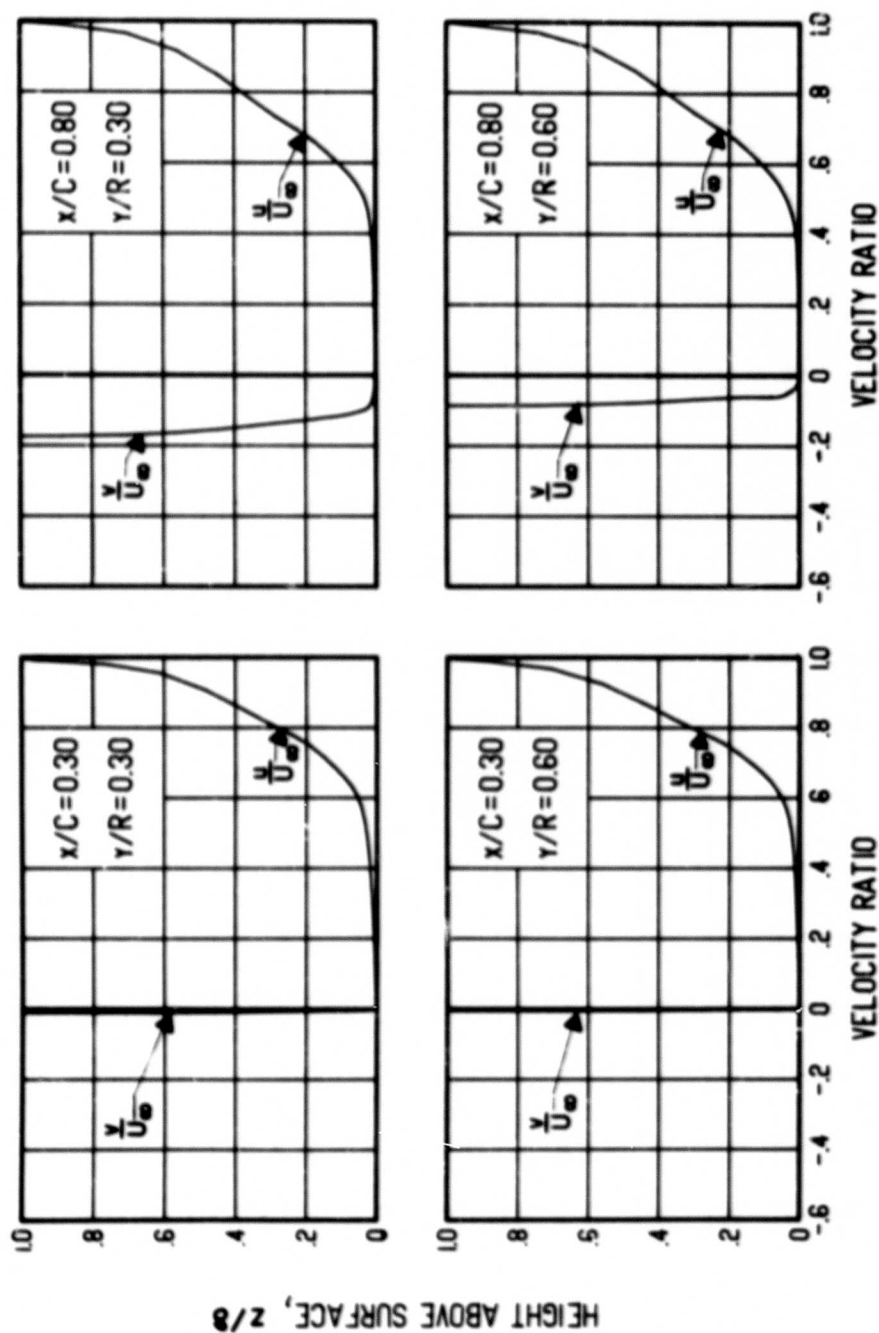
(b) $dCp/d(x/C) = 2$

Figure 37. Continued.
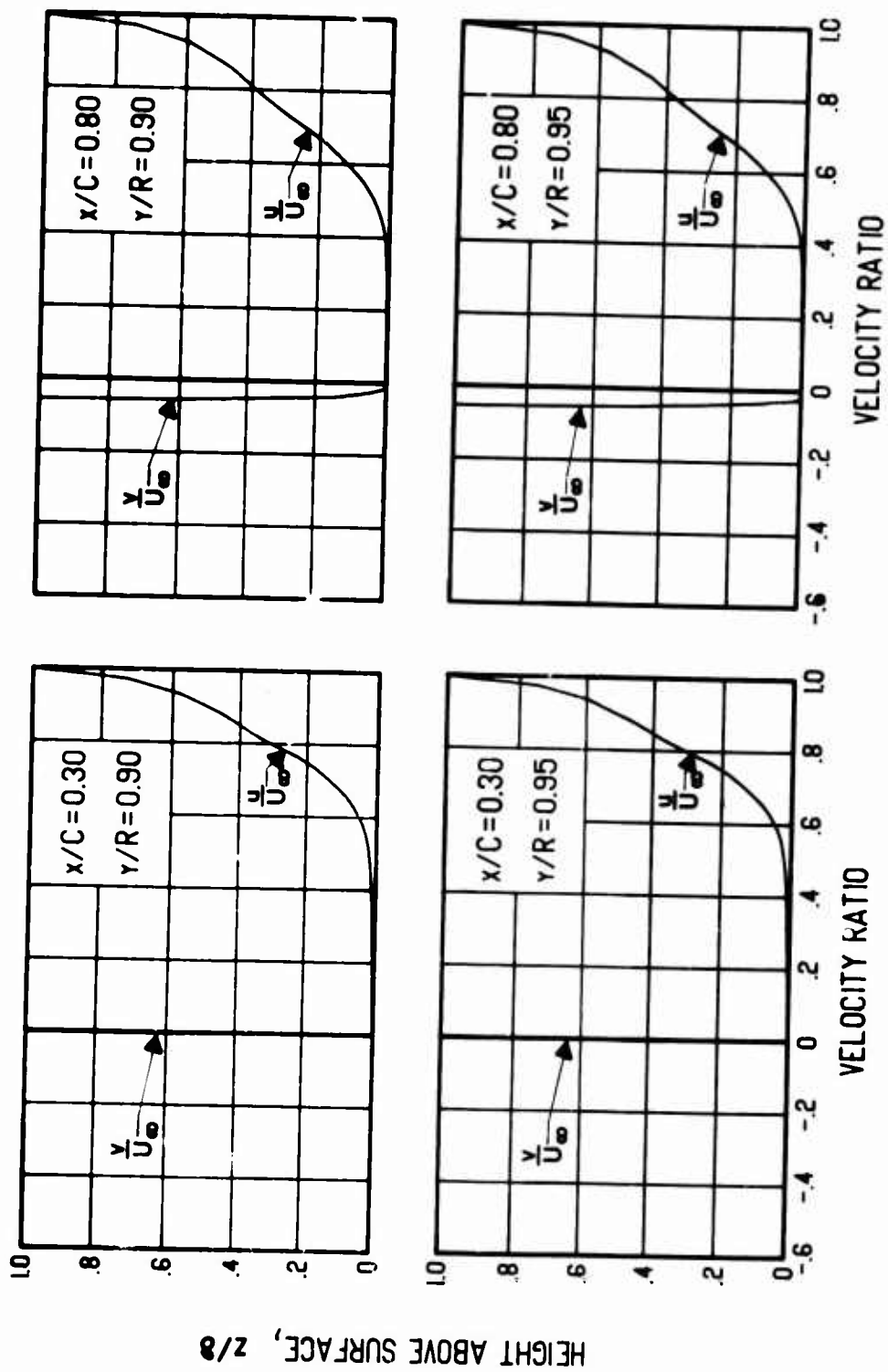
(b) Concluded.

Figure 37. Concluded.

207
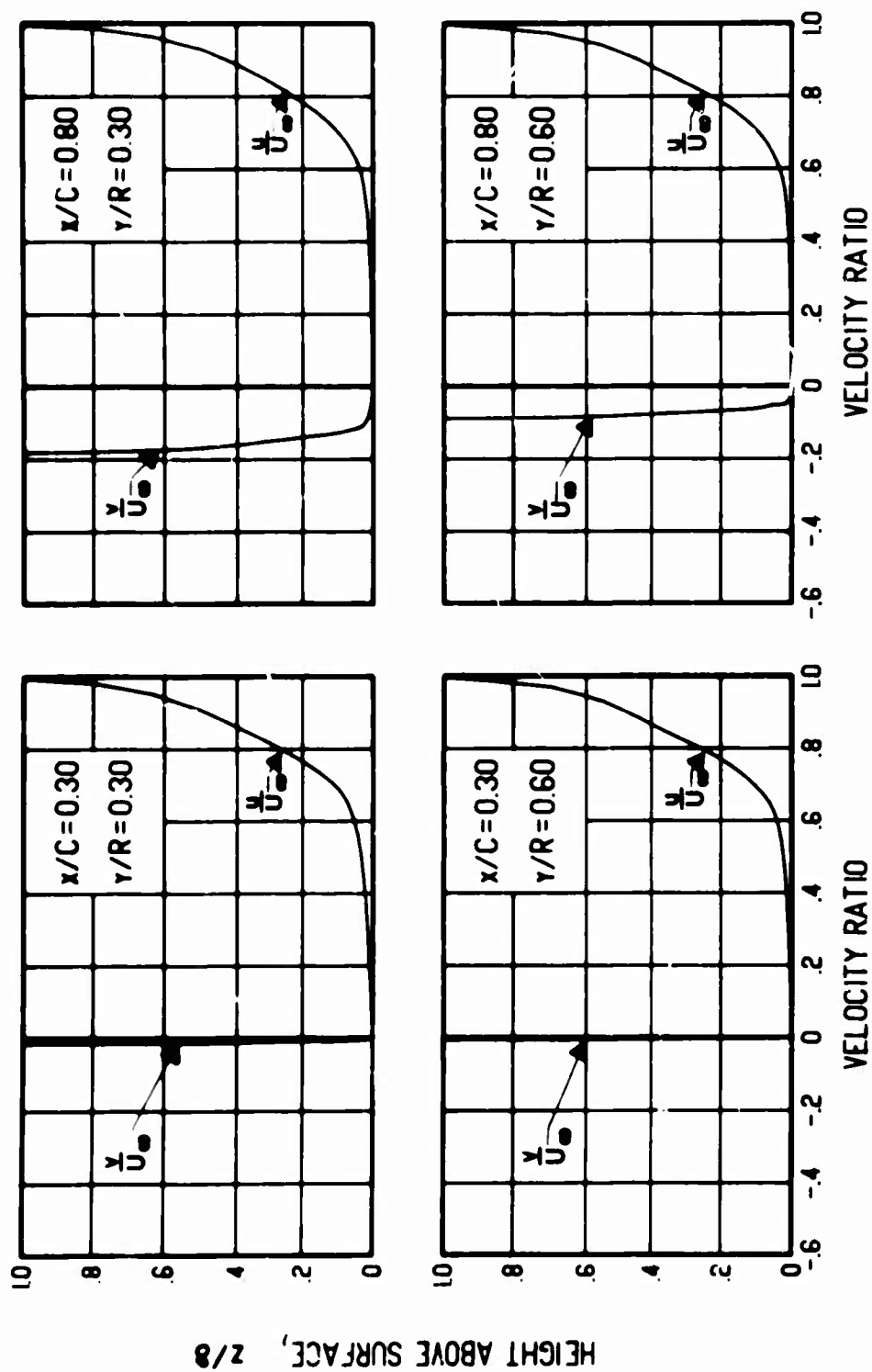
Figure 38. Chordwise and Spanwise Velocity Profiles for Various Vortex Strengths, Blade Radius = 10 ft, Ω = 60 rad/sec, $dCp/d(x/C)$ = 0, Surface Radius of Curvature = 4.125 ft.

(a) Γ/h = +25 ft/sec

(a) Concluded.

Figure 38. Continued.

(b) $\Gamma/h = -25$ ft/sec

Figure 38. Continued.

(b) Concluded.

Figure 38. Continued.

(c) $\Gamma/h = +50$ ft/sec

Figure 38. Continued.

212

(c) Concluded.

Figure 38. Continued.

213

(d) Γ/h = -50 ft/sec

Figure 38. Continued.

214

(d) Concluded.

Figure 38. Concluded.

Figure 39. Chordwise and Spanwise Velocity Profiles for Various Pressure
Gradients, Blade Radius = 10 ft, Ω = 60 rad/sec,
Γ/h = 0 ft/sec, Surface Radius of Curvature = 4.125 ft.

(a) $dC_p/d(x/C)$ = 1

(a) Concluded.

Figure 39. Continued.

(b) $dC_p/d(x/C) = 2$

Figure 39. Continued.

HEIGHT ABOVE SURFACE, z/8

214

(b) Concluded.

Figure 39. Concluded.
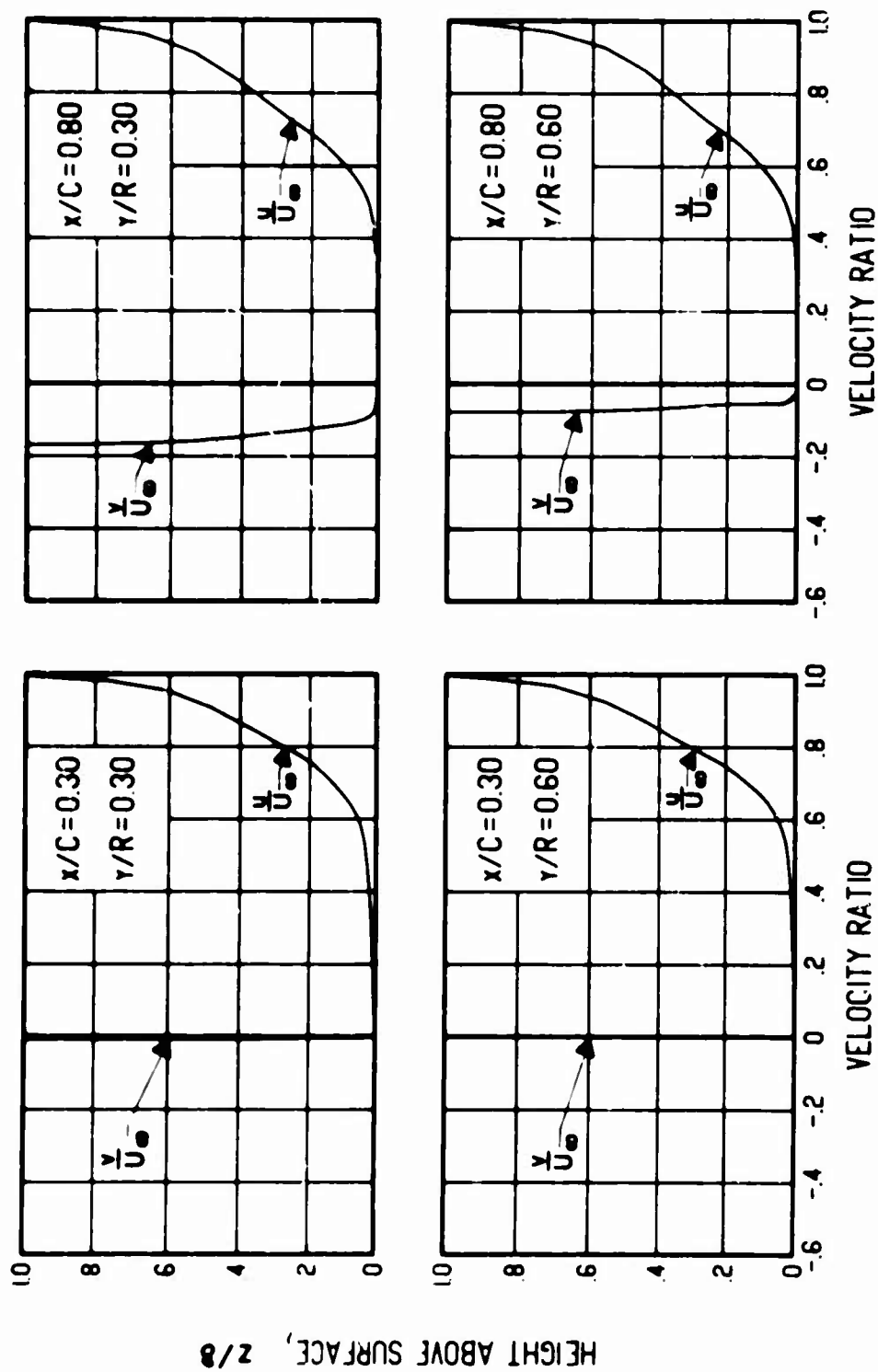
Figure 40. Chordwise and Spanwise Velocity Profiles for Various Vortex Strengths, Blade Radius = 10 ft, Ω = 60 rad/sec, $dCp/d(x/C)$ = 2, Surface Radius of Curvature = 4.125 ft.

(a) Γ/h = +50 ft/sec

(a) Concluded.

Figure 40. Continued.
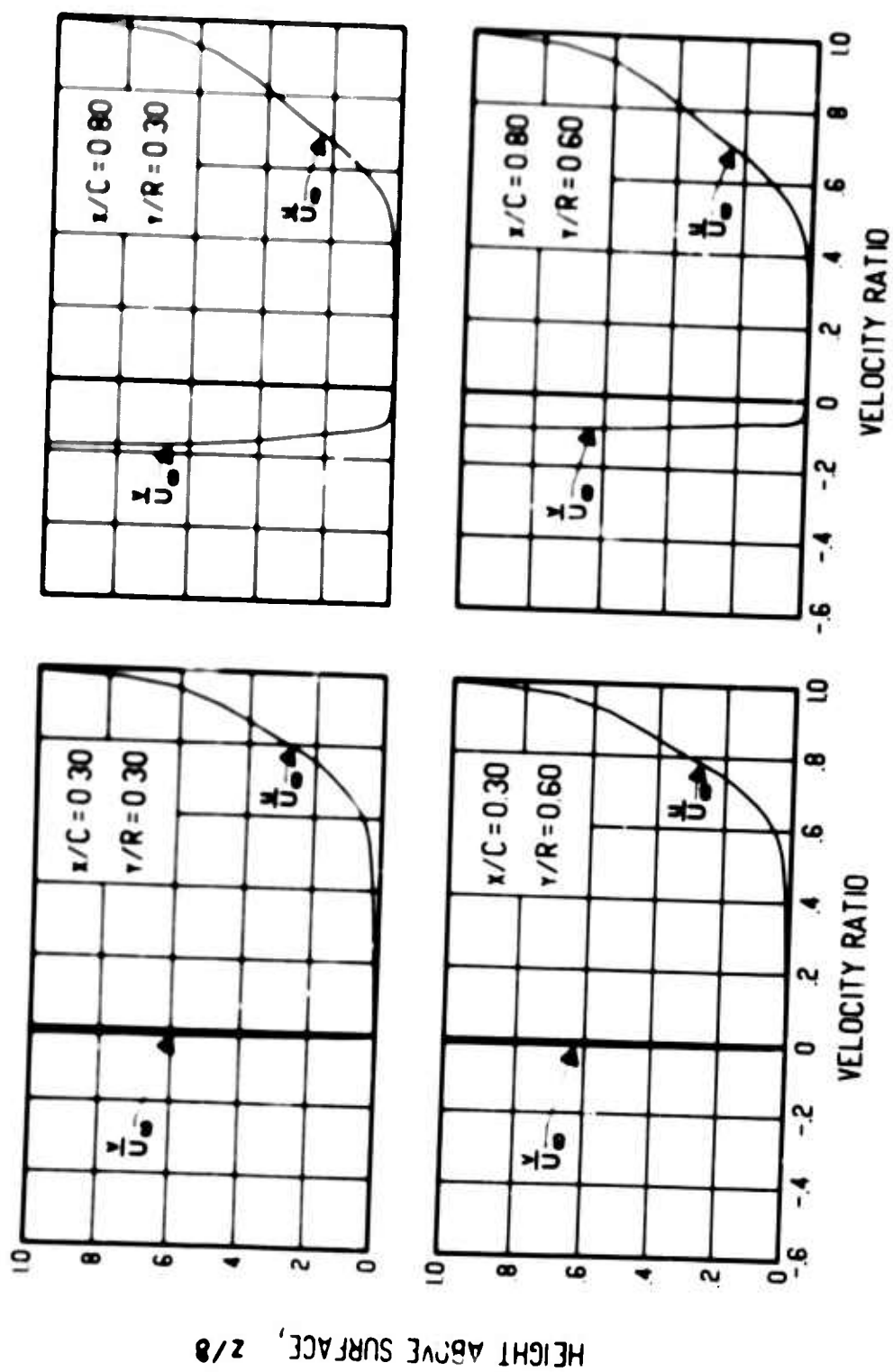
(b) $\Gamma/h = -50$ ft/sec

Figure 40. Continued.

HEIGHT ABOVE SURFACE, z/8

222

(b) Concluded.

Figure 40. Concluded.
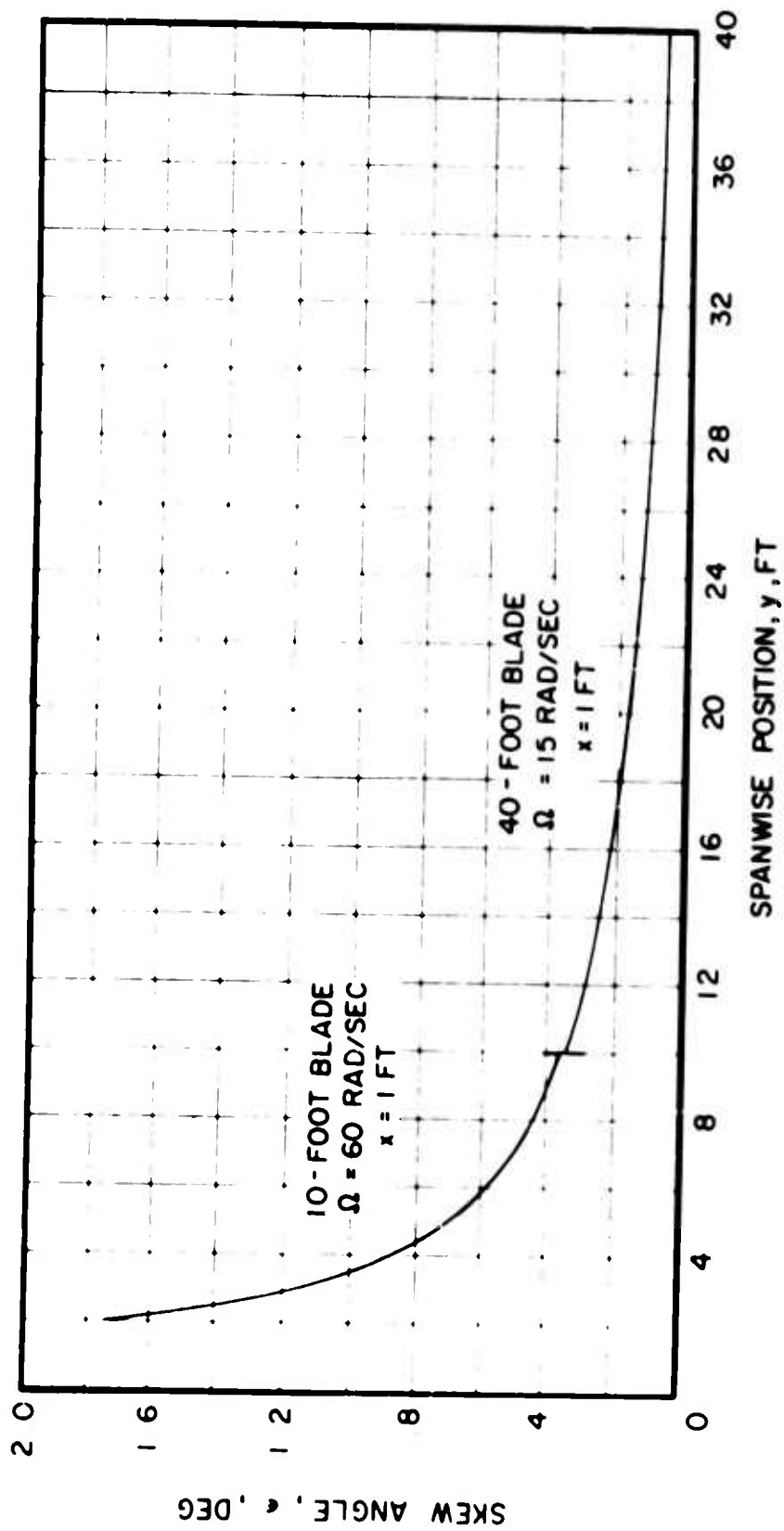
(a) Integral Method

Figure 41. Typical Effect of Angular Velocity on Skew
Angle Predicted by the Two Methods.
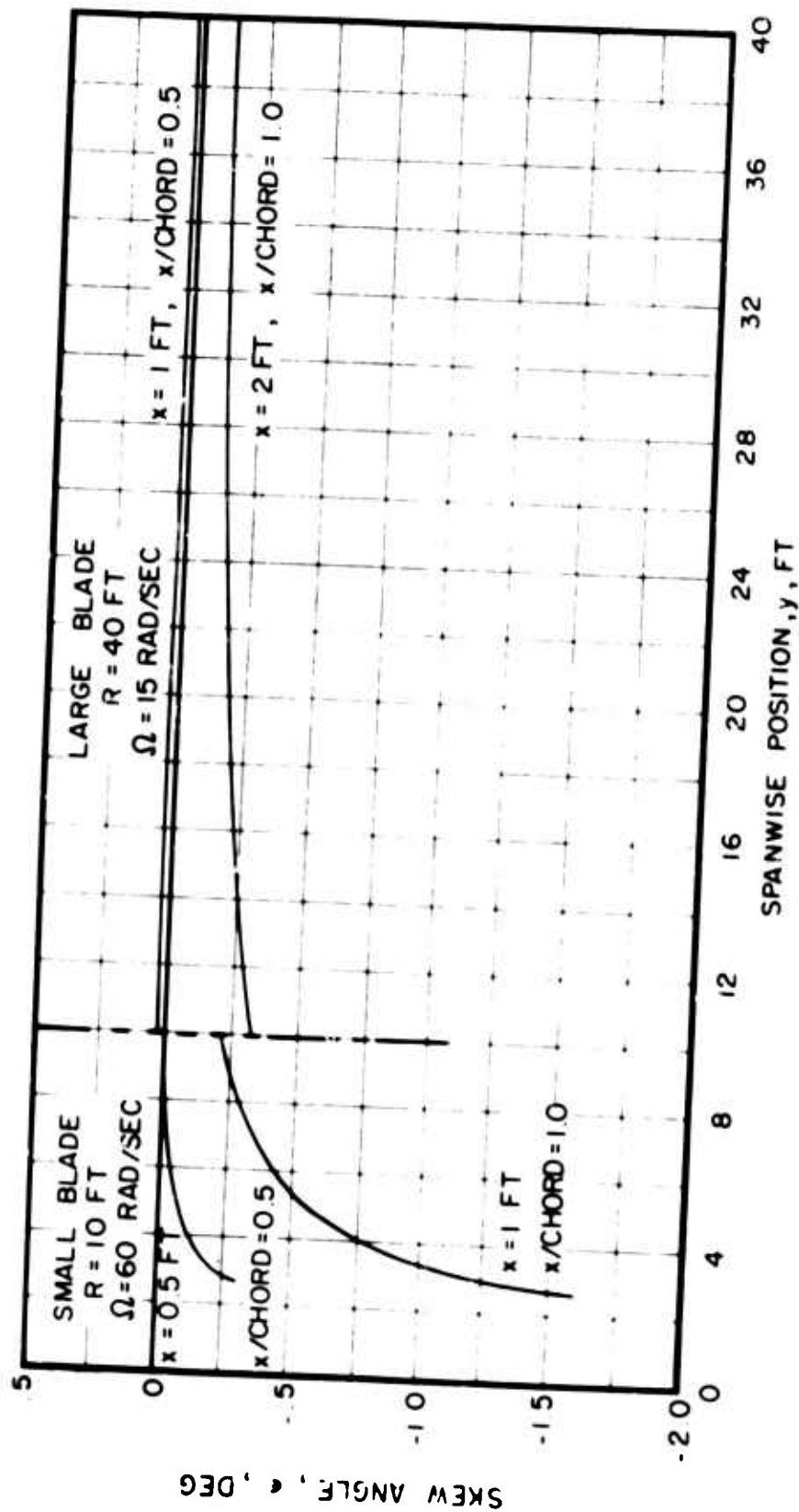
(b) Differential Method

Figure 41. Concluded.
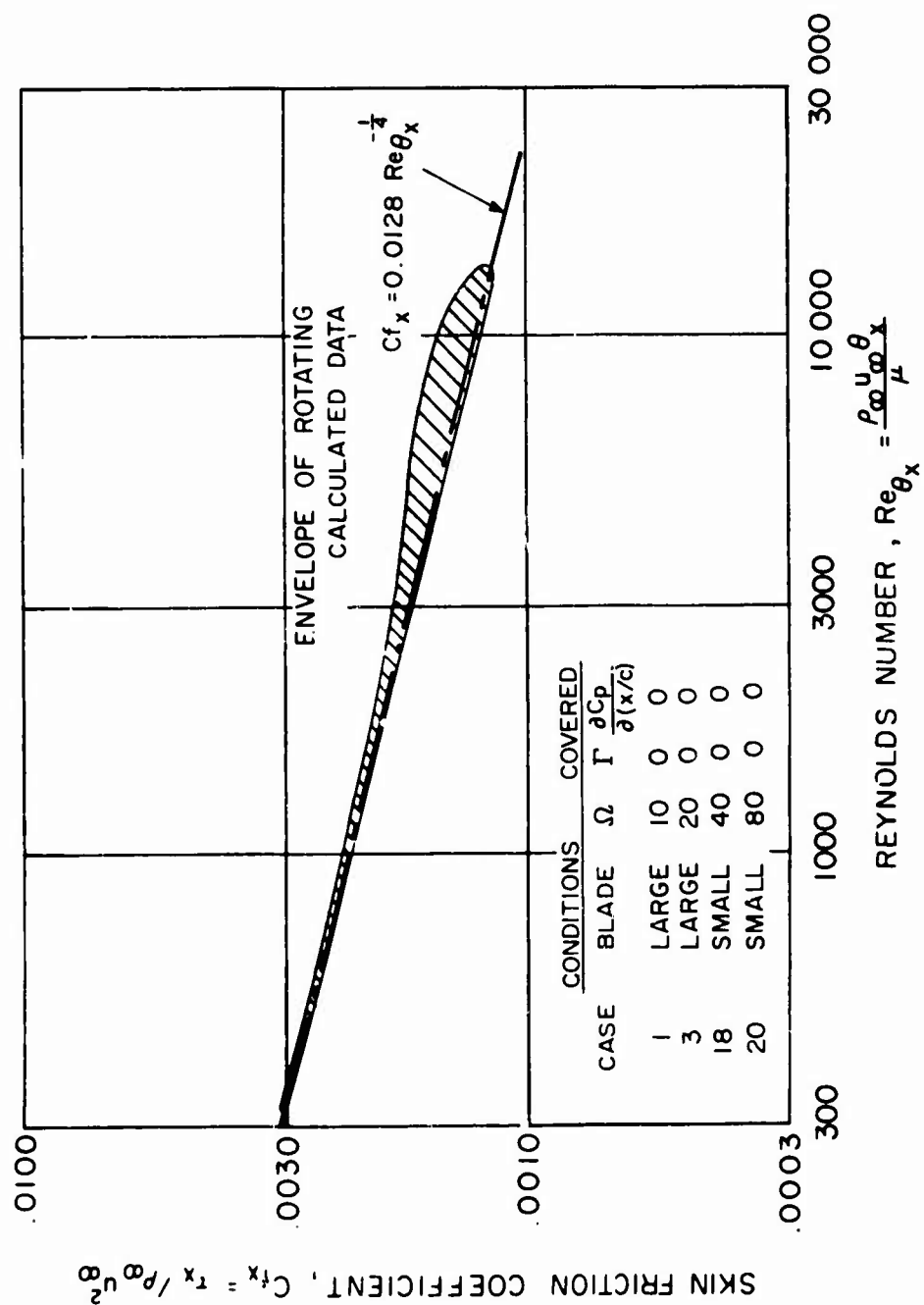
Figure 42. Effect of Angular Velocity on Chordwise Skin Friction.

Figure 43. Typical Effect of Vortex Crossflow on Spanwise Variation of Displacement Thickness and Skew Angle, $\partial C_p / \partial (x/C) = 0$, x/chord = 0.8, Ω = 15 rad/sec.

(a) Integral Method
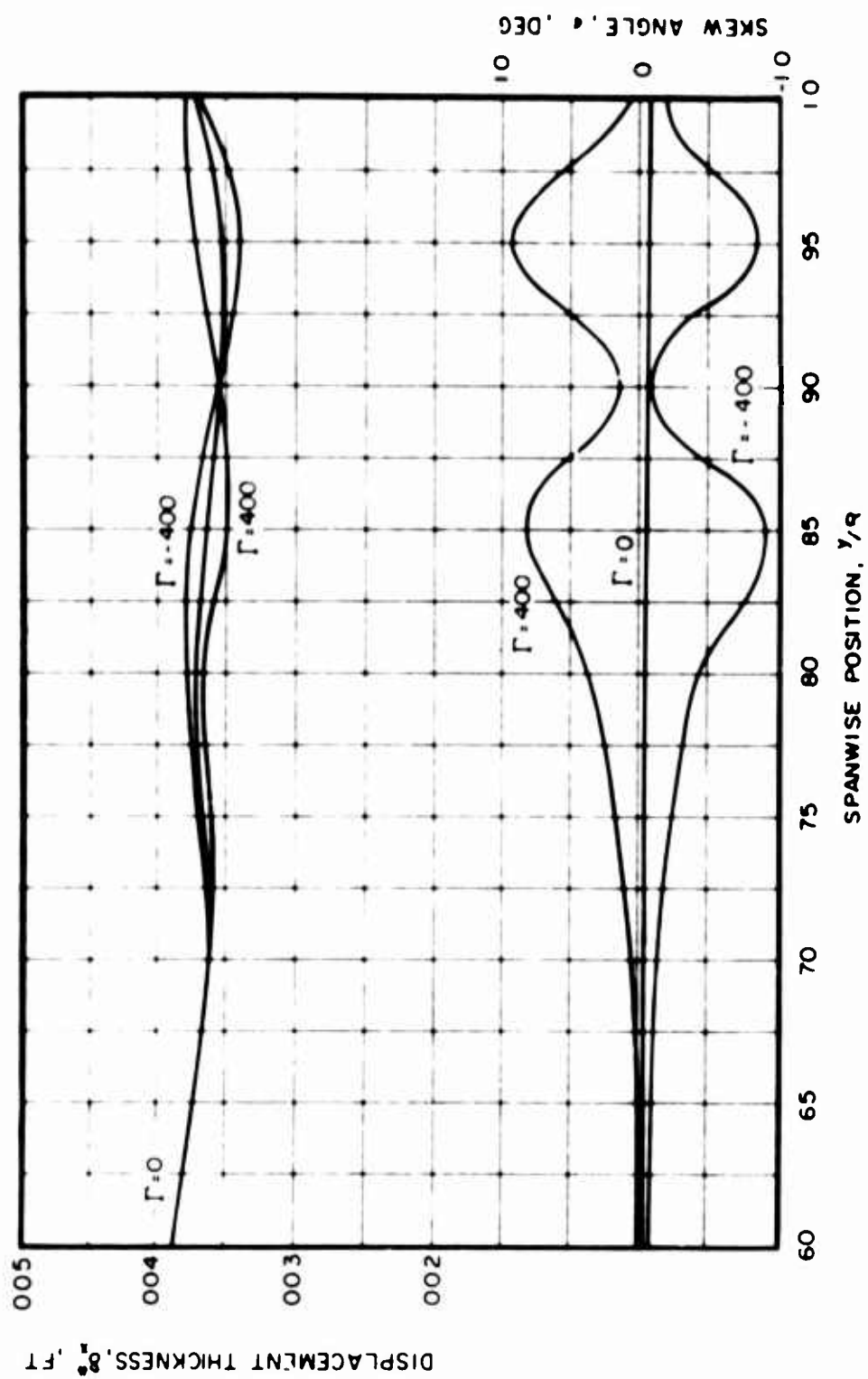
(b) Differential Method

Figure 43. Concluded.

228
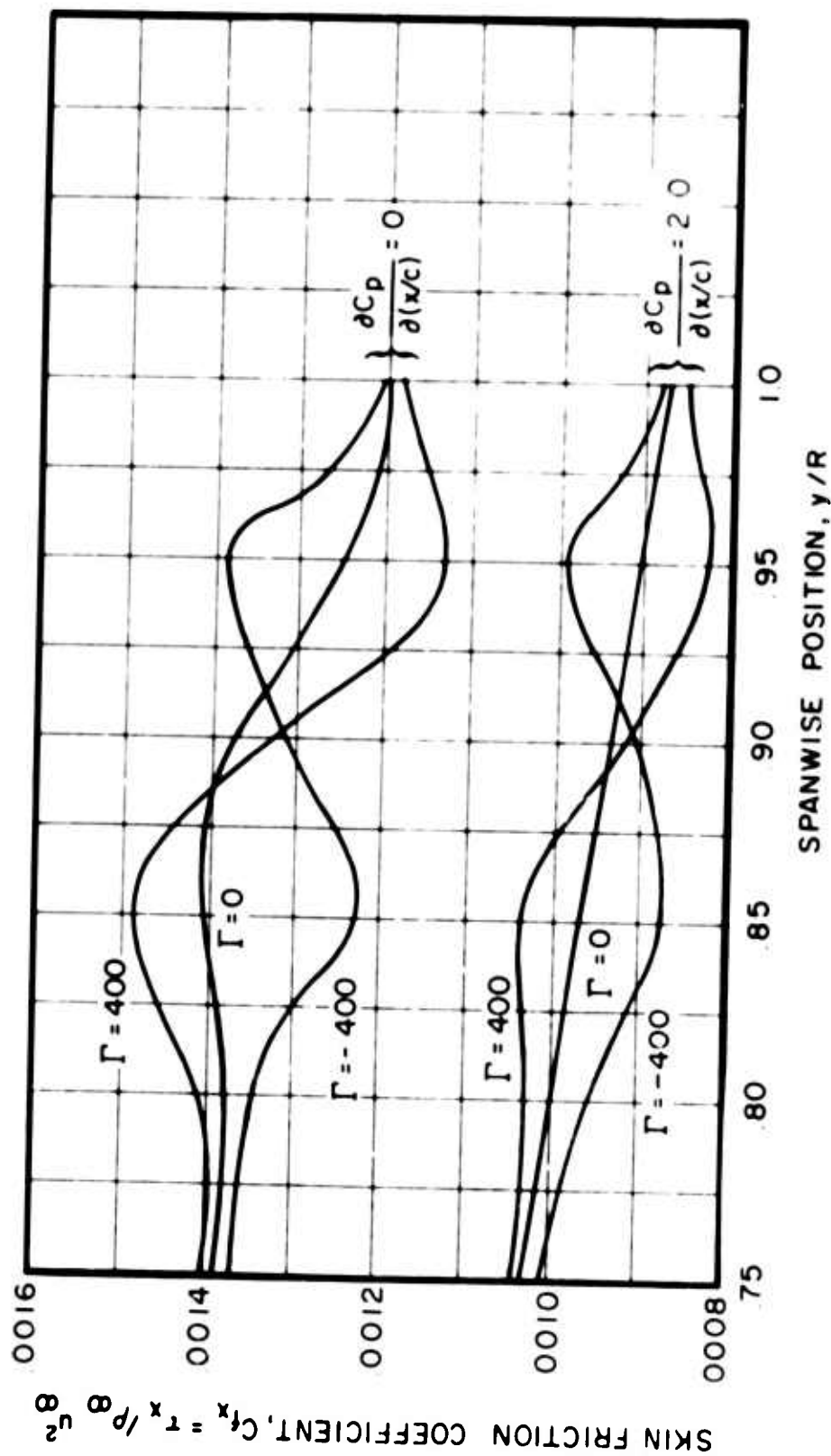
Figure 44. Typical Effect of Vortex Crossflow on Spanwise
Variation of Chordwise Skin Friction Coefficient,
$\partial C_p/\partial(x/C) = 0$, x/chord = 1.0.
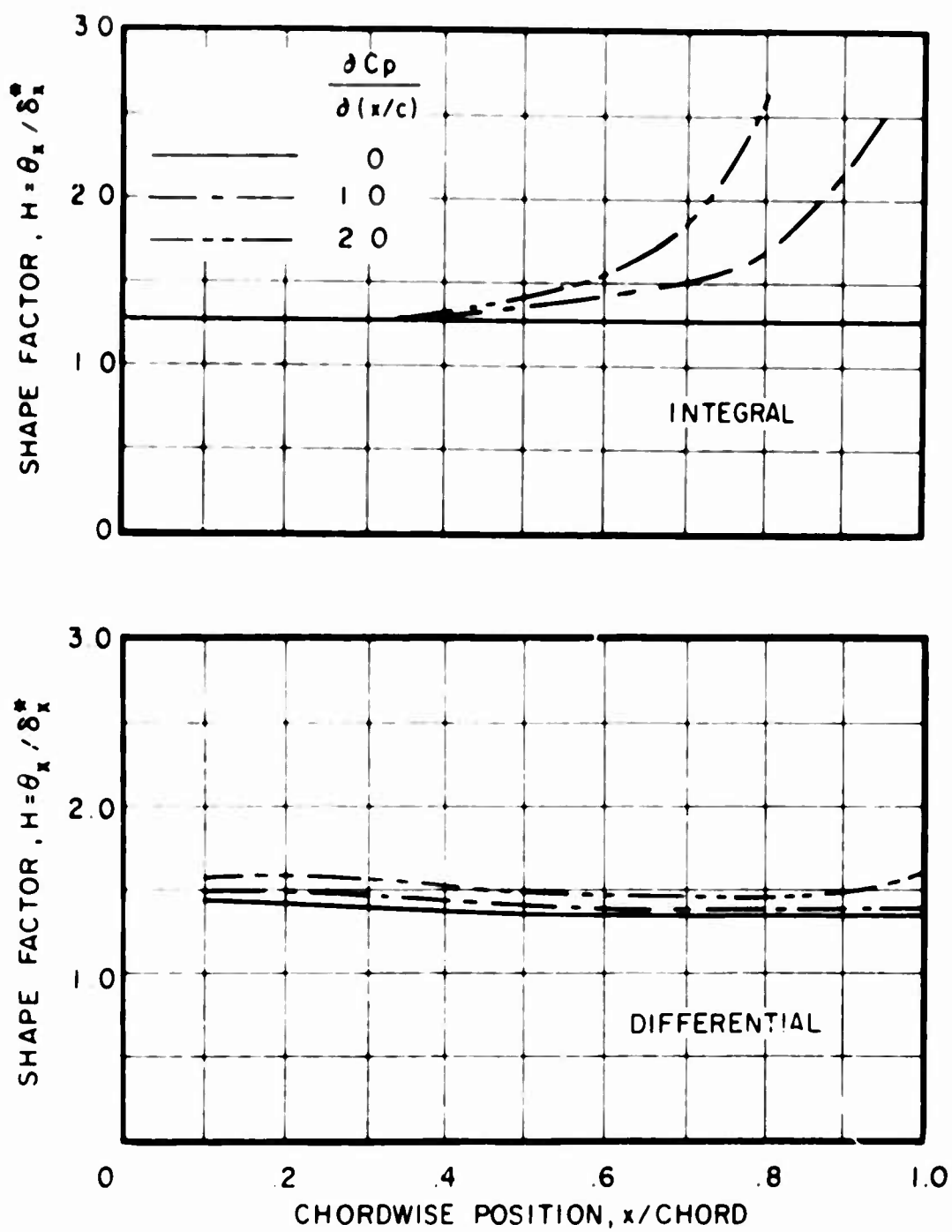
Figure 45. Typical Effect of Pressure Gradient on Chordwise
Variation of Shape Factor, H, $\partial C_p/\partial(x/C) = 0, 1, 2$,
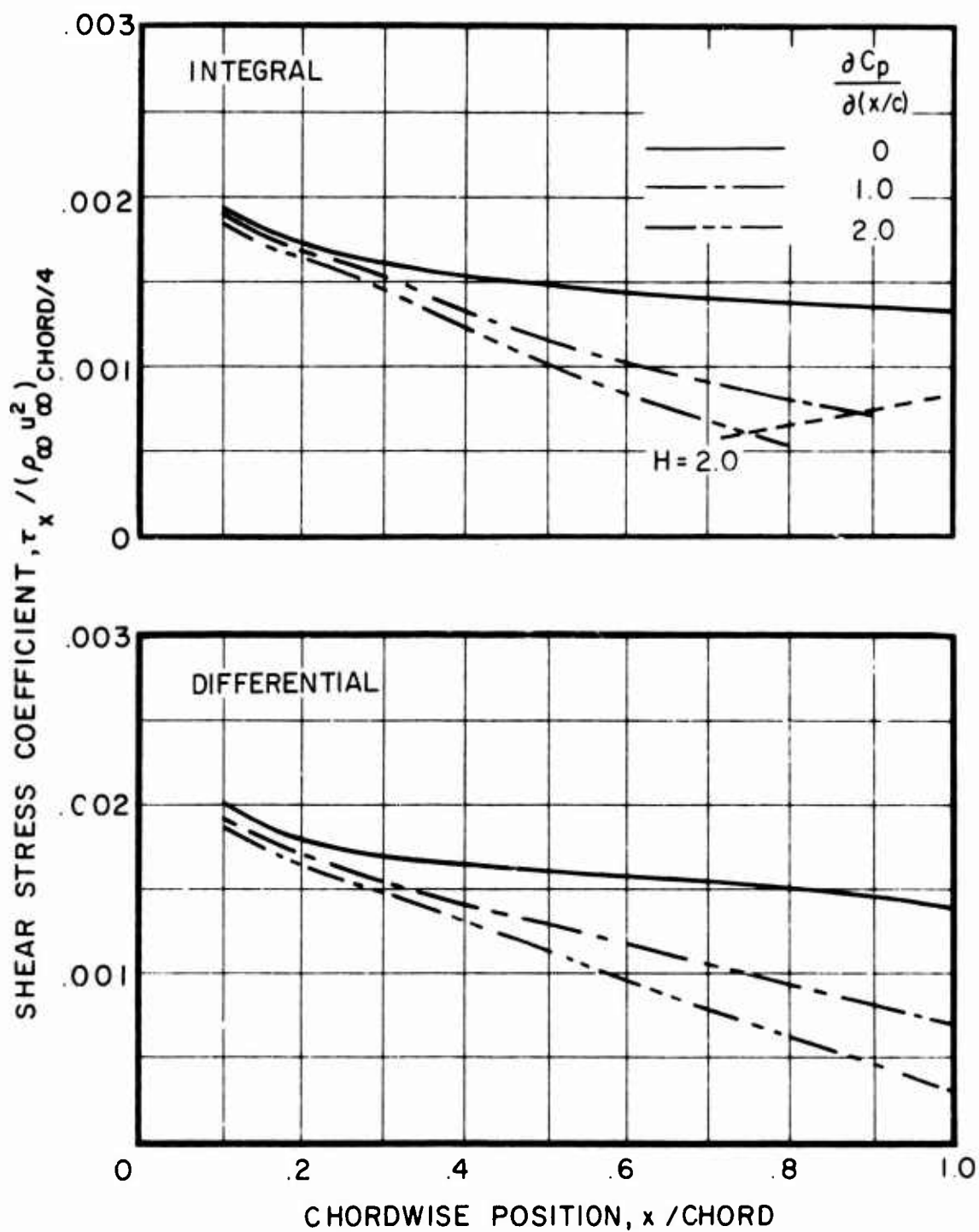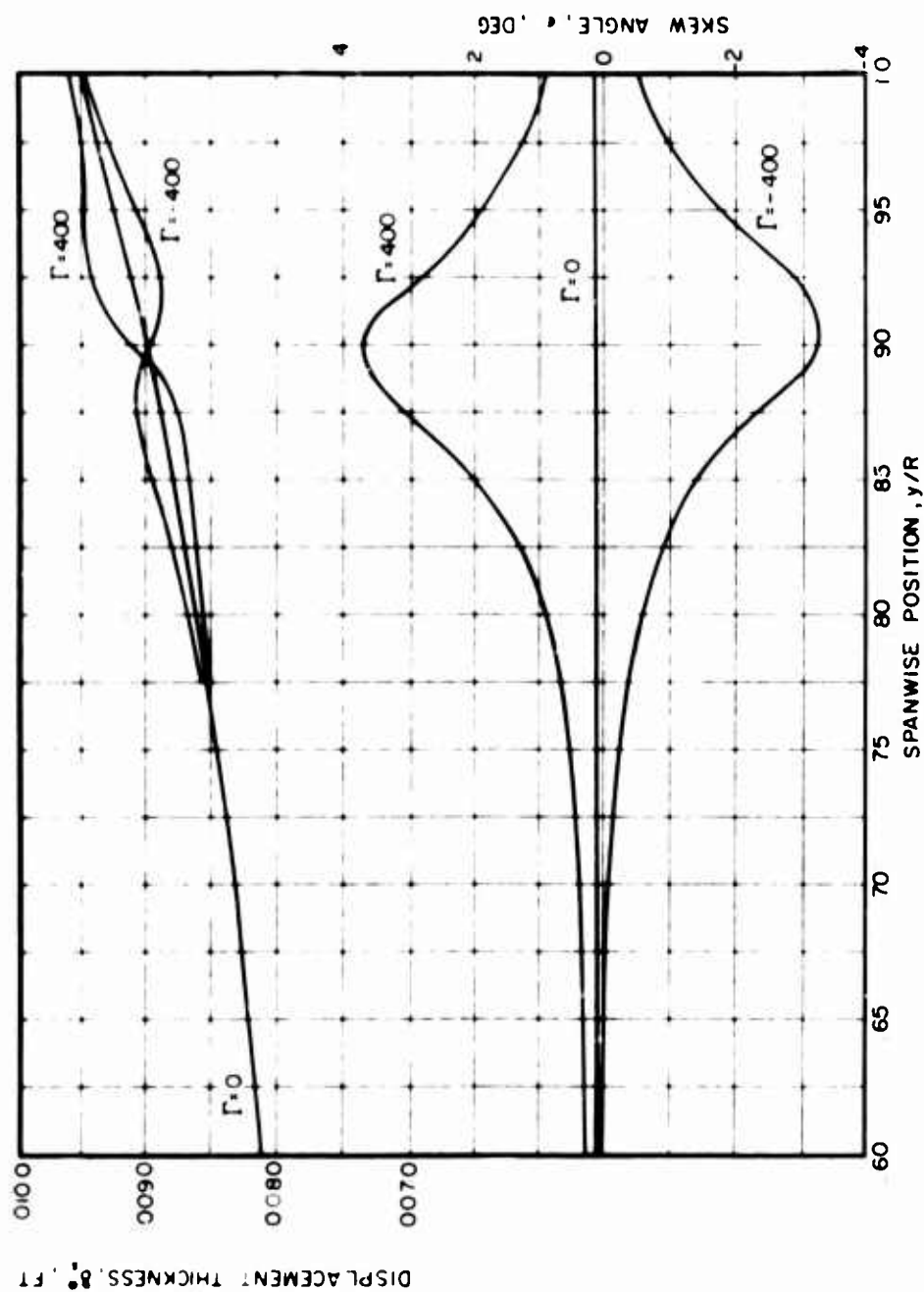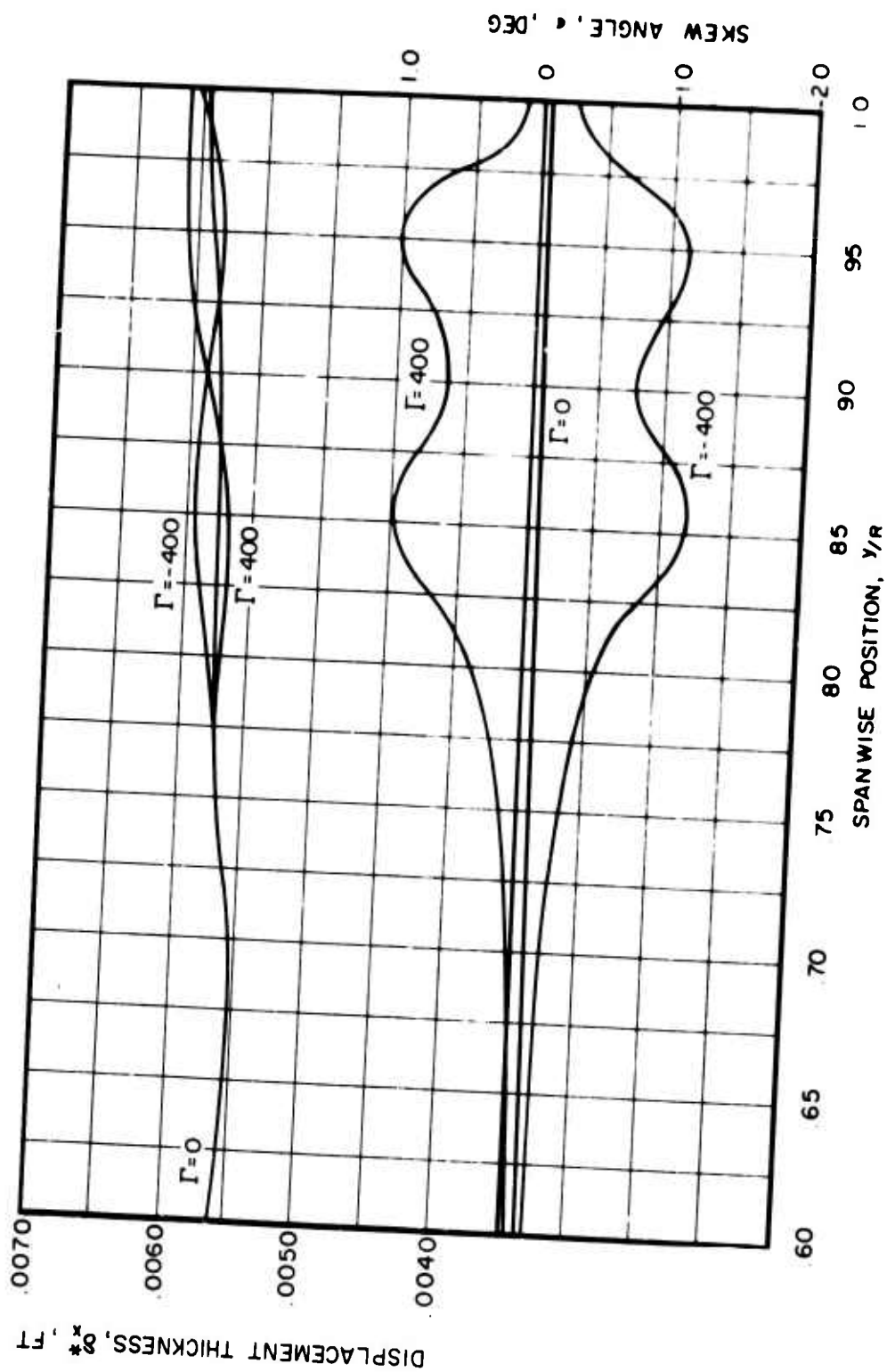$y/R = 0.9$, $\Omega = 15$ rad/sec, $\Gamma = 0$.

Figure 46. Typical Effect of Pressure Gradient on Chordwise
Variation of Chordwise Shear Stress,
$\partial C_p / \partial (x/C) = 0, 1, 2$, $y/R = 0.9$, $\Omega = 15$ rad/sec,
$\Gamma = 0$.

Figure 47. Typical Effect of Vortex Crossflow on Spanwise Variation of Displacement Thickness and Skew Angle, $\partial C_p / \partial (x/C) = 2$, $x/Chord = 0.7$, $\Omega = 15$ rad/sec.

(a) Integral Method

(b) Differential Method
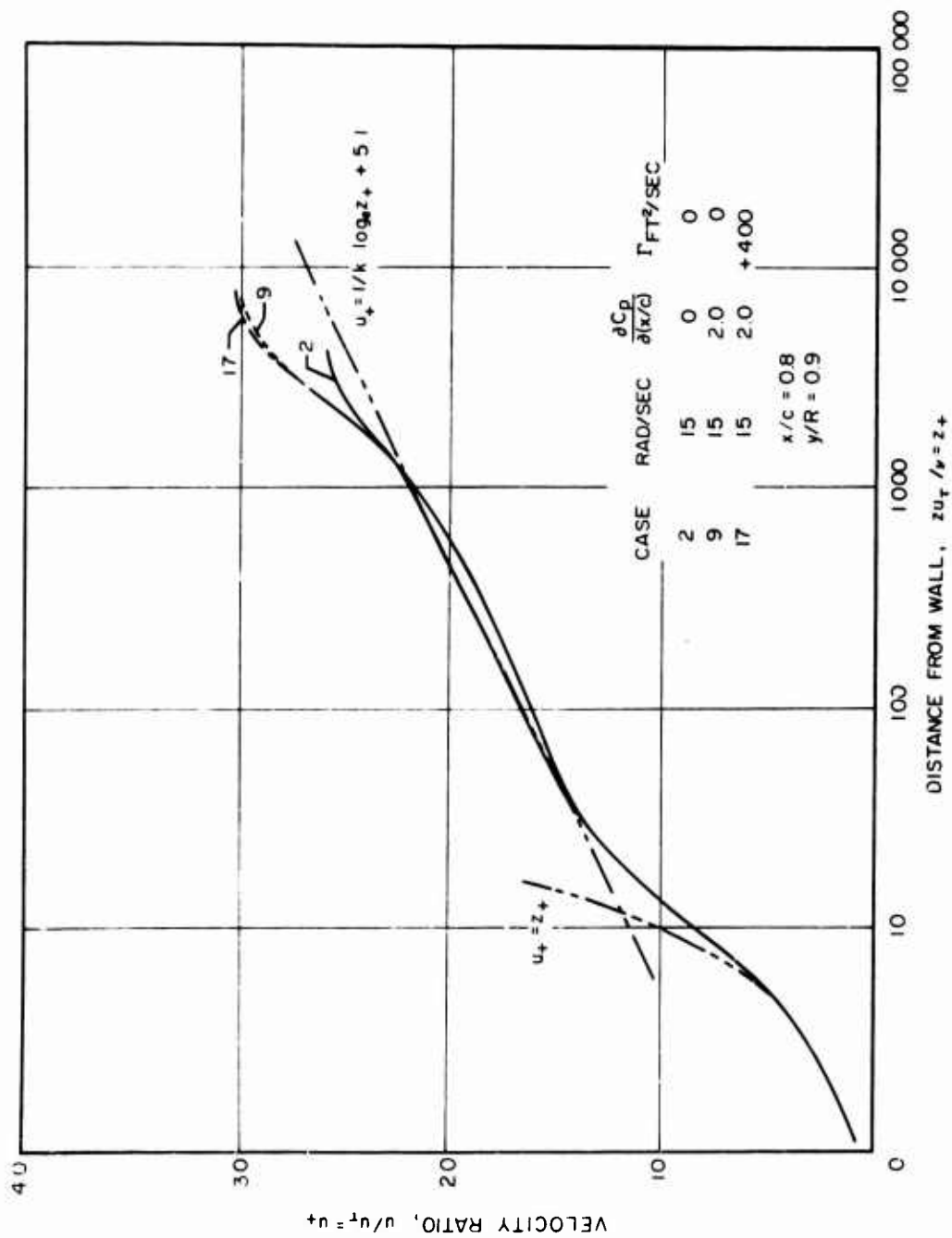
Figure 47. Concluded.

233

Figure 48. Comparison of Typical Calculated Velocity Profiles with Two-Dimensional Law of the Wall/Law of the Wake Form.
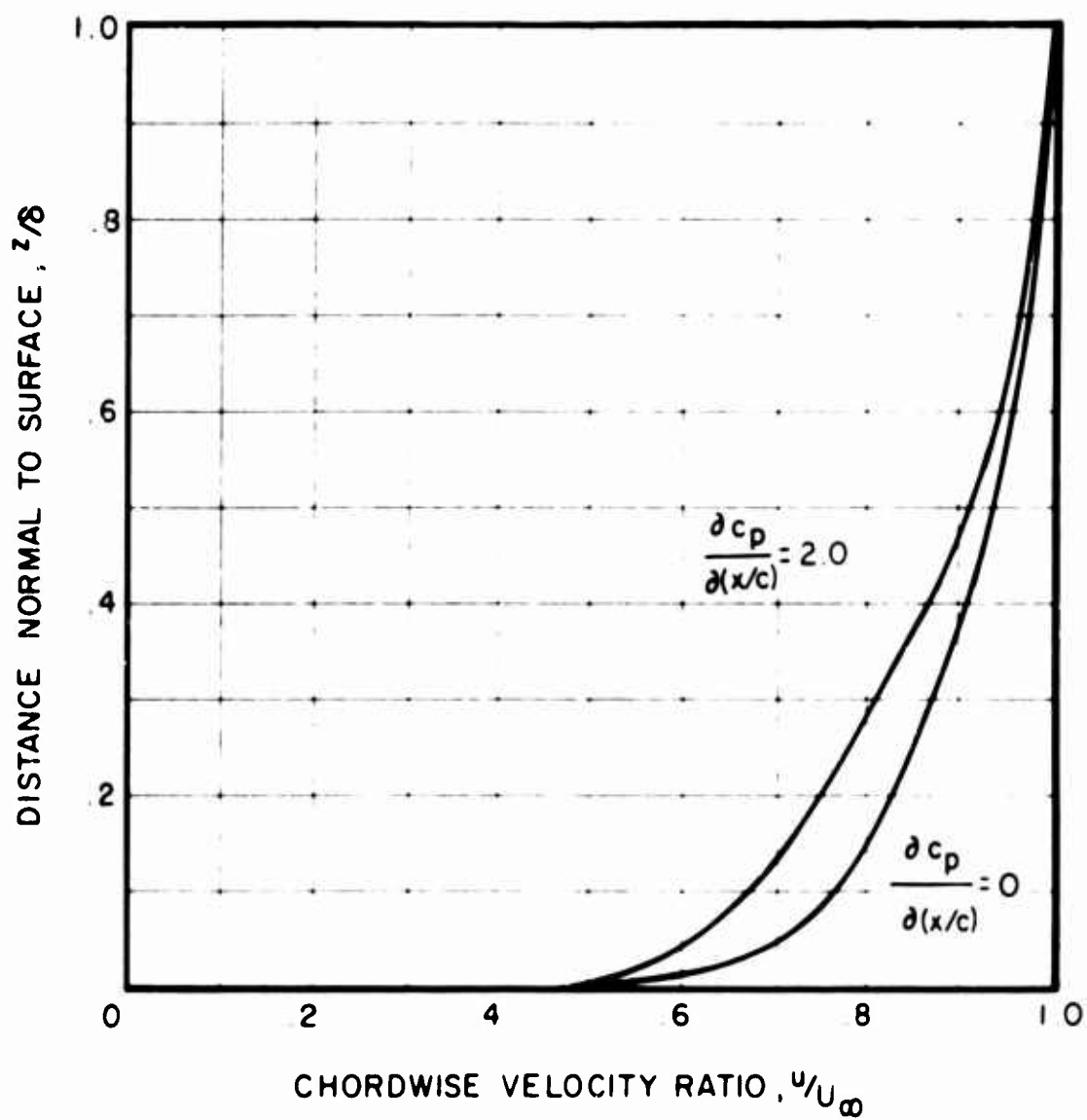
234

Figure 49. Typical Effect of Pressure Gradient on Chordwise
            Velocity Profiles, $\partial C_p/\partial(x/C) = 0, 2$,
            x/Chord = 0.8, y/R = 0.9, Ω = 15 rad/sec, Γ = 0.
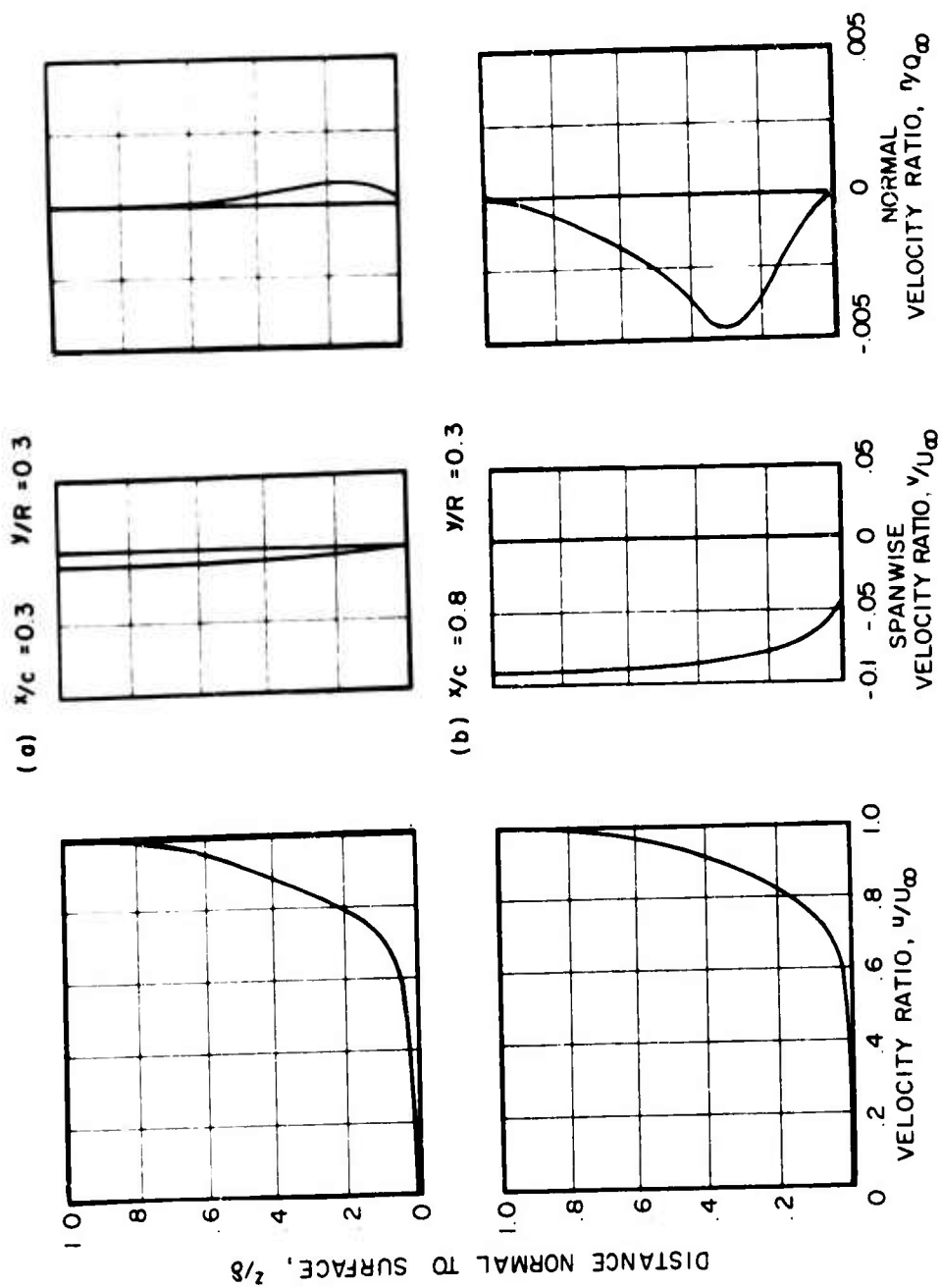
235

Figure 50. Comparison of Typical Chordwise, Spanwise and Normal Velocity Profiles.

236
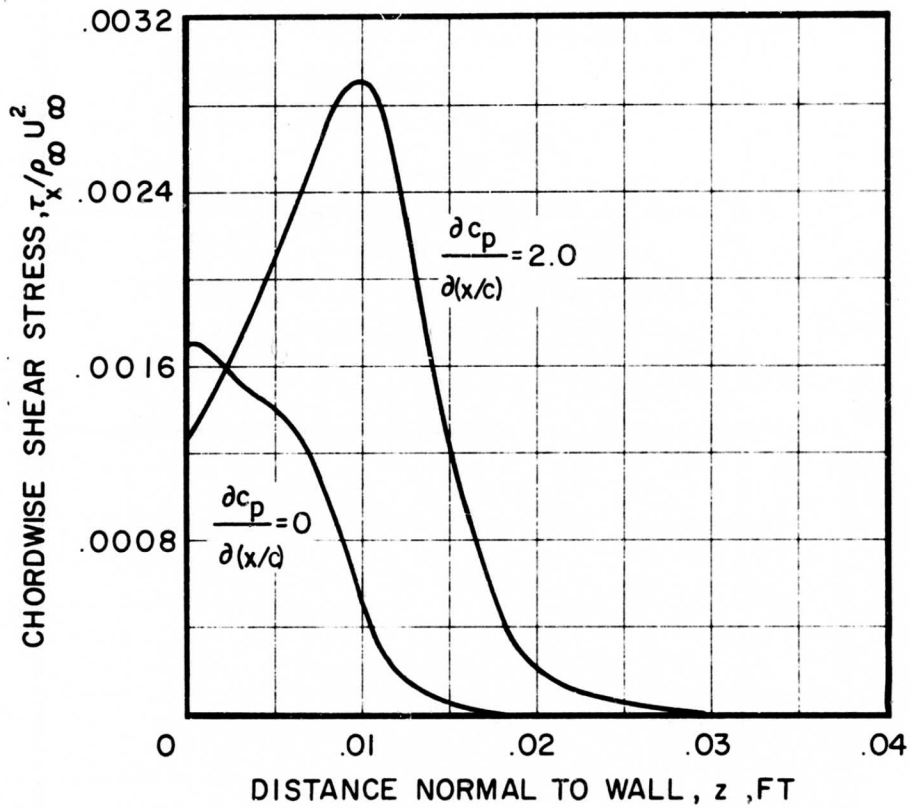
Figure 51. Typical Variation of Chordwise Shear Stress
Normal to the Surface, x/Chord = 0.8,
y/R = 0.6, Ω = 60 rad/sec, Γ = 0.

237
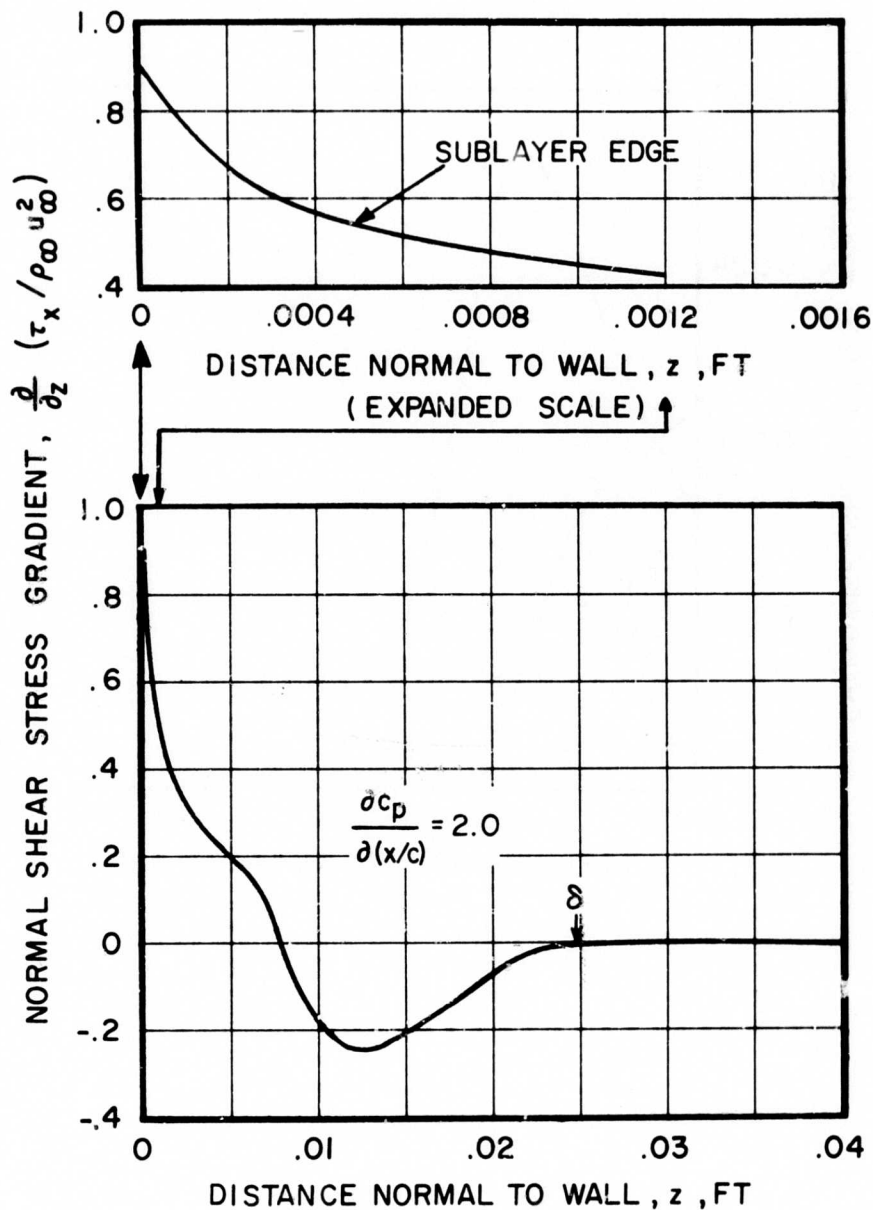
Figure 52. Typical Variation of the Normal Gradients of
Chordwise Shear Stress Normal to the Surface.
x/Chord = 0.8, y/R = 0.6, Ω = 60 rad/sec, Γ = 0.

238

LITERATURE CITED

1. von Karman, Theodore, UBER LAMINARE UND TURBULENTE REIBUNG, ZAMM, Vol. 1, 1921, pg. 233.

2. Sears, W. R., THE BOUNDARY LAYERS OF YAWED CYLINDERS, Journal Of The Aeronautical Sciences, Vol. 15, No. 1, January 1948, pg. 49.

3. Smith, P. D., CALCULATION METHODS FOR THREE-DIMENSIONAL TURBULENT BOUNDARY LAYERS, R. &. M. No. 3523, December 1966.

4. Dwyer, H. A., SOLUTION OF THE THREE-DIMENSIONAL BOUNDARY LAYER EQUATIONS BY A NUMERICAL METHOD, General Electric, Missile and Space Division, Report R675D54, August 1967.

5. Nash, J. F., THE CALCULATION OF THREE-DIMENSIONAL TURBULENT BOUNDARY LAYERS IN INCOMPRESSIBLE FLOW, Journal Of Fluid Mechanics, Vol. 37, Part 4, 1969, pg. 625.

6. Cochran, W. G., THE FLOW DUE TO A ROTATING DISK, Proceedings Of The Cambridge Philosophical Society, Vol. 30, 1934, pg. 365.

7. Fogarty, L. E., and Sears, W. R., POTENTIAL FLOW AROUND A ROTATING ADVANCING CYLINDRICAL BLADE, Journal Of The Aeronautical Sciences, Vol. 17, No. 19, September 1950, pg. 599.

8. Fogarty, L. E., THE LAMINAR BOUNDARY LAYER ON A ROTATING BLADE, Journal Of The Aeronautical Sciences, Vol. 18, No. 4, 1951, pg. 247.

9. Mager, A., GENERALIZATION OF BOUNDARY LAYER MOMENTUM INTEGRAL EQUATIONS TO THREE-DIMENSIONAL FLOWS INCLUDING THOSE OF ROTATING SYSTEM, NACA Report No. 1067, 1952.

10. Horlock, J. H., and Wordsworth, J., THE THREE-DIMENSIONAL LAMINAR BOUNDARY LAYER ON A ROTATING HELICAL BLADE, Journal Of Fluid Mechanics, Vol. 23, Part 2, 1965, pg. 305.

11. McCroskey, W. J., and Yaggy, P. F., LAMINAR BOUNDARY LAYERS ON HELICOPTER ROTORS IN FORWARD FLIGHT, AIAA Paper 68-70, Presented at the 6th AIAA Aerospace Sciences Meeting, New York, January 1968.

12. Young, W. H., and Williams, J. C., THE BOUNDARY LAYER ON ROTATING BLADES IN FORWARD FLIGHT, AIAA Paper 70-50, Presented at the 8th AIAA Aerospace Sciences Meeting, New York, January 1970.

13. McCroskey, W. J., and Dwyer, H. A., CROSSFLOW AND UNSTEADY BOUNDARY LAYER EFFECTS ON ROTATING BLADES, AIAA Paper 70-50, Presented at the 8th AIAA Aerospace Sciences Meeting, New York, January 1970.

14. Lindfield, A. W., Pinsent, H. G., and Pinsent, P. A., APPROXIMATE METHODS FOR CALCULATING THREE-DIMENSIONAL BOUNDARY LAYER FLOW ON WINGS, Boundary Layer and Flow Control, Oxford, England, Pergamon Press Ltd., 1961.

15. Weatherburn, C. E., ADVANCED VECTOR ANALYSIS, London, England, G. Bell and Sons, Ltd., 1960.

16. Schlichting, H., BOUNDARY LAYER THEORY, Sixth Edition, New York, McGraw-Hill, Inc., 1968.

17. Shapiro, A. H., THE DYNAMICS AND THERMODYNAMICS OF COMPRESSIBLE FLUID FLOW, New York, The Ronald Press Company, 1954.

18. Kline, S. J., Morkovin, M. V., Sovran, G., and Cockrell, D. J., Computation of Turbulent Boundary Layers - 1968 AFOSR-IFP-Stanford Conference, Stanford University, California, 1968.

19. McDonald, H., and Camarata, F. J., AN EXTENDED MIXING LENGTH APPROACH FOR COMPUTING THE TURBULENT BOUNDARY LAYER DEVELOPMENT, United Aircraft Research Laboratories, Computation of Turbulent Boundary Layers - 1968 AFOSR-IFP-Stanford Conference, Vol. 1, Stanford University, California, 1968, pg. 83.

20. McDonald, H., THE EFFECT OF PRESSURE GRADIENT ON THE LAW OF THE WALL IN TURBULENT FLOW, Journal of Fluid Mechanics, Vol. 35, Part 2, 1969, pg. 311.

21. von Doenhoff, A. E., and Tetervin, N., DETERMINATION OF GENERAL RELATIONS FOR THE BEHAVIOR OF TURBULENT BOUNDARY LAYERS, NACA Report No. 772, 1943.

22. Ludweig, H., and Tillman, W., INVESTIGATIONS OF THE WALL SHEARING IN TURBULENT BOUNDARY LAYERS, NACA TM 1285, 1950.

23. Squire, H. B., and Young, A. D., THE CALCULATION OF THE PROFILE DRAG OF AEROFOILS, R. & M. No. 1838, British A.R.C., 1938.

24. Lizak, A. A., TWO-DIMENSIONAL WIND-TUNNEL TESTS OF AN H-34 MAIN ROTOR AIRFOIL SECTION, Sikorsky Aircraft Division of United Aircraft, USAAVLABS Technical Report 60-53, U. S. Army Aviation Materiel Laboratories, Fort Eustis, Virginia, September 1960.

25. Clark, D. R., and Leiper, A. C., THE FREE WAKE ANALYSIS, Sikorsky Aircraft Division of United Aircraft Corporation, AHS 25th Annual National Forum Proceedings, May 1969.

26. Jenney, D. S., Olson, J. R., and Landgrebe, A. J., A REASSESSMENT OF ROTOR HOVERING PERFORMANCE PREDICTION TECHNIQUES, Sikorsky Aircraft Division of United Aircraft Corporation, AHS 23rd Annual National Forum Proceedings, May 1967.

27. Coles, D., THE LAW OF THE WAKE IN THE TURBULENT BOUNDARY LAYER, _Journal of Fluid Mechanics_, Vol. 1, 1956, pg. 191.

28. Rannie, W. D., _Journal of Aeronautical Sciences_, Vol. 23, 1956, pg. 485.

APPENDIX

Determination of Sublayer Shear Stress Gradients

It has been demonstrated by several authors, but most recently in Reference (20), that in two-dimensional flow the shear stress gradient normal to the wall may be represented, in the region close to the wall, by the expression

$$\frac{\partial \tau}{\partial z} = A_0 + A_2 u_+^2$$

where A_0 and A_2 are constants obtained from the equation of motion evaluated at the wall and u_+ is the commonly employed velocity ratio u/u_τ. If the law of the wall is assumed valid in three-dimensional flow, then similar relations may be derived in three-dimensional flows. They will be

$$\frac{\partial \tau_x}{\partial z} = \frac{dp}{dx} - 2\Omega\rho v - \rho\Omega^2 x + u_\tau u_+^2 \frac{\partial}{\partial x}(u_\tau)$$

$$\frac{\partial \tau_y}{\partial z} = \frac{dp}{dy} + 2\Omega\rho u - \rho\Omega^2 y + u_\tau \frac{v}{u} u_+^2 \frac{\partial}{\partial x}(u_\tau)$$

(63)

Expanding Equations (63) and substituting for the pressure gradients gives the expanded form

$$\frac{\partial \tau_x}{\partial z} / \rho_\infty U_\infty^2 = -2\left[\frac{\Omega}{U_\infty}\right]\left[\frac{\rho}{\rho_\infty} s - \frac{V_\infty}{U_\infty}\right] - \left[\frac{\Omega}{U_\infty}\right]^2 \left[\frac{\rho}{\rho_\infty} - 1\right] x$$

$$+ \left[\frac{\rho}{\rho_\infty} c^2 - 1\right]\frac{1}{U_\infty}\frac{\partial U_\infty}{\partial x} + \left[\frac{\rho}{\rho_\infty} sc - \frac{V_\infty}{U_\infty}\right]\frac{1}{U_\infty}\frac{\partial U_\infty}{\partial y} + \frac{\rho}{\rho_\infty}\frac{c^2}{2Cf_x}\frac{\partial Cf_x}{\partial x}$$

$$\frac{\partial \tau_y}{\partial z} / \rho_\infty U_\infty^2 = +2\left[\frac{\Omega}{U_\infty}\right]\left[\frac{\rho}{\rho_\infty} c - 1\right] - \left[\frac{\Omega}{U_\infty}\right]^2 \left[\frac{\rho}{\rho_\infty} - 1\right] y$$

$$+ \left[\frac{\rho}{\rho_\infty} c^2 - 1\right]\frac{1}{U_\infty}\frac{\partial V_\infty}{\partial x} + \left[\frac{\rho}{\rho_\infty} sc - \frac{V_\infty}{U_\infty}\right]\frac{1}{U_\infty}\frac{\partial V_\infty}{\partial y} + \frac{\rho}{\rho_\infty}\frac{s}{c}\frac{c^2}{2Cf_x}\frac{\partial Cf_x}{\partial x} \quad (64)$$

Terms involving gradients of the chordwise shear stress in the spanwise direction and all gradients of the spanwise shear stress are of small order and have been dropped from Equations (64).

The equations may be simplified to

$$\frac{\partial \tau_x}{\partial z} = A_0 + A_1 f_x(z) + A_2 u_+^2 \qquad (65)$$

and

$$\frac{\partial \tau_y}{\partial z} = B_0 + B_1 f_y(z) + B_2 u_+^2$$

The middle term, absent in the two-dimensional form, is a result of the presence of the Coriolis and centrifugal terms.

The fit to the profiles outside the sublayer was carried out through the u_+^2 term. A curve was fitted through the five points just outside the sublayer and the coefficients A_2 and B_2 in Equations (65) were forced to give agreement. This means essentially that the chordwise gradient of the skin friction is being determined from the normal gradient of shear stress outside the sublayer.